

**Exploring Models of Lensing Galaxies -  
On Bridging the Gap between Observations, Models, and Simulations**

---

**Dissertation**

**zur**

**Erlangung der naturwissenschaftlichen Doktorwürde  
(Dr. sc. nat.)**

**vorgelegt der**

**Mathematisch-naturwissenschaftlichen Fakultät**

**der**

**Universität Zürich**

**von**

Philipp Denzel

**von/aus**

Deutschland

**Promotionskommission**

Prof. Dr. Romain Teyssier (Vorsitz)

Prof. Dr. Prasenjit Saha (Leitung der Dissertation)

Prof. Dr. Robert Feldmann

Dr. Ignacio Ferreras

**Zürich, 2020**



Doctoral Dissertation

**Doctoral Dissertation**

**Exploring models of lensing galaxies**

**On bridging the gap between observations, models, and simulations**

Philipp Denzel

October 6, 2020

University of Zürich



For the one who will never read it.

– Philipp Denzel



*"... ipsa quoque adsiduo labuntur tempora motu,  
non secus ac flumen. neque enim consistere flumen,  
nec levis hora potest, sed ut unda inpellitur unda,  
urgeturque prior veniente urgetque priorem,  
tempora sic fugiunt pariter pariterque sequuntur  
et nova sunt semper. nam quod fuit ante, relictum est,  
fitque, quod haut fuerat, momentaque cuncta novantur.  
Cernis et emensas in lucem tendere noctes,  
et iubar hoc nitidum nigrae succedere nocti..."*

*While time itself glides on with ceaseless motion, not unlike a river. And like the stream that cannot stay, neither can the restless hour. Like wave impelled by wave, it hastens onward, both driven by and driving the next, so flee the times as they are being followed, and always they are anew. For what was, has ceased to be, and will become what never has been, and the moments are all renewed. You see, the departing darkness tends into the light, like the radiating heavenly body leads into the night.*

– Ovid Metamorphoses, Liber XV, 179-187



# Abstract

Galaxies changed our view of the Universe and of the nature of the fundamental forces repeatedly. They are tracers of the Universe's large-scale structure and its evolution for the last 13 billion years or more. They are also "factories" where cold hydrogen gas fuels the formation of stars, which leads to the production of heavier elements, and eventually to life. Moreover, it appears that the luminous matter in galaxies only accounts for 1 to 5% of their entire mass, and the rest is seemingly invisible. The exact nature of their "dark" components is perhaps the gravest enigma of modern science. Exploring and understanding galaxies, their formation, and evolution is therefore of paramount interest to cosmology, particle physics, astronomy, and astrophysics.

In this thesis, we explore how models of galaxies can be incorporated with observations of the strong gravitational lensing phenomenon in order to test galaxy formation theories. Despite the unique circumstances leading to lensing systems which provide the opportunity to unravel otherwise hidden properties of their lensing galaxies, lens-modelling attempts have yet to consistently yield quantifiable constraints on galaxy formation scenarios. Conventional lens-modelling techniques use a set of parameters to describe the form of lensing galaxies. Here, we first examine free-form lens models and apply measured time delays of lensed quasars in order to constrain the cosmological parameter for the rate of cosmic expansion, the Hubble constant, but also to optimize the lens models themselves. Furthermore, a particularly interesting study of an extraordinary lensing system is presented for which lens models indicate a distinct type of galaxy, a fossil group galaxy, which is considered the final phase of a group galaxy's evolution. We then investigate drawbacks and issues of such free-form lens models in a blind-study with simulated lenses. While conventional techniques conveniently and efficiently generate models, they remain rather simplified. Galaxy-formation simulations on the other hand, are highly tuned to produce realistic galaxy models from first principles. For this reason, we tested the plausibility of utilizing such simulations for a direct comparison to lensing data. At last, we propose a novel strategy which efficiently matches projected galaxy models from simulations to lensing observations and evaluates relative posterior probabilities of the underlying galaxy formation scenarios. In future, such methods are essential for upcoming wide-field surveys, as they will increase the number of galaxy lenses, and thus the workload, possibly a hundredfold.



# Preface

This thesis consists of a long introduction which should convey background information and a good summary of all following chapters, and connect them in a single line-of-thought. The subsequent chapters, describe individual projects (with designated code names) which were or are to be published in scientific journals.

In order to avoid confusion and arguments about mathematical correctness, I here emphasize that throughout the text, I tried my best to keep consistency: for vectors I used bold notation, and since in lensing theory most things are calculated on a 2D surfaces, the nabla operator  $\nabla$  denotes gradients on those surfaces. Likewise, the inverse Laplace operator denoted  $\nabla^{-2}$ , describes the integral form of a Laplace equation (and formally corresponds to a convolution with a “free-space” Green’s function).

Being Prasenjit Saha’s PhD student, one eventually learns to realize that units are tools to point out relations between different physical observables, and that 1 solar mass and 5 microseconds can sometimes express the same concept. Similarly, 1 Astronomical Unit has 500 seconds, and 1 year has pretty much  $20'000\pi$  times more. As soon as those relations become implicit, it is natural to forget about the not-so-important G’s and c’s and one may even dare to set them 1. I tried my best to make my mathematical formulations and estimates easy to read, but if at some point in the thesis the units of an equation or a statement seem to have mysteriously vanished (usually on purpose to emphasize the important quantities), I refer to the Appendix which might list some of the keys to solve the puzzle.

Finally, I would like to thank a couple of dear friends and colleagues. First of all to Prasenjit Saha for all his help and guidance. He always was a catalyst and supporter of the more creative ideas, and convinced me that the unconventional paths taken are much more fun, especially if they improve and motivate change in old-fashioned and outdated matters. To Sampath Mukherjee, for all his support and supply of lens-friendly galaxy-formation scenarios. To Jonathan Coles, who always had useful advice when it was needed. To Liliya L. R. Williams, for lending me her expertise in all things lensing, even if sometimes it was very early in the day for her. Also to Ignacio Ferreras, who taught me how to decipher stellar light and bring some colour to my lens maps. Next, to Rafael Souza Lima and Tomas Tamfal for their camaraderie. They were the greatest office mates, and were always up for interesting scientific musings. (We especially enjoyed talking about the warped side of the Universe and grand unification theories.) My time in the Institute for Computational Science was made engaging, enjoyable, and fun by so many others as well. I owe thanks to each one of them. But my biggest thanks go to my parents and my brother. Without their support in all aspects, my academic journey would simply have not been possible.



# Contents

<b>Abstract</b>	vii
<b>Preface</b>	ix
<b>Contents</b>	xi
<b>1 Introduction</b>	1
1.1 The expanding Universe . . . . .	4
1.2 Lens models . . . . .	8
1.3 Galaxies . . . . .	12
1.4 Summary . . . . .	18
1.4.1 Inferring the Hubble constant . . . . .	20
1.4.2 Lens recovery of SW05 . . . . .	21
1.4.3 Models of simulations . . . . .	22
1.4.4 The lens-matching method . . . . .	23
<b>2 DELAYS</b>	25
2.1 Introduction . . . . .	27
2.2 The lens systems . . . . .	30
2.2.1 B1608+656 . . . . .	30
2.2.2 DESJ0408-5354 . . . . .	32
2.2.3 HE0435-1223 . . . . .	32
2.2.4 PG1115+080 . . . . .	32
2.2.5 RXJ0911+0551 . . . . .	33
2.2.6 RXJ1131-1231 . . . . .	33
2.2.7 SDSSJ1004+4112 . . . . .	33
2.2.8 WFIJ2033-4723 . . . . .	33
2.3 Lens reconstruction method . . . . .	34
2.3.1 GLASS . . . . .	34
2.3.2 Point-image data . . . . .	36
2.3.3 Extended image data . . . . .	36
2.3.4 TDLMC . . . . .	36
2.4 Results . . . . .	39
2.4.1 Arrival-time surfaces . . . . .	39
2.4.2 Convergence maps . . . . .	39
2.4.3 Synthetic images . . . . .	40
2.4.4 $H_0$ posterior distribution . . . . .	41
2.4.5 Comparison with TDLMC . . . . .	42
2.5 Conclusion . . . . .	43
2.6 Figures . . . . .	45
<b>3 FOSSIL</b>	55
3.1 Introduction . . . . .	57
3.2 The system J143454.4+522850 . . . . .	58
3.3 The lensing mass . . . . .	61
3.4 The stellar mass . . . . .	63
3.5 Comparison with simulations . . . . .	65
3.6 Discussion . . . . .	67

<b>4 ADLER</b>	<b>69</b>
4.1 Introduction . . . . .	71
4.2 Theory . . . . .	73
4.2.1 Arrival-time surface . . . . .	73
4.2.2 Lensing Roche potential . . . . .	73
4.2.3 Lensing mass quadrupole . . . . .	74
4.2.4 Image formation . . . . .	74
4.3 Methods . . . . .	75
4.3.1 SEAGLE . . . . .	75
4.3.2 GLASS . . . . .	76
4.3.3 Source reconstruction and synthetic images . . . . .	77
4.3.4 Model comparison . . . . .	78
4.4 Results . . . . .	79
4.4.1 Lens reconstructions . . . . .	80
4.4.2 Convergence map comparison . . . . .	81
4.4.3 Roche potential comparison . . . . .	82
4.5 Conclusion . . . . .	85
4.6 Figures . . . . .	87
<b>5 MATCH</b>	<b>99</b>
5.1 Introduction . . . . .	101
5.2 The plausible-match method . . . . .	102
5.2.1 Data adaptation . . . . .	103
5.2.2 Synthetic images . . . . .	104
5.3 SEAGLE . . . . .	106
5.3.1 A Constant Feedback (FBconst) . . . . .	107
5.3.2 Temperature variation in AGN heating (AGNdT8) . . . . .	107
5.4 The observed systems . . . . .	108
5.4.1 SDSSJ0029–0055 . . . . .	108
5.4.2 SDSSJ0737+3216 . . . . .	109
5.4.3 SDSSJ0753+3416 . . . . .	109
5.4.4 SDSSJ0956+5100 . . . . .	109
5.4.5 SDSSJ1051+4439 . . . . .	110
5.4.6 SDSSJ1430+6104 . . . . .	110
5.4.7 SDSSJ1627–0053 . . . . .	110
5.5 Results . . . . .	111
5.5.1 Images . . . . .	111
5.5.2 Source reconstructions . . . . .	112
5.5.3 Mass maps . . . . .	112
5.5.4 Lensing Roche potentials . . . . .	113
5.6 Discussion . . . . .	113
5.7 Figures . . . . .	115
<b>APPENDIX</b>	<b>123</b>
<b>A Mathematical approximations</b>	<b>125</b>
<b>Bibliography</b>	<b>127</b>

# List of Figures

1.1 Mock lens image of M82 . . . . .	1
1.2 Conceptual research graph . . . . .	3
1.3 Lensing geometrics . . . . .	10
1.4 The Milky Way: APOD 2008 January 4 . . . . .	13
1.5 Stellar-to-lens mass ratios of lensing galaxies . . . . .	18
2.1 The main result: Hubble constant posterior . . . . .	30
2.2 Composite HST images of the time-delay lenses . . . . .	31
2.3 Arrival-time surfaces of the time-delay lenses . . . . .	46
2.4 Convergence models of the time-delay lenses . . . . .	47
2.5 Radial profiles of mean enclosed convergences . . . . .	48
2.6 Principal component projections of WFIJ2033-4723's convergence model . . . . .	49
2.7 Comparison of synthetic lensed images to photometric data . . . . .	50
2.7 (Continued) Note that RXJ0911+0551 east is shown mirror-inverted. . . . .	51
2.8 Ensemble of Hubble constant values . . . . .	52
2.9 Ensemble of Hubble time values . . . . .	52
2.10 Ensemble of cosmological critical density values . . . . .	52
2.11 Results from the Time Delay Lens Modelling Challenge . . . . .	53
3.1 Composite image of SW05 . . . . .	59
3.2 The neighbourhood of SW05 . . . . .	60
3.3 Arrival-time surface of the ensemble-average model for SW05 . . . . .	62
3.4 Synthetic-images and source fits from the ensemble-average lens model . . . . .	63
3.5 Spectral energy distribution of 12 stellar population synthesis base models . . . . .	64
3.6 Stellar-to-lens mass surface density map . . . . .	65
3.7 Enclosed mass profiles of SW05 in comparison with FIRE galaxy models . . . . .	66
3.8 Derived velocity dispersion profiles of SW05 in comparison with FIRE galaxy models . . . . .	68
4.1 Lensing degeneracies demonstrated . . . . .	72
4.2 Source-reconstruction and Roche-scalar optimized synthetic images . . . . .	84
4.3 SEAGLE lens images . . . . .	88
4.4 Synthetic images of SEAGLE models . . . . .	89
4.5 Arrival-time surfaces of SEAGLE models . . . . .	90
4.6 True convergence maps of SEAGLE lenses . . . . .	91
4.7 Convergence maps of SEAGLE models . . . . .	92
4.8 Averaged convergence profiles of SEAGLE ensemble models . . . . .	93
4.9 Ellipticity graphs of SEAGLE models . . . . .	94
4.10 True Roche-potential contours of SEAGLE lenses . . . . .	95
4.11 Roche-potential contours of SEAGLE models . . . . .	96
4.12 $\chi^2$ vs. Roche scalar of SEAGLE reconstructions . . . . .	97
5.1 Radial profiles of the entire catalogue . . . . .	103
5.2 SDSSJ0029-0055: plots of the most plausible match . . . . .	116
5.3 SDSSJ0737+3216: plots of the most plausible match . . . . .	117
5.4 SDSSJ0753+3416: plots of the most plausible match . . . . .	118
5.5 SDSSJ0956+5100: plots of the most plausible match . . . . .	119

5.6	SDSSJ1051+4439: plots of the most plausible match . . . . .	120
5.7	SDSSJ1430+6104: plots of the most plausible match . . . . .	121
5.8	SDSSJ1627-0053: plots of the most plausible match . . . . .	122

## List of Tables

2.1	Input parameters for point-image models of the time-delay galaxies . . . . .	38
2.2	Reduced least squares from the source reconstructions of the time-delay systems.	41
5.1	Selected test cases from the SLACS survey . . . . .	108
5.2	Most plausible matches for each SLACS lens . . . . .	111





# 1

## Introduction

On May 29, 1919 during a total solar eclipse, three scientists, Eddington, Dyson, and Davidson, tried to find out what effect, if any, is produced by a gravitational field on the path of a light ray traversing it [1]. During a thoroughly prepared expedition, they measured the deflection of positions of stars in the well-known Hyades constellation caused by the mass of the Sun as predicted by the theory of gravity, general relativity. This was the first observation of gravitational lensing, as well as the first predicted and validated effect of general relativity [2].

Effectively, gravitational lensing is entirely analogous to optical lenses. In fact, to produce the distorted light signatures like they are observed in gravitational lens systems, one only needs a stem and the base from a wine glass and move it in front of a light source. [phdenzel.github.io/zurich-lens/](https://phdenzel.github.io/zurich-lens/) provides an interactive toy example of such a situation. In optics, the lens comprises a glass sheet of variable thickness. It deflects light by an amount proportional to the local depth. The physical process which causes the change of direction when a ray traverses a glass lens, is called refraction. It describes the delay, i.e. decrease in speed of light, due to the change of media and therefore a change in direction. While the result of lensing is the same for both optical and gravitational lenses, the latter causes the delay and deflection due to the change of the felt gravitational potential as light moves through it. The rather rare occurrence of a perfect alignment of a background source, a quasar for instance, and a massive foreground lens in which the imaged source is distorted in a way such that it can be observed multiple times or even as a ring wrapping around the lens, is called *strong* gravitational lensing. Figure 1.1 demonstrates such a case with a mock lens.



1.1 The expanding Universe . . . . .	4
1.2 Lens models . . . . .	8
1.3 Galaxies . . . . .	12
1.4 Summary . . . . .	18
Inferring the Hubble constant	20
Lens recovery of SW05 . . . . .	21
Models of simulations . . . . .	22
The lens-matching method .	23

**Figure 1.1:** Mock lens observation: The left image shows the "Cigar Galaxy" M82 cutout from [APOD 2020 May 15](#). The right image demonstrates what it could look like, if for instance a small black hole with the mass of the Sun would replace the Moon. The right image was generated using my lens mock code: `lensing.js` [3]. *Image Credit & Copyright: Dietmar Hager, Torsten Grossmann*

More specifically, the deflection in gravitational lensing is of the order of  $4M/R$ , where  $M$  is the mass of the lens and  $R$  its size. Strong gravitational lensing occurs when the apparent size  $R/D$  of the aligned lens at a distance  $D$  is comparable to that deflection [4]. In fact, although the underlying physical process is all the same, gravitational lensing is

categorised into three types based on the observational techniques and mass or size regimes: and *micro*, *strong*, and *weak* lensing. Note that in the following equation and the entire introduction of this thesis, we assume  $c = G = 1$ , which enables us to express distances and masses in units of seconds, mass densities and velocity gradients in units of square seconds etc.

$$\begin{array}{ll} \text{micro} & \frac{4M}{R} \gg \frac{R}{D} \\ \text{strong} & \frac{4M}{R} \gtrsim \frac{R}{D} \\ \text{weak} & \frac{4M}{R} < \frac{R}{D} \end{array} \quad (1.1)$$

Microlensing is in many cases due to small, compact, and massive objects such as stars, or even exoplanets around stars. While it technically also projects a source in multiple images, their angular separation is typically of the order of microarcseconds — hence the name — and therefore impossible to resolve with even the most modern telescopes. Nevertheless, in microlensing the changes in the source alignments express as changes in apparent brightness, which is detectable over an observation period of  $\sim 100$  days. Weak lensing on the other hand, happens when the gravitational field of the lens is not strong enough to create multiple images, and the observable effect is a distortion which is only detectable in a statistical sense.

Most gravitational lenses lie at cosmological distances, and only very massive, large, and mass-concentrated objects can in this case lead to strong lensing features. Galaxies are vast cosmic islands of stars, gas, dust, and mainly non-luminous matter held together by gravity. This puts them in an ideal mass and size range to act as such strong-lensing systems. Based on most recent observations, it is estimated that there are more than 2 trillion galaxies in the Universe [5], however so far less than a thousand gravitational lenses have been found across various data sets. This makes them quite the rare beasts in comparison... at least for now. Future space and ground-based telescope missions however, such as the *Square Kilometer Array* (SKA), the *Vera Rubin Observatory* (formerly known as *Large Synoptic Survey Telescope*, or LSST), the *James Webb Space Telescope* (JWST), and *Euclid* are expected to find orders of magnitudes more. This is very promising for science, because, due to their very special circumstances, lensing galaxies and their configurations can be modelled and give otherwise unobtainable insights into galaxy structure. The task of lens models is to describe particular shapes of the lensing galaxy's mass distribution which produces deflections of one or more background sources which agree with the observed lensed images. The fact that gravity and thus lensing is indiscriminate of the kinds of matter which cause the deflections, makes it all the more interesting. In this regard, gravitational lenses are often seen as 'proof'<sup>1</sup> for invisible and non-luminous matter, commonly called *dark matter*, without which the observed deflections due to galaxies cannot be explained by general relativity.

[5]: Conselice et al. (2016)

1: Not the only proof, as explained in following sections.

Finding connections between these matter components, how they assembled, and how they dynamically interact within galaxies is still subject of ongoing research. Solving galaxy formation and evolution is a crucial part in understanding the evolution of the Universe as a whole and the physical laws driving it. During the last two decades, large-scale

hydrodynamical simulations have yielded great successes and managed to produce galaxy models which agree with astronomical observations incredibly well. In contrast, lens models still struggle to conform with physical properties and are hard to interpret. Some describe lens reconstruction techniques as ‘black art’ [6], perhaps because they produce models which are, if at all, only barely motivated by physical processes which are believed to be key in the dynamics of galaxies. Another reason might be the confusion seeded by very opposing opinions<sup>2</sup> of how these lens models should be constructed. Nevertheless, while there are advocates for certain (and not other) approaches, they all agree that these lens systems are, scientifically speaking, highly valuable and promise to uncover mysteries surrounding galaxy evolution, the nature of dark matter, galaxy substructures, and the expansion of the Universe.

The main theme of this thesis is to explore old and new ways of connecting the three cornerstones of lensing research, *lensing galaxies* from observations, *lens models* which try to reproduce observations, and *simulations* of galaxies. The following chapters detail projects with that aim, each designated by a project name: DELAYS (Chapter 2), FOSSIL (Chapter 3), ADLER (Chapter 4), and MATCH (Chapter 5).

[6]: Meylan et al. (2006)

2: Excerpt from Meylan et al. [6]: “I will argue that the parametric models are all that is needed to model lenses and that they provide a better basis for understanding the results than non-parametric models (but the reader should be warned that if Prasenjit Saha was writing this you would probably get a different opinion).”

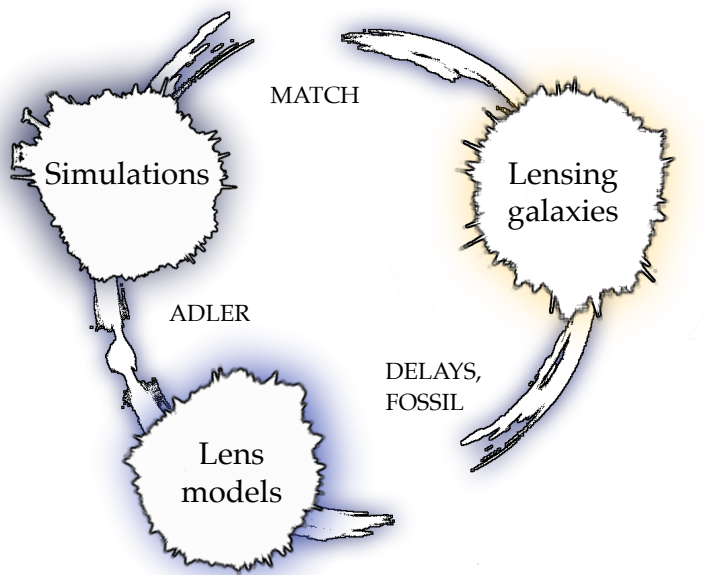


**Figure 1.2:** Conceptual graph: the outline of this fictional lensing system perfectly construes the current state of lensing research. Simulations of galaxies have been shown to be physically realistic and have successfully been inferred by lens models in (blind) tests. However, lens models still struggle to uniquely describe lensing galaxies in observations and a direct link from simulations to lensing galaxies has so far never even been explored before. The projects in the subsequent chapters thematise these subjects and their connections.

Attempts to describe lensing galaxies with models of lens systems have been made since the very first discovery by Walsh et al. [7] in 1979. In Chapter 2 and 3, new techniques were developed to optimise lens recovery — still rather traditionally — with time delay measurements or stellar population synthesis models respectively. Even with more physical information on the lensing galaxies, the models were difficult to properly constrain and revealed certain issues and limitations. The subsequent project in Chapter 4 reports on a blind test which further explores these problems with mock lenses from large-scale hydrodynamical simulations. Particularly hard to solve is the issue of degeneracies, the fact that a lens configuration can be caused by many, differently shaped lenses, which is a long-known, inherent limitation to lens models. It also proposes analysis techniques which can be employed in this case to isolate these problems. Finally, Chapter 5 gives proof-of-concept for an entirely new

[7]: Walsh et al. (1979)

strategy, a lens ‘matching’ technique, which provides a direct link from simulations to lensing galaxies in observations.

The following sections introduce the subsequent chapters and cover some basics and related topics in the schematic of Figure 1.2. They elaborate on a few key aspects in cosmology (Section 1.1), some basic lensing theory (Section 1.2), and theoretical and observational background related to galactic dynamics, in particular focusing on topics relevant to galaxies in lensing systems (Section 1.3). Finally, the subsequent chapters are put into context and shortly summarized in Section 1.4.

## 1.1 The expanding Universe

Like most fundamental theories in physics which helped in the present-time understanding of our Universe and the interactions within, general relativity was formulated in the early 20th century. While the word was spreading of Einstein’s construct of the supposedly quasi-static Universe which involved a ‘cosmic constant’ to keep it so, Vesto Melvin Slipher and Edwin Hubble performed the key measurements which provided the connection between theory and observations. By 1923, Slipher’s hard work yielded a compilation of velocity estimates for 41 galaxies. Remarkably, most of those galaxies were receding from us, and thus appeared redshifted<sup>3</sup>. Half a decade afterwards, Edwin Hubble investigated the relation between his distance measurements to these galaxies and their radial velocities. Thereby, he effectively measured an apparently constant velocity gradient in units of  $\text{km s}^{-1} \text{Mpc}^{-1}$ . This constant was later named after him, the *Hubble constant*  $H_0$ . Through this velocity gradient he realised something, which could arguably be called the birth of modern cosmology: the concept of an expanding Universe would explain why all galaxies are receding from us and each other [8, 9]. The outward motion of galaxies resulting from the uniform expansion of the Universe is best observable at very high distances where the local, mutual gravitational interaction between galaxies is subdominant. This behaviour is commonly referred to as the *Hubble flow*.

Hubble’s realisation was an impressive leap of thought, even more so, since the prevalent idea of the Universe at the time was synonymous to today’s picture of our own galaxy, the Milky Way, beyond which the existence of anything else was uncertain. Only around 1920, astronomers started considering that what they called nebulae were in fact extragalactic ‘island universes’ that is entirely other galaxies. Today, there are ‘standard’ recipes for recreating and improving upon Hubble’s results<sup>4</sup> by gathering distance and velocity or redshift estimates to galaxies and other astronomical objects which are much further away. While this might seem like a simple task, the matter of measuring distances relates to problems with which cosmology struggles still today.

The most ‘human’ method of measuring distances is the *parallax*. It essentially utilises the same principles as the human eye. With two points of observation, an astronomical, stereoscopic vision is achieved from which the distance can be estimated. However, with even the most sophisticated technologies reaching high angular resolution, parallax has only very little reach. Since the main objective in cosmology is to study the

<sup>3</sup>: The recession velocity of a galaxy can be measured by the (Doppler) shift of its spectral lines, i.e. redshift.

[8]: Kirshner (2004)  
[9]: Hubble (1929)

While one would expect such a finding to be highly cited, Hubble’s publication interestingly counts only 73 official citations at the time of writing.

<sup>4</sup>: He determined the Hubble constant by the slope of his iconic diagram with roughly  $H_0 \approx 500 \text{ km/s/Mpc}$ . Today, most measurements yield an  $H_0$  of around 70 km/s/Mpc.

Universe's large-scale structures from birth to the present, this technique is relatively ineffective as it rarely reaches objects able to probe the Hubble flow. Still, it is generally used as calibration for other techniques with longer reach. An especially powerful application of the parallax is the measurement of distances to galaxies containing megamasers, gas clouds with water molecules which catalyse the emission of coherent microwave radiation. Distances to these emission points can be determined to incredible precision with long baseline interferometers and spectral monitors. Another strong influence of the parallax technique is reflected in the distance unit 'parallax second' which is usually shortened to *parsec* and ubiquitously employed in astronomy and astrophysics. It is the distance where 1 astronomical unit (AU; the nominal distance of Earth to the Sun) spans 1 arcsecond on the sky. Using A.1 and A.2, we can write:

$$1 \text{ pc} = 1 \text{ AU} \times \tan(1 \text{ arcsec})^{-1} \approx 10^8 \text{ lightsec} \quad (1.2)$$

Distance measurements sensitive to the expansion of the Universe have to rely on different strategies.

In an expanding, flat Universe many different measures of distances can be defined. For example, it can be very useful to factor out the expansion and define the so-called *comoving distance*

$$D_{\text{comov}} = \frac{1}{H_0} \int_0^z \frac{d\zeta}{\sqrt{\Omega_m(1 + \zeta)^3 + \Omega_r(1 + \zeta)^4 + \Omega_\Lambda}}. \quad (1.3)$$

where  $z$  is the redshift of the light to which the distance is measured, and  $\Omega_i = \rho_i/\rho_c$  are the relativistic, non-relativistic, and dark energy components, normalised by the cosmological critical density  $\rho_c$ . Every component contributes at various scales differently to the expansion or contraction of the Universe, and therefore have to be considered separately when distances are measured. In a flat Universe, the cosmological critical density is its average density  $\propto H_0^2/G$ . The comoving distance does not change with time, assuming the observers are moving with the Hubble flow. Another measure which is especially often used in the context of lensing, is the *angular-diameter distance* which is defined as an object's physical size over its angular size as viewed from Earth. It can also be written as

$$D_{\text{ang}} = \frac{D_{\text{comov}}}{(1 + z)} \quad (1.4)$$

It is the distance which freezes the Universe at the time when the light which is used to measure it, is emitted. This leads to a very peculiar behaviour that beyond some redshift the angular-diameter distance actually decreases with increasing redshift.

For a long time, light from very bright sources represented the only way of measuring distances in astronomy<sup>5</sup>. Just like lighthouses acted as distance markers and warning signals for reefs and promontories to mariners since ancient times, bright light sources called *standard candles* provide the means for the most common method to determine distances for the purpose of probing the Hubble flow. For such objects, the intrinsic luminosity  $L$  can be measured or determined theoretically without measuring their distance. By observing their apparent light flux  $F$  dimmed by traversing the vastness of space, a *luminosity distance* can

5: As explained below, gravitational waves changed the game in more than one way.

be determined

$$D_{lum} = \sqrt{\frac{L}{4\pi F}} \quad (1.5)$$

which happens to relate with  $D_{lum} = (1 + z) D_{comov}$  to the comoving distance. Cepheids for instance, variable stars for which the intrinsic luminosity depends on their periodic behaviour of brightness fluctuations, are long-known standard candles. Their luminosity-period relation was discovered by Henrietta Leavitt in 1912 and enabled the first distance measurements reaching past the edge of the Milky Way to the Andromeda Galaxy (M31). The brightest standard candles known to astronomers however are Type-Ia Supernovae (SNeIa). They are a special variant of Supernova in which a white dwarf in a binary star system accretes mass. Due to this process, the exact energy available at the time of Supernova and thus its standardizable intrinsic luminosity is given by the Chandrasekhar mass limit of  $1.44M_{\odot}$ .

Yet while there is no single method which is applicable to all ranges of distances. Thus, a common procedure in the measurement of the Hubble constant is the *cosmic distance ladder*, in which one distance measurement iteratively provides calibration for the next, with the end of the rung being the farthest reaching SNeIa. Methods based on the distance-redshift relation are often called 'late' measurements.

Opposed to these are the 'early' measurements, which are based on completely different physical processes. Instead of a distance measurement, the 'early' measurements determine the Hubble constant and other cosmological constants, with angular modes of temperature on the Cosmic Microwave Background (CMB). For instance, the monopole temperature of the CMB evolves with

$$\dot{T}_{\text{CMB}} = -H_0 T_{\text{CMB}}(t). \quad (1.6)$$

The current temperature of the CMB is known to be around  $T_{\text{CMB}}(0) = 2.725$  K. So, with a Hubble constant of the order of  $70 \text{ km s}^{-1} \text{ Mpc}^{-1}$ , this yields a change in temperature of roughly  $-0.2 \text{ nK/yr}$  and could be measured with future detectors over a long period of time. The common method however to infer  $H_0$  is based on the multipole-temperature fluctuations of the CMB. The particular structure at angular sizes in the CMB arises due to baryonic acoustic oscillations (BAO) which are an imprint of pressure waves in the primordial baryon-photon plasma. Therefore, the amplitudes of the BAO peaks depend on the baryon-density component of the Universe through which the Hubble constant can be indirectly determined. Such methods obtain estimates which are independent of the cosmic distance ladder employed by 'late'-Universe measurements.

The separation between 'early' and 'late' measurements of the Hubble constant has been emphasised in the last decade, because of a discrepancy in the results they yielded. While measurements of late-Universe probes indicate a Hubble constant of around  $H_0 = 74.0 \pm 1.4 \text{ km s}^{-1} \text{ Mpc}^{-1}$  [10, latest results obtained by the SH0ES project (Supernovae  $H_0$  for the Equation of State) which measures the Hubble constant using Supernovae], 'early'-Universe measurements generally yield a lower value of  $H_0 = 67.4 \pm 0.5 \text{ km s}^{-1} \text{ Mpc}^{-1}$  [11, most recent inference of the cosmological

[10]: Riess et al. (2019)

parameters from the Planck collaboration]. In the comparison of the values and uncertainties of such determinations, it becomes apparent that there is a discrepancy at a  $4.5\sigma - 5.5\sigma$ -level<sup>6</sup> between these two opposing sides. This means that there is roughly a 1 in 20'000'000 chance of both measurements being different on accident, which indicates a problem with either one or both methods. The seemingly only way to resolve this so-called *Hubble tension*, without completely changing the concordance model of cosmology, is to find some so-far unknown systematic errors in the measurements which would account for the discrepancies. As it currently stands however, the Hubble tension appears to force the rejection of the most successful cosmological concordance model, the  $\Lambda$  cold-dark matter model ( $\Lambda$ CDM).

For this reason, it is crucial to have as many independent methods of obtaining estimates for the Hubble constant as possible, each with sufficient precision to resolve the tension. In the past couple of years, gravitational lenses were believed to provide a third perspective on the issue and possibly resolve the discrepancies surrounding the value of  $H_0$ . While other methods are based on standardizable luminosity measurements or the angular power spectrum of the CMB, gravitational lenses induce differences in travel times of light rays, so-called time delays, which can be measured in the lensed images of quasars and other time-variable sources over a period of days to years. These time delays set the scale of the lensing system and are proportional to the inverse of the Hubble constant, the Hubble time. Through these time delays, the recovery of the lensing-mass distribution therefore allows an independent measurement of the Hubble constant from a completely different physical process. A measurement of such a kind was first discussed by Refsdal [12]. He proposed the possibility of measuring a supernova strongly lensed by a foreground galaxy. The relatively short burst of light from the supernova would follow two different paths to the observer and appear at different locations with a time delay of several months. So far, only two of such gravitationally lensed supernovae have been detected, SN Refsdal and SN iPTF16geu [13, 14]. In a subsequent publication Refsdal developed the idea even further and proposed measurements of other cosmological parameters to test entire cosmological models with lensing time delays [15]. To date, around 30 time-delay galaxy systems of lensed quasars have been monitored (see [16, 17] for some recent reports), of which 8 systems have been thoroughly studied by several collaborations. Despite this, inferences of  $H_0$  still seem to yield inconclusive results ranging from 67 to almost  $75 \text{ km s}^{-1} \text{ Mpc}^{-1}$ . While there is some controversy around the potential of using time-delays of galaxy lenses to obtain determinations of  $H_0$  at a precision comparable to other late measurements, future detections of many more systems might improve the precision of such methods.

Even so, it is unlikely for a single method to resolve the Hubble tension alone. However, another promising approach to determine distances has emerged. Light signals weaken with the square of their distance as described by equation (1.5). This means a signal will be 4 times less bright at twice the distance, which is generally the case for long-range physical laws, be it the gravitational force, electro-magnetic force, or most kinds of radiation. Of course, for a constant progress out into the cosmos, the demand on technologies is twice as high and pushes them

[11]: Planck Collaboration et al. (2018)

6: depending on the exact measurements being compared

[12]: Refsdal (1964)

[13]: Kelly et al. (2015)

[14]: Goobar et al. (2017)

[15]: Refsdal (1966)

[16]: Millon et al. (2020)

[17]: Millon et al. (2020)

7: a highly non-classical effect!

to their limits. Recently however, the detection of gravitational waves changed the game. When two massive, compact objects such as black holes orbit each other and start to inspiral, some amount of energy is emitted in form of gravitational waves<sup>7</sup>. A major advantage over their electro-magnetic counterpart is that the signal strength of gravitational waves decreases with distance linearly. The benefits of this become immediately apparent: if one would manage to build a detector which is 100 times as sensitive, it could measure distances 100 times as far into the Universe, rather than 10 times as far with a light detector which was 100 times as sensitive. The reason for the linear dependence on distance lies in the method how the signal is generated and measured. The easiest way of generating electro-magnetic waves is to move charges back and forth which creates dipole radiation, commonly known as light. Due to the conservation of momentum, this is not possible for gravitational waves which instead consist of quadrupole radiation. These kinds of radiations are fundamentally different when it comes to their detection. While light simply gets absorbed in the detector and changes the energy level of the detected signal, gravitational waves induce stretching and compression in the detector, called strain which is proportional to the amplitude of the wave. While the energy of gravitational waves still falls with the square of the distance, their amplitude decrease with the distance linearly, which is ultimately the reason of the farther reach of distance measurements based on gravitational waves. In the future, this method of measuring distances will be crucial in resolving the discrepancies in the measurements of the Hubble constant [18].

[18]: Abbott et al. (2017)

[19]: Newton (1704)

[20]: Huygens (1690)

## 1.2 Lens models

In the early days of modern science, Newton suspected light could be deflected by massive bodies, which would imply light consists of particles [19]. His contemporary Huygens however convincingly demonstrated the conformity of light within a coherent wave theory, thereby explaining phenomena such as reflection, refraction, and polarisation of light [20]. Nowadays, we know both concepts may be used as descriptions for light. Similarly, the phenomenon of gravitational lensing can be thought of as either the delaying and folding of wavefronts, or the curving of light-particle geodesics. While both concepts are equivalent, the multiplicative imaging of light sources seems more intuitive in the wavefront picture.

Thus, let us consider an arbitrary path of a light ray along a wavefront through a gravitational potential  $\Phi$  with travel time

$$t = \int \frac{d\lambda}{v} \quad (1.7)$$

where  $\lambda$  is the parametrisation along the path, and  $v$  is its speed which is slower than the speed of light in unperturbed spacetime ( $c = 1$ ) due to the delay caused by the gravitational potential. The Poisson equation connects the gravitational potential to a mass-density distribution

$$\Delta\Phi = 4\pi\rho. \quad (1.8)$$

which is commonly called the 'lens'. Fermat's principle<sup>8</sup> tells us that the

8: which—as it turns out—can be directly translated from Newtonian physics to general relativity as shown by e.g. Nityananda et al. [21].

travel time for such a light ray passing through the lens is stationary with respect to small variations in its path. In addition, these paths have to move along null geodesics on any stationary or non-stationary metric. In an astrophysical setting, gravitational potentials are usually non-relativistic<sup>9</sup>, i.e.  $\Phi \ll 1$ , and only weakly perturb the flat, unperturbed Minkowski metric  $h_{\mu\nu} = (1 - 1 - 1 - 1) \cdot \mathbb{1}$ . Thus, we can write the metric and its line element as

$$\begin{aligned} g_{\mu\nu} &= h_{\mu\nu} + 2\Phi\delta_{\mu\nu} \\ ds^2 &= g_{\mu\nu}dx^\mu dx^\nu = (1 + 2\Phi)dt^2 - (1 - 2\Phi)dx^2. \end{aligned} \quad (1.9)$$

where  $\delta_{\mu\nu}$  is the Kronecker symbol and describes the trace of the metric. Since light propagates on null geodesics with  $ds = 0$ , we get

$$\frac{1}{v} = \left| \frac{dx}{dt} \right|^{-1} = \sqrt{\frac{1 - 2\Phi}{1 + 2\Phi}} \approx 1 - 2\Phi. \quad (1.10)$$

Moreover, the direction of the light path changes at a rate proportional to the gradient perpendicular to  $v$ , which means the total deflection is the integrated change along the path

$$\alpha = - \int \left( v \nabla \frac{1}{v} \right) d\lambda \approx 2 \int \nabla \Phi d\lambda \quad (1.11)$$

The travel-time difference along the perturbed path due to the locally slower speed of light in comparison to its speed in non-diluted spacetime is called the *Shapiro delay* [22]

$$\Delta t_{\text{Shapiro}} = \int \left( \frac{1}{v} - 1 \right) d\lambda = -2 \int \Phi d\lambda. \quad (1.12)$$

In general relativity, delays and deflections — notions of space and time — are dependent on the reference frame used. Since observations of gravitational lensing are by nature in the observer frame, it makes sense to derive lensing properties in that frame. To that end, we now consider the travel times of all paths from the source to the observer's entire sky<sup>10</sup>. The observer at the end of these light paths can only detect lensed images at certain angular positions  $\theta$  on the sky, which are at a normal direction to the wavefronts (a direct consequence of Fermat's principle), originating from a source at an unobservable angle  $\beta$ .

A diagrammatic representation of such a lens configuration and its geometry from the observer's perspective is shown in Figure 1.3. At any position  $\theta$  (whether an image is observable or not), the travel time of a light ray from a fixed source position  $\beta$ , also called arrival time, is given by the Shapiro time delay on the purely geometrical, unperturbed travel time [23]

$$t(\theta) = t_{\text{geom}}(\theta, \beta) + \Delta t_{\text{Shapiro}}(\theta). \quad (1.13)$$

As illustrated in Figure 1.3, the geometric path is bent by the deflection angle  $\alpha$  and for small values  $\alpha \propto (\theta - \beta)$ . Due to the added path length compared to the direct path from the intrinsic source position, the geometric time delay is proportional to  $\frac{1}{2}(\theta - \beta)^2$ . In the observer frame, these time delays have to be scaled with appropriate factors of angular diameter distances to the lens  $D_L$  at a redshift  $z_L$ , to the source  $D_S$  at a redshift  $z_S$ , and from the lens to the source  $D_{LS}$  (see Figure 1.3

9: the Sun's potential for example is at its edge around  $\Phi \sim 2 \times 10^{-6}$ .

[22]: Shapiro (1964)

10: The observer sees a 2D surface!

[23]: Blandford et al. (1986)

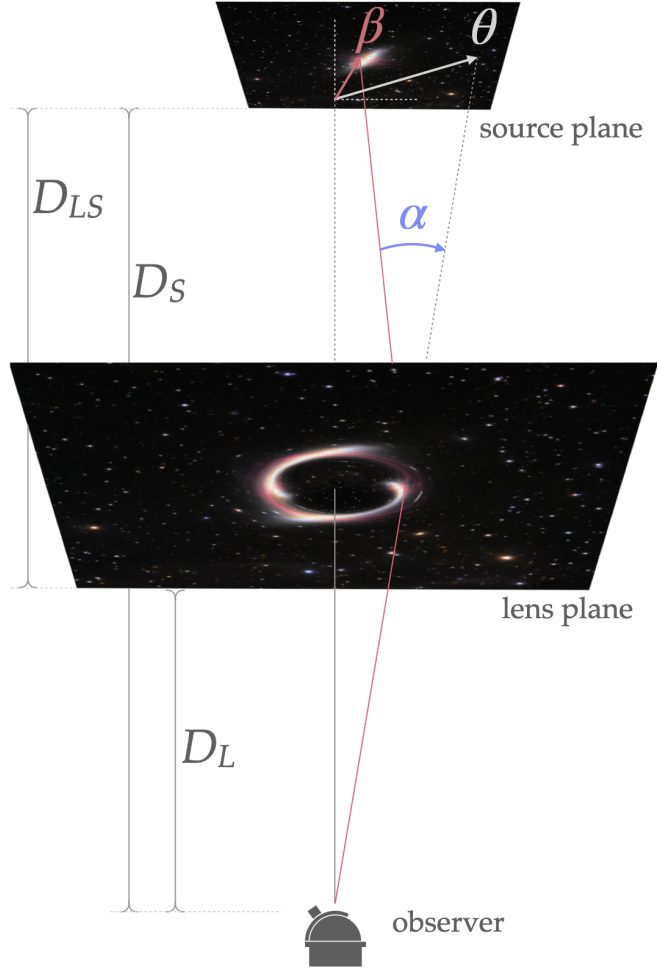


**Figure 1.3:** A diagram of a lensing system's geometry. The distance to the lens plane is usually measured as an angular diameter distance  $D_L$ , and to the source plane as  $D_S$ . The angular diameter distance from the lens plane to the source plane is usually designated with  $D_{LS}$ . From an observer's perspective, images appear to originate from an angular position  $\theta$  (white), however due to the lens-induced deflection  $\alpha$  (blue), the true light path (in red) is bent and originates from the intrinsic source position  $\beta$ . The diagram furthermore suggests how the observable position  $\theta$  is geometrically composed of the unknowns  $\beta$  and  $\alpha$ .

11: Note that in a general cosmological context angular diameter distances are not additive, i.e.  $D_{LS} \neq D_S - D_L$ .

for details)<sup>11</sup>

$$\begin{aligned} t_{\text{geom}} &= \frac{(1+z_L)}{2} \frac{D_L D_S}{D_{LS}} (\theta - \beta)^2 \\ \Delta t_{\text{Shapiro}} &= -2(1+z_L) \int_0^{z_S} \Phi(\theta, \zeta) d\zeta, \end{aligned} \quad (1.14)$$

where  $\zeta$  is the line-of-sight coordinate. The distance to the lens and the source  $D_S$  are always much larger than the line-of-sight extent of the lens itself. This is what allows the so-called *thin-lens* approximation which allows the definition of a relativistic two-dimensional (2D) *lens potential*, the projection of a three-dimensional potential onto the 'lens plane'

$$\psi(\theta) = \frac{2D_{LS}}{D_L D_S} \int_0^{z_S} \Phi(\theta, \zeta) d\zeta, \quad (1.15)$$

12: in integral form the operator is a convolution with the Green's function  $G(\theta') = (2\pi)^{-1} \log |\theta'|$

Just as the Poisson equation (1.8) in 3D relates the Newtonian potential to a mass-density distribution, there is a 2D inverse Laplace operator<sup>12</sup>  $\nabla^{-2}$  which connects a surface mass-density distribution  $\kappa$  to the lensing potential

$$\begin{aligned} \psi(\theta) &= 2\nabla^{-2}\kappa \\ \kappa(\theta) &= \frac{4\pi D_{LS} D_L}{D_S} \int \rho(\theta, \zeta) d\zeta. \end{aligned} \quad (1.16)$$

Also called *convergence*,  $\kappa$  itself is in fact dimensionless, as it is in units of

the *critical surface density* scaling  $(4\pi D_{LS} D_L / D_S)^{-1}$ . It characterises the 'compactness' of a lensing system and describes a limit beyond which a mass distribution produces multiple images from a source behind the lens, i.e. a mass and area limit at which a system is strongly lensing.

Finally, inserting equation (1.14), (1.15), and (1.16) into equation (1.13), yields the travel times up to an arbitrary constant as a functional surface of observed angular positions, called the *arrival-time surface*

$$\begin{aligned} t(\theta) &= (1 + z_L) \frac{D_L D_S}{D_{LS}} \tau \\ \tau &= \frac{1}{2}(\theta - \beta)^2 - \psi(\theta), \end{aligned} \quad (1.17)$$

where  $\tau$  describes the dimensionless arrival-time surface in cosmological scaling. While it is a rather abstract construct<sup>13</sup> and is not entirely observable, the study of  $\tau$  and its derivatives can explain most of a lensing phenomenon.

The first derivative is another formulation of Fermat's principle

$$\begin{aligned} \nabla \tau &= 0 \\ \theta &= \beta + \nabla \psi = \beta + \alpha, \end{aligned} \quad (1.18)$$

where equation (1.11) was used to insert  $\alpha = \nabla \psi$ . From Figure 1.3, this relation between the deflection, intrinsic source, and observable source is also evident, and is often called the ray-tracing or *lensing equation*.<sup>14</sup>

The lensing equation is especially important for reconstructing mass distributions of observations. The left-hand side of the second equation (1.18) is observable and measurable, whereas the right-hand side terms are unknown and thus have to be modelled. In general terms, lens modelling is the process of finding credible mass distributions of lensing galaxies (or clusters) which are able to reproduce the observed deflections of a background source. There are several strategies of how one can go about constructing such mass distributions.

A very popular approach consists of building parametric models whose shape is determined by a set of parameters. The philosophy behind it is to match the number of parameters to the sparsity of observables. This often means, flexibility and complexity is traded for simplicity by eliminating unimportant parameters, which makes the choice of the right parameters especially crucial. The advantage of such methods is the high efficiency with which such models can be generated.

Contrary to parametric models, free-form models use a much higher number of parameters usually in form of small components which are superposed to build the lens. These components can in principle use of any form basis function such as Bessel functions or isothermal spheres, however most commonly square mass tiles, or pixels are used to assemble the lens mass distribution. The advantage of free-form methods lies in the flexibility they have to build various shapes of models, but this is also their most critiqued aspect, as too much flexibility easily leads to unphysical models which contradict galaxy formation and evolution theory. Another rather irrelevant argument usually made against free-form models is that they tend to hide parameters which describe dominant features of a lens amongst many less important ones.

13: however, it is closely related to real-space wavefronts

14: The second derivative  $\nabla \nabla \tau$  is the inverse magnification tensor which explains how small displacements in the source plane take effect on the lens plane.

In this context, it is very useful to think of an arbitrary surface-density distribution in terms of multipoles:

$$\kappa(\theta) = \langle \kappa_0(\theta) \rangle_\phi + \sum_{m=1}^{\infty} \langle \kappa_m(\theta) \rangle_\phi e^{im\phi} \quad (1.19)$$

where the individual components  $\langle \kappa_m(\theta) \rangle_\phi$  are angular averages over the surface density, expressed in polar coordinates. It corresponds much to the idea that galaxies consist of a main body of matter and many smaller substructures orbiting around it. The monopole  $\kappa_0$ , dipole  $\kappa_1$  and quadrupole  $\kappa_2$  are usually considered the most important components. While the monopole only leads to radial deflections, the higher-order multipoles also include angular terms which are composed of two parts containing the interior and exterior poles. The angular structure in the lens is mainly determined by three components: (i) the luminous lens galaxy including its stars, gas, and dust, (ii) the dark matter in the halo of the galaxy, and (iii) the perturbations from nearby objects or objects along the line of sight. The most common angular term included by lens models is the external shear which describes the exterior poles of the quadrupole.

[24]: Young et al. (1980)

[25]: Young et al. (1981)

[26]: Saha (2000)

[27]: Gomer et al. (2019)

[28]: Kochanek (2020)

[29]: Harvey et al. (2019)

[30]: Warren et al. (2003)

[31]: Barnabè et al. (2007)

[32]: Ferreras et al. (2007)

[33]: Shajib et al. (2020)

In fact, Young et al. [24] reported the first lens model which already involved all components up to the quadrupole expressed in terms of an elliptical mass distribution using a small set of parameters. Already then, they identified essentially every important lensing-related issue, and in particular realized that there are many different mass distributions which can lead to identical lensing configurations [25]; these degeneracies represent an inherent limitation to lens reconstructions [26]. They create many misconceptions about lens models even amongst experts, as often times a single family of models is not able to fully describe lensing observables [27, 28]. To reduce or even break degeneracies, modern lens reconstruction techniques try to constrain their models with additional data besides the image positions such as relative fluxes of the images, arc-like extended images, stellar photometry to describe the dynamics and inner structure of the lensing galaxies, or time delays between the images [29–33].

### 1.3 Galaxies

The current scientific consensus within the cosmological paradigm is that all matter in the Universe was created roughly a Hubble time ( $H_0^{-1} = 13.7$  Gyr) ago during a singularity known as the Big Bang. Afterwards, a rapidly expanding and cooling phase began, and all matter was almost uniform in distribution. Over the course of these several billion years, spontaneous fluctuations on top of this uniform distribution grew, slightly denser regions of matter became gravitationally bound to each other. Eventually, they formed primordial galaxies of hydrogen gas enveloped by a large dark matter halo. In these proto-galaxies, cold and over-dense molecular clouds gravitationally collapsed to form the first stars. These stars were rather massive and burnt through their hydrogen fuel quickly. Such stars generally end in violent supernovae through which they reintroduce heavier elements<sup>15</sup> back into their gas environ-

<sup>15</sup>: commonly termed *metals* in astrophysics whose aggregates form *dust*

ment, the *interstellar medium* (ISM). The interplay of these components form a dynamical, self-regulatory, but chaotic system and settle into a morphological state of the galaxy. The study of these dynamical processes and their correlations therefore can uncover crucial clues to the formation history and structure of galaxies.

The endeavour of measuring the dynamics of galaxies was and still is complicated, even more so within the Milky Way. Earth is revolving around our Sun, and the Solar System is orbiting around the Galactic centre, which means relative motions have to be carefully examined. From some locations on Earth, a dense strip of starlight is visible across the night sky which is indicative of the Galaxy's disk structure.

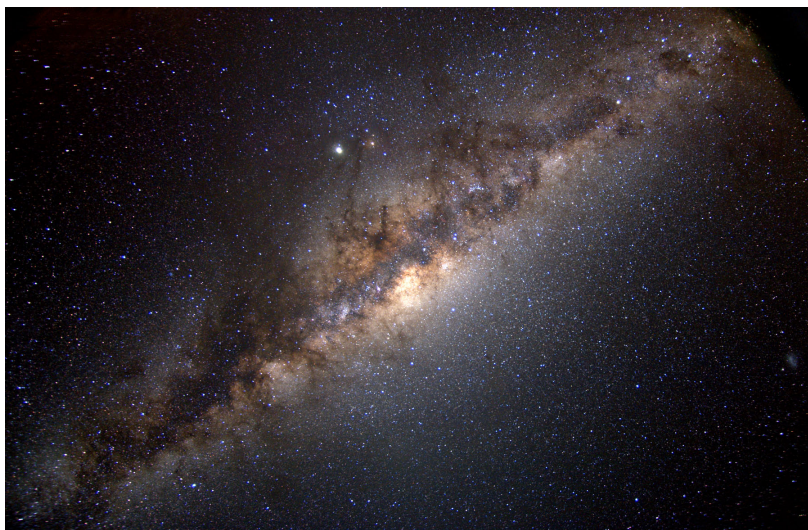


**Figure 1.4:** APOD 2008 January 4: The Milky Way at 5000 meters.  
View on our own galaxy from within (recorded in the Chilean Andes). The band of the dense collection of stars from the disk and the Galactic centre is partially covered by the typical extinction features due to dust clouds. It indicates that the Milky Way possesses a stellar disk.  
*Credit & Copyright: Serge Brunier*

From far away it is quite easy to recognise the typical morphology of other galaxies through direct observations<sup>16</sup>. Measuring their rotational properties already becomes increasingly difficult, but deducing the shape and rotation patterns of the Milky Way from within is an undertaking of its own.

A seemingly random and dense distribution of stars as it appears in galaxies should in principle collapse towards its potential well. Despite the expansion of the Universe, this would eventually lead to the collapse of entire galaxies into their centres. Like in many other astrophysical scenarios, pressure gradients can take a stabilising role, balance gravity, and thereby prevent complete collapse. These balancing pressures depend on different physical processes and generally define limiting scales. For some galaxies, e.g. ellipticals, the stars' random motions are the dominant drivers towards stability, for spiral galaxies it is the rotation about their disk's centre. In contrast to orbiting systems such as the Sun and Earth, where most of the mass is located near the guiding centre of the orbits, the Milky Way's mass distribution is more complex and extended with different elements such as various forms of hydrogen gas, dust, stars, and stellar remnants. In general, the study of galactic rotation through stars can yield insights not only into the galaxy's morphology, but also into its formation history and mass composition.

Weighing galaxies is not an easy task either, partially because most of their components are invisible, dark matter being the most elusive amongst them. However, much like tree branches move in the wind, orbits of stars

16: provided the telescope has enough angular resolution

still feel the gravitational pull from the mass inside them, independent of the nature of the matter. Stars in a more massive galaxy will move with higher orbital speeds than in lower-mass galaxies; more formally, the mass  $M$  inside the (circular) orbit of radius  $r$  is  $M(< r) \propto V^2 r$ , where  $V$  is the orbital speed of the star. Accordingly, by measuring the velocities of stars at a particular distance from the centre, a mass estimate for the galaxy can be calculated, which is a simple application of Newton's first law combined with Kepler's law. It is equivalent to assuming the galaxy is in hydrostatic equilibrium formulated by the virial theorem

$$\begin{aligned} V^2 &= \frac{M(< r)}{r} \\ 2E &= -U, \end{aligned} \quad (1.20)$$

[34]: Binney et al. (2008)  
[35]: Zwicky (1933)

[36]: Hulst (1951)  
[37]: Muller et al. (1951)  
[38]: van de Hulst et al. (1954)  
[39]: Schechter (1980)  
[40]: Davies et al. (1983)

[41]: Bosma (2017)  
[42]: Ablimit et al. (2020)  
[43]: Cautun et al. (2020)

where  $E$  and  $U$  are the kinetic and potential energy respectively [34, 35]. When the individual orbits of stars cannot be resolved in e.g. spiral galaxies, other 'tracers' can be used such as atomic hydrogen gas measured through 21-cm line radiation in the radio spectrum [36–38], or as perturbations in the optical wavelengths. For ellipticals, the velocity dispersion  $\sigma$  measured by the spread of spectral absorption lines is the observable which analogously measures their mass as  $M(< r) \propto \sigma^2 r$  [39, 40]. The observables measured are, in most cases, treated as dynamical equilibria, or temporal averages and therefore yield (by implicitly assuming the ergodic theorem) 1-dimensional (1D) models such as the rotation curve  $V(r)$  [41–43]. It characterises the orbital velocity as a function of distance from the galactic centre. By measuring how  $V(r)$  behaves with increasing radius, we can draw conclusions about the Milky Way's size, total mass, and the distribution thereof. For instance, a solid-body rotation  $V \propto r$  would mean that the enclosed mass ideally increases with  $r^2$ , Keplerian orbits go as  $V \propto r^{-1/2}$ , whereas  $V \propto \text{const.}$  is a result of the enclosed mass increasing as  $r$ . This makes it a powerful tool to investigate the mass distribution of galaxies.

However, on rare occasions, some galaxies can function as strong gravitational lenses, and reveal even more details about their internal structure. These rare phenomena occur when a source aligns with a massive galaxy acting as a lens and is multiply imaged or appears as an Einstein ring. This depends on the gravitational potential of the galaxy which in turn is related to its entire mass and the distribution thereof. As a consequence, the separation of the images to the lens is determined by the mass inside (see the strong lensing case of equation (1.1)), which is typically of the order of 1 arcsec for galaxies at cosmological distances. Moreover, lenses are rarely perfectly aligned and circular in the real world, but have angular structure, which produces distorted configurations of source images. This is what allows us to go beyond 1D models and infer a lens model in form of a 2D mass distribution (more details on this are discussed in Section 1.2). Hence, gravitational lenses provide a unique opportunity to study distant galaxies and their structure on scales which are difficult to infer with other methods. Unfortunately, this type of analysis is limited to lensing systems which are relatively rare, as previously mentioned. To get an idea of just how rare such lensing events are, we will next try to estimate the number of lensed sources based on the Milky Way's kinematics.

The Milky Way's rotation curve can be probed through its stars directly.

To that end, the relevant observables are the radial velocity  $v_z$ , the tangential velocity  $v_t$ , distance from Earth  $d$ , and the longitude on the sky  $l$ . Measurements of these quantities can be combined to the so-called *Oort's constants*

$$\begin{aligned} A &= \frac{v_z}{d \sin 2l} \\ B &= \frac{v_t}{d} - A \cos 2l. \end{aligned} \quad (1.21)$$

A caveat is the assumption that the stars, including the Sun, are on circular orbits, which is only approximately true. Moreover, it assumes the Milky Way has a monotonically decreasing, symmetric potential. Again, this is not entirely true as spiral arms can introduce over-densities which manifest as asymmetries and locally break monotonic behaviour in the potential. Still, within their limits the Oort's constants are very useful, because they can be rewritten as

$$\begin{aligned} A &= -\frac{1}{2} \left[ \frac{dV}{dr} - \frac{V_0}{R_0} \right] \\ B &= -\frac{1}{2} \left[ \frac{V_0}{R_0} + \frac{dV}{dr} \right]. \end{aligned} \quad (1.22)$$

Recent measurements from the Gaia survey determined these constants with  $A = 15.3 \pm 0.4 \text{ km s}^{-1} \text{ kpc}^{-1}$  and  $B = -11.9 \pm 0.4 \text{ km s}^{-1} \text{ kpc}^{-1}$  [44]. These constants express the shear and vorticity of the disk in the solar neighbourhood. The shear essentially measures a deviation from solid-body rotation, the vorticity how the angular momentum varies with small changes in radius. Adding both yields the velocity gradient  $A + B = -\frac{dV}{dr}$ , which seems to be relatively flat with  $3.4 \text{ km s}^{-1} \text{ kpc}^{-1}$  as was expected from previous and alternative investigations.

[44]: Bovy (2017)

From the velocity gradient the mass density for the Milky Way can be estimated as follows

$$\begin{aligned} \rho_{MW} &\sim \frac{(A + B)^2}{2\pi} \\ &\sim 10^{-33} \text{ s}^{-2} \end{aligned} \quad (1.23)$$

As a rough estimate, this is of the order of the total mass of the Milky Way within its size volume  $\sim M_{MW}/R_{MW}^3$ , as long as the assumptions of the Oort's constants are valid. This is obviously not the case outside the edge of the Galaxy. However, the size of the Milky Way is not clearly known. The issue lies in the ambiguity regarding the definition of the edge of the Galaxy. In the literature the ' $R_{200}$ ' is frequently used, sometimes also called the 'virial' radius within which the mean density equals 200 times the cosmological critical density. Another less back-of-the-envelope definition is the 'splashback' radius, a caustic manifested in a drop in density or radial velocity. At roughly half the splashback radius an edge can be defined where virialized material has completed at least two pericentric passages. For the Milky Way this radius is at about  $R_{MW} \sim 290 \text{ kpc}$  [45], and seems to define an edge where our assumptions should still hold.

[45]: Deason et al. (2020)

Generalizing and assuming that the Milky Way is an average galaxy in the Universe, we can compare the mass density of the Milky Way to the

cosmological matter density

$$\rho_m = 0.3 \times \frac{3H_0^2}{8\pi} \sim 10^{-37} \text{ s}^{-2}, \quad (1.24)$$

which is roughly 30% of the average energy-density in the Universe. The ratio of these two quantities should yield the number of Milky-Way-like galaxies within the galaxy's volume. Within a cubic volume of  $\sim (c/H_0)^3$  which corresponds roughly to a tenth of the diameter of the observable Universe and  $10^4$  times farther than the edge of the Milky Way, this number is roughly

$$10^{12} \times \frac{\rho_m}{\rho_{MW}} \sim 10^8.$$

Typical strong-lensing galaxies cover roughly an area of  $10^{-10}$  square radians on the sky, which means that within a tenth of the observable Universe 1% of sources are strongly lensed by galaxies. Of course, this number is based on the mass and dimensions of the Milky Way and with it the assumption our Galaxy be average. Since the Milky Way is actually more massive than the average galaxy, the estimate constitutes a lower limit.

It was further implicitly assumed all galaxies are distributed homogeneously and isotropically within the considered volume. These are structural consequences of what is known as the *cosmological principle*. It states that on a sufficiently large scale the properties of the Universe are the same for all observers, which is equal to say that the same physical laws apply throughout. Extensive testing of these fundamental postulates to the measurable level seem to confirm<sup>17</sup> a statistically homogeneous distribution of galaxies on large scales. On local scales however, the picture is much more interesting. The  $\Lambda$ CDM model predicts clustering along filamentary structures within a web-like system of dark matter strings. Once formed, galaxies evolved together in larger galactic structures called groups, clusters and superclusters. Over time, gravity within these systems forces them closer and closer, until they eventually collide in a series of mergers. The outcome of these mergers depends on the mass of the galaxies in the collision. Smaller 'dwarf' galaxies can be disrupted by larger ones and turned into streams of stars which orbit the galactic core. When large galaxies of similar size come together, their spiral structure is generally lost, and the merged galaxies become a giant elliptical galaxy. Through these mergers, a hierarchical spectrum of various galaxy types forms.

Ultimately, all galaxies within a group or cluster will eventually become gravitationally bound to each other and merge into a giant elliptical galaxy. Such almost or fully merged systems are known as 'fossil groups'. They are always dominated by a single, very luminous and thus massive central galaxy, around which other galaxies are at least two magnitudes less luminous and therefore much smaller. During their comparatively fast merging process, the intra-group gas medium heats up. Cooling times in these regions are much higher than a Hubble time, and thus a large-scale X-ray halo around the original main galaxy remains. Fossil groups which have already fully merged, appear today as massive, completely isolated elliptical galaxies with such group-like X-ray halos.

<sup>17</sup>: although not conclusively; see Migkas et al. [46] for a report of possible deviations from isotropy.

As a final product of galaxy merging within a galaxy group, the mass range of such fossil group galaxies starts at  $\sim 10^{13} M_{\odot}$  and exceeds the average mass of galaxies by orders of magnitude.

In recent years, ever more elaborate large-scale hydrodynamical and N-body simulations have been implemented, which displayed such hierarchical merging schemes, and produced incredibly realistic galaxies. Simulations generally use the field of density fluctuations analogous to the ones observed in the CMB as initial conditions and progress the entire system in time according to the cosmological concordance model. They demonstrate that galaxy formation is driven by the growth of the underlying large-scale structure and the formation of dark matter haloes. Galaxies form through condensation of gas at the centres of the potential wells of these dark haloes. The galaxies' subsequent evolution is usually governed by a plethora of sub-grid models which are adapted to reproduce properties due to astrophysical effects below the resolution level such as supernova winds and quasar feedback, in this context often called AGN (active galactic nucleus) feedback. Based on theoretical predictions from such simulations, physical properties of galaxies related to baryons<sup>18</sup> should be naturally in tight correlation with the mass of the dark haloes by which they are hosted. In particular, the total mass in stars contained in galaxies reveals interesting behaviour of how star formation is regulated within, when compared to the mass of their dark matter halos.

*Halo abundance matching* is a technique which allows such a comparison and results in an empirical correlation between galaxy and halo properties [47]. Following an Occam's razor approach, the technique directly matches observed galaxy number densities for a given property (such as luminosity) to theoretical halo number densities obtained through simulations. The latest Planck survey [11] measured a baryonic-to-total mass ratio of  $\Omega_b/\Omega_m \sim 0.14$  within the  $\Lambda$ CDM model. If light 'traces' mass this cosmological average should hold for galaxies of all masses. Abundance-matched galaxies however indicate that on small scales light does no longer simply trace mass and predict the star formation of galaxies to be suppressed at both the low and high ends of the mass spectrum, due to various astrophysical effects such as tidal stripping<sup>19</sup>, Supernovae and AGNs. Generally, having more concentrated baryonic matter will increase the stellar-to-halo mass fraction while astrophysical feedback processes which disperses baryonic matter decreases it. Supernovae have the tendency to impact galaxies with lower halo masses the strongest by kinematically removing gas from star-forming regions, whereas AGNs are especially effective in preventing the formation of stars in higher mass galaxies through heating and dispersing of the star-forming gas.

In contrast to abundance matching and similar methods which usually rely purely on theoretical predictions of the halo-mass number density, lensing provides once again an alternative to compare mass components of galaxies based on observational estimates. Since lenses can be used to probe the distribution of every kind of matter in galaxies, especially the region within the lensed images, enclosed masses inferred by lens models yield a fair estimate on the total mass of a galaxy. Through stellar kinematics and colours of the stellar population in the lensing galaxy, luminous matter can be distinguished from the dark. Figure 1.5 shows such an analysis for lenses discovered by the citizen science Space Warps

18: a collective term for all luminous matter in order to differentiate it from dark matter and dark energy.

[47]: Moster et al. (2012)

[11]: Planck Collaboration et al. (2018)

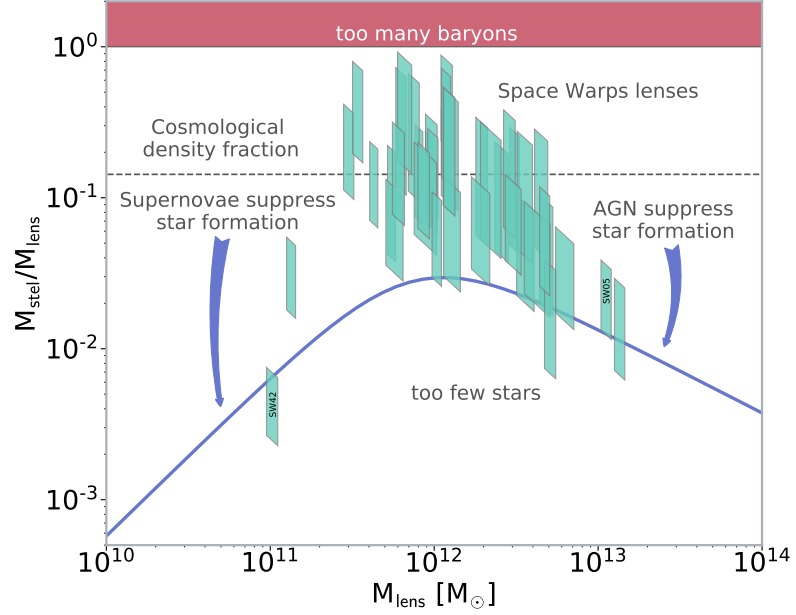
19: depletion of a galaxy's gas and stellar mass reservoir due to strong tidal forces from neighboring galaxies

[47]: Moster et al. (2012)

[48]: Künig et al. (2018)

project in comparison with results from abundance matching by Moster et al. [47]. Initial modelling of these lenses was done by a small group of citizen-science volunteers lead by Künig et al. [48], and repeated by me. For two of these lens models J1434+522 and J2217+015 (annotated in Figure 1.5 with SW05 and SW42, respectively) stellar-mass estimates were obtained through fitting stellar population synthesis models to the observed photometry, which yields more precise results compared to the previous estimates (more details on the stellar-mass estimation are given in Section 1.4.2 and Chapter 3).

**Figure 1.5:** Stellar-to-lens mass ratios of lensing galaxies (turquoise) from the Canada-France-Hawaii Telescope Legacy Survey (CFHTLS) in comparison with abundance-matched halo masses [blue line; cf. Moster et al. 47] and the cosmological density fraction  $\Omega_b/\Omega_m$  (dashed line). The lenses were discovered by the Space Warps citizen-science community and modelled by a smaller group of volunteers using the SpaghettiLens software stack by Künig [49]. Künig et al. [48] presented their final results and estimated stellar-mass contents obtained through comparison with stellar populations. The annotated lens models SW05 and SW42 have been refined by me (and collaborators) using Markov-chain Monte-Carlo simulations to marginalize over various sets of stellar population synthesis models, yielding much preciser stellar-mass and lens-mass estimates; for details see Chapter 3.



## 1.4 Summary

20: with the help and guidance of colleagues listed in the beginning of each chapter.

The previous sections introduced gravitational lensing and related topics in a general context. Here, my own contributions<sup>20</sup> to these fields, in particular strong gravitational lensing are introduced and summarised.

Section 1.2 describes how the study of the arrival-time surface explains the occurrence of multiple images; see equation (1.17). Extremal points where  $\nabla\tau = 0$ , are the only positions where the arrival-time surface is observable. Thus, any mass distribution  $\kappa$  which preserves these points up to a constant, is a valid solution to the lensing equation (1.18). In fact, lensing is subject to various forms of degeneracies which cause the system to have even infinitely many solutions. An especially troublesome form is the steepness or mass-sheet degeneracy, which becomes apparent if equation (1.17) is slightly rewritten as

$$\tau(\theta) = 2\nabla^{-2}(1 - \kappa) - \theta \cdot \beta \quad (1.25)$$

where the  $\frac{1}{2}\beta^2$  was discarded, because it is constant for all  $\theta$ . In this form it is evident that scalar transformations, corresponding to replacing the terms with  $(1 - \kappa) = \lambda(1 - \kappa')$  and  $\beta = \lambda\beta'$ , rescale the entire arrival-time surface by an arbitrary factor  $\lambda$  and change its shape, but leave the image structure and their relative magnifications invariant.

The scarceness of lensing observables and the resulting degeneracies are arguably the greatest challenge for modelling lenses. Some modelling strategies respond to this problem by solving for many solutions to the linear problem defined by

$$\nabla \tau(\boldsymbol{\theta}) = 0. \quad (1.26)$$

GLASS, a modern free-form modelling framework by Coles et al. [50], is especially efficient in solving for large ensembles of models for this problem. However, despite constraining its solution space with physical and regularization priors, many mass distributions built by this free-form modeller do not describe realistic galaxies. Chapter 2 and 3 (summarised in Section 1.4.1 and 1.4.2) present lens models which were generated by GLASS, but further constrained with specific physical ancillary information about the lensing galaxy in order to obtain more realistic mass-distribution models.

[50]: Coles et al. (2014)

In Chapter 2 (and Section 1.4.1), we used ensembles of free-from models of time-delay lenses to infer the Hubble constant. Each model consisted of 8 lenses for which time delays, that is differences in arrival-times between lensed images  $\tau(\boldsymbol{\theta}_i) - \tau(\boldsymbol{\theta}_j)$ , were required to fit the measured data. We confirmed that time delays are extremely effective in constraining the mass distribution of lensing galaxies, and help produce more realistic models.

In Chapter 3 (and Section 1.4.2), we combined a free-form lensing analysis with stellar mass models to reduce degeneracies in the inner region of a very massive galaxy, the lens of SW05 (see Figure 1.5). The photometry of the lensing galaxy was modelled and combined with light-to-stellar mass estimates obtained through marginalization over various stellar population synthesis models. Subtracting the stellar mass from the lens mass distribution furthermore yielded a high-resolution dark matter map of the galaxy’s halo.

Both of these works presented highly constrained state-of-the-art lens models, which accurately reproduced lens image positions, but nonetheless exhibited a substantial scatter in their lens mass distributions and uncertainty in derived results due to the steepness degeneracy. The steepness-degeneracy transformations motivate the definition of another quantity which is introduced in Chapter 3, the *lensing Roche potential*

$$\begin{aligned} \mathcal{P}(\boldsymbol{\theta}) &= \frac{1}{2}\boldsymbol{\theta}^2 - 2\nabla^{-2}\kappa(\boldsymbol{\theta}) \\ \tau(\boldsymbol{\theta}) &= \mathcal{P}(\boldsymbol{\theta}) - \boldsymbol{\beta} \cdot \boldsymbol{\theta}. \end{aligned} \quad (1.27)$$

The advantage of the lensing Roche potential is that unlike the arrival-time surface, steepness-degeneracy transformations leave its shape invariant. This is especially useful in comparisons of different model  $\kappa$ , as variations due to changing levels of steepness degeneracy can be isolated through their lensing Roche potentials, i.e.  $\mathcal{P}$  can be normalised without problems and then compared using scalar products.

Applying Fermat’s principle to the lensing Roche potential by inserting (1.27) into equation (1.26) yields

$$\boldsymbol{\beta} = \nabla \mathcal{P}(\boldsymbol{\theta}) \quad (1.28)$$

which describes how source positions are mapped onto extended images; also see equation (1.18). These provide more constraints than individual point-image positions, but represent non-linear priors in  $\kappa$  and thus can not be efficiently integrated to free-form lensing frameworks such as GLASS.

For this reason, I developed an analytical framework `gleam` [51] which includes post-processing filters for ensembles of arbitrary mass distributions. It provides extended-image least-squares fitting diagnostics, such as entire source-plane and synthetic lens-plane reconstructions (synthetics for short). In Chapter 4 (and Section 1.4.3), it was blind-tested against 15 synthetic lenses from hydrodynamical simulations. We ran the diagnostics on ensembles of free-form models and filtered for models which concur with the extended-image data. The final results of the tests were sobering, because they pointed out the gravity of the steepness degeneracy problem, even after highly constraining the models with extended images. In fact, that originally motivated the introduction of the lensing Roche potential and a method to isolate the degeneracy in a comparison.

All previous works inevitably demonstrated the necessity to employ much more intricate galaxy models than is conventionally done. Correspondingly, the study in Chapter 5 (and Section 1.4.4) gives proof-of-concept for a novel ‘modelling-free’ approach in which galaxies from hydrodynamical simulations are directly matched to lensing observations using the `gleam` framework. The proposed methodology promises great potential as it is straight-forward to scale up to big data sets. Moreover, we propose several ways to extend the methodology to further include common lensing constraints in order to test various galaxy-formation scenarios against each other.

In the following subsections, each of my studies mentioned above and detailed in the remaining chapters is described and summarised in the same order.

### 1.4.1 Inferring the Hubble constant

Chapter 2 presents an estimate of the Hubble constant using time delays of previously well-studied systems, with a critical study of the uncertainties. With an analysis on 8 time-delay lenses, we determined the Hubble constant with a value of

$$H_0 = 71.8_{-3.3}^{+3.8} \text{ km s}^{-1} \text{ Mpc}^{-1}$$

Contrary to other studies of the same systems, our inferred value is compatible with both the early and late measurements, with a tension of less than  $1.5\sigma$ . With a precision of 5%, the measurement is unfortunately not able to contribute to the resolution of the Hubble tension. In fact, the investigation revealed that, if a 1% level is at all obtainable, it would require a joint-analysis of many more time-delay measurements of quadruply imaging lens systems (quads). Unfortunately, it cannot be ruled out that time-delay galaxy lenses naturally exhibit an inherent scatter which prevents a precise determination of the Hubble constant at a 1% level.

It was not the only  $H_0$  determination through lensing observations recently; the H0LiCOW collaboration [52] reported on a Hubble constant of  $73.3^{+1.7}_{-1.8} \text{ km s}^{-1} \text{ Mpc}^{-1}$  from 6 time-delay lenses a year before, and the STRIDES collaboration [33] determined a value of  $74.2^{+2.7}_{-3.0} \text{ km s}^{-1} \text{ Mpc}^{-1}$  from a single lens. However, while those works assumed parametric forms for the lenses, our study explores many different lens models and attempts to marginalize over lensing degeneracies. Although degeneracies are often neglected in lensing studies, it is known for a long time that a single family of lens mass distributions is able reproduce the same observables, but still yield different values for the Hubble constant. Therefore, studies with the aim of inferring the Hubble constant need to solve for (ideally) all possible solutions of mass distributions in order to retrieve a complete model. The study produced 8000 lens mass distributions with 1000 values for the Hubble constant. Most interestingly, the values appeared to be asymmetrically distributed, which might indicate that the errors on  $H_0$  could be non-Gaussian.

[52]: Wong et al. (2020)

[33]: Shajib et al. (2020)

These results were not entirely unexpected since the investigation was actually a continuation of ideas gathered during a participation in a scientific blind study [53] in which 50 simulated time-delay lenses were analysed by several research groups. It discovered that most other current lens recovery methods are accurate to only about 6%, even with acclaimed precision over nearly 1%. In comparison with the study presented in Chapter 2, it became apparent that the lens simulations considerably differed from real observations and that the uncertainties in the inference of  $H_0$  from mock lenses were higher. Besides the obvious numerical deviations, the radial distribution of lens images of the simulated lens set was relatively narrow which provided only little constraints on the slope of the galaxy-density profiles and consequently on  $H_0$ . This could mean that there exists a limit to the accuracy on  $H_0$  achievable with time-delay galaxy lenses, which ultimately might preclude them to infer  $H_0$  on a level required to resolve the Hubble tension. Nonetheless, gravitational lenses are excellent cosmological probes. Especially cluster lenses do not exhibit this limitation and might still recover the Hubble constant with sufficient precision to contribute to the resolution of the Hubble tension.

[53]: Ding et al. (2020)

## 1.4.2 Lens recovery of SW05

In Chapter 3, we report a lens model of a special gravitational lens J143454.4+522850 (SW05). It was discovered by the Space Warps citizen science campaign, and initially modelled by a smaller group of volunteers under the lead of Küng et al. [48]. From the initial investigation, it became apparent that follow-ups of SW05 would yield interesting results as its mean radial image separation at 5 arcsec is unusually high for a lensing galaxy which would put it in a mass range close to  $\sim 10^{13} \text{ M}_\odot$ .

[48]: Küng et al. (2018)

Therefore, we free-form modelled the lens mass dsitribution again using GLASS with similar results. However, there were several issues which have been improved upon the initial model. For one, the redshift estimates for the lens and the source were previously based on multi-band colours alone, which comes with high uncertainties. Thus, we used the Bayesian photometric redshift estimator `bpz` by Benítez [54] to obtain preciser

[54]: Benítez (2000)

21: an ellipticals surface brightness profile  
 [55]: Bruzual et al. (2003)

[56]: Chabrier (2003)

22: as long as the gas mass of the lensing galaxy is negligible

[57]: Hopkins et al. (2014)

23: especially further away from the radial band around the images

results for the lens redshift of  $z_l = 0.63$ . The source redshift had since been measured spectroscopically to  $z_s = 2.96$ .

Furthermore, the photometry of the lensing galaxy was fitted using a Sérsic surface profile<sup>21</sup>. Afterwards, this light model was fitted to spectral templates of 12 stellar-population base models [55]. These were marginalised over formation epoch, star-formation time scale, and stellar metallicities; the 12 base models had 3 different stellar metallicities, and 4 different age ranges over which the star formation was assumed constant. Integration of the stellar populations with a Chabrier Initial Mass Function [56], yielded a relation of the luminosity of galaxies to their stellar masses; hereby, the extinction by dust which generally reddens their spectra had to be accounted for. This resulted in a better and improved stellar mass estimate and a stellar mass distribution for the lens of SW05. Final mass estimates (lower limits) for the lensing galaxy of SW05 were  $(1.42 \pm 0.28) \cdot 10^{13} M_\odot$  for the total mass, and  $(3.04 \pm 0.22) \cdot 10^{11} M_\odot$  for the total mass in stars. This is consistent with an early-type elliptical galaxy with a mass in the galaxy group range.

Lens models inherently account for all mass components of the galaxy. This means if the stellar mass distribution of a galaxy is known, it can be disentangled from the lens mass map and an estimate for the dark matter distribution<sup>22</sup> remains. Likewise, we presented a high-resolution dark matter map for the lensing galaxy of SW05. Moreover, the analysis allowed to reconstruct the kinematics of the galaxy, which suggested the probability of missing mass in form of hot intra-galactic gas distributed around the outskirts of the galaxy. This is indicative of a specific type of elliptical galaxy, a *fossil group galaxy*. To confirm these suspicions, the results were finally compared to state-of-the-art hydrodynamical simulations from FIRE [Feedback In Realistic Environments; 57].

### 1.4.3 Models of simulations

Free-form lens models like the ones produced by GLASS can generally have almost any shape<sup>23</sup> and still fit point-images in observations. So, the only choice is to generate as many solutions as possible that are consistent with the data, and try to find statistical tendencies which might indicate likely features a lens might have. Thereby, a lens investigator can be tempted to introduce personal preferences and confirmation biases into the modelling process. Thus, we performed a blind-study on simulated lenses in order to equitably test our free-form approach. Chapter 4 reports the results of this study.

In total, 15 galaxies from the EAGLE (Evolution and Assembly of GaLaxies and their Environment) suite of hydrodynamical simulations were projected onto the lens plane and raytraced using the SEAGLE pipeline. The resulting lens systems mock SDSS (Sloan Digital Sky Survey) observations. They feature prominent, extended images and arcs, and their lensing galaxies incorporate galaxy formation schemes which were shown to be in good agreement with observations with respect to star formation rates, total stellar luminosity and colours, and evolution of the galaxy stellar mass function and sizes.

In the initial phase of the blind-study, these simulated lens systems were free-form modelled such that they conformed with image-point

positions in the data. After some diagnostics to ensure the overall validity of the ensembles, we computed synthetics (with fitted sources) for each of the 15'000 mass models along with least squares corresponding to their fitting quality. Including the entire extended image data in the synthetics demonstrated that many ensemble models agree with the image positions, but fail to reproduce more subtle features of the lensed images. Thus, such models were filtered out of the ensembles, which elevated the overall quality of the lens models considerably.

After the subsequent unblinding of the true convergences, the shape, compactness, and ellipticity of the mass models were analysed and compared to the originals. The modelled Einstein radii<sup>24</sup> matched very accurately in comparison to the true mass distributions, which was generally expected, as they are closely tied to main modelling input that is the radial positions of the observed images. Correspondingly, the rough shapes of the models also agreed well in the comparison. However, the ellipticity of the modelled mass distributions were systematically too low, and their circularly averaged profiles similarly were too shallow. This is a typical manifestation of the steepness degeneracy, which means that even when models are tightly constrained with extended image data, there are still multiple convergence maps which reproduce the observations.

Since the study used simulations for which the mass distributions were known a priori, the modelled mass maps corresponding to the best fitting results can in principle be found by comparison; however, the steepness degeneracy makes direct comparisons problematic. Thus, we introduced a novel method to directly compare shapes of convergence maps through their lensing Roche potentials (see equation 1.27) for which the steepness degeneracy is isolated. Specifically, the similarity of two mass distributions can be evaluated with the scalar product of their normalised lensing Roche potentials. With the steepness degeneracy finally factored out, the models agreed relatively well with the true convergences on average, but were generally too round.

#### 1.4.4 The lens-matching method

Lens modelling techniques conventionally build lenses based on recipes which aim to efficiently reproduce shapes and slopes of galaxies, as they are usually observed. Such methods therefore suppress or even completely ignore the evolutionary processes of galaxies and the physical properties which form and drive them. In contrast, cosmological hydrodynamical simulations have progressed remarkably in recent years and employ semi-analytical models which imitate star formation processes and thereof resultant feedback effects on smallest scales to play through various galaxy-formation scenarios.

Chapter 5 reports on a proof-of-concept study which proposes an alternative strategy, the *plausible lens match* method, to recover lenses and explain observations. It is demonstrated with a catalogue of 554 galaxies from the cosmological hydrodynamical simulation suite EAGLE which were projected onto differently oriented convergence maps using the SEAGLE pipeline. Galaxies from two different formation scenarios were included in the catalogue. The in total 1662 convergence maps<sup>25</sup> are then

24: the average radius of the area of critical density; see the paragraph after equation (1.16) for details.

25: for each galaxy three axial projections were performed

directly matched to 7 SLACS (Sloan Lens Advanced Camera System) observations using the `gleam` framework [51].

The matching process consisted of three main steps: (i) First, the convergence maps were rescaled to the appropriate redshifts of the lens observations, (ii) then a range of maps with plausible Einstein radii were pre-selected, (iii) and finally optimal alignments between the convergence maps and the observations were determined based on the goodness of fit of their synthetic images. Amongst all maps from the catalogue, the ones with reduced  $\chi^2$  from the synthetic fitting close to 1 can be considered plausible matches which are consistent with the entire extended image data.

While it was generally thought impossible to find matching galaxies from simulations, the method found plausible matches for all 7 test cases. The fact that mass reconstructions of lensing galaxies is non-unique makes this possible. The plausible lens match method shows great potential as it can easily be scaled up to efficiently match thousands of observations with minimal intervention. Moreover, it provides direct constraints on galaxy-formation scenarios, without the systematic errors that come with the modelling of lenses. However, the initial tests were kept simplistic, so improvements and optimizations will have to be made in order to have statistically significant results:

- While the initial tests only used three orientations of the simulations, more projections should yield more matches.
- Line-of-sight structures, i.e. shear components (see Section 1.2 for details), have been disregarded in the tests, but might be crucial for other lensing systems.
- The pollution of light from the lensing galaxy in the lensed images can contribute to systematic errors in the calculation of synthetic images. In order to avoid this problem, some process which (automatically) subtracts the lensing galaxy's light from the data is more ideal than the lens masking which was used in the tests.
- Stellar mass estimates derived from stellar population synthesis models may be compared to stellar masses of the simulations, and thus yield better constraints on galaxy formation scenarios.
- Since simulations are computed in phase-space, stellar kinematics provide another way of filtering through the catalogue of candidates.
- Although time delays are still relatively rare for galaxy lenses, they would enable the inference of  $H_0$  and other cosmological parameters in the context of cosmological galaxy formation theory.

With all these improvements, plausible lens matching should present a future-proof method to deal with the expected flood of gravitational lens discoveries.

# 2 DELAYS

Original title:

## THE HUBBLE CONSTANT FROM EIGHT TIME-DELAY GALAXY LENSES

Philipp Denzel<sup>1,2</sup>, Jonathan P. Coles<sup>3</sup>, Liliya L. R. Williams<sup>4</sup>, Prasenjit Saha<sup>2,1</sup>

1 Institute for Computational Science, University of Zurich, 8057 Zurich, Switzerland

2 Physics Institute, University of Zurich, 8057 Zurich, Switzerland

3 Physik-Department, Technische Universität München, James-Franck-Str. 1, 85748 Garching, Germany

4 School of Physics and Astronomy, University of Minnesota, 116 Church Street SE, Minneapolis, MN 55455, USA

2.1 Introduction . . . . .	27
2.2 The lens systems . . . . .	30
B1608+656 . . . . .	30
DESJ0408-5354 . . . . .	32
HE0435-1223 . . . . .	32
PG1115+080 . . . . .	32
RXJ0911+0551 . . . . .	33
RXJ1131-1231 . . . . .	33
SDSSJ1004+4112 . . . . .	33
WFIJ2033-4723 . . . . .	33
2.3 Lens reconstruction method . . . . .	34
GLASS . . . . .	34
Point-image data . . . . .	36
Extended image data . . . . .	36
TDLMC . . . . .	36
2.4 Results . . . . .	39
Arrival-time surfaces . . . . .	39
Convergence maps . . . . .	39
Synthetic images . . . . .	40
$H_0$ posterior distribution . . . . .	41
Comparison with TDLMC . . . . .	42
2.5 Conclusion . . . . .	43
2.6 Figures . . . . .	45

Published in:

*arXiv e-prints*, arXiv:2007.14398, July 2020

## Abstract

We present a determination of the Hubble constant from the joint, free-form analysis of 8 strongly, quadruply lensing systems. In the concordance cosmology, we find  $H_0 = 71.8^{+3.9}_{-3.3}$  km/s/Mpc with a precision of 4.97%. This is in agreement with the latest measurements from Supernovae Type Ia and Planck observations of the cosmic microwave background. Our precision is lower compared to these and other recent time-delay cosmography determinations, because our modelling strategies reflect the systematic uncertainties of lensing degeneracies. We furthermore are able to find reasonable lensed image reconstructions by constraining to either value of  $H_0$  from local and early Universe measurements. This leads us to conclude that current lensing constraints on  $H_0$  are not strong enough to break the “Hubble tension” problem of cosmology.

## 2.1 Introduction

In the flat  $\Lambda$ -cold dark matter model of cosmology ( $\Lambda$ CDM), the rate at which the Universe expands on large scales is

$$\frac{da}{dt} = H_0 \left( \frac{\Omega_m}{a} + \frac{\Omega_r}{a^2} + \Omega_\Lambda \right)^{1/2} \quad (2.1)$$

where  $a$  is the scale factor and  $t$  is the cosmic time. The Hubble constant  $H_0$  is defined as the  $\dot{a}/a$  at the current epoch and sets the overall scale. The fractional contribution of the non-relativistic and relativistic mass-energy and dark energy components is captured by the  $\Omega_i = \rho_i/\rho_c$  parameters, which are normalized by

$$\rho_c = \frac{3H_0^2}{8\pi G} \quad (2.2)$$

the cosmological critical density. Local variations (galaxies) around the mean density arise from an initial fluctuation spectrum described by further cosmological parameters. This model [for a ‘skeptic’s guide’ see [\[59\]](#)] succeeds in describing a multitude of phenomena including the accelerating rate of expansion, the statistics of fluctuations both in the local Universe and in the cosmic microwave background (CMB), and the abundances of the light elements. Yet despite an increasing number of successes with measurements of unprecedented precision, some unsolved puzzles remain. Among these is the tension in the values of  $H_0$  from standard candles [in particular,  $74.0 \pm 1.4$  km/s/Mpc from the SH0ES (Supernovae  $H_0$  for the Equation of State) project by [\[10\]](#) and from the CMB [most recently  $67.4 \pm 0.5$  km/s/Mpc from the Planck collaboration [\[11\]](#)].

[\[59\]](#): Scott (2018)

[\[10\]](#): Riess et al. (2019)

[\[11\]](#): Planck Collaboration et al. (2018)

These measurements (sometimes called ‘late’ and ‘early’) represent two fundamentally different strategies for measuring cosmological parameters, and involve completely different physical processes. The first of these involves a redshift-distance relation, whereby one measures how the comoving distance

$$r(a) = c \int \frac{dt}{a(t)} \quad (2.3)$$

(or some variant of it) depends on redshift  $z = 1/a - 1$ . Standard-candle methods, gravitational-lensing time delays, and anticipated methods using gravitational-wave sources all use redshift-distance relations. In contrast, measurements of cosmological parameters from the CMB or from baryon acoustic oscillations use a different strategy, where the main observable is the angular power spectrum on the sky of acoustic oscillations in the Universe from epochs when structure growth was linear. The angular scale of the largest features is set by the apparent size of the horizon  $\theta_h(a)$  at the relevant redshift where

$$\theta_h^{-1}(a) = \frac{r(0)}{r(a)} - 1. \quad (2.4)$$

There is no explicit redshift-distance relation involved. Instead,  $H_0$  is inferred through the effect of the component densities  $\propto H_0^2/G$  on the acoustic oscillations. Comparing the  $H_0$  values from these completely different physical processes is an important test of the  $\Lambda$ CDM paradigm. If the ‘Hubble tension’ is confirmed as a discrepancy, many alternative

[60]: Knox et al. (2020)

[61]: Sandage et al. (2006)  
[62]: Freedman et al. (2012)  
[63]: Riess et al. (2016)  
[64]: Riess et al. (2018)  
[10]: Riess et al. (2019)  
[18]: Abbott et al. (2017)

[11]: Planck Collaboration et al. (2018)  
[68]: Hinshaw et al. (2013)

[69]: Abbott et al. (2018)  
[70]: Abbott et al. (2018)  
[71]: Alsing et al. (2016)  
[72]: Hildebrandt et al. (2016)  
[73]: Anderson et al. (2012)

[23]: Blandford et al. (1986)

[17]: Millon et al. (2020)

[12]: Refsdal (1964)  
[15]: Refsdal (1966)

[24]: Young et al. (1980)  
[74]: Saha et al. (2006)  
[75]: Schneider et al. (2014)  
[76]: Wagner (2018)  
[77]: Denzel et al. (2020)

cosmological theories will need to be considered [see e.g. 60].

For the redshift-distance relation, thermonuclear supernovae (SNeIa) as standard candles have been the leading method for some time [10, 61–64]. The uncertainty in this technique is mainly that the intrinsic brightness of SNeIa is difficult to determine, and requires a ‘distance ladder’ for calibration from other distance measurements in the local Universe [65–67]. Distance measurement using gravitational waves has only recently become feasible [18] and is especially interesting because no separate calibration is required. The period and period derivative (chirp) of a gravitational-wave binary give  $1 + z$  times the orbital energy of the binary. The two gravitational-wave polarisations have amplitudes of orbital energy divided by distance times inclination-dependent factors. If both polarisations are measured, inclination and distance both get measured. From acoustic oscillations, the CMB results from Planck [11] and earlier from WMAP [Wilkinson Microwave Anisotropy Probe; 68] are the best known, but there are also several measurements of cosmological parameters using a combination of galaxy clustering, weak lensing, baryonic acoustic oscillations, and primordial nucleosynthesis [69–73].

Gravitational-lensing time delays present another form of redshift-distance relation, involving multiple distances within one system. As lensing time delays are the subject of the present paper, we introduce the basic equation here, in the variational formulation following Blandford et al. [23] with small changes of notation. Consider a virtual light ray originating at a source at  $\beta$  on the sky, and at distance  $D_S$  from the observer. In front of the source, at redshift  $z_L$  and distance  $D_L$  from the observer, lies a gravitational lens consisting of a thin mass distribution  $\Sigma(\theta)$ . The virtual ray gets deflected at the lens and reaches the observer from  $\theta$  on the sky. The arrival-time surface  $t(\theta)$  of this virtual light ray is

$$\frac{t(\theta)}{(1+z_L)} = \frac{D_L D_S}{2c D_{LS}} (\theta - \beta)^2 - \frac{8\pi G}{c^3} \nabla^{-2} \Sigma(\theta) \quad (2.5)$$

where  $D_{LS}$  is the distance from the lens to the source. Although these are all angular-diameter distances, and hence  $D_{LS} \neq D_S - D_L$ , the distances are still strictly proportional to  $c/H_0$ . That is,  $H_0^{-1}$  sets the scale of equation (2.5). Real light rays correspond to  $\nabla t(\theta) = 0$ , namely minima, saddle points, and maxima of  $t(\theta)$ , and these are the locations of multiple images. If the source varies in time, the differences (or time delays) between  $t(\theta_i)$  at multiple images can be measured. For variable sources such as quasars the differences in arrival times are usually of the order several days to a year. With accurate measurements of the time delays, it is possible to determine a time scale which is proportional to  $H_0^{-1}$ . This makes strong gravitational lenses excellent cosmological probes because they enable a determination of  $H_0$  completely independent of the cosmic distance ladder. Lensing time delays have therefore been the subject of many observational campaigns, the most recent results reported in Millon et al. [16] and Millon et al. [17].

The early theoretical work [12, 15] considered pointlike sources and lenses. But as soon as lenses were discovered, it became clear that extended mass distributions  $\Sigma(\theta)$  and extended sources would need modelling. The resulting model-dependence of inferences was noted already in the first paper modelling lensing data [24] and has been explored in many later works [e.g. 74–77]. If there are many lensed sources at different

redshifts, each lensed into multiple images,  $\Sigma(\theta)$  will be well constrained by them. Ghosh et al. [78] estimate that if there are 1000 lensed images, a single precise time-delay measurement would measure  $H_0$  to sub-percent accuracy, and that this may be feasible with JWST observations of cluster lenses. Galaxy lenses, however, rarely have more than one source lensed into four images, so the best strategy is to combine many lenses. Sereno et al. [79] report a 10% uncertainty on  $H_0$  using 18 time-delay lenses. Smaller uncertainties on  $H_0$  are possible—2.5% from six lenses by the H0LiCOW collaboration [ $H_0$  Lenses in COSMOGRAIL’s Wellspring; 52] and 4% uncertainty from a single lens [33]—if it is assumed that galaxy lenses follow certain parametric forms. Recent studies suggest that these uncertainties increase if the effect of lensing degeneracies are considered [80]. In a recent blind test involving several research groups, the Time Delay Lens Modelling Challenge [TDLMC; 53], the currently achievable error level in the recovery of simulated  $H_0$  from up to 16 lenses was found to be 6%.

[79]: Sereno et al. (2014)

[52]: Wong et al. (2020)

[33]: Shajib et al. (2020)

[80]: Birrer et al. (2020)

[53]: Ding et al. (2020)

The Hubble constant is commonly expressed in units of km/s/Mpc. This choice reflects Hubble’s law by stating that the Hubble constant is the recession speed of a target galaxy over its distance. However, it is arguably more natural to think of the Hubble constant as a reciprocal time or frequency. Of course, the Hubble time  $H_0^{-1}$  is already in units of Gyr and proportional to the age of the Universe. In the current epoch, the Hubble parameter seems to be close to steady and consequently, distances scale (nearly) exponentially with  $a \propto e^{Ht}$  due to the increasingly dominant dark-energy density component. In this context, it may be much more favourable to express the Hubble constant in SI units or SI derivations such as attohertz ( $a\text{Hz} = 10^{-18} \text{ s}^{-1}$ ). One should recall that the following are all equivalent:

$$\begin{aligned} H_0 &= 70.0 \text{ km/s/Mpc} = 2.27 \text{ aHz} \\ H_0^{-1} &= 14.0 \text{ Gyr} \\ \frac{3}{8\pi G} H_0^2 &= 5.16 \text{ GeVm}^{-3} \end{aligned}$$

These new units of attohertz then convey that large-scale structures undergo e-foldings with a frequency of roughly 2.3 aHz. We can compare this current day value to that of the very early Universe where 60 e-folds may have occurred in  $\sim 1$  s [81].

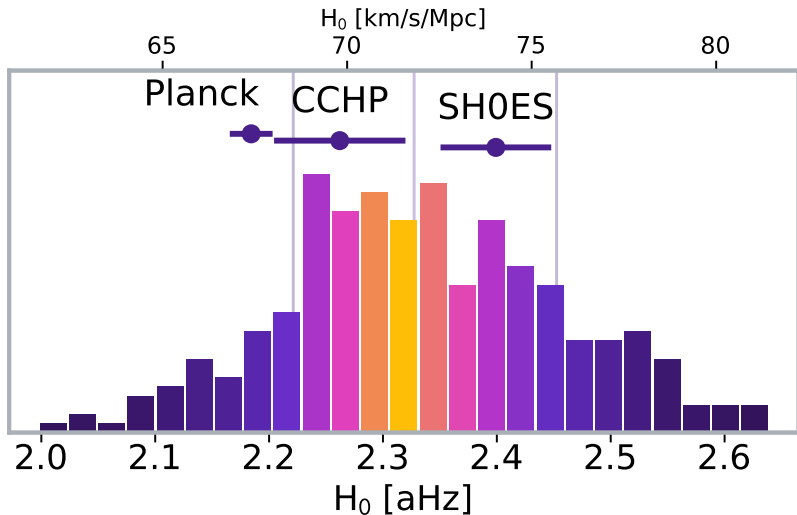
[81]: Allahverdi et al. (2020)

In this paper, we infer  $H_0$  from 8 free-form time-delay lenses using the most recent observational data available and more flexible modelling methods. Additionally, we explore the effect of lensing degeneracies on  $H_0$ , which is the inherent limitation to all lensing observables [26]. We demonstrate that due to these degeneracies it is possible to find solutions which fit values of  $H_0$  measured through early and late-Universe probes. Our main findings are summarized in Figure 2.1.

[26]: Saha (2000)

In Section 2.2 below, we describe the eight lenses used in this work: B1608+656, DESJ0408-5354, HE0435-1223, PG1115+080, RXJ0911+0551, RXJ1131-1231, SDSSJ1004+4112, and WFIJ2033-4723. For each system we give an account of the research history, a short description of the image configuration and point out any other special features. Next, in Section 2.3, we describe the numerical techniques and methods employed

**Figure 2.1:** The main result: an ensemble of  $H_0$  values inferred from the joint modelling of eight four-image time-delay lenses. Vertical lines indicate the median 68 per-cent confidence range of  $H_0 = 2.33^{+0.13}_{-0.11}$  aHz =  $71.8^{+3.9}_{-3.3}$  km/s/Mpc. To make the median furthermore easily discernible, the colouring of the histogram's bars corresponds to the cumulative probability centred around the median (yellow-magenta-blue-black goes from 1 to 0). Horizontal error bars indicate recent measurements from other methods for comparison: Planck [11], CCHP [the Carnegie-Chicago Hubble Program; 67], and SH0ES [the Supernovae  $H_0$  for the Equation of State; 10]. A discussion of units can be found in the introduction.



to analyse the lenses and determine  $H_0$ . We list precisely what information was used to model and constrain the lens reconstructions. Here, Section 2.3.4 describes the TDLMC in which our lens-modelling methods have been initially tested for the purpose of inferring  $H_0$ . In Section 2.4, we present the detailed results of our work, namely the lens models, and derived quantities such as radially-averaged enclosed mass profiles, time-arrival surfaces, synthetic images, and posterior distributions of  $H_0$ , and moreover of the Hubble time and critical density. Relevant results from the TDLMC are discussed in Section 2.4.5. Finally in Section 2.5, we summarize the main findings and discuss possible implications.

## 2.2 The lens systems

The light travel time of the individual images differ if strongly lensed systems lie at cosmological distances. However, measuring time delays is a very time-consuming process and only a handful of systems are currently known with accurate and robust values. Due to computational constraints and their strong presence in the literature, we limited our analysis to the following 8 lenses shown in Figure 2.2. In this section, we briefly describe the lenses and note the time delays with the image ordering provided in the respective literature. In subsequent sections, and as listed in Table 2.1, we consistently relabel the images as ABCD in arrival-time order.

### 2.2.1 B1608+656

This system was discovered during the first phase of the Cosmic Lens All-Sky Survey (CLASS). The system contains two lensing galaxies and clearly shows four quasar images on radio wavelengths, whereas its Einstein ring is better visible in the optical spectrum. Further data collection yielded redshifts for the lens  $z_l = 0.630$ , the source  $z_s = 1.394$ , and hints that the lens consists of two merging galaxies [83, 84]. After multiple seasons of monitoring [85–87] and several robustness tests [88, 89] time delay measurements converged to  $\Delta t_{AB} = 31.5^{+2.0}_{-1.0}$ ,  $\Delta t_{CB} = 36.0^{+1.5}_{-1.5}$ , and  $\Delta t_{DB} = 77.0^{+2.0}_{-1.0}$  days with arrival-time order BACD. Since its discovery,

[85]: Fassnacht et al. (1999)

[86]: Fassnacht et al. (1999)

[87]: Fassnacht et al. (2002)

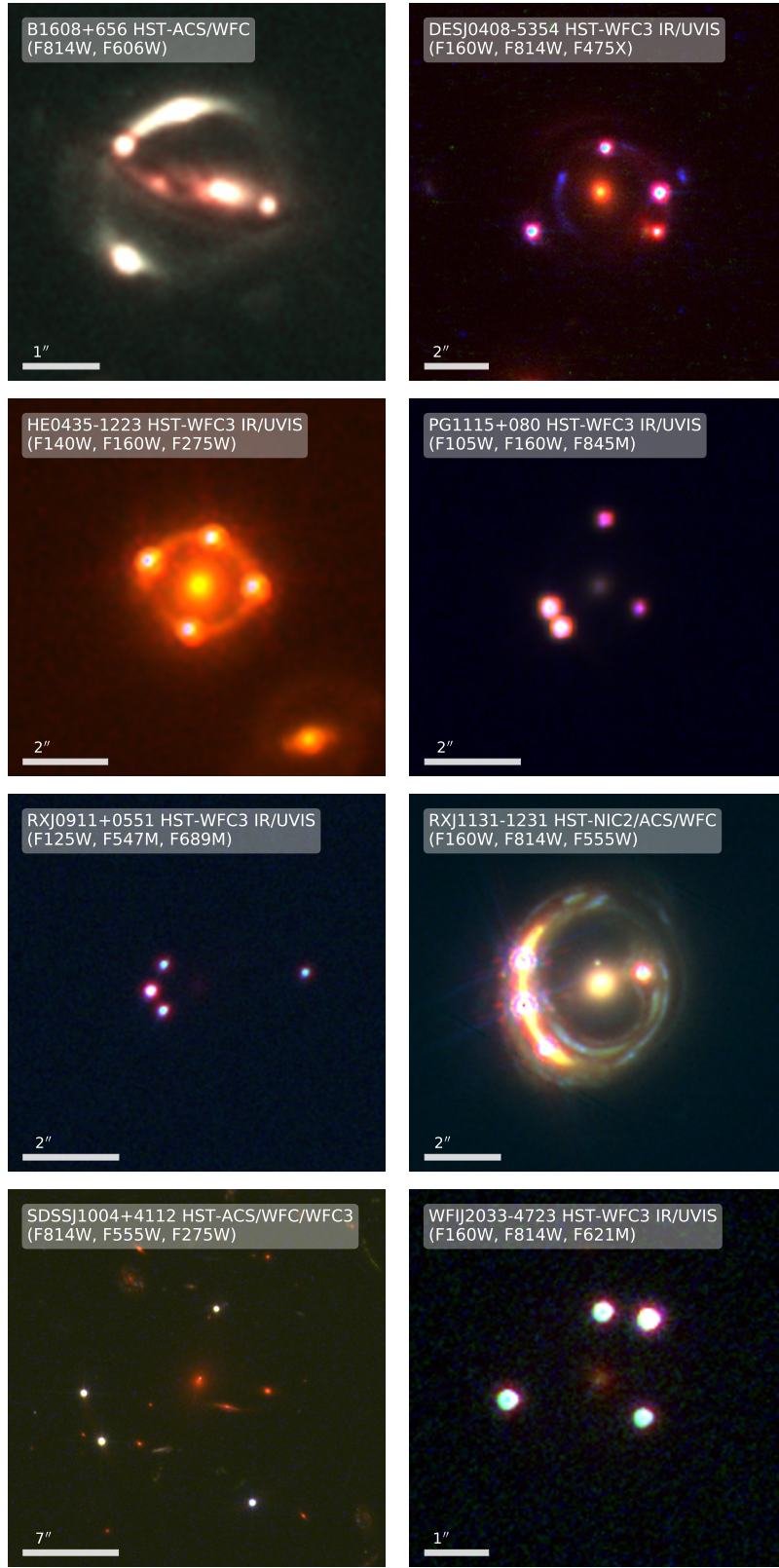


**Figure 2.2:** Composite HST images of the modelled lens systems centred on the main lens. The image data were stacked using 2 or 3 bands in the UV/Visible, optical, or near-infrared with an individually modified method described by Lupton et al. [82]. The exact camera system and filters are listed in the label ordered by R, G, and B colour channels. In all images north is up and east is left.

- [90]: Koopmans et al. (1999)
- [91]: Williams et al. (2000)
- [92]: Koopmans et al. (2003)
- [93]: Fassnacht et al. (2004)
- [94]: Suyu et al. (2010)
- [52]: Wong et al. (2020)

- [95]: Lin et al. (2017)
- [96]: Courbin et al. (2018)
- [97]: Agnello et al. (2017)
- [33]: Shajib et al. (2020)

many lens modellers have used the system for a determination of  $H_0$  [52, 90–94].

### 2.2.2 DESJ0408-5354

This system was found and confirmed only recently in the Dark Energy Survey (DES) Year 1 (Y1) data. Subsequent spectroscopic observations using the Gemini South telescope confirmed a quasar in the source with redshift  $z_s = 2.375$ , and the central lens as an early-type galaxy with redshift  $z_l = 0.597$  [95]. Simultaneously, high-cadence photometric monitoring results by [96] report time-delays measurements of  $\Delta t_{AB} = -112.1^{+2.1}_{-2.1}$ ,  $\Delta t_{AD} = -155.5^{+12.8}_{-12.8}$ , and  $\Delta t_{BD} = 42.4^{+17.6}_{-17.6}$  days with arrival-time order ABCD. Follow-up investigations revealed the presence of a second set of multiple images at different redshifts [97], which places it amongst the richest discoveries of lenses so far. In depth analysis of this system by the STRong-lensing Insights into Dark Energy Survey collaboration [STRIDES; 98] determined  $H_0 = 74.2^{+2.7}_{-3.0}$  [33].

### 2.2.3 HE0435-1223

- [99]: Wisotzki et al. (2002)
- [100]: Morgan et al. (2005)
- [101]: Kochanek et al. (2006)
- [102]: Sluse et al. (2017)
- [105]: Tihhonova et al. (2018)
- [106]: Nierenberg et al. (2017)
- [16]: Millon et al. (2020)

Wisotzki et al. [99] reported the discovery of this system. It has a lensed QSO at redshift  $z_s = 1.689$  in a crossed image configuration. The redshift  $z_l = 0.454$  of the lensing galaxy was measured three years later by Morgan et al. [100], and time delays were reported the following year by Kochanek et al. [101]. The system has recently been the focus of many studies by the H0LiCOW collaboration which provided a spectroscopic survey [102], a mass model [103], newly measured time delays [104], and external convergence field models [105]. Moreover, Nierenberg et al. [106] investigated the lens' substructure with a WFC3 grism narrow-line survey. The latest report by Millon et al. [16] estimates the time delays as  $\Delta t_{AB} = -9.0^{+0.8}_{-0.8}$ ,  $\Delta t_{AC} = -0.8^{+0.8}_{-0.7}$ ,  $\Delta t_{AD} = -13.8^{+0.8}_{-0.8}$ ,  $\Delta t_{BC} = 7.8^{+0.9}_{-0.9}$ ,  $\Delta t_{BD} = -5.4^{+0.9}_{-0.8}$ , and  $\Delta t_{CD} = -13.2^{+0.8}_{-0.8}$  days with arrival-time order CADB.

### 2.2.4 PG1115+080

- [107]: Weymann et al. (1980)
- [108]: Christian et al. (1987)
- [109]: Kundic et al. (1997)
- [111]: Schechter et al. (1997)
- [113]: Bonvin et al. (2018)

The so-called *triple quasar* is the second gravitational lens ever discovered Weymann et al. [107]. Only after its naming, it was shown that the seemingly brightest image was—according to generic lens theory—in fact a blend of two separate images. The elliptical lensing galaxy was detected only 7 years after its discovery by Christian et al. [108]. Kundic et al. [109] and Tonry [110] independently measured the redshift of the lens to be  $z_l = 0.311$ . The potential to constrain cosmological parameters was realized early and time delays were first measured by Schechter et al. [111], and soon after improved by Barkana [112]. The latest time delays were reported by [113] as  $\Delta t_{AB} = 8.3^{+1.5}_{-1.6}$ ,  $\Delta t_{AC} = 9.9^{+1.1}_{-1.1}$ , and  $\Delta t_{BC} = 18.8^{+1.6}_{-1.6}$  days with arrival-time order CA<sub>1</sub>A<sub>2</sub>B.

## 2.2.5 RXJ0911+0551

Bade et al. [114] confirmed this system to be gravitationally lensing after follow-up observations of candidates from the ROSAT All-Sky Survey (RASS). It shows a complex image configuration with one image particularly far from the other three, requiring a large external shear component Burud et al. [115]. It was suspected that the origin of the high shear was a nearby cluster, which was finally discovered two years later by Kneib et al. [116]. Hjorth et al. [117] measured a time delay of  $\Delta t_{AB} = 146^{+8}_{-8}$  days with arrival-time order BA<sub>1</sub>A<sub>2</sub>A<sub>3</sub>, where B is the distant and leading component image, and A<sub>i</sub> the combination of the other three.

[114]: Bade et al. (1997)

[115]: Burud et al. (1998)

[116]: Kneib et al. (2000)

## 2.2.6 RXJ1131-1231

The system has been serendipitously unveiled during polarimetric imaging of radio quasars by Sluse et al. [118]. The redshifts of the lens and source were measured as  $z_l = 0.295$  and  $z_s = 0.658$  [119]. HST imaging shows a detailed Einstein ring from the host galaxy of the multiply imaged quasar. Substructure-analyses by Claeskens et al. [120] and Suyu et al. [121] furthermore point out a satellite of the lensing galaxy, identifiable as a small, bright spot north of the lens. An extensive time delay estimation was obtained from a 9-year optical monitoring using three different numerical methods between all possible pairs of quasar images with arrival-time order BCAD by Tewes et al. [122]. Due to the high quality of observational data available, the system has been subjected to modelling methods and cosmographic analyses in many previous works e.g. Holanda, Birrer et al., Birrer et al., Suyu et al. [89, 123–125].

[118]: Sluse et al. (2003)

[119]: Sluse et al. (2007)

[120]: Claeskens et al. (2006)

[121]: Suyu et al. (2013)

[122]: Tewes et al. (2013)

[89]: Holanda (2016)

[123]: Birrer et al. (2016)

[124]: Birrer et al. (2017)

[125]: Suyu et al. (2017)

## 2.2.7 SDSSJ1004+4112

With its multiple quasar images at a separation of 14.62arcsec, this system is the largest and rarest object in our set [126]. As expected from such a giant, it was shown to be a cluster dominated by dark matter [127, 128]. Since time delays are of the order of  $c^{-3}GM$  it is only natural to expect much higher delays for cluster lenses. Oguri [129] used mass models of the lensing galaxies to predict time delays of  $\Delta t_{AD} \sim 1218$  days and Mohammed et al. [130] demonstrated how useful such a time delay measurement would be for constraining its substructure. After more than 3.5 years of data collection the time delays were estimated as  $\Delta t_{BA} = 40.6^{+1.8}_{-1.8}$ ,  $\Delta t_{CA} = 821.6^{+2.1}_{-2.1}$ , and  $\Delta t_{AD} > 1250$  days with arrival-time order CBAD [131, 132].

[126]: Inada et al. (2003)

[127]: Oguri et al. (2004)

[128]: Williams et al. (2004)

[130]: Mohammed et al. (2015)

[131]: Fohlmeister et al. (2008)

[132]: Fohlmeister et al. (2007)

## 2.2.8 WFIJ2033-4723

Very similar to B1608+656 (see 2.2.1) and PG1115+080 (see 2.2.4), WFIJ2033-4723 is a quad in a fold configuration with two images almost blending. It was discovered by Morgan et al. [133] during an optical imaging ESO survey. The quasar images are considerably brighter than the foreground lens galaxy whose redshift  $z_l = 0.661$  was measured by Eigenbrod et al. [134]. The redshift of the quasar images  $z_s = 1.662$  were confirmed

[133]: Morgan et al. (2004)

[134]: Eigenbrod et al. (2006)

[135]: Sluse et al. (2012)

[136]: Bonvin et al. (2019)

by Sluse et al. [135]. The most recent time delay measurements report  $\Delta t_{AB} = 36.2^{+0.7}_{-0.8}$ ,  $\Delta t_{AC} = -23.3^{+1.2}_{-1.4}$ , and  $\Delta t_{BC} = -59.4^{+1.3}_{-1.3}$  days with arrival-time order BA<sub>1</sub>A<sub>2</sub>C [136].

## 2.3 Lens reconstruction method

[50]: Coles et al. (2014)

[137]: Küng et al. (2015)

[138]: Bruderer et al. (2016)

[48]: Küng et al. (2018)

[140]: Saha et al. (2004)

[79]: Sereno et al. (2014)

[141]: Saha et al. (2006)

The lenses were reconstructed using the free-form modelling code GLASS\* [50] plus recent developments by Denzel et al. [77]. GLASS has previously been used for several studies of galaxy lenses [48, 137, 138] and cosmological parameters [139] although not for  $H_0$ , other than the TDLMC. However the related older code PixeLens<sup>†</sup> has been used to estimate  $H_0$  [79, 140, 141].

### 2.3.1 GLASS

To formulate the method, we introduce the usual dimensionless density  $\kappa$  and arrival time  $\tau$

$$\begin{aligned}\Sigma(\theta) &= \frac{c^3}{4\pi GH_0} \frac{d_L d_S}{d_{LS}} \kappa(\theta) \\ H_0 t(\theta) &= (1 + z_L) \frac{d_L d_S}{d_{LS}} \tau(\theta)\end{aligned}\quad (2.6)$$

where  $d_L$  is  $D_L$  with the dimensional factor  $c/H_0$  taken out. In terms of these, the arrival time becomes

$$\tau(\theta) = \theta \cdot \beta + \frac{1}{2} |\theta|^2 - 2\nabla^{-2}\kappa(\theta). \quad (2.7)$$

In free-form or pixellated lens reconstruction, the mass distribution

$$\kappa(\theta) = \sum \kappa_n Q(\theta - \theta_n) \quad (2.8)$$

is represented as a collection of pixels where  $Q(\theta - \theta_n)$  is a square (or other profile) and  $\theta_n$  is its centroid. The contribution  $\nabla^{-2}Q(\theta)$  of a square to the arrival time can be calculated analytically [142].

[142]: AbdelSalam et al. (1998)

The pixels  $\kappa_n$  are arranged in concentric ‘pixel rings’ centred on the lensing galaxy. The central pixel can be refined into sub-pixels in order to better resolve steep cusps. The  $\kappa_n$  values are required to satisfy the following prior inequality constraints.

1. All mass densities must be non-negative:  $\kappa_n \geq 0$ .
2. In order to keep the mass distribution relatively smooth, no mass tile can exceed twice the average of its neighbors.
3. The local density gradient  $\nabla\kappa$  should point within  $\alpha = 60^\circ$  of radially inwards:

$$\mathbf{R}\nabla\kappa \geq 0, \quad \mathbf{R}^\top \nabla\kappa \geq 0$$

where  $\mathbf{R} = \mathbf{R}(\alpha)$  is a rotation.

\* GLASS: <http://ascl.net/1806.009>

<sup>†</sup> PixeLens: <https://ascl.net/1102.007>

4. The average density  $\langle \kappa \rangle_i$  of mass within a ring  $i$  at radius  $R_i$  must have a profile that is steeper than  $R^{-s}$ :

$$R_i^{-s} \langle \kappa \rangle_i - R_{i+1}^{-s} \langle \kappa \rangle_{i+1} \geq 0$$

This still allows for twisting iso-density contours and significantly varying ellipticities with radius. In this work we set  $s = 0$ , requiring only that the circularly averaged mass not increase with radius, which is rather conservative.

Additionally, since the pixels cover only a relatively small, finite surface, external shear from, e.g., a nearby galaxy, can be added to equation (2.7), as a two-component shear

$$\gamma_1(\theta_x^2 - \theta_y^2) + 2\gamma_2 \theta_x \theta_y \quad (2.9)$$

where  $(\gamma_1, \gamma_2)$  are constant shear components. Furthermore, neighbouring galaxies can be modelled as point masses (or other distributions) whose contributions also add to equation (2.7).

Multiple-image data from observations further constrain the mass distribution:

1. The arrival time must be stationary at the observed image locations. That is, for all image locations  $\theta_i$  we require  $\nabla \tau(\theta_i) = 0$ . For one image, such an equation simply relates the unknown source position to the image position, so it does not constrain the mass distribution. Additional images from the same source do, however, constrain the mass distribution, because the source position has already been determined by the first image.
2. The elements of the inverse magnification tensor  $\nabla \nabla \tau(\theta)$  are constrained by inequalities to enforce supplied image parities. These are not known a priori, but have to be inferred by the investigator based on the brightness of the images, time-delay data, and test runs.
3. The time delay  $\tau(\theta_i) - \tau(\theta_j)$  between images must reproduce the observed time delays.

These equality and inequality constraints are all linear in the mass tiles  $\kappa_n$ , the source position  $\beta$ , the external shear components  $\gamma_1, \gamma_2$ , any additional point masses, and finally  $H_0$ . As a result, in the high-dimensional space of these quantities, there is a convex polytope inside which all points satisfy the prior and data constraints. Lubini et al. [143] developed an algorithm for uniformly sampling high-dimensional polytopes, which is implemented in GLASS. The following definitions are used in GLASS modelling:

[143]: Lubini et al. (2012)

- A lensing mass  $\Sigma$  is made up of  $\sim 200$  pixels, whose values are individually adjustable subject to the constraints discussed above.
- A *model* is the set of a mass distributions  $\Sigma_i$ , shear terms, etc. for all eight lenses which reproduce the respective image and time-delay data and share a common value for  $H_0$ .
- An *ensemble* is a set of 1000 models drawn uniformly from the space of solutions that satisfy the above constraints.

### 2.3.2 Point-image data

Table 2.1 lists the point-image and time-delay data used in this study. We also indicate the locations of external galaxies approximated as point masses.

The following settings were also used.

- The mass pixels were arranged in a discretised circular disc 17 pixels in diameter. The central pixel was further refined into  $3 \times 3$  sub-pixels. The side length of the mass pixels was between  $0.19''$  and  $0.35''$  with SDSSJ1004+4112 being an exception at  $1.4147''$ . Note that  $\tau(\theta)$  is not discretised.
- All models allowed for external shear.
- A flat cosmology with  $(\Omega_m, \Omega_\Lambda) = (0.27, 0.73)$  was assumed.

### 2.3.3 Extended image data

The procedure thus far uses solely the centroidal positions of the multiply imaged quasars. We now incorporate the full photometric data of the extended images as described in Denzel et al. [77] and related earlier work [48].

As images appear where  $\nabla\tau(\theta) = 0$ , we first define a lens mapping  $L(\theta, \beta)$ , which is equivalent to the more commonly known lens equation. An extended image produced by an extended source can then be written as

$$I(\theta) = \int L(\theta, \beta) S(\beta) d^2\beta. \quad (2.10)$$

For each of the  $1000 \times 8$  lens masses in an ensemble we generate synthetic images by fitting a source brightness distribution  $S(\beta)$  such that the extended image  $I$  further convolved by a point spread function  $P(|\theta - \theta'|)$

$$\int P(|\theta - \theta'|) L(\theta', \beta) S(\beta) d^2\theta' d^2\beta \quad (2.11)$$

optimally fits the data. The extended image is linear in the source brightness distribution, so fitting is straightforward.

### 2.3.4 TDLMC

In January 2018, the Time Delay Lens Modelling Challenge was initiated. Ding et al. [146] explained the experimental design and invited scientists to model 50 simulated Hubble Space Telescope (HST) observations of mock lens systems. The challenge was divided into three ‘rungs’ each featuring a set of 16 lenses which increased in modelling difficulty. Additionally, the ‘Evil’ team, the designers of the challenge, provided a calibration rung containing 2 lenses along with the entire information about the systems. For all other lenses, an HST mock image of the lens, the redshifts of source and lens, external convergence estimates, velocity dispersion estimates, the time delays, a noise map, and a point-spread function (PSF) map were provided. Based on this information, the challenge for the ‘Good’ teams was to infer  $H_0$ , which was randomly fixed between 50

[77]: Denzel et al. (2020)

[48]: Küng et al. (2018)

[146]: Ding et al. (2018)

and 90 km/s/Mpc by the Evil team, for each rung for a fixed background cosmology. With final submission on September 8th 2019, the TDLMC finished its submission phase, and the results were thoroughly evaluated [53].

[53]: Ding et al. (2020)

We have participated in this challenge and were able to further test our free-form modelling techniques extensively with focus on  $H_0$  inference during and after it.

These kinds of tests on simulated data always come with some caveats. In particular, mock lenses in rung3 were derived from hydrodynamical simulations of galaxies. Expectedly, this limits the quality of lens simulations to the one of the used simulations. In particular, the resolution of the galaxies were known to be insufficient to resolve the inner regions of the galaxies. Some of the limitations on the other hand were discovered post-unblinding, such as inconsistencies with the kinematics due to the removal of substructure, and the halo truncation at the virial radius, which does not follow isodensity contours and potentially biases  $H_0$ .

Moreover, during the challenge we have noticed that the simulated lenses differ from observed ones in at least one important aspect: the radial spread of the images around the lens center is considerably wider, by about a factor of 2, in observed lenses compared to the simulated ones (also see Gomer & Williams 2020, MNRAS, submitted).

Nevertheless, we have learned much from the TDLMC and applied our new strategies to the models presented in this publication. In Section 2.4.5 we present the accuracy and precision of our TDLMC results, and compare the precision to that of the present work.

**Table 2.1:** Input parameters used to model the gravitational lens systems. The images of each lens are ordered according to arrival times (earliest on top). Time delays have been recalculated accordingly. Image coordinates  $x, y$  are relative to the center of lensing galaxy. The measured redshifts  $z_L$  and  $z_S$  correspond to the lens and source redshifts. To account for any significant external lensing contribution (besides external shear), we added point masses at the positions where galaxies of similar redshift are visible in the field. Every lens has been subjected to rigorous investigations in the past as explained in Section 2.2; the references to the works used particularly in this study are cited here: (1): Koopmans et al. [90]; (2): Fassnacht et al. [85]; (3): Fassnacht et al. [87]; (4): Koopmans et al. [92]; (5): Lin et al. [95]; (6): Courbin et al. [96]; (7): Millon et al. [16]; (8): Bonvin et al. [104]; (9): Sluse et al. [144]; (10): Kochanek et al. [101]; (11): Morgan et al. [145]; (12): Tonry [110]; (13): Barkana [112]; (14): Weymann et al. [107]; (15): Eulaers et al. [88]; (16): Hjorth et al. [117]; (17): Burud et al. [115]; (18): Bade et al. [114]; (19): Birrer et al. [123]; (20): Tewes et al. [122]; (21): Sluse et al. [119]; (22): Sluse et al. [118]; (23): Fohlmeister et al. [132]; (24): Fohlmeister et al. [131]; (25): Williams et al. [128]; (26): Oguri et al. [127]; (27): Inada et al. [126]; (28): Bonvin et al. [136]; (29): Eigenbrod et al. [134]; (30): Morgan et al. [133].

System	$x$ [arcsec]	$y$ [arcsec]	$z_L$	$z_S$	Time delays [days]	Point mass $x, y$ [arcsec]	Reference
B1608+656	-0.82,	1.28	0.63	1.39		(0.14, 0.79)	(1); (2); (3); (4)
	1.10,	0.42			$31.5 \pm 1.5,$		
	0.68,	1.20			$4.5 \pm 1.5,$		
	-0.23,	-0.64			$41 \pm 1.5$		
DESJ0408-5354	1.25,	-2.15	0.597	2.375			(5); (6)
	0.04,	1.86			$112.1 \pm 2.1,$		
	1.26,	1.77			$42.4 \pm 17.6,$		
	-1.37,	0.15			$155.5 \pm 12.8$		
HE0435-1223	1.35,	-0.36	0.454	1.689			(7); (8); (9); (10)
	-1.18,	-0.07			$2.1 \pm 0.78,$		
	-0.06,	-1.09			$6 \pm 1.07,$		
	0.19,	1.13			$8.37 \pm 1.31$		
PG1115+080	0.11,	1.37	0.311	1.735			(11); (12); (13); (14)
	-0.79,	-0.87			$13.3 \pm 0.9,$		
	-1.06,	-0.43					
	0.86,	-0.46			$11.7 \pm 1.5$		
RXJ0911+0551	-2.27,	0.29	0.769	2.763		(-0.76, 0.66)	(15); (16); (17); (18)
	0.96,	-0.10			$146 \pm 8,$		
	0.70,	-0.50					
	0.69,	0.46					
RXJ1131-1231	1.39,	1.64	0.295	0.658		(0.51, -0.14)	(7); (19); (20); (21); (22); (12)
	-0.96,	2.06			$1.50 \pm 2.49,$		
	0.29,	2.13			$9.61 \pm 1.97,$		
	-0.23,	-1.18			$87 \pm 8$		
SDSSJ1004+4112	8.85,	-4.44	0.68	1.74			(23); (24); (25); (26); (27)
	-5.76,	-6.36			$821.6 \pm 2.1,$		
	-2.46,	-8.19			$40.6 \pm 1.8,$		
	-2.37,	4.64					
WFJ2033-4723	0.60,	1.35	0.661	1.66			(28); (29); (30)
	0.31,	-1.21			$35.5 \pm 1.4,$		
	0.86,	-0.66					
	-0.88,	-0.23			$27.1 \pm 1.4$		

## 2.4 Results

Most of the results in this paper come from an ensemble of 1000 eight-lens models required to reproduce the point-image and time-delay data. This ensemble was also subsequently filtered according to how well extended images could be reproduced. We consider the average of the ensemble, and also the variation within the ensemble. Because the model ensemble is constructed using linear constraints, any weighted average of ensemble members is also a valid model.

Apart from the main ensemble, we produced two further models using the same image and time-delay data, but constrained to the  $H_0$  values from Planck and SH0ES mentioned at the beginning of this paper, to demonstrate their compatibility. Furthermore, we compare distribution of inferred  $H_0$  to models for the mock data from the TDLMC in Section 2.4.5.

### 2.4.1 Arrival-time surfaces

Figure 2.3 shows contour maps of the arrival time  $\tau(\theta)$  from the average models of the main ensemble. The orientation in this figure is different from Figure 2.2 but consistent with subsequent figures. In the classification of Saha et al. [147] HE0435-1223 is a core quad, RXJ1131-1231 a long-axis quad, RXJ0911+0551 a short-axis quad, while the rest are inclined quads. The minima and saddle point appear at the correct image locations, as required, and there are no indications of spurious additional images.

[147]: Saha et al. (2003)

### 2.4.2 Convergence maps

Figure 2.4 shows convergence maps  $\kappa(\theta)$  of the ensemble-average models. The maps exhibit the typical pixellated structure stemming from the free-form technique. Contrary to earlier work imposing inversion symmetry in most cases [148, 149] all the lens models allow for asymmetry, which seems to be an important feature, in e.g., DESJ0408-5354 and RXJ0911+0551. Rough shapes and orientations seem to agree with previous reconstructions [33, 150–153]. The area within the black contours on the maps indicate a supercritical density with  $\kappa \geq 1$ . This area defines a scale which can be expressed as the Einstein radius and formally corresponds to the radius where  $\langle \kappa \rangle_{R_E} = 1$ .

[148]: Saha et al. (2006)  
[149]: Paraficz et al. (2010)

[150]: Chantry et al. (2010)  
[151]: Wynne et al. (2018)  
[33]: Shajib et al. (2020)  
[152]: Yoo et al. (2005)  
[153]: Saha et al. (2007)

In Figure 2.5 the value for the Einstein radius can easily be read off (as vertical lines). It shows the distribution of average enclosed  $\kappa$  as a function of radial distance from lens centre for the entire ensemble. The ensemble-average profile is depicted in red. As it is typical for (good) lens reconstructions, the spread in the Einstein radius is minimal and usually accurate due to the strong constraints coming from the images themselves which usually lie at comparable radii. Conversely, the spread within the ensemble towards center is much greater ranging from cored profiles to almost cusp-like centres. This too was expected due to the lack of constraints at these radii. Note that all profiles are in units of  $\kappa$  which is the surface density scaled to the critical density for each lens, giving them the appearance of having seemingly similar mass contents. Particularly

for SDSSJ1004+4112, the masses exceed magnitudes of (normal) galaxies and clearly reach cluster scales.

Since free-form lens-reconstruction ensembles can in principle contain many differently shaped density maps, it is important to investigate dominant as well as secondary features across all models in an ensemble. As explained in Section 2.3, these models represent solutions from a high-dimensional space, treating each mass tile as a parameter. To do this we carried out a principal-components analysis (PCA) of the ensemble [similar to 48, 130]. A PCA yields a representation of the mass distribution for the  $k$ -th lens ( $k = 1, 2, \dots, 8$ ) of the form

$$\kappa^{(k)}(\boldsymbol{\theta}) = \bar{\kappa}^{(k)}(\boldsymbol{\theta}) + \sum_p c_p \Delta\kappa_p^{(k)}(\boldsymbol{\theta}) \quad (2.12)$$

where  $\bar{\kappa}^{(k)}$  is the ensemble-average lensing mass (as shown in Figure 2.4), while  $\Delta\kappa_p^{(k)}$  is the  $p$ -th principal component, and  $c_p$  is a coefficient. The  $\Delta\kappa_p^{(k)}$  are orthonormal by construction. Note that the coefficients  $c_p$  do not depend on  $k$ , but are common for all eight lenses. Each of the  $c_p$  has a range of values across the ensemble: the coefficient  $c_1$  of the first principal component has the largest range, while  $c_{100}$  stays close to zero. Thus, PCA filters and sorts the ensemble for its most salient features. Figure 2.6 shows an example of lens models projected into the PCA-feature space. It considers the lens WFIJ2033-4723 and the 1st, 2nd, 5th, and 100th principle components. For each of these, we display the projection

$$\bar{\kappa}^{(k)}(\boldsymbol{\theta}) + c_p \Delta\kappa_p^{(k)}(\boldsymbol{\theta}). \quad (2.13)$$

for the 16th and 84th percentile values of  $c_p$ . This figure illustrates the variety of models within an ensemble, but concurrently also identifies regions in the convergence maps which have been constrained to a higher degree and thus have low variance. As observed in Figure 2.5, the convergence maps are typically well constrained around the notional Einstein ring (indicated by a black contour in Figures 2.4 and 2.6), since in most cases by the 5th principal component its shape already does not vary anymore.

### 2.4.3 Synthetic images

Another rather affirming result is presented by the synthetic images from source reconstructions using the ensemble-averaged lens models. In the least-squares fitting discussed in Section 2.3.3, a Poisson noise in the photometry was assumed  $\sigma_\theta^2 = g^{-1}|D_\theta^{\text{obs}}|$  where  $g$  is the gain or counts per photon. The source reconstructions yielded reduced  $\chi^2$  which are listed in Table 2.2.

The reduced least-squares provide a standardized measure of the synthetic's quality. A  $\chi^2 = 1$  means the synthetic image differs from the data only on noise level and provides an ideal fit. However, since the observations come from different camera systems, wavelength bands, and dates ranging from 2004 to 2018, the data contains various signal-to-noise ratios (SNR). Consequently, a  $\chi^2$  of say 1.5, is easier to reach for a relatively old and noisy image, compared to one taken with a more modern system with a lower SNR. The scatter of  $\chi^2$  within a lens system is typically only between 1 or 2, in the case of SDSSJ1004+4112 about 8. The least squares

[130]: Mohammed et al. (2015)  
[48]: Künig et al. (2018)

System	Date	$\chi^2$	$\chi^2_{\text{Planck}}$	$\chi^2_{\text{SH0ES}}$
B1608+656	2004-08-24	1.24	1.22	1.26
DESJ0408-5354	2018-01-17	3.90	4.01	3.78
HE0435-1223	2011-04-11	3.88	3.70	3.88
PG1115+080	2013-03-23	1.99	1.90	1.99
RXJ0911+0551	2012-10-19	8.97	9.78	9.17
RXJ1131-1231	2004-06-24	8.18	9.63	8.94
SDSSJ1004+4112	2010-06-07	102.67	102.53	100.74
WFJ2033-4723	2013-05-03	6.17	6.27	5.93

from the source reconstructions of the models which were constrained with values of  $H_0$  from Planck and SH0ES (see Section 2.1) were labelled  $\chi^2_{\text{Planck}}$  and  $\chi^2_{\text{SH0ES}}$ .

The synthetic images from averages of the main ensemble for each lens are shown in Figure 2.7. Apart from a few minor details, all lensed features have successfully been reconstructed with astonishingly low  $\chi^2$  (SDSSJ1004+4112 being an exception). In some cases, e.g. for B1608+656, RXJ0911+0551, and WFJ2033-4723, the shape of the quasar images are slightly warped, perhaps due to too high shear components. In B1608+656 and WFJ2033-4723, flux ratios between some of the quasar images also noticeably differ. RXJ1131+01231, although the quasar images and most of the fainter Einstein ring are fitted relatively well for this system, shows artifacts which contribute the majority of errors. The origin of the artifacts are unclear.

The synthetic image of SDSSJ1004+4112 shows much fainter images than the original. This probably comes from the fact that the cluster galaxies induce much higher deflection angles and therefore more space for errors than for much smaller strongly-lensing galaxy systems. Problems with SDSSJ1004+4112 were expected since it is a cluster lens with many details which have been missed during the modelling. The considerably higher  $\chi^2$  in Table 2.2 compared to the other systems are a sign of such problems. In part, the high  $\chi^2$ -values are explained by bad fits of the lower brightness regions around the notional Einstein radius. These differences are discernible in Figure 2.7 upon close inspection of the original and the synthetic image side by side. Another source of errors are the cluster galaxies which have not been masked properly.

#### 2.4.4 $H_0$ posterior distribution

In Figure 2.8 and 2.9, the posterior distribution of values for  $H_0$  and  $H_0^{-1}$  from the main ensemble model are depicted. These do not yet include constraints from the extended image data. We furthermore investigated whether the quality of source reconstructions correlated with  $H_0$ . For this reason, we optimized the ensemble models in a post-processing step by calculating synthetic images for each model in the ensemble (as described in the previous subsection). Only a fraction of the models with the best overall  $\chi^2$  (excluding SDSSJ1004+4112) was kept and the rest discarded. Several fractions were tested, ranging from 10 to 80 per-cent. The  $H_0$  posterior of the 30 per-cent-filtered ensemble is shown in Figure 2.1. Interestingly, this had no noticeable effect on the spread, no matter how many models were filtered out. This suggests that better source

**Table 2.2:** Reduced  $\chi^2$  from the source-reconstruction fitting. The first column refers to least squares from the main ensemble model's average.  $\chi^2_{\text{Planck}}$  and  $\chi^2_{\text{SH0ES}}$  are the corresponding least squares from the ensembles which have been constrained to fixed values of  $H_0$  from Planck and SH0ES.

reconstructions of time-delay lenses will not place tighter constraints on  $H_0$ . In particular, Figure 2.1 shows the median of the distributions at

$$H_0 = 2.33_{-0.11}^{+0.13} \text{ aHz} = 71.8_{-3.3}^{+3.9} \text{ km/s/Mpc}$$

and

$$H_0^{-1} = 13.7_{-0.7}^{+0.7} \text{ Gyr},$$

each at 68% confidence.

The Hubble constant is also equivalent to the cosmological critical density density  $\rho_c$  (see 2.2). The distribution of  $\rho_c$  values in the main ensemble is displayed in Figure 2.10 in units of  $\text{GeV/m}^3$ . Its median has a value of  $\rho_c = 5.4_{-0.5}^{+0.6} \text{ GeV m}^{-3}$ , at 68% confidence. For values of  $H_0$  ranging from 60 to 80 km/s/Mpc the critical density corresponds to roughly 1 to 2 alpha particles per cubic metre. This is the quantity which should be compared to the early measurements, as those generally constrain  $H_0$  through the baryon or matter densities  $\propto H_0^2$ .

The spread in the distribution of  $H_0$  is large, in fact the ensemble contains solutions ranging from 60 to more than 80 km/s/Mpc. This means that any value of  $H_0$  is in principle consistent with the data constraints and priors. The reason for this lies for the most part in how the free-form technique builds convergence maps. It explores the degenerate solution space for the lens equation coupled with a few physical and regularization priors. At first, this spread could imply that the solutions have not been properly constrained or regularized. However, as shown in the previous Section 2.4.3, the models are able to reproduce the extended lens photometry quite well (with only one exception). This suggests that the models are in fact on average physically viable. Note that the extended lens photometry didn't go into the modelling process.

Another interesting observation about the  $H_0$  distribution is that its error distribution does not appear to be Gaussian, in fact the distribution in Figure 2.1 is clearly asymmetric. In astronomy, most analyses generally use a Gaussian error distribution, firstly, because of the central limit theorem, and secondly, because the assumption simplifies the estimation of unknown parameters. However, with realistic data, we do not know the probability distribution of the errors, nor whether it has any concrete mathematical form consistent from one observation to another. The wings of a Gaussian fall off quickly, meaning two or three  $\sigma$  residuals are very unlikely to occur. From experience, however, we know such deviations are far more common. Thus, an error distribution such as a Lorentzian or a Voigt profile which have a well-defined peak with wider wings, might be more reasonable estimates for realistic data. Even more flexible is the Tukey g-and-h [154] distribution which allows for asymmetric wings. Likewise, a 1 per-cent determination of the Hubble constant which implicitly uses Gaussian errors, might actually have overestimated the precision of the measurement.

[154]: Yan et al. (2019)

#### 2.4.5 Comparison with TDLMC

Our TDLMC participation was very helpful in guiding the modelling procedure carried out in this paper. The most striking conclusion we drew from our TDLMC participation was that as soon as double systems

entered the analysis, our  $H_0$  inference tended to much lower values; at times even lower than the asserted range of possible values. After rung1 however, we decided to include a joint-analysis containing only quad systems, along with other combinations of quads and doubles. The best results were achieved this way and are shown as histograms of our  $H_0$  posteriors in Figure 2.11.

It is apparent that this distribution is considerably wider than the one we obtained in the present work, Figure 2.1 and 2.8. Part of the reason for this could be the difference in the radial spread of images around the lens center, mentioned in Section 2.3.4. If images are confined to a narrow band around the lens center, as in TDLMC quads, the steepness, or mass sheet degeneracy will be more rampant, which will lead to a wider range of derived  $H_0$  values. Observed quads span a wider range of radial image positions, resulting in narrower  $H_0$  distributions.

While our TDLMC models have a very large spread across the entire range of possible  $H_0$  values, their median  $H_0$  seems to determine the truth values quite accurately. This does not mean that our techniques are able to consistently recover the truth values, but it still shows potential.

## 2.5 Conclusion

The Hubble constant has come a long way from the value of  $\sim 500 \text{ km/s/Mpc}$  implied by the historic Figure 1 in Hubble [9]. Sandage [155] had improved the measurement to  $H_0 \approx 75 \text{ km/s/Mpc}$  or  $H_0^{-1} \approx 13 \text{ Gyr}$  with an uncertainty of a factor of two. Debates over a factor of two were still continuing in Sandage et al. [156] versus Vaucoleurs et al. [157]. Today,  $H_0$  has been constrained to within 10 per-cent, but the debates between “low” and “high” values remain, as do the legacy units of  $\text{km/s/Mpc}$ . In view of the continuing debate over the value of  $H_0$ , lensing time delays as a technique for measuring  $H_0$  are very interesting, because they span a variety of redshifts and are free of the “twilight zone” [see 158] characteristic of the distance-ladder methods.

[9]: Hubble (1929)

[156]: Sandage et al. (1982)

[158]: Sandage et al. (1974)

In this paper, we have presented a determination of the Hubble constant  $H_0 = 2.33_{-0.11}^{+0.13} \text{ aHz} = 71.8_{-3.3}^{+3.9} \text{ km/s/Mpc}$  through the joint free-form modelling of eight time-delay lenses using the most recent observational data. This value is consistent with both early and late Universe studies. We further demonstrate this fact by modelling these lenses in secondary ensembles which have fixed values of  $H_0$  typical for CMB-based and SNeIa-based methods. Accordingly, these secondary ensemble models exhibit just as many or few problems as the main lens ensemble. We have analysed the models based on their arrival-time surfaces, convergence maps, and circularly-averaged density profiles and have found only minor shortcomings. Furthermore, the models’ projection properties have been tested by generating synthetic images using the source-reconstruction method presented in Denzel et al. [77]. Thereby, we have extended our analysis to data which have not initially been employed in the lens reconstructions. The results of this test affirmed the physical validity of our models, and so, the synthetic images and thereby the entire photometric data are finally used to constrain the ensemble further in a post-processing step. This had no notable effect, suggesting that

[77]: Denzel et al. (2020)

optimizations of source reconstructions only weakly constrain  $H_0$ . In our study, we have not (yet) considered phase-space models, or stellar kinematics, which might be able to further constrain our models.

As of the time of writing, a 1% determination of  $H_0$  through lensing has yet to be reported. Nevertheless, even if such a measurement existed, only several repetitions with different data sets could confirm the accuracy of these measurements. As already discussed in Section 2.4.4, when we assess data, it is entirely unknown what kind of error distribution can be assumed. Thus, only if several measurements of  $H_0$  across different observations consistently reach a 1 per-cent level, they are robust against the choice of errors. However, the TDLMC [53] suggests that while many lens-modelling techniques excel in reconstructing simple simulations based on parametric models, but decrease in consistency when faced with more general lenses taken from galaxy-formation simulations. As cautioned in several works [e.g. 27, 28] due to lensing degeneracies a single family of models is able to reproduce the same lensing observables, but return different values of  $H_0$ . Free-form techniques keep consistency in accuracy and precision when the complexity of the lens is increased, as expected from their greater flexibility.

Interestingly, our new estimate of  $H_0$  improves upon the precision of our measurements reported in the TDLMC. In the challenge, the simulated quads appeared to be slightly rounder with very little variation in the radial distance of the images. The real observations considered in this study appear to have a larger variation. We conjecture that a wider radial distribution of the lensed images puts tighter constraints on the slope of the density profile, and therefore provides tighter constraints on the Hubble constant. From our experience in the TDLMC, we also conclude that the most accurate joint inference of  $H_0$  comes from modelling only quad systems. In addition to the more elliptical lens-image separations, we have improved upon the TDLMC in precision by increasing the number of simultaneously modelled quad systems from 4 to 8. This implies that minor improvements might be possible by increasing the number of modelled systems alone, provided they contain new information which is able to further constrain  $H_0$ .

It may turn out that in galaxy lenses degeneracies impose a limit which can hardly be broken, and results similar to  $H_0$  reported in this study perhaps are the best we can hope to attain. If this turns out to be the case, time delays for galaxy lenses can still be useful, by reversing the problem and using them together with  $H_0$  from other methods to constrain substructure in lenses [130].

[130]: Mohammed et al. (2015)

The situation is different in cluster lenses. Recently, Ghosh et al. [78] considered cluster lenses with a time-delay quasar (such as SDSS J1004+4112 in this work) but also hundreds of other lensed sources at many redshifts, making up  $\sim 1000$  images in all. With that many lensing constraints (expected to be achieved by JWST), a 1% measurement of  $H_0$  from lensing time delays appears feasible.

[78]: Ghosh et al. (2020)

[53]: Ding et al. (2020)

[27]: Gomer et al. (2019)

[28]: Kochanek (2020)

## Acknowledgments

PD acknowledges support from the Swiss National Science Foundation. This research is based on observations made with the NASA/ESA Hubble Space Telescope obtained from the Space Telescope Science Institute, which is operated by the Association of Universities for Research in Astronomy, Inc., under NASA contract NAS 5-26555. These observations are associated with programs #10158, #15320, #12324, #12874, #9744, and #10509.

## Data availability

The data underlying this article are available at the STScI (<https://mast.stsci.edu/>; the unique identifiers are cited in the acknowledgements). The derived data generated in this research will be shared on request to the corresponding author.

## 2.6 Figures

This section contains all figures which are referenced in previous sections.

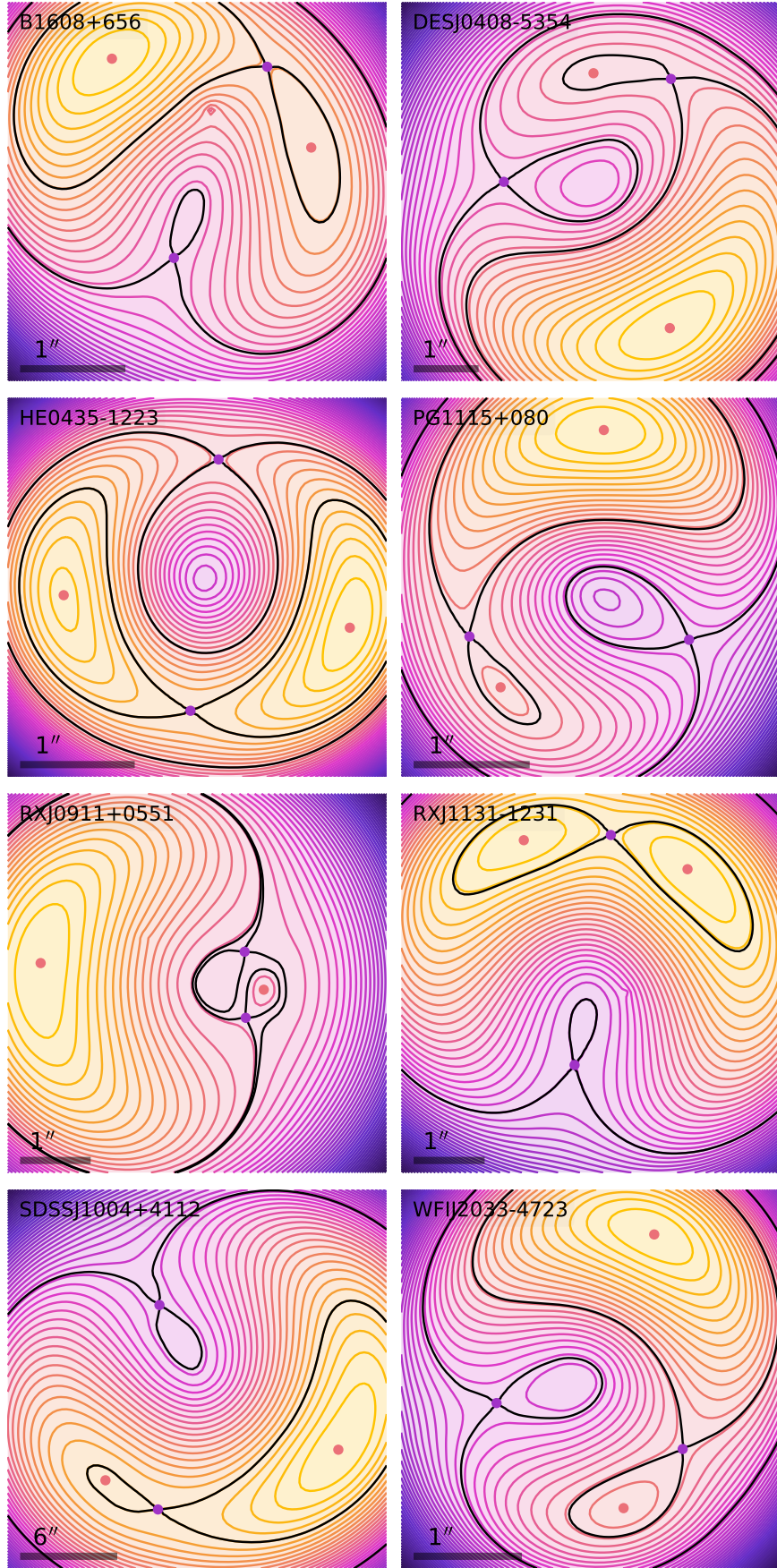


**Figure 2.3:** Arrival-time surfaces of the ensemble-average models. The image-position constraints with minimum and saddle parity are indicated by red and purple dots respectively. Contours passing through saddle points are in black. The scale bar on the lower left in each panel shows the angular scale in arcseconds. Orientations are arbitrary, and RXJ0911+0551 is mirror-inverted, but consistent with the following figures.

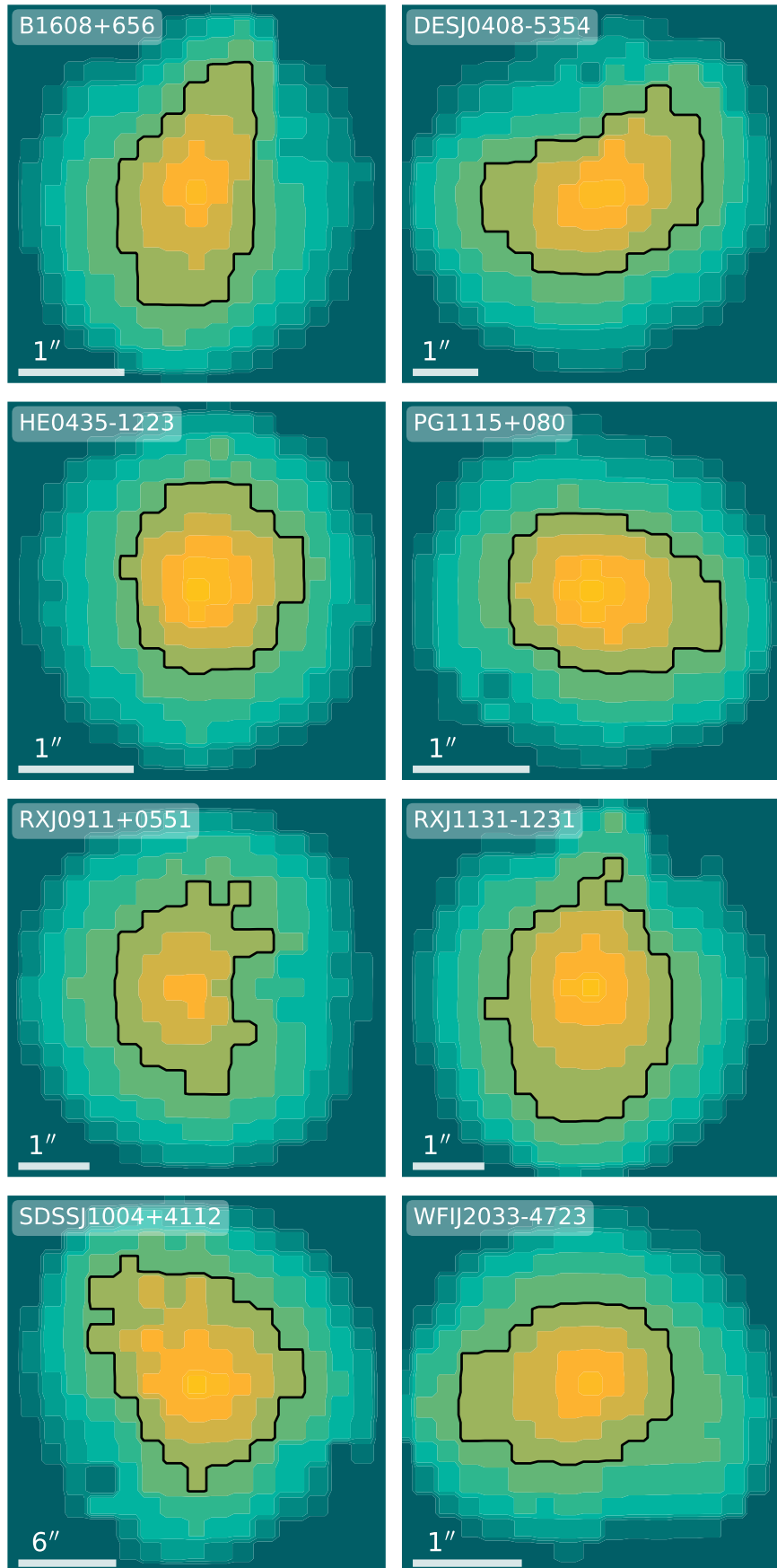


**Figure 2.4:** Model-convergence maps (ensemble averages) of all lenses. Black contours indicate a  $\kappa = 1$ . Scales and orientations are identical to the corresponding panels in Figure 2.3.

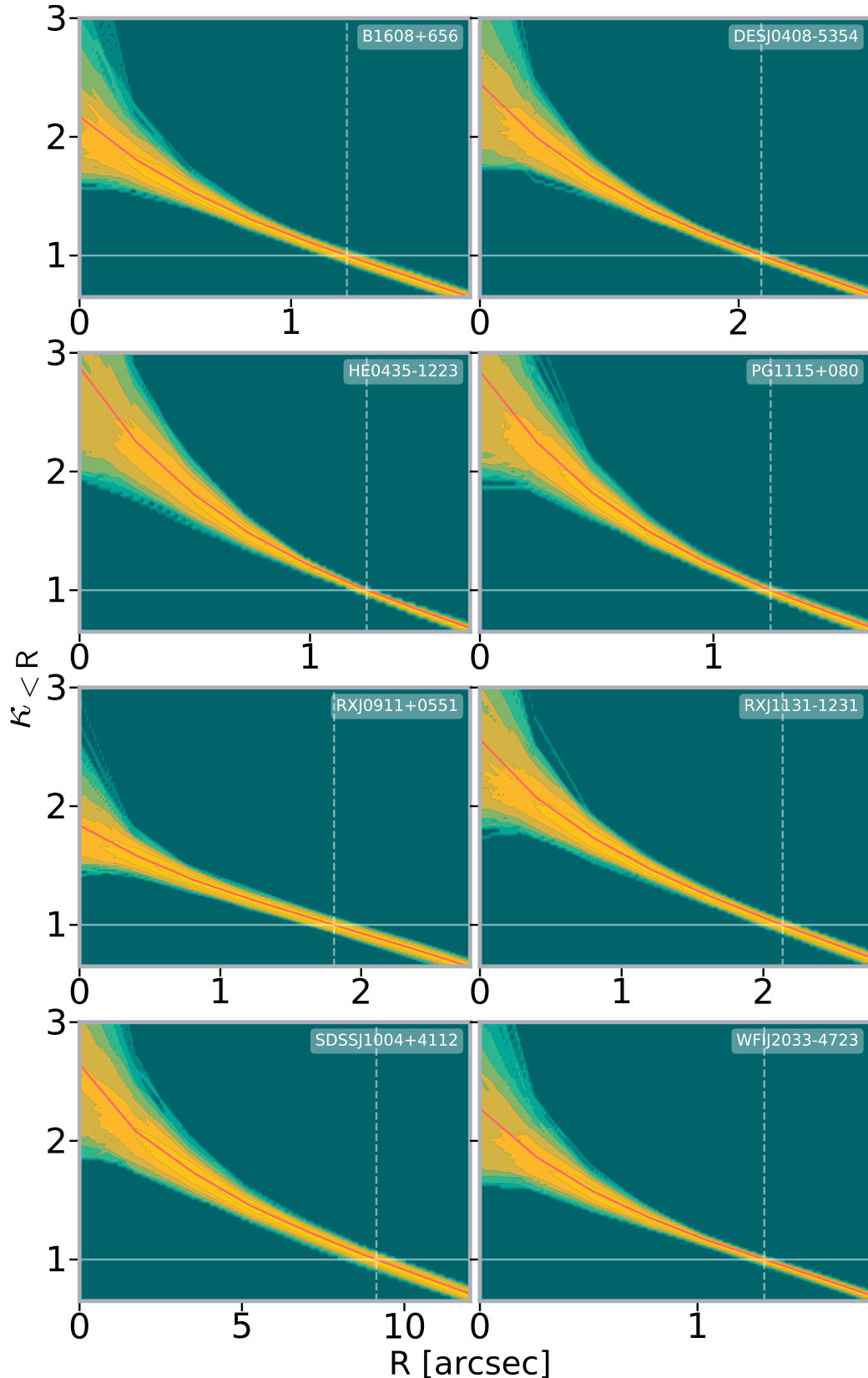


**Figure 2.5:** Radial profiles of the mean enclosed  $\kappa$  within a given projected radius from the centre of the modelled galaxy. The model ensemble is represented with a coloured region with a gradient from green to yellow indicating its number density of models. The red line describes the ensemble average. The vertical dashed line shows the notional Einstein radius (that is, the radius with mean convergence of unity) for the ensemble average.

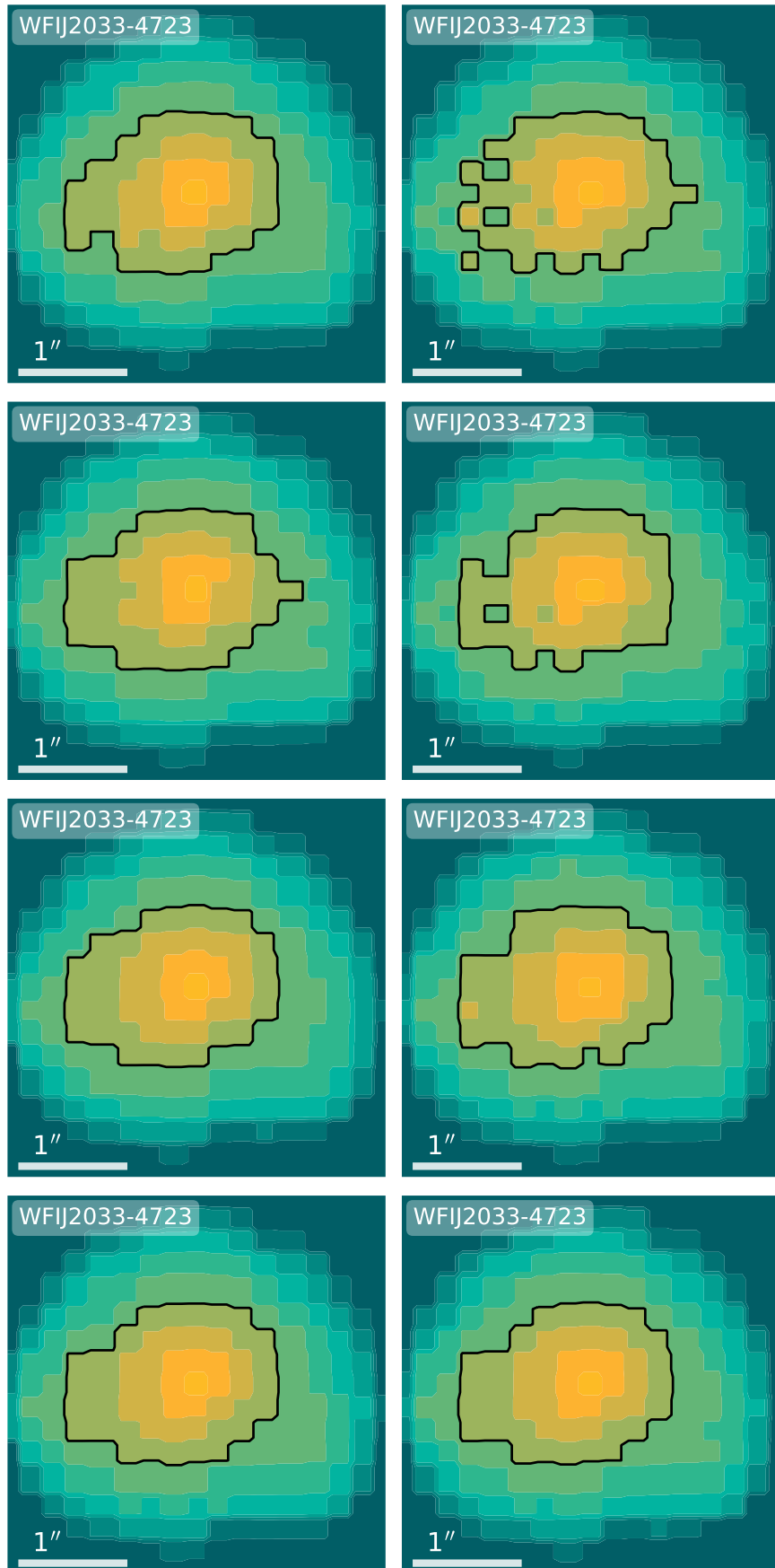


**Figure 2.6:** Variation of the convergence maps for WFIJ2033-4723 across the ensemble. (The ensemble average appears in the bottom-right panel of Figure 2.4.) The top row shows the 16th and 84th percentile projections along the first principal component. The other rows refer to the 2nd, 5th and 100th principal components. See text near equation (2.13) for details.

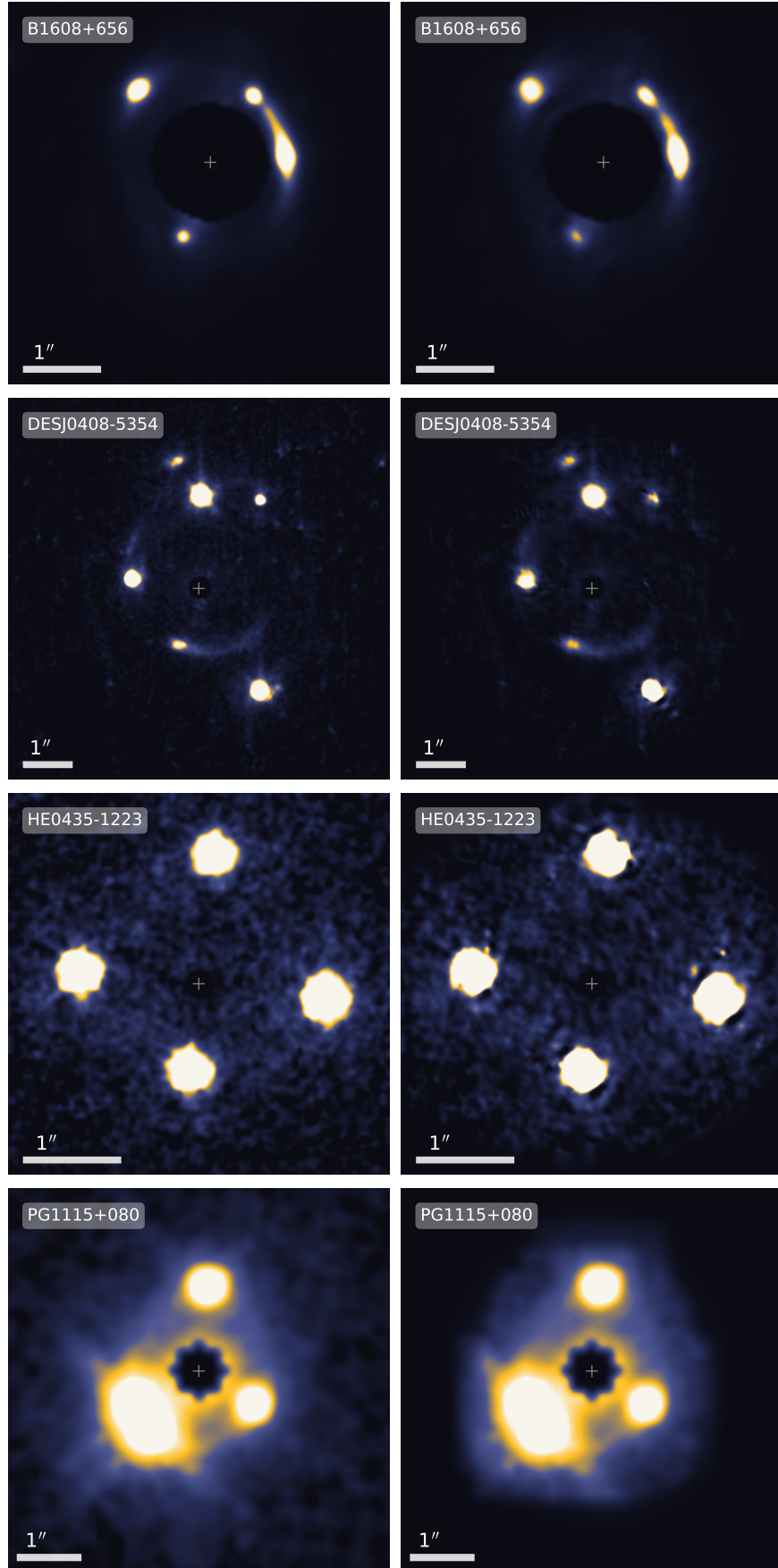


**Figure 2.7:** Photometric lens data and synthetic images produced using the ensemble-average model of each lens. The maps are in arbitrary units of brightness, but for each row adjusted to the same brightness levels. To avoid contamination of the lensed images by the lens light, a circular region around the lens has been masked with its center indicated by a cross and roughly corresponding to the modelled lens position. The scale bar on the lower left in each panel shows the scale in arcseconds.

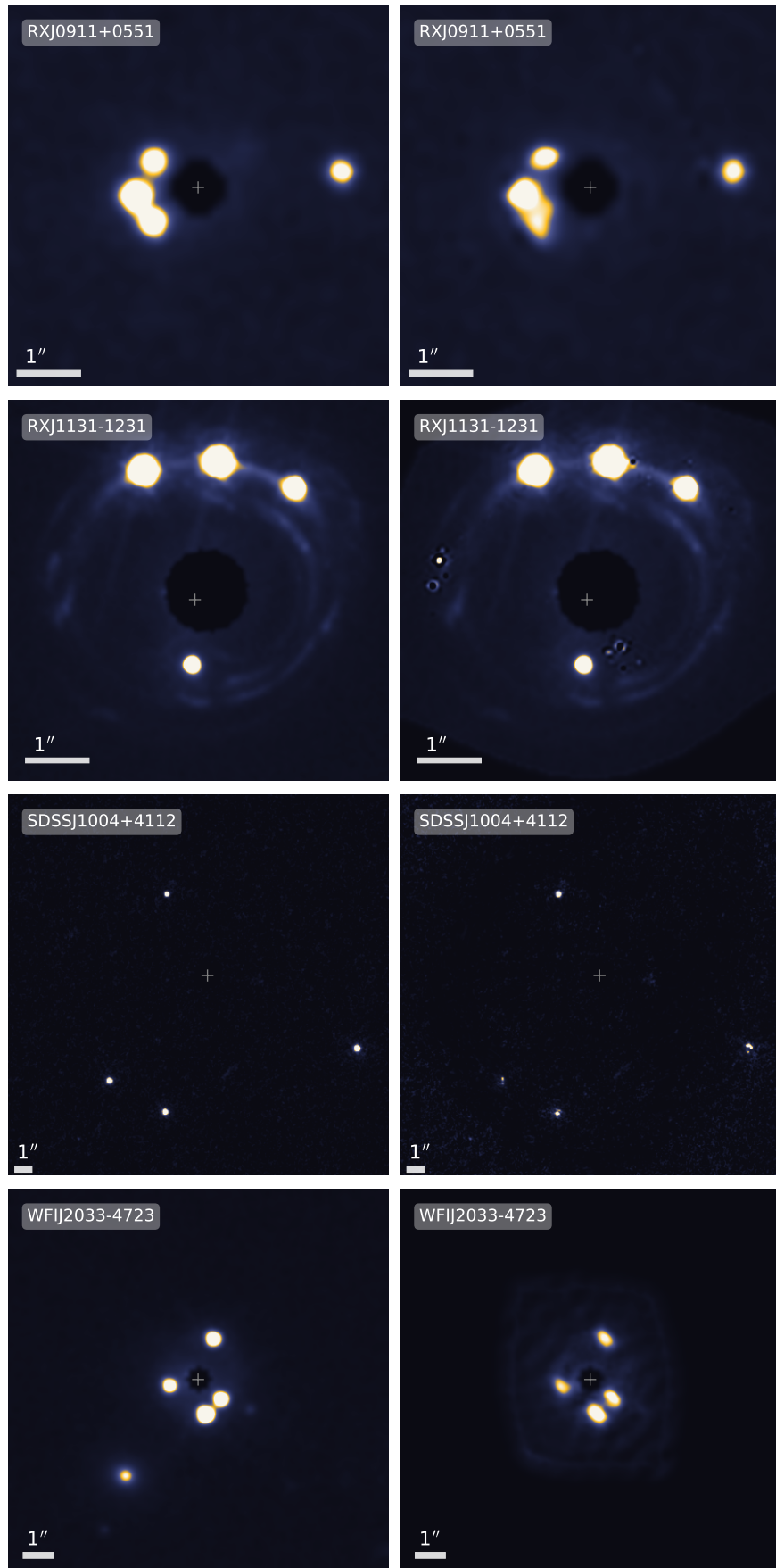


**Figure 2.7a:** (Continued) Note that RXJ0911+0551 east is shown mirror-inverted.

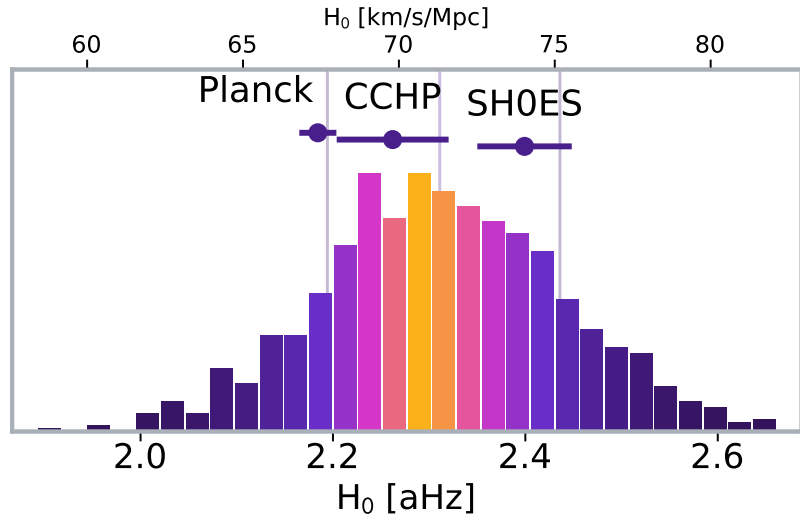


**Figure 2.8:** Histogram of the entire ensemble's  $H_0$  values. The ensemble consists of 8 simultaneously modelled quad systems. The vertical lines indicate 16th, 50th, and 84th percentiles of the distribution. To make the median furthermore easily discernible, the colouring of the histogram's bars corresponds to the cumulative probability centred around the median (yellow-magenta-blue-black goes from 1 to 0). Horizontal error bars indicate recent measurements from other methods for comparison: Planck [11], CCHP [the Carnegie-Chicago Hubble Program; 67], and SH0ES [the Supernovae  $H_0$  for the Equation of State; 10]

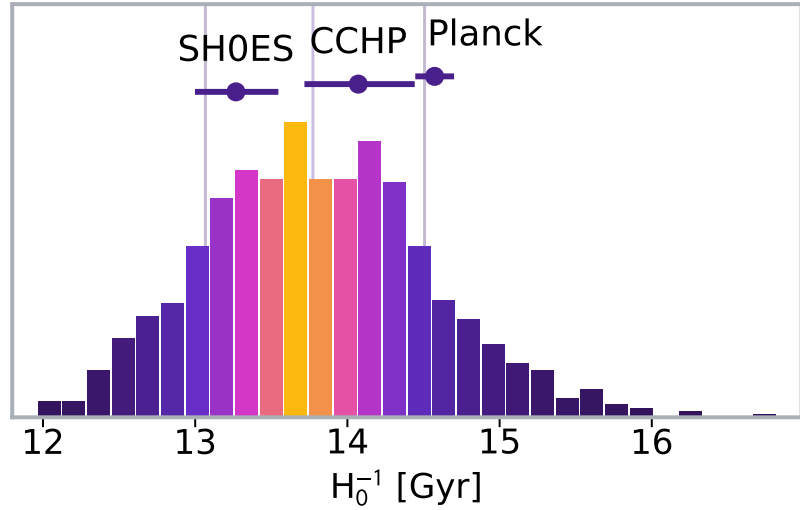


**Figure 2.9:** Histogram of the entire ensemble's  $H_0^{-1}$  values, corresponding to the distribution in Figure 2.8.

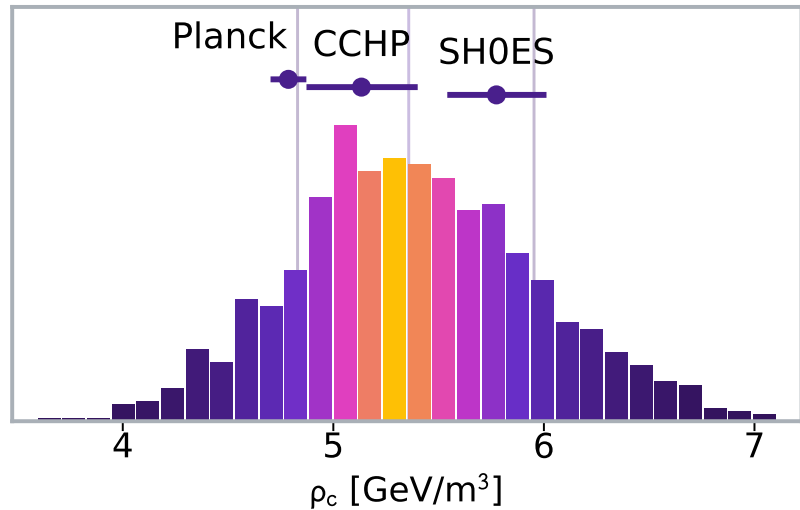


**Figure 2.10:** Histogram of the entire ensemble's  $H_0^2$  values in form of the cosmological critical density  $\rho_c = 3/(8\pi G)H_0^2c^2/e$  in GeV/m³, following Figure 2.8 and 2.9. It corresponds to an energy density of roughly 1 or 2 alpha particles per cubic metre.

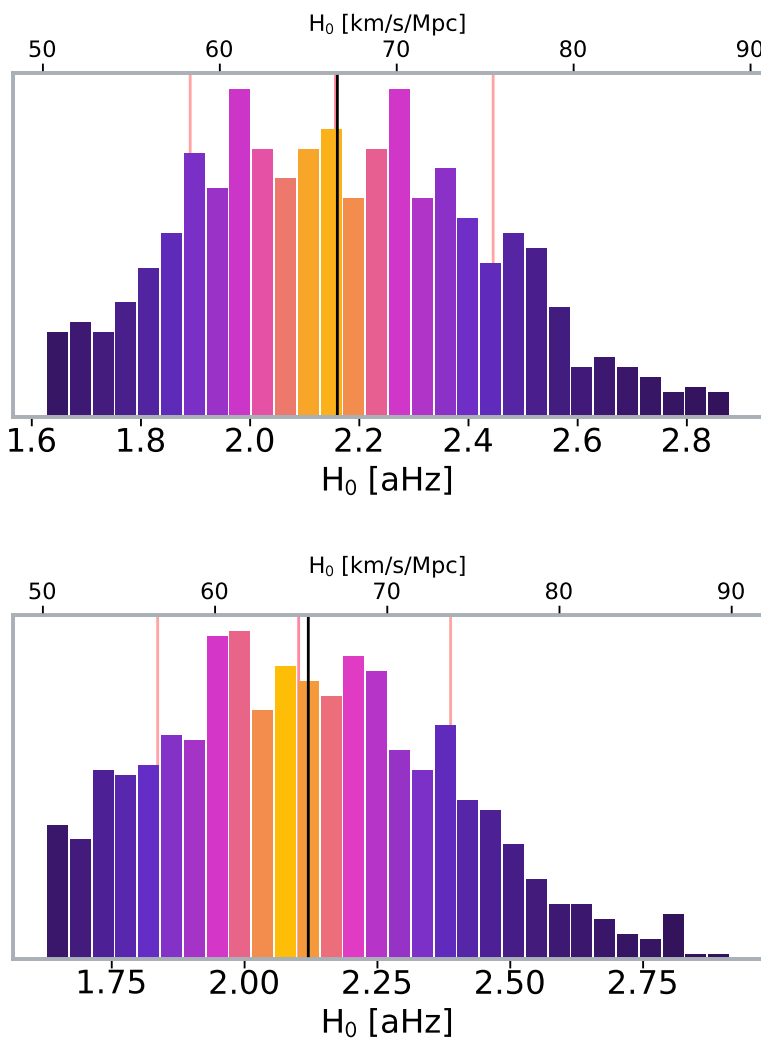


**Figure 2.11:** Best results for rung2 (top) and rung3 (bottom) of the TDLMC. Generally, we obtained best results from ensembles containing only quads which were simultaneously modelled. The ensembles each consist of 4 quad systems from the corresponding rung of the challenge. For these models an additional prior was used which required  $H_0$  to be higher than 50 and lower than 90 km/s/Mpc. Red vertical lines indicate the median 68 per-cent confidence range of  $H_0 = 66.5^{+8.9}_{-8.1}$  km/s/Mpc for rung2 and  $H_0 = 64.9^{+8.8}_{-8.2}$  km/s/Mpc for rung3. To make the median furthermore easily discernible, the colouring of the histogram bars corresponds to the cumulative probability centred around the median (yellow-magenta-blue-black goes from 1 to 0). The black vertical lines indicate the truth value for  $H_0$  of the corresponding TDLMC rung. Note that these were the *best* results of each rung. The final submission also included models further from the truth, especially when they included doubles.



# FOSSIL

# 3

3.1 Introduction . . . . .	57
3.2 The system J143454.4+522850	58
3.3 The lensing mass . . . . .	61
3.4 The stellar mass . . . . .	63
3.5 Comparison with simulations	65
3.6 Discussion . . . . .	67

Original title:

## THE LENS SW05 J143454.4+522850: A FOSSIL GROUP AT REDSHIFT 0.6?

Philipp Denzel<sup>1,2</sup>, Prasenjit Saha<sup>2,1</sup>

In collaboration with:

Xanthe Gwyn Palmer<sup>3</sup>, Onur Çatmabacak<sup>1</sup>, Jonathan Coles<sup>4</sup>, Claude Cornen<sup>5</sup>, Ignacio Ferreras<sup>6</sup>, Robert Feldmann<sup>1</sup>, Rafael Küeng<sup>2</sup>, Dominik Leier<sup>7</sup>, Aprajita Verma<sup>3</sup>

<sup>1</sup> Institute for Computational Science, University of Zurich, 8057 Zurich, Switzerland

<sup>2</sup> Physics Institute, University of Zurich, 8057 Zurich, Switzerland

<sup>3</sup> Sub-department of Astrophysics, University of Oxford, Denys Wilkinson Building, Keble Road, Oxford, OX1 3RH, UK

<sup>4</sup> Physik-Department, Technische Universität München, James-Franck-Str. 1, 85748 Garching, Germany

<sup>5</sup> Zooniverse, c/o Astrophysics Department, University of Oxford, Oxford OX1 3RH, UK

<sup>6</sup> Mullard Space Science Laboratory, University College London, Holmbury St Mary, Dorking, Surrey RH5 6NT, UK

<sup>7</sup> DB, Germany

To be submitted to:

*Monthly Notices of the Royal Astronomical Society*

## Abstract

Fossil groups are considered to be the end product of natural galaxy group evolution in which group members sink towards the center of the gravitational potential due to dynamical friction, and finally merge into a single, massive, and (x-ray) bright elliptical. Since gravitational lensing depends on the mass of a foreground object, its mass concentration, and distance to the observer, we can expect lensing effects of such fossil groups to be particularly strong.

In this paper, we consider the exceptional system J143454.4+522850, labelled SW05 by the Space Warps discovery service. We combine lens models with population-synthesis models for the stellar mass to separate the total mass of the lens into the two main components in galaxies, stars and dark matter, thereby producing dark matter-maps for the lens. The observed enclosed mass profiles were additionally compared with state-of-the-art galaxy formation simulations, which shows interesting differences between observation and simulations. These differences, as well as the lens model on itself, finally lead us to the conclusion that SW05 may be a fossil group. It would represent the first direct comparison of a fossil groups' dark matter halo with its stellar component in the center. We finally put forth the idea of a diagnostic for the identification of fossil groups through gravitational lensing by looking for the lack of certain features in the lens models.

### 3.1 Introduction

The currently most tested cosmological concordance model, the  $\Lambda$  cold dark matter model ( $\Lambda$ CDM), provides initial conditions for the formation and evolution of galaxies. Large-scale cosmological simulations serve as a framework which explores different galaxy formation scenarios within  $\Lambda$ CDM from first principles. Although they all have different treatments for the baryonic components and the physical mechanisms involved in galaxy formation, the latest generation of simulation suites such as EAGLE [Evolution and Assembly of GaLaxies and their Environments; 159], FIRE [Feedback In Realistic Environments; 57], and Illustris [160] make remarkably accurate predictions. In particular, they stand in general agreement regarding the growth of primordial density fluctuations by gravitational instability in an expanding Universe, leading to the formation of dark halos. In such scenarios, proto-galaxies form through cooling and condensation of gas at the centres of their potential wells [161].

As a consequence, galaxies are usually found in clusters or groups [162], and during their lifetime such group galaxies undergo an extensive series of mergers [163, 164]. Eventually devoiding its entire neighbourhood, a single elliptical galaxy of group-scale mass is thought to form, called a fossil group galaxy [165, 166]. Indeed, numerical simulations by Barnes [167] first motivated such a hierarchical merging scenario [see also 168]. Since then, there have been several supporting reports on x-ray sources identified as fossil groups [169, 170]. Because most fossil systems found to date lie within  $z < 0.2$ , fossil galaxy groups most likely are old, undisturbed systems due to the lack of major mergers. While some luminous galaxies experience major merger events in their evolution, fossil group galaxies acquire their mass typically through minor merger events where the mass ratio to their collision companion is 0.3 or less. In fact, simulations show that fossil systems can assemble half of their mass in dark matter already by redshift  $z > 1$ , and that the assembled mass at any redshift is generally higher in fossil than in regular groups [171]. Since this merging process is relatively fast compared to the cooling times of their surrounding gas at the order of one to several Hubble times, fossil groups are usually found embedded in giant, x-ray luminous gas halos [172]. If a fossil system has not fully merged yet, another criterion by which it can be identified is a gap in brightness of at least 2 magnitudes (in the  $r$ -band) between the two brightest galaxies in the group [173, 174].

As fossil groups are very massive with a high mass concentration, we can expect very strong lensing effects along their line of sight [175]. In fact, imagine a group galaxy of a mass around  $M \sim 10^{13} M_\odot$  at a cosmological distance of  $D \sim 1$  Gpc. From such a system constellation we would expect an Einstein radius of around  $(4GM/(c^2D))^{1/2} \simeq 10$  arcsec which is relatively large compared to image separations observed for single galaxy lenses. Strong gravitational lens systems make for exciting, but rare tools for astronomers to independently study galaxies. The morphology of lens systems and their image configurations allow one to infer mass contents and surface density profiles [e.g., 176–181]. On that note, it is important to realize that the gravitational deflection of light is independent of the nature of the matter, that is, lensing is equally affected by baryonic

[159]: Crain et al. (2015)

[161]: White et al. (1978)

[162]: Tully (1987)

[163]: Mamon (1988)

[164]: Tempel et al. (2017)

[165]: Ponman et al. (1994)

[166]: Jones et al. (2003)

[169]: Santos et al. (2007)

[170]: La Barbera et al. (2009)

[171]: Dariush et al. (2007)

[172]: Mulchaey (2000)

[173]: Dariush et al. (2010)

[174]: Zarattini et al. (2014)

[175]: Schirmer et al. (2010)

[176]: Auger et al. (2010)

[177]: Leier et al. (2011)

[178]: Whitaker et al. (2014)

[179]: Leier et al. (2016)

[180]: Collett et al. (2017)

[181]: Nightingale et al. (2019)

[182]: Johnson et al. (2018)

and dark matter. While lens models of various forms have been used to constrain mass contents, stellar mass fractions, and dark matter profiles, and even cosmological parameters, so far these estimates have not yet been translated to constraints on galaxy formation scenarios. However, a recent study by Johnson et al. [182] estimates that a substantial percentage of lensing systems within the group mass range are fossil or pre-fossil groups. If this is indeed the case, models of such lenses could provide a new and separate diagnostic — besides the common criteria to identify fossil groups through x-ray observations — for determining whether a lens in question is in fact fossil as opposed to a different group incarnation. Thus, models of such lenses could potentially yield constraints on galaxy formation scenarios.

In this paper, we present models for the system J143454.4+522850 (SW05) of the lensing mass and of the stellar mass from stellar population synthesis, followed by a comparison with galaxy models of similar mass from galaxy-formation simulations, which indicate some differences compared with regular early-type galaxies and that the system may indeed be a fossil group.

The paper is organized as follows. In Section 3.2, the lens system is introduced in detail and its environment thoroughly investigated. Section 3.3 presents free-form lens models of SW05 and several derived diagnostics in order to obtain a goodness-of-fit estimation. Section 3.4 describes the methodology yielding light-to-stellar mass estimates from stellar population synthesis models and consequently a spatially 2D-resolved stellar-to-lens mass fraction map. In Section 3.5 these models are compared to simulated galaxies of similar mass range and Section 3.6 summarizes the results and discusses the feasibility of SW05 as a fossil group galaxy candidate.

## 3.2 The system J143454.4+522850

[183]: More et al. (2016)

[48]: Küng et al. (2018)

J143454.4+522850 or SW05 was discovered in the Space Warps citizen-science project [183]. Out of the 29 promising lens candidates in that work, SW05 probably has the best lens image quality. It is a relatively large gravitational lens with four clearly separated images within a radial distance between 3.5 and 5.25 arcsec from the centre (see Figure 3.1). Subsequently, Küng et al. [48] identified SW05 as a high-mass galaxy with  $\sim 10^{13} M_{\odot}$  and a relatively low stellar-mass fraction using lens models. This is very exciting as it provides opportunity to probe low star-formation efficiency environments.

In this paper we model both the stellar component and dark matter halo of this lens. We compare these mass profiles to state-of-the-art galaxy simulations. Finally, we explore the possibility that features — or the lack thereof — in lensing models can be used to determine whether or not a group lens is fossil.

[54]: Benítez (2000)

The redshift of the lensing galaxy and the source images were determined with the widely used Bayesian photometric redshift estimator `bpz`\* by [54]. It fits the spectral energy distribution (SED) of the provided multi-band photometric data with templates, until the maximum-likelihood redshift

---

\* <http://www.stsci.edu/~dcoe/BPZ/>

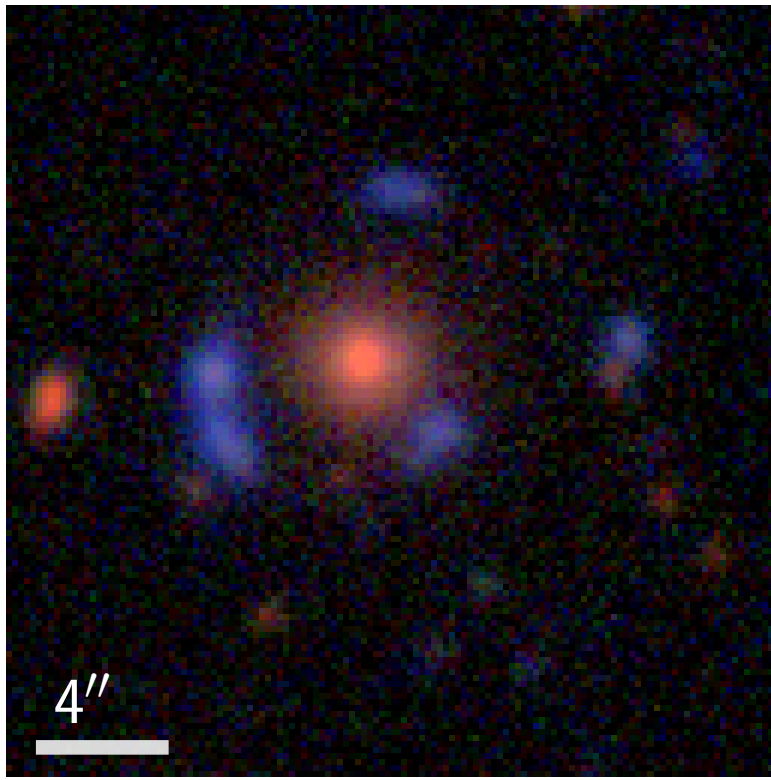


**Figure 3.1:** Stacked observational picture of SW05: Observational data from CFHTLS (stored in the CFHT Science Archive) was taken with the wide-field imager MegaPrime in five optical bands ( $u$ ,  $g$ ,  $r$ ,  $i$ , and  $z$ ). The false-colour image was generated using a stacking procedure according to [82], where the  $i$ ,  $r$ , and  $g$  bands are transformed into rgb colours.

is found. Photometric redshifts have the advantage over spectroscopic redshifts that they are much less time consuming to obtain, and often provide good enough estimates for most purposes. SW05's lens redshift was determined with bpz to be most likely at  $z_l = 0.63 \pm 0.16$ . However, bpz was not able to determine the source's redshift photometrically with enough credibility such that a default redshift from the MegaPipe pipeline was used for the lens model at  $z_s = 3.00$ . Accurate redshifts are not essential for the lensing models, as a change in redshift (of the lens and the source) can be implemented by simply rescaling the critical surface density, and can therefore easily be adjusted to any other redshift. Moreover, the lens models for SW05 seem to be rather insensitive to changes in the source redshift. Contrarily, a change in lens redshift can considerably impact the results of the photometry-based analysis for the stellar-mass estimation.

During the analysis of SW05, spectroscopic redshifts were measured which confirmed the lens redshift, and came close to the used source redshift at around 2.96.

Figure 3.2 shows an inspection of the wider field of SW05. It is the first indication for SW05 being a fossil group galaxy candidate as its neighbourhood is relatively clear of galaxies at similar brightness and redshift. As it is unlikely for such a massive galaxy to evolve in isolation, a classification as a fossil group galaxy is a real possibility.

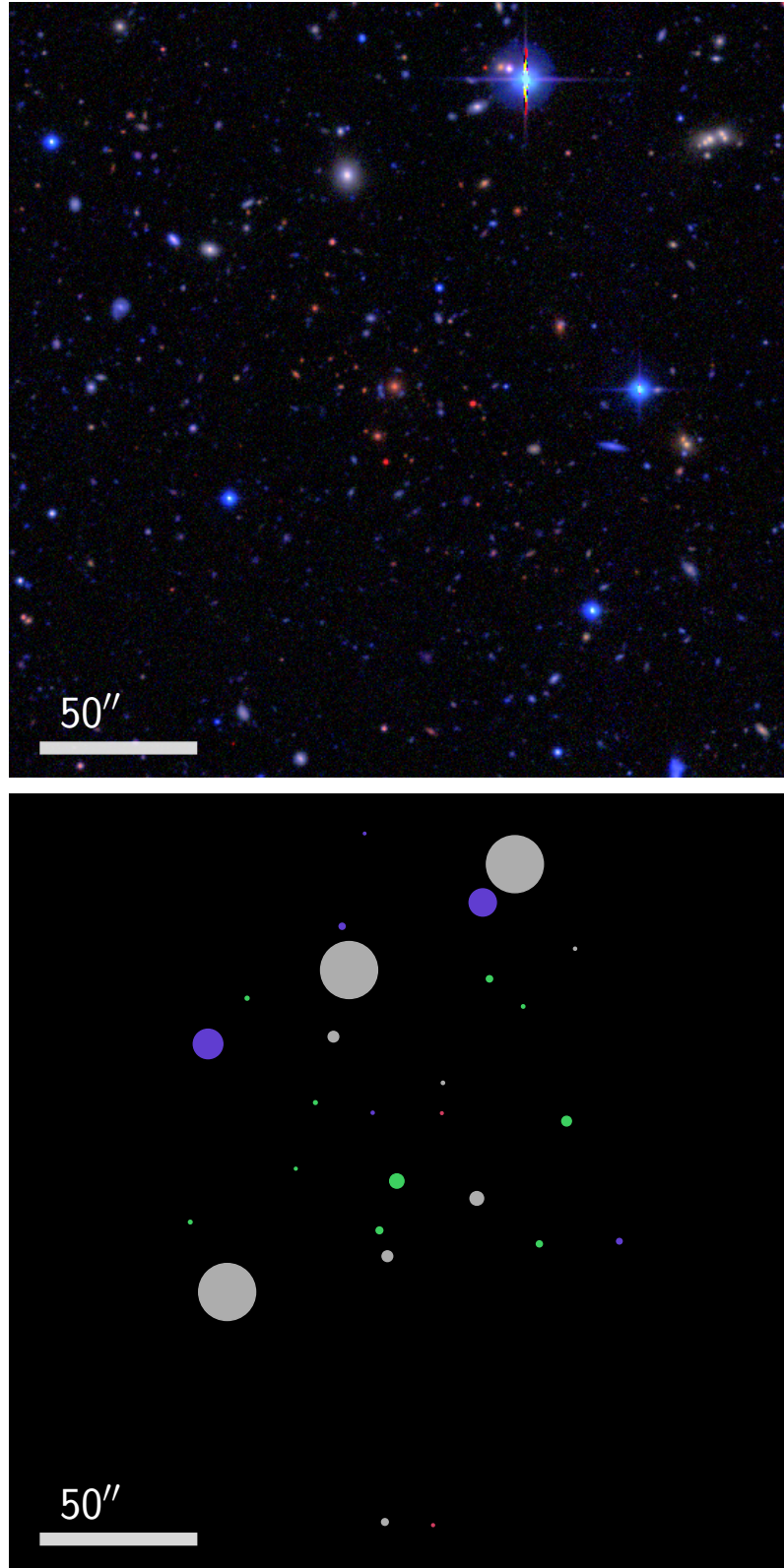


**Figure 3.2:** The upper panel shows a composite image of the neighbourhood of SW05 from CFHTLS. All the image parameters, including the stacking procedure is the same as for Figure 3.1. The lower panel shows pinpointed objects with different colour coding, designating how close their redshift is to SW05. Green dots are for objects within a redshift range of  $\pm 0.1$ . Red dots stand for objects further redshifted, blue dots for further blue-shifted objects. Grey dots have undetermined redshifts, and consist of mostly stars and other non-galactic objects. The size of the dots indicated their relative brightness. The scale bar has a length of 50 arcsec which corresponds to a linear distance of roughly 360 kpc at the lens redshift.

### 3.3 The lensing mass

The lens modelling was done with the reliable free-form modelling code GLASS<sup>†</sup> [for software details see 50]. The free-form modelling technique is a reaction to the many degeneracies from which lens models inherently suffer due to the lack of lensing observables to uniquely specify a lens [26, 74]. In contrast to conventional parametric models, free-form models allow the modelling to stay flexible by constructing its mass distributions  $\Sigma(\theta)$  from a high number of base elements. GLASS in particular (similar to the free-form modelling tool PixeLens by [140]) uses “mass tiles”  $\Sigma_n$  to construct its lens models according to  $\Sigma(\theta) = \sum_n \Sigma_n Q(\theta - \theta_n)$  where  $Q$  a square-pixel profile and  $\theta_n$  its centroid. The observed source-image point positions  $\theta$  provide the linear constraints on the intrinsic source position  $\beta$  and the mass components  $\kappa_n$ . Here, the lens is built of 14 rings of pixels around its center with a total of 497 pixels. However, this does not uniquely define the lens mass distribution and in order to obtain reasonable models, their solution space is further constrained with inequality priors as follows:

1. All mass tiles must have non-negative densities:  $\Sigma_n \geq 0$ .
2. To ensure smoothness in the mass distribution, each mass pixel is limited to twice the average of its neighbours.
3. The local density gradient should point within  $\alpha = 45^\circ$  of radially inwards which assures concentration of the lens and more importantly suppresses additional lens images which might appear otherwise.
4. The average density  $\langle \Sigma \rangle_i$  of mass within a concentric pixel rings is required to not increase with radius. This still allows for twisting iso-density contours and significantly varying ellipticities with radius.

Additionally, to account of any mass component outside the finite model surface, the lens modelled allowed for a two-component external shear  $\gamma$ . Solutions are then sampled using a customized Monte-Carlo random-walk method [143]. The final model consisted an ensemble of 1000 solution sets of  $(\Sigma_n, \beta, \gamma)$  for the image point positions. Figure 3.6 shows the pixelized mass distribution of the ensemble’s average as light contours. The model assumed a flat cosmology with  $(\Omega_m, \Omega_\Lambda, H_0^{-1}) = (0.28, 0.72, 13.7 \text{ Gyr})$ .

[26]: Saha (2000)

[74]: Saha et al. (2006)

To verify the validity of these lens models, two main diagnostics have been used. Firstly, inspection of the arrival-time surface (see Küng et al., Küng et al. [48, 137]) is an ideal test to invalidate certain models in the ensemble, as additional images and uneven contours, indications of unphysical solutions, are easily discernible. Minima, and saddle-points, correspond to points where the gradient of the arrival-time surface is 0 and indicate detectable source-image positions. Maxima are usually not detectable as they are highly demagnified. In general the arrival-time surface should

1. reproduce the source image positions on the lens plane,
2. not produce more extrema than the observation shows,

[143]: Lubini et al. (2012)

[137]: Küng et al. (2015)

[48]: Küng et al. (2018)

---

<sup>†</sup> <https://ascl.net/1806.009>

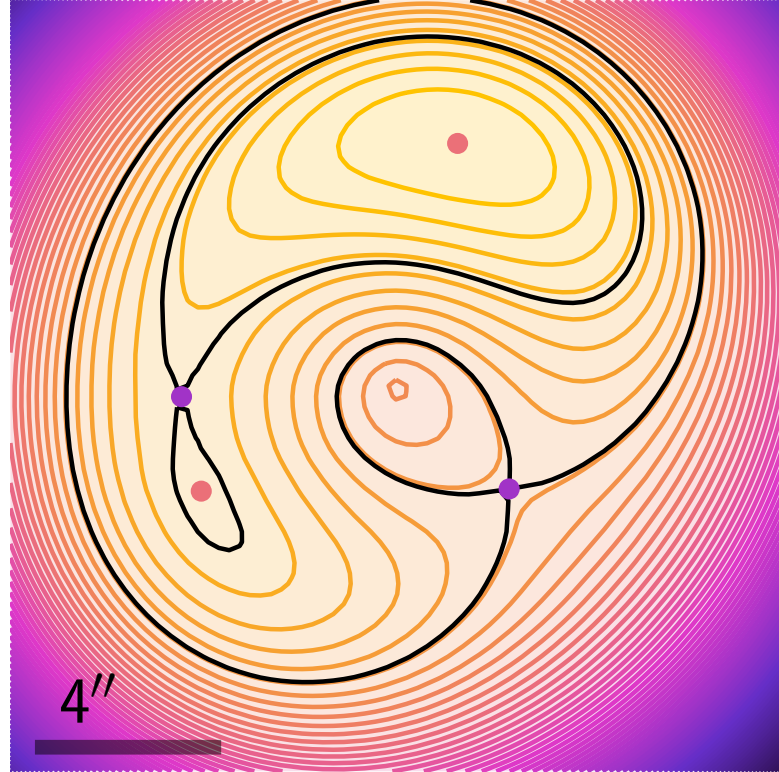


**Figure 3.3:** Arrival surface of SW05’s models. This gives the light travel times for virtual light paths from the source to the observer. Its maxima, minima, and saddle-points are an illustration of Fermat’s principle, which states that arrival times must be extreme for paths along which light rays travel. The black lines show the saddle-point contours of the surface, the coloured lines general surface contours.

3. and have reasonable delay times relative to each other.

Figure 3.3 shows the arrival-time surface of the ensemble-average model of SW05.

The high sensitivity of the lens models to the exact image positions is still a troubling issue. An automated search algorithm is quite unreliable due to the generally high signal-to-noise ratios in the data from CFHTLS. Especially with spatially extended images, such as arcs, the correct positions are at times even for human eyes arbitrary, and a slight shift can cause the mass model of the lens to change moderately, at times even drastically.

Thus, the second diagnostic takes the entire photometric data, rather than single image points, into account by reconstructing the lensed source from the image plane using the mass distribution of the ensemble average solution. This is done with `gleam`<sup>†</sup> (Gravitational Lens Extended Analysis Module) by PD (see Denzel et al. [77] for details). It uses a simple least-square fitting method to produce synthetic lens images as shown in Figure 3.4. Here, the photometric data in the *g*, *r*, and *i* bands were fitted with synthetic images, with an average reduced  $\chi^2_v \sim 2.10$ , and produced a synthetic composite images in the upper right panel (in comparison to the data on the left-hand side). The pixel-wise residuals between observed data and synthetic, scaled by noise, is shown in the bottom row on the right-hand side. The reconstructed source composite is shown in the same row on the left-hand side. These fits further provide excellent diagnostics and confirm the validity of the underlying mass model, as the synthetic image is well reproduced in 3 different bands,

[77]: Denzel et al. (2020)

<sup>†</sup>  <https://github.com/phdenzel/gleam>

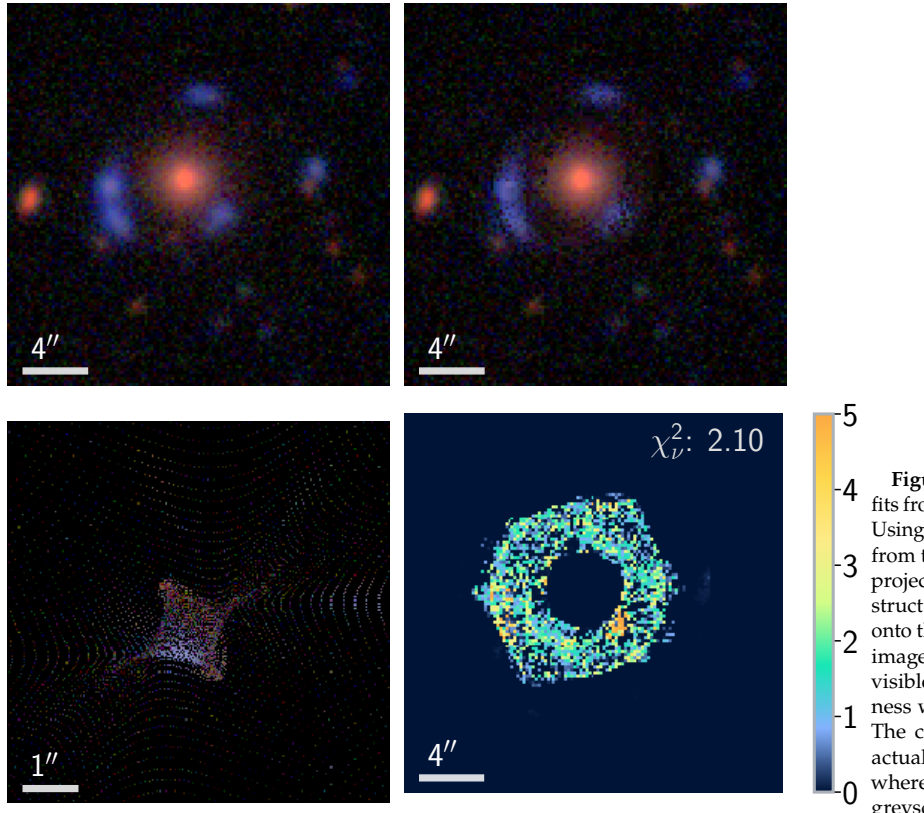


**Figure 3.4:** Synthetic-images and source fits from the ensemble-average lens model. Using the modelled lens potential inferred from the mass maps, the observed data is projected onto the source plane to reconstruct the original source. A re-projection onto the image plane results in a synthetic image which provides a diagnostic, i.e. a visible measure of the models' accuracy when compared to the observation. The coloured pixels represent the light actually affected by the lensing potential, whereas unaffected pixels are shown in greyscale.

and the reconstructed source is relatively consistent. While a match of synthetic image with the observation does not necessarily mean that the true model from the degenerate solution space has been found, the inverse argument can still be used to invalidate a solution.

### 3.4 The stellar mass

The galaxy brightness models of SW05 were obtained by fitting a Sérsic surface profile with a Markov-chain Monte-Carlo ensemble sampler *emcee* § [184]. This feature is part of the `gleam` module and was preferred over already existing codes, such as GALFIT ¶ or Imfit ||, because it was more convenient to integrate into the Python-based analysis pipeline. In future, an expansion of the model libraries to other brightness profile functions is planned, such as a general exponential, Gaussian, Moffat, and King profiles.

[184]: Foreman-Mackey et al. (2013)

The light-to-stellar mass models for the lensing galaxy of SW05 were obtained using (again) a Markov-chain Monte-Carlo approach. The integrated photometric data is fitted to spectral templates of 12 stellar populations base models [55] depicted in Figure 3.5. The base models are marginalized over redshift, formation epochs, star-formation time scale, and stellar metallicity. By integrating the stellar populations with an Initial Mass Function [Chabrier IMF; see 56, 185], the mass distribution of a population of stars at birth can be related to the luminosity of

[55]: Bruzual et al. (2003)

[185]: Salpeter (1955)

[56]: Chabrier (2003)

§ <https://github.com/dfm/emcee>

¶ <https://users.obs.carnegiescience.edu/peng/work/galfit/galfit.html>

|| <http://www.mpe.mpg.de/~erwin/code/imfit/>

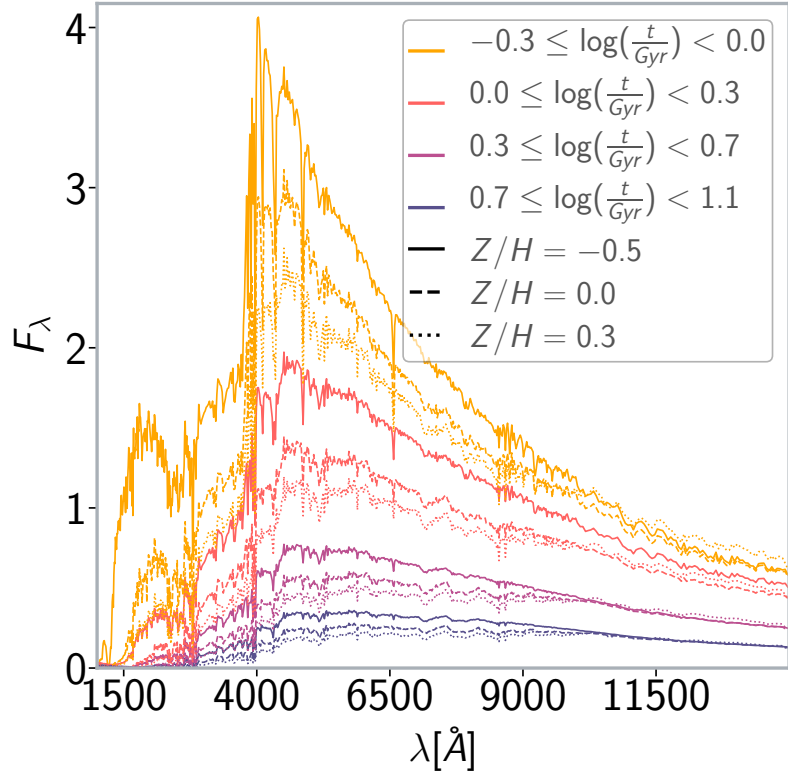


**Figure 3.5:** The spectral energy distributions of 12 stellar population synthesis base models in solar units. The 12 base models combine 3 different metallicities  $[Z/H]$ , and four age ranges  $t$  over which a constant star formation rate was assumed. They are fitted to the integrated flux from observations in order to obtain the stellar mass.

[186]: Cardelli et al. (1988)

[187]: Cardelli et al. (1989)

galaxies; we thereby accounted for extinction by dust following Cardelli et al., Cardelli et al. [186, 187]. Finally, combining the light-to-stellar mass estimates with the Sérsic model, yields a stellar surface mass density map.

Finally, having modelled the entire mass of the lens and the stellar mass component separately, they were superimposed with a standard 2D interpolation scheme. The result is demonstrated as a stellar-to-lens mass fraction map in Figure 3.6. It is a circular 2D false-colour map with 12 mass tiles — or pixels — in radius, which describes the stellar and total surface densities generated from the ensemble’s models. By default the mass models have a range of almost twice the maximal image separations from the lensing galaxy. Since the image separation of SW05 is relatively large compared to the other lenses discovered in the Space Warps project, its surface density was mapped with a high pixel scale. For this reason the central region of the lens map was adaptively refined in order to resolve potential cusps. The result is a spatially large map, in which the high concentration of stars in the center is clearly evident from the redder region. The blue region at larger radii is an indication of lower stellar-to-lens mass fraction for which dark-matter is the dominating component. The dark matter in the SW05’s average model mass totals up to a lower limit of  $(1.12 \pm 0.08) \cdot 10^{13} M_\odot$ , while the lower limit on the stellar mass amounts to  $(3.04 \pm 0.22) \cdot 10^{11} M_\odot$ . Since the stellar-to-total mass fraction has a large range, the mass fraction was stretched in the false-colour map with a cube root to make subtle differences in the stellar halo in red colour stretch farther out (assuming that the stellar mass profile is monotonically decreasing) and thus easier to see with the human eye. In general, the galaxy model shows the expected features. If there is any high stellar mass content, it can be found in the center of

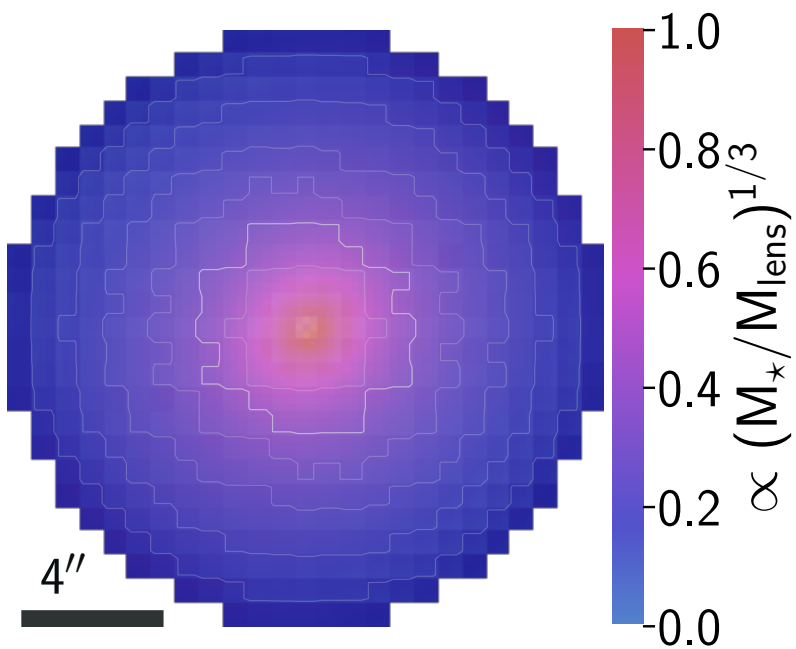


**Figure 3.6:** False-colour map of the surface mass density (fraction of stellar to lensing surface mass density) in the lensing galaxy. Three components were used for the colour mapping, stellar-to-lens surface mass density fraction  $f = (\Sigma_{\text{stel}}/\Sigma_{\text{lens}})^{e_f}$ , lensing surface mass density normalization  $A = \Sigma_{\text{lens}}^{e_A}$ , and the fractional uncertainty in the lensing surface mass density  $\Delta = (\Sigma_{\text{error}}/\Sigma_{\text{lens}})^{e_\Delta}$ , where  $e_f$ ,  $e_A$ , and  $e_\Delta$  are arbitrarily adjustable exponents. Those are necessary due to the fact that the visual perception of colours is highly non-linear. As colour coordinates in the hsv colour space,  $f \in [2/3, 1]$  was taken to be the hue,  $A \in [0, 1]$  the value, and  $(1 - \Delta) \in [0, 1]$  the saturation. Thus, with increasing  $f$  the colour changes from blue (dominating dark matter content) to red (high stellar mass content), with increasing  $A$  the shading changes from dark (low total mass content) to full colour (high total mass content), and with increasing  $\Delta$  the colour saturation changes from full colour (low uncertainty) to white (high uncertainty). The grey lines describe contours of equal surface density, where the brightest contour indicates the level of critical surface density, i.e. a convergence of 1.

the galaxy. The dark matter is located in a extended halo which always dominates the total matter content, especially towards the outskirts of the galaxy. Only a single sample is — of course — not enough to make a conclusive statement about typical galaxy structure and formation. Nevertheless, based on our knowledge of stellar and gas dynamics in nearby galaxies, these features were expected. Moreover, an important note to emphasize is that the evident features here, emerge from an independent, completely different study to standard galaxy structure studies.

### 3.5 Comparison with simulations

The plot in Figure 3.7 displays the models' cylindrically-averaged cumulative mass profiles. At the Einstein radius (the images lie between 22–38 kpc and the Einstein radius is around the middle of this range), the lensing galaxy in SW05 is estimated to contain already more than  $(7.01 \pm 1.06) \cdot 10^{12} M_\odot$  dark matter and approximately  $(2.58 \pm 0.19) \cdot 10^{11} M_\odot$  of matter in stars. At distances in the order of the image separations the uncertainties in the lens mass are at their lowest. At diverging radii the uncertainties grow, forming a characteristic butterfly-shaped envelope, caused by the well-known steepness degeneracy problem [26, 74]; here the shape is only slightly recognizable, since a logarithmic scaling was used on both axes. Another factor alleviating the steepness degeneracy is the comparably high image quality and overall size of the lensing system, which allows for a precise fix of the image's positions, which in turn makes the estimation of the total mass content more accurate. The errors in the stellar mass distribution arises from the compatibility of the observed photometric data at the determined redshift with multiple base models to different degrees. The base models differ mostly in metallicity

[26]: Saha (2000)

[74]: Saha et al. (2006)

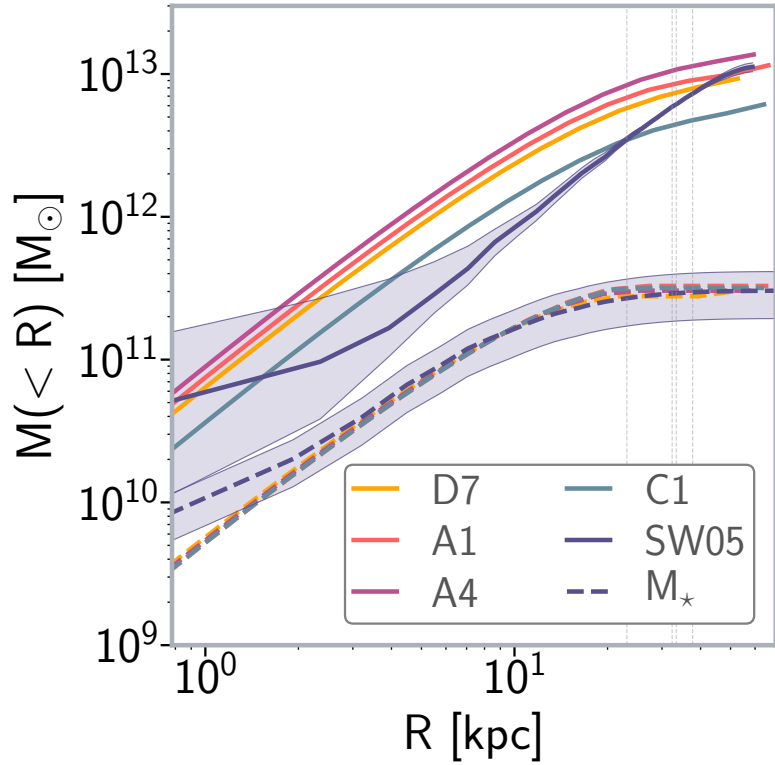


**Figure 3.7:** Cumulative mass profiles of the lensing galaxy models and galaxies from MassiveFIRE simulations [A1, A4, C1, D7 188, 189]. The solid curves (lens model in dark-blue) denotes the ensemble median of the enclosed total mass, the dashed curves (lens model in dark-blue) the ensemble median of the enclosed stellar mass. The grey areas show the 99.7 % Bayesian confidence range, where the lens models fall in. The enclosed lens mass is best constrained in the region where the source’s images were observed (vertical thin dotted lines). Towards the galaxy model’s outskirts and especially the center the errors grow significantly due to lensing degeneracies.

and star-formation history, however the uncertainty in redshift dominates the errors in the stellar mass.

[188]: Feldmann et al. (2016)  
[189]: Feldmann et al. (2017)

Comparing the observation to the simulations, we clearly see differences. The compared galaxy models were taken from MassiveFIRE simulations [A1, A4, C1, D7 188, 189]. The simulation profiles were recovered with the halo finder AMIGA [190, 191]. Because galaxy formation simulations usually are performed in 6D, the AMIGA halo finder provides the output as spherically averaged profiles of stellar and dark matter particles. To have a fair comparison however, they were re-averaged within a cylindrical volume, and re-integrated along the  $z$  coordinate to yield a projected 2D mass profile of the simulated galaxies. To make the comparison easier the simulated profiles were scaled in mass to have the same total stellar mass and in radius to have the same stellar mass at the half-light radius. Among the simulation profiles themselves, there are almost no differences except in the total mass. The observed mass profile seems to have a shallower mass profile, causing the enclosed mass profile to be steeper. The enclosed stellar mass profiles also show differences. The stellar mass profile is more concentrated for the lens model, whereas the simulations seem to have slightly more extended stellar mass regions in the center.

The explanation for differences between simulations and lens models could lie in the observation itself. Assuming the simulations describe a mass profile for a typical galaxy, the differences could hint to the observation being atypical.

## 3.6 Discussion

Despite only having determined photometric redshifts, there is little doubt that SW05 is indeed a lensing system, and its lens is one of the most massive lensing galaxies known so far. That said, spectroscopic redshifts, to once and for all confirm that the candidate is a lens and more importantly improve the precision of its mass estimates, are desirable. Its mass estimate fits with what we would expect from a very massive elliptical galaxy, with a mass in the galaxy group range. Its stellar mass dominates the center, but in total only makes up for 2 % of the entire mass. These results suggest that SW05 is a fossil group. The first indication is the lack of features in the lens models. Fossil groups clear their neighbourhood from any other group members at comparable redshift through mergers.

If there would be any other group members, it would become evident in the lens models as an external shear component giving rise to an ellipticity in the mass maps. In SW05's lens models there is little ellipticity to begin with. There seems to be a slight tendency to ellipticity towards the upper left quadrant in Figure 3.6. However inspecting Figure 3.2, we see only one possible group member candidate, which can be found in the lower left quadrant. The lens models therefore indicate that there is no other major group member in the neighbourhood of SW05, which supports our conclusion. This explanation also seems to fit with the discrepancies in the comparison to galaxy formation simulations.

The stellar mass in SW05 accounts for around 2 per-cent of the total mass. However, this is not necessarily equal to the entire baryonic mass in the lensing galaxy. There could be a substantial mass content in gas, which would radiate in an energy range of

$$\left(\frac{GM}{c^3}\right) \left(\frac{c}{r}\right) \times 1 \text{ GeV} \sim 5 \times 10^{-8} \text{ keV} \times \left(\frac{M}{M_\odot}\right) \times \left(\frac{r}{\text{pc}}\right)^{-1} \sim 10 \text{ keV.} \quad (3.1)$$

This falls in the x-ray range, of which no observational data was taken so far, but would definitely be interesting. This also means that if we were looking at the CMB sky, with high spatial resolution, this object would fall under the influence of the Sunyaev-Zel'dovich effect. However due to the small size of the object an interferometric base line of  $\sim 100$  meters would be required for such a detection.

The plot in Figure 3.8 describes the same trend. The formal velocity dispersion is derived from the mass profiles [cf. 192]

[192]: Leier (2009)

$$\sigma^2 = \frac{2}{3\pi} \frac{GM(r)}{r} \quad (3.2)$$

where  $M(r)$  is the mass at a certain radius  $r$  from the center. It shows the simulations reaching a maximum in their velocity dispersion profile at smaller radii from the center compared to the observation, indicating that the observed galaxy must have more gas at higher radii, which supports an accretion or merging scenario. This also means that the total mass of SW05 could be well above  $10^{13} M_\odot$  if the galaxy model was extended to even higher radii.

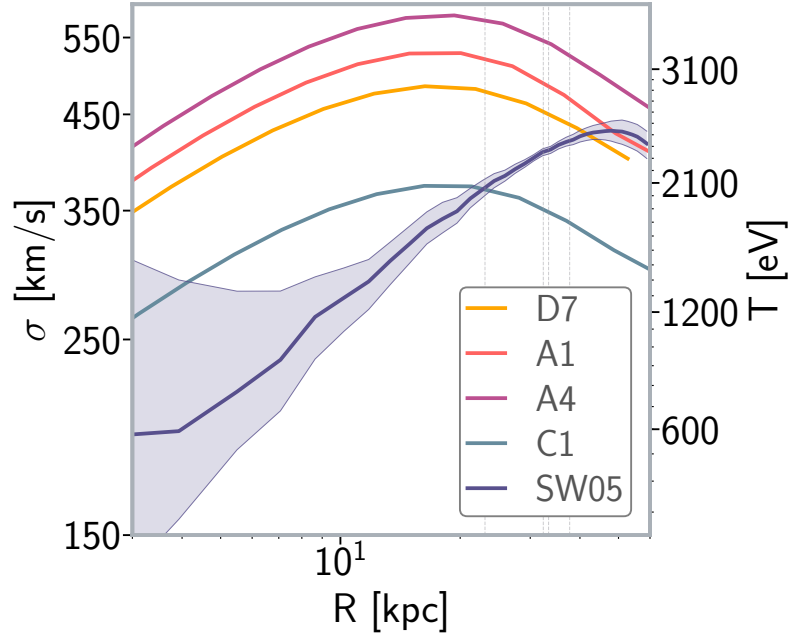


**Figure 3.8:** The velocity dispersion profile for SW05 and galaxies from simulations:  $\sigma$  is formally derived from the mass profiles shown in Figure 3.7 according to equation (3.2). On the right y-axis the corresponding temperature values are denoted in units of eV according to equation (3.3).

The velocity dispersion can formally be converted into a temperature with

$$T(r) = \frac{m_p \sigma(r)^2}{e} \quad \text{in units of eV} \quad (3.3)$$

where  $m_p$  is a proton mass,  $\sigma(r)$  the velocity dispersion profile, and  $e$  the elementary charge. The right  $y$ -axis of Figure 3.8 shows such a conversion. This temperature should be of the same order as the temperature at which the gas in the outskirts of the galaxy radiates. The maxima for the observed and simulated galaxies have values around  $\sigma \sim 400$  km/s and  $T \sim 2$  keV.

In conclusion, the study presented in this paper identifies a gravitational lens of group mass-scale as a fossil group galaxy candidate. In the future, this analysis could very well be applied to other lensing groups to help in the identification of fossil groups.

## Acknowledgments

PhD acknowledges support from the Swiss National Science Foundation.

Original title:

**LESSONS FROM A BLIND STUDY OF SIMULATED LENSES:  
IMAGE RECONSTRUCTIONS DO NOT ALWAYS REPRODUCE TRUE  
CONVERGENCE**

Philipp Denzel<sup>1,2</sup>, Sampath Mukherjee<sup>3</sup>, Jonathan P. Coles<sup>4</sup>, Prasenjit Saha<sup>2,1</sup>

4.1 Introduction . . . . .	71
4.2 Theory . . . . .	73
Arrival-time surface . . . . .	73
Lensing Roche potential . . . . .	73
Lensing mass quadrupole . . . . .	74
Image formation . . . . .	74
4.3 Methods . . . . .	75
SEAGLE . . . . .	75
GLASS . . . . .	76
Source reconstruction and synthetic images . . . . .	77
Model comparison . . . . .	78
4.4 Results . . . . .	79
Lens reconstructions . . . . .	80
Convergence map comparison . . . . .	81
Roche potential comparison . . . . .	82
4.5 Conclusion . . . . .	85
4.6 Figures . . . . .	87

1 Institute for Computational Science, University of Zurich, 8057 Zurich, Switzerland

2 Physics Institute, University of Zurich, 8057 Zurich, Switzerland

3 STAR Institute, Quartier Agora - Allée du six Août, 19c B-4000 Liège, Belgium

4 Physik-Department, Technische Universität München, James-Franck-Str. 1, 85748 Garching, Germany

Published in:

*Monthly Notices of the Royal Astronomical Society*. 492.3, pp. 3885–3903, Jan. 2020

## Abstract

In the coming years, strong gravitational lens discoveries are expected to increase in frequency by two orders of magnitude. Lens-modelling techniques are being developed to prepare for the coming massive influx of new lens data, and blind tests of lens reconstruction with simulated data are needed for validation. In this paper we present a systematic blind study of a sample of 15 simulated strong gravitational lenses from the EAGLE suite of hydrodynamic simulations. We model these lenses with a free-form technique and evaluate reconstructed mass distributions using criteria based on shape, orientation, and lensed image reconstruction. Especially useful is a lensing analogue of the Roche potential in binary star systems, which we call the *lensing Roche potential*. This we introduce in order to factor out the well-known problem of steepness or mass-sheet degeneracy. Einstein radii are on average well recovered with a relative error of  $\sim 5\%$  for quads and  $\sim 25\%$  for doubles; the position angle of ellipticity is on average also reproduced well up to  $\pm 10^\circ$ , but the reconstructed mass maps tend to be too round and too shallow. It is also easy to reproduce the lensed images, but optimizing on this criterion does not guarantee better reconstruction of the mass distribution.

## 4.1 Introduction

Since the first discovery of a strongly lensing galaxy [7] these systems have been used to study a range of scientific questions: the dark-matter (DM) density profile in galaxies and possible substructure [see 176, 193–198], the star formation efficiency and stellar mass function [see 48, 177, 179], cosmological parameters [79, 125, 149, 199], and the structure of lensed active galactic nuclei [see 135, 200, 201].

[7]: Walsh et al. (1979)

In the coming years many more lens discoveries are anticipated, increasing the number of galaxy lenses from  $\sim 10^3$  to  $\sim 10^5$  [202]. To prepare for this stream of new gravitational lensing data, it is important to have the tools to process information efficiently and correctly. Recent work to this end mainly aims to improve the efficiency with which gravitational lenses are analysed. In the verification of lens candidates, machine-learning-based projects and citizen science programs have been established, working concurrently, as well as complementary, to confirm and select interesting objects [183, 203–205]. Since the numbers of gravitational lenses will be too high for experts to model all by themselves, efforts have been made to create crowd-sourced lens-modelling tools such as SpaghettiLens by Küng et al. [137][49], or automatic modellers like AutoLens by Nightingale et al. [206], and the machine-learning code Ensaï by Hezaveh et al. [207].

[202]: Oguri et al. (2010)

Since all the aforementioned scientific questions require reconstruction of the mass distributions of lenses, it is important for lens-modelling techniques to be rigorously tested. It is an intrinsic problem of gravitational lensing that many plausible mass distributions are able to explain observed data. This was actually pointed out in the very first paper on lens modelling [24] and is generally known as lensing degeneracy [see 26]. Some degeneracies can be removed by adding additional information such as kinematics, but there exist complex degeneracies [74, 75] whose systematic effect on modelling has yet to be explored. Figure 4.1 illustrates the sometimes surprising character of lensing degeneracies. It is clear that blind tests of lens modelling with simulated data are needed. Such tests have already been performed on cluster lenses in the format of a challenge in which 10 groups participated and tested their various modelling methods [208].

[137]: Küng et al. (2015)

[206]: Nightingale et al. (2018)

[207]: Hezaveh et al. (2017)

The technique of free-form lens reconstruction is a response to the problem of lensing degeneracies. Free-form lens modelling deliberately uses underconstrained models and explores lensing degeneracies in a high-dimensional parameter space. The lens mass distribution is built out of a superposition of a large number of small components, with only few assumptions about the global properties of the distribution, such as smoothness, non-negative masses, no extra images, or being centrally concentrated. Early free-form models used regularization [209], but a better strategy is to generate a whole ensemble of models which all fit the data with a range of different mass distributions [91, 140, 143]. If the parameter space is properly defined and sampled, the possibility is high that the *true* solution is contained within the ensemble model. A drawback of such solution sampling strategies is that ensembles often also contain physically unrealistic models which are in conflict with our current understanding of galaxy evolution. Such unrealistic models might

[24]: Young et al. (1980)

[26]: Saha (2000)

[74]: Saha et al. (2006)

[75]: Schneider et al. (2014)

[208]: Meneghetti et al. (2017)

[209]: Saha et al. (1997)

[91]: Williams et al. (2000)

[140]: Saha et al. (2004)

[143]: Lubini et al. (2012)

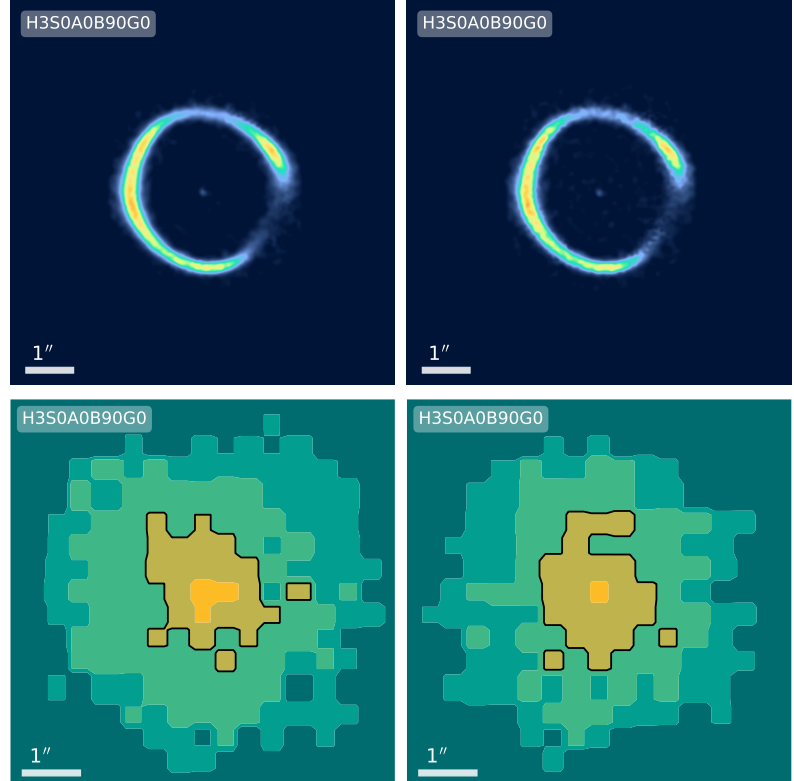


**Figure 4.1:** An example of the degeneracy of lens reconstructions. The two lower panels show two different surface mass distributions (black lines indicate convergence  $\kappa = 1$ ). The upper panels show lensed images produced by these mass maps. The projected images are still very similar to each other, even though the mass maps show clear differences in both shape and slope. This illustrates that many different mass distributions may result in the same projected image configuration.

bias the ensemble average, and post-processing with further non-linear constraints is then required to filter the ensemble.

This paper explores methods to evaluate and test the quality of ensemble models from (free-form) lens-modelling tools, and specifically GLASS [50] in a blind study. In a first phase, we reconstructed 15 lenses from the EAGLE suite [Evolution and Assembly of GaLaxies and their Environment; 210] simulated with SEAGLE (Simulating EAGLE Lenses) by Mukherjee et al. [211], unaware of the actual mass distribution of the lenses. We investigated the mapping properties between source and lens plane of the individual models in the ensemble by creating *synthetic images*, which are recovered by using the lensing data to reconstruct the source plane and reprojecting back on to the lens plane. The quality of the data was then evaluated by comparing the synthetic images to the original data. Moreover, the arrival-time surfaces and mass distribution maps of each model in the model ensembles were visually inspected and evidently flawed models were filtered out. In a second phase, three mass distributions were unveiled and compared with the models. The three lenses were chosen to cover most distinguishing key properties of all lenses such as doubles, quads, and visible maxima. The reason for only unveiling three lenses in the beginning was to be able to improve on the rest of the lens set. In the third phase, all lens reconstructions were revised and finally compared with the simulated mass distributions.

This paper is structured as follows: Section 4.2 gives an overview of the theoretical framework necessary to understand the methods detailed in Section 4.3. In Section 4.4. we report on the results obtained during the analysis in the different phases, and in Section 4.5 the results are discussed and summarized.

[50]: Coles et al. (2014)

[210]: Schaye et al. (2014)

[211]: Mukherjee et al. (2018)

## 4.2 Theory

### 4.2.1 Arrival-time surface

Lensing can be expressed as arrival times of paths from the source to the observer which are extremal when the path corresponds to an actual light ray according to Fermat's principle. For a source at  $\beta$  the arrival time for light coming to the observer from position vector  $\theta$  on the sky, is following Blandford et al. [23]

[23]: Blandford et al. (1986)

$$t(\theta) = \frac{1+z_L}{2} \frac{D_L D_S}{c D_{LS}} (\theta - \beta)^2 - (1+z_L) \frac{8\pi G}{c^3} \nabla^{-2} \Sigma(\theta) \quad (4.1)$$

where  $D_L$ ,  $D_S$ , and  $D_{LS}$  are angular diameter distances from observer to lens, observer to source, and lens to source,  $z_L$  is the redshift of the lens,  $\Sigma(\theta)$  the sky-projected density of the lens, and  $\nabla^{-2}$  is an inverse Laplacian in 2D. The expression (4.1) depends, through the distances, on both source and lens redshifts. In cluster lensing, there are typically multiple sources at different redshift and sometimes multiple lens redshifts as well. In galaxy lensing, it is very rare to have more than a single lens and a single source. Hence, it is convenient to take out the redshift dependence and consider a scaled arrival time without the dependence on the redshifts. Writing

$$\begin{aligned} \Sigma(\theta) &= \frac{c^2}{4\pi G} \frac{D_L D_S}{D_{LS}} \kappa(\theta) \\ t(\theta) &= (1+z_L) \frac{D_L D_S}{c D_{LS}} \tau(\theta) \end{aligned} \quad (4.2)$$

and discarding the constant  $\frac{1}{2}\beta^2$  we have

$$\tau(\theta) = \frac{1}{2}\theta^2 - 2\nabla^{-2}\kappa(\theta) - \theta \cdot \beta. \quad (4.3)$$

The dimensionless surface density  $\kappa(\theta)$  is known as the convergence. Through equation (4.2)  $\kappa = 1$  corresponds to a critical surface density (for circular lenses, this lies within the Einstein radius) which characterizes the lens system. The function  $\tau(\theta)$  is known as the arrival-time surface. It is not itself observable, but still very useful since other relations can be derived from it [see e.g. 212]. In particular, the lens equation

[212]: Courbin et al. (2002)

$$\nabla \tau(\theta) = 0 \quad (4.4)$$

is just Fermat's principle applied to the arrival time while the inverse magnification tensor equals the matrix of second derivatives of  $\tau(\theta)$ .

### 4.2.2 Lensing Roche potential

We now introduce a further insightful quantity. Let us rewrite the arrival time (4.3) slightly as

$$\begin{aligned} \tau(\theta) &= \mathcal{P}(\theta) - \theta \cdot \beta \\ \mathcal{P}(\theta) &= \frac{1}{2}\theta^2 - 2\nabla^{-2}\kappa(\theta) \\ &= 2\nabla^{-2}(1 - \kappa(\theta)). \end{aligned} \quad (4.5)$$

The term  $\mathcal{P}$  amounts to solving a 2D Poisson for a potential and then adding a centrifugal term. That is reminiscent of the Roche potential in celestial mechanics, and so we will call  $\mathcal{P}$  the *lensing Roche potential*. It is like the arrival-time surface without the tilting term  $\boldsymbol{\theta} \cdot \boldsymbol{\beta}$ , and it represents the arrival-time surface for a source at the coordinates origin. The lensing Roche potential also amounts to solving Poisson's equation with  $1 - \kappa$  as the notional source.

Consider what happens if we multiply  $1 - \kappa$  by a constant factor  $\lambda$ . This changes the steepness of the mass distribution. Then,  $\mathcal{P}$  will also get multiplied by  $\lambda$ . If  $\boldsymbol{\beta}$  is simultaneously multiplied by  $\lambda$ , the net result is to multiply  $\tau$  by  $\lambda$ . This operation leaves the extremal points unchanged. That means the images are also unchanged, except that the overall magnification gets multiplied by  $1\lambda$  because we have rescaled the whole source plane. This is the steepness degeneracy (also called the mass-sheet degeneracy). In fact, changing  $\tau(\boldsymbol{\theta})$  in a way that does not affect the extremal points will not change the images, so there are really infinitely many degeneracies [26]. But the steepness degeneracy is the simplest and most severe. The advantage of  $\mathcal{P}$  is that the steepness degeneracy only multiplies it by a constant, and does not change its shape. Hence, a normalized lensing Roche potential offers a convenient way of comparing different models with the effect of the steepness degeneracy taken out.

[26]: Saha (2000)

### 4.2.3 Lensing mass quadrupole

Apart from the Einstein radius, which measures the total mass in the lensing region, the shape and orientation of the lensing mass are also of interest. We can probe these by considering the 2D inertia tensor

$$I = \frac{1}{\pi} \begin{pmatrix} \int \kappa(\boldsymbol{\theta}) \theta_x^2 d\boldsymbol{\theta} & \int \kappa(\boldsymbol{\theta}) \theta_x \theta_y d\boldsymbol{\theta} \\ \int \kappa(\boldsymbol{\theta}) \theta_y \theta_x d\boldsymbol{\theta} & \int \kappa(\boldsymbol{\theta}) \theta_y^2 d\boldsymbol{\theta} \end{pmatrix} \quad (4.6)$$

and its eigenvectors and eigenvalues. The position angle  $\phi$  of the lens is given by the angle between one of the eigenvectors of (4.6) and a unit basis vector. The semimajor and semiminor axes are given by  $a = 2\sqrt{\lambda_1}$  and  $b = 2\sqrt{\lambda_2}$  where the  $\lambda_i$  are the eigenvalues. The ratio  $q = b/a$  is a measure of the ellipticity of the mass distribution.

### 4.2.4 Image formation

The lens equation (4.4) defines a mapping from  $\boldsymbol{\beta}$  to  $\boldsymbol{\theta}$ . Let  $L(\boldsymbol{\theta}, \boldsymbol{\beta})$  denote that mapping. Then, a source-brightness distribution  $s(\boldsymbol{\beta})$  will produce an image brightness distribution

$$d(\boldsymbol{\theta}) = \int L(\boldsymbol{\theta}, \boldsymbol{\beta}) s(\boldsymbol{\beta}) d\boldsymbol{\beta}. \quad (4.7)$$

This applies if there is perfect resolution on the sky. In general, there will be smearing by the PSF, say  $P(\theta, \theta')$ . Hence

$$\begin{aligned} d(\theta) &= \int M(\theta, \beta) s(\beta) d\beta \\ M(\theta, \beta) &= \int P(\theta, \theta') L(\theta', \beta) d\theta'. \end{aligned} \quad (4.8)$$

This mapping is linear in the source brightness  $s(\theta)$ , but completely non-linear in the mass distribution. Additionally to the smearing effect by the point-spread function (PSF), the observed image will contain a foreground and noise. Despite the simplicity of equation (4.8), mass reconstructions of lenses are far more complex. A source brightness can be generated by many different mass distributions. Thus, it is insufficient to optimize mass distributions based on source brightness, and in most cases special information is needed to break those degeneracies.

## 4.3 Methods

In this section, we summarize the methodology used in this work. We first describe the SEAGLE pipeline [211] and how mock lenses were created (Section 4.3.1). We then describe the modelling strategy followed in this work with GLASS code (Section 4.3.2) and summarize the source reconstruction process (in Section 4.3.3) and comparison with the lens modelling (in Section 4.3.4).

[211]: Mukherjee et al. (2018)

### 4.3.1 SEAGLE

SEAGLE is a lens-simulation pipeline based on the EAGLE suite of hydrodynamical simulations of the formation of galaxies and supermassive black holes in a  $\Lambda$ -cold dark matter universe [159, 210, 213]. EAGLE galaxies are in good agreement with observations of the star formation rate, passive fraction, Tully–Fischer relation, total stellar luminosity of galaxy cluster and colours [214], the evolution of the galaxy stellar mass function and sizes [215, 216], and rotation curves [217]. The subgrid physics employed in EAGLE is based on that developed for OWLS [Over-Whelmingly Large Simulations 218]. In this paper, we have chosen to use the reference model L100N1504 which has a maximum proper softening length of 0.7 kpc [see Table 1 in 159, 210].

[210]: Schaye et al. (2014)  
[159]: Crain et al. (2015)  
[213]: McAlpine et al. (2016)

We apply the SEAGLE pipeline – which incorporates the GLAMER [219, 220] ray-tracing code and the parametric lens-modelling code LENSED [221, 222] – to selected galaxies from the simulations based on their stellar mass and create their DM, stellar, and gas surface mass density maps with their corresponding lensed images and convergence maps.

[214]: Trayford et al. (2015)  
[215]: Furlong et al. (2015)  
[216]: Furlong et al. (2017)  
[218]: Schaye et al. (2010)

The SEAGLE pipeline automatically identifies and extracts samples of (lens) galaxies from the Friends-Of-Friend (FoF) catalogues of the EAGLE simulations. After selecting the galaxy identifiers using an initial selection function, we identify the desired GroupNumber, and SubGroupNumber (numbers assigned to FoF group and subgroup, respectively) and select their particles (gas, DM, and stars). The particles of each galaxy from the simulations are rotated in three different axes and

[210]: Schaye et al. (2014)  
[159]: Crain et al. (2015)

[211]: Mukherjee et al. (2018)

[223]: Mukherjee et al. (2019)

[219]: Metcalf et al. (2014)

[220]: Petkova et al. (2014)

converted into projected surface density maps (or generally referred to as ‘mass maps’). The surface density maps are created in units of solar masses per pixel on grids of  $512 \times 512$  pixels (for more details of the lensing galaxies, size, and pixel scale of mass maps [see table 2 in 211]. Hereby, the entire galaxy and its local environment are taken into account [see section 3.2 in 223]. They are used as input to the ray-tracing lensing code GLAMER [219, 220]. We then choose a source redshift for GLAMER to convert these mass maps into convergence maps. For each convergence map, the critical curves and caustics are calculated to determine where a source has to be placed in order to create multiple-lensed images.

An elliptical Sérsic brightness profile of the source was used with index  $n = 1$ , apparent magnitude = 23 in the HST-ACS (Advanced Camera for Surveys) F814W filter (AB system) placed at a redshift of  $z_s = 0.6$  to mimic SLACS (Sloan Lens ACS Survey) lenses. The source has an effective radius of 0.2 arcsec, a position angle  $\phi_s = 0^\circ$  and a constant axis ratio  $q_s = 0.6$ . The pixel scale (0.05 arcsec), the PSF, and noise correspond to an HST-ACS F814W exposure of typically 2400 s. The final resulting images are exported in standard fits-file format and have sizes of  $161 \times 161$  pixels of 8.0 arcsec side length (all parameter values are motivated from SLACS lenses, e. g. Koopmans et al., Newton et al. [224, 225]). We randomly choose 15 lensed EAGLE galaxies and their convergence maps (see Figures 4.3 and 4.6).

The nomenclature of the lenses depends on their halo, subhalo, and projection catalogue. A number following ‘H’ refers to the halo number, ‘S’ gives the subhalo, and letters ‘A/B/G’ refers to the projection the galaxy has undergone in Cartesian coordinates i.e.  $\alpha, \beta$  and  $\gamma$  respectively. Although the names of the lenses have a meaning, it is not important in the context of this paper, and for simplicity we will rather refer to the lenses by their position in the figures.

### 4.3.2 GLASS

The lens modelling was performed with the free-form modelling code GLASS [50]. The strategy behind GLASS [and with its precursor PixeLens 140] is the following.

First,  $\kappa(\theta)$  is not a simple parametrized form but a free-form map made up of a few hundred mass tiles or pixels. The arrival time is then

$$\begin{aligned} \tau(\theta) &= \frac{1}{2}\theta^2 - \theta \cdot \beta - 2 \sum_n \kappa_n \psi_n(\theta) \\ \psi_n(\theta) &= \nabla^{-2} Q_n(\theta) \end{aligned} \quad (4.9)$$

where  $\kappa_n$  is the density of the  $n$ -th mass tile and  $Q_n(\theta)$  represents its shape. Each tile is a square and its contribution  $\nabla^{-2} Q_n(\theta)$  can be worked out exactly [142]. The mass tiles are mostly of equal size, but smaller tiles are used in the very central region. We refer to  $\sim 200$  tiles as low resolution and  $\sim 450$  tiles as high resolution.

Next, point-like features on the images that correspond to a common source are identified using a peak finding algorithm on the lensed images. This provides a set of linear equation for  $\kappa_n$  and  $\beta$ . These equations have

[142]: AbdelSalam et al. (1998)

infinitely many solutions, from which we sample an ensemble of lens models, according to the following priors:

1.  $\kappa_n \geq 0$ ,
2. at each image position, the eigenvalues of  $\nabla\nabla\tau(\theta)$  correspond to minima, saddle points, or maxima in Fermat's principle, as specified for that image,
3. each  $\kappa_n$  is limited to twice the average of its neighbours, to ensure a reasonably smooth distributions,
4. the local density gradient is required to point within a specified angle (by default  $45^\circ$  but usually  $80^\circ$  in this work) of the centre,
5. azimuthally averaged density profiles must decrease with increasing radius,
6. a constant two-component, external shear is allowed, but each component limited to 0.3.

Nominal lens and source redshifts of  $z_L = 0.5$  and  $z_S = 3.0$  and a concordance cosmology with  $(\Omega_m, \Omega_\Lambda, H_0^{-1}) = (0.3, 0.7, 14 \text{ Gyr})$  were assumed, as this information was unknown during the blind phase. These values do not enter the results however, as the subsequent analysis is entirely in terms of  $\kappa$ .

### 4.3.3 Source reconstruction and synthetic images

GLASS treats a source as a point on the source plane that can map on to multiple points on the image plane. Its solutions consist of ensembles of convergence maps which are constrained to reproduce the given image positions from some inferred source position. In reality, we have extended images from extended sources. Extended sources can be emulated by simply using multiple point-like features. For detailed image reconstruction, however, we use a new strategy, an extension of the method used by Küng et al. [48], involving post-processing the model ensemble from GLASS as follows.

[48]: Küng et al. (2018)

For each model in the GLASS ensemble, we compute a discrete version  $M_{\theta\beta}$  of the lensing and PSF-smearing map  $M(\theta, \beta)$  in equation (4.8), by considering  $\theta$  values at pixel locations. We then solve for the source-brightness distribution  $S_\beta$  such that the synthetic image

$$D_\theta = \sum_\beta M_{\theta\beta} S_\beta \quad (4.10)$$

best fits the observed brightness  $D_\theta^{\text{obs}}$  in a least-squares sense. That is to say, we minimize

$$\chi^2 = \sum_\theta \frac{(\sum_\beta M_{\theta\beta} S_\beta - D_\theta^{\text{obs}})^2}{\sigma_\theta^2} \quad (4.11)$$

for each model in the GLASS ensemble. Once the source-brightness distribution has been fitted, it can be reinserted into (4.10) to generate a synthetic image.

- [30]: Warren et al. (2003)
- [226]: Dye et al. (2005)
- [227]: Brewer et al. (2006)
- [228]: Suyu et al. (2006)
- [229]: Vegetti et al. (2009)
- [230]: Tagore et al. (2014)

This procedure is formally similar to lens inversion methods previously used by Warren et al., Dye et al., Brewer et al., Suyu et al., Vegetti et al., Tagore et al. [30, 226–230], and many others. In their case, the extended lens images help constrain the source-brightness model and the parametric lens model simultaneously. For such methods, equation (4.11) is usually supplemented with regularization terms to penalize noisy solutions. A problem which Warren et al. [30] already pointed out is that regularization produces too smooth source-brightness distributions and lead to a bias in the model. Moreover, it was found that mass models are rather insensitive to regularizations if an optimal source pixel size is chosen. Here, the methodology is different. We use equation (4.11) to solve for synthetic images with already modelled mass maps and thereby test our models’ mapping properties. Since we are only interested in the lensed images, regularizations are not necessary.

The uncertainty of an observation corresponding to  $\sigma_\theta$  in equation (4.11) generally has several sources, and depends on the optical devices in use. The simplest to model is the photon noise

$$\sigma_\theta^2 = g^{-1} D_\theta^{\text{obs}} \quad (4.12)$$

where  $g$  is the gain or counts per photon. We also assumed a further uniform noise field to mimic other noise sources.

No luminosity and kinematic information about the lensing galaxy was included in the data, nor was any information about the light distribution of the unlensed source. Not having light from the lensing galaxy has one benefit, namely not polluting the lensed image, but also has disadvantage of removing potentially useful information about the lens.

- [231]: Behnel et al. (2011)
- [232]: Jones et al. (2001)

The above is implemented in python so to easily interface with GLASS, but uses optimized parts written in cython [see 231] and C. To solve the linear inverse problem it relies on methods provided in the module `scipy.sparse` and `scipy.sparse.linalg` [see 232]. Computationally, the most expensive operation is the construction of the sparse matrix  $L_{\theta\beta}$  which when multiplied with the PSF yields  $M_{\theta\beta}$ , because matrix multiplication routines are highly optimized in most frameworks.

#### 4.3.4 Model comparison

Individual models of the lens reconstruction ensemble were compared to the SEAGLE lens models to evaluate their goodness of fit.

First, the resemblance of the convergence maps was investigated. As gravitational lensing is foremost determined by the total mass content of the lens, the ensemble models’ Einstein radii — which are a measure of the total mass contained within — were compared to the SEAGLE models. By definition, the scale of the Einstein radius is set where the radial profile of the convergence crosses  $\kappa = 1$ , thus for non-circular lenses we adapt the definition of a notional Einstein radius where  $\langle \kappa \rangle_{R_E} = 1$ .

Additionally, the shape and orientation of the lens were analysed. The inertia ellipse’s semiminor to semimajor axial ratio  $q$  acts as a shape parameter and was determined with equation (4.6). The orientation was determined by the position angle  $\phi$  as described in Section 4.2.3. It can be

determined up to an ambiguity of  $\pm\pi$ , provided the lens is not perfectly round (which happens in the limit of  $q \rightarrow 1$ ). To combat this degeneracy, we define a complex ellipticity

$$\epsilon = \frac{1-q}{1+q} e^{2i\phi} \quad (4.13)$$

which combines the ellipticity and the position angle following Mukherjee et al. [211]. With this definition, round lenses will fall closer to the origin no matter what position angle, whereas more elliptical lenses move away from the origin at an angle given by the position angle.

[211]: Mukherjee et al. (2018)

As mentioned before, the relation between convergence and synthetic image is degenerate. This means, if the convergence exactly matches the ‘true’ convergence, the synthetic image and the observed data will be indistinguishable. Slight changes in the convergence however do not linearly translate to the synthetic image, and vice versa. A straightforward comparison of the model’s convergence to the ‘true’ convergence map is thus insufficient. We therefore use the Roche potential as in equation (4.5) as a basis of comparison. The best-fitting model in the ensemble can be found with the maximum modulus of the inner product of the modelled lensing Roche potential  $\mathcal{P}^{\text{mod}}$  and the lensing Roche potential of the original convergence map  $\mathcal{P}^{\text{orig}}$ .

$$\max\langle P^{\text{orig}}, P^{\text{mod}} \rangle = \max \left| \frac{\int \mathcal{P}^{\text{orig}}(\theta) \mathcal{P}^{\text{mod}}(\theta) d\theta}{\sqrt{\int |\mathcal{P}^{\text{orig}}|^2 d\theta} \sqrt{\int |\mathcal{P}^{\text{mod}}|^2 d\theta}} \right| \quad (4.14)$$

Since the Roche potentials are independent of the source position and the inner product is normalized, the mass-sheet degeneracy is completely eliminated. The mass-sheet degeneracy not only affects a mass distribution’s overall amplitude by adding (or subtracting) an arbitrary number of mass sheets of critical density, but more importantly also changes its scale and steepness. This means, even though a model’s convergence profile might not show perfect match in its slope, it can very well be a valid solution.

## 4.4 Results

The sample of 15 SEAGLE lenses is described in Section 4.3.1 and shown in Figure 4.3. These lensed images were prepared by SM. PD, in consultation with JC and PS, reconstructed the lenses from these data. Besides the mass centroid of the lensing galaxy and the PSF used to blur the lensed images, no other information about the lenses was provided to the modellers.

The lens reconstructions were done in two phases. In the first phase, three lenses were unblinded early, in order to test and improve the pipeline. In the second phase, PD modelled the other 12 lenses unaware of the truth held by SM.

The lenses in the top row were chosen for the first phase because of their diverse lensed image configuration. As shown in Figure 4.3, the lens on the left is a quad lens with an almost ring-like image configuration,

which is present in most regular quads and doubles in the sample, the lens in the middle is a double with a wide arc image and a less extended image slightly closer to the lens, and the lens on the right is one of five systems presenting a fifth non-demagnified image, which is always a maximum of the arrival time. This subset covers the most typical lens properties in the entire sample (from a lens modeller's perspective). After the comparison of the three lens models with their actual convergence, the lens-modelling procedure was adjusted to be better prepared for the second phase.

In the second phase, the remaining lenses were reconstructed with the actual convergence maps veiled. The latter were then revealed for comparison, but no further changes to the models were allowed.

It is important to note that our goal during the lens reconstruction was not simply to optimally reproduce the lenses images, but to find an ensemble sampling the possible mass maps.

#### 4.4.1 Lens reconstructions

The lens modelling directly yields ensembles of  $\kappa$  maps for the lenses. Synthetic images for each mass map in the ensemble were constructed and a  $\chi^2$  was evaluated for each image according to equation (4.11). In each ensemble at least half of all synthetic images gave bad fits to the image data, however for 12 of the 15 lenses there was at least one synthetic image which fit the data well. Figure 4.4 shows the synthetic image with the minimal  $\chi^2$  in the ensemble, for each lens. As described in Section 4.3.3, the synthetic images were constructed by projecting the data from the image plane on to the source plane using the model to calculate the deflection angles, and reprojecting back on to the image plane. Interestingly, and against our initial expectations, low-resolution models often seem to produce better synthetic images. The reduced  $\chi^2$  values never get to 1, indicating that the best fits are dominated by systematic errors in the model fitting. The high-resolution images have reduced  $\chi^2$  of  $\sim 2.5$ , whereas the low-resolution images have values as low as 1.7.

Although it is sometimes possible to spot irregularities and unphysical features in the mass maps from simple inspection, it is generally easier to review the contours of the derived arrival-time surface (4.9). Arrival-time surfaces become very intuitive to interpret once the saddle-point contours have been drawn, as they already schematically resemble lensed arcs and can visually be compared to the image data. Figure 4.5 shows arrival-time surfaces of the ensemble-average models of each lens. Saddle-point contours are indicated in black, and image position constraints for minima, saddle-points, and maxima in blue, purple, and red respectively. The models by construction reproduce point-like image features at the correct positions. But they can also show additional spurious images, easily identifiable as local extrema. Ensemble averages tend to suppress these spurious images. The arrival-time surfaces from GLASS are highly sensitive to the image positions. In our experience, good models produce nice smooth-looking arrival-time surface, but so do some bad models; whereas ragged-looking arrival-time surfaces invariably indicate bad models. Slight shifts in the image positions might result in significantly

different arrival-time surfaces and mass maps. The fact that the lenses have extended, and sometimes almost ring-shaped images, aggravates this difficulty. As the time delays were unknown, the parity of the extrema was uncertain as well. In some cases, a trial-and-error approach had to be adopted until a credible model was obtained, with others an educated guess could be made based on the distances of the images to the lens and their brightness.

During the reconstructions, the prior parameters in GLASS were tweaked to obtain a satisfactory arrival-time surface of the ensemble average in each case. Additionally, we filtered out a percentage of the worst  $\kappa$  maps from the distribution of  $\chi^2$ , and by mere construction improved the ensemble average's synthetic image. This gave considerable improvements for ensembles with a wide variety in its models, however only slight changes for ensembles with a less diverse set.

#### 4.4.2 Convergence map comparison

The  $\kappa$  maps used by SM to generate the lenses are shown in Figure 4.6. Apart from the top row, these were hidden during the modelling process. The modelling generated ensembles of  $\kappa$  maps, and the ensemble averages are shown in Figure 4.7. The modelled convergence maps show the mass-tile structure of the free-form method, whereas the actual maps have higher pixel resolution. A direct comparison of the convergences was expected to be insufficient due to the well-known problem of degeneracies. The numerically best-fitting convergence map of an ensemble according to

$$\min_{\text{model}} \sum_i (\kappa_i^{\text{truth}} - \kappa_i^{\text{model}})^2 \quad (4.15)$$

produced bad or mediocre synthetic images in all lens models, which further confirmed our suspicion. We visually inspected all ensembles each with 1000 individual models. In some ensembles, the ellipticities and position angles had little spread and were definitive, but in others, the models showed an ambiguity of  $\pm\pi$  in their position angles. We therefore compared the radial profiles and ellipticities, as follows.

Figure 4.8 shows the average enclosed  $\kappa$  as a function of radial distance from lens centre. The formal Einstein  $R_E$  corresponds to  $\langle \kappa \rangle_{R_E} = 1$ . The Einstein radii are well recovered and have a median relative error of 4.3 per cent over the entire set of quads; for some quads, the Einstein radius had an error as low as 1.0 per cent, and was slightly overestimated for others with maximally 15.7 per cent, but in all cases the errors were smaller than the pixel sizes. The Einstein radii for double systems were less accurate with an average error of 24.8 per cent. But even so, the profiles are systematically too shallow. It is interesting, however, that the model profiles (green-yellow bands) could be brought much closer to the correct profiles (red curves) by multiplying  $1 - \kappa$  by a constant. This transformation is nothing but the steepness degeneracy, which does not affect the images.

Figure 4.9 compares the complex ellipticity (4.13) for the model ensembles with the SEAGLE values. Without exception, the lens models tend to be too round. This makes it more difficult to determine a position angle for the models. Nevertheless, in all but two cases the position angle was

roughly recovered with a median error of  $\pm 9.4^\circ$ . This is also observable by comparing corresponding maps in Figures 4.6 and 4.7.

The problematic lenses are in the bottom row, especially the two in the middle and right-hand panels. In both cases, the position angles are off by almost  $90^\circ$ . This is evident in Figure 4.9 as the ellipticity of the ensemble model is in the quadrant opposite to the one of the SEAGLE simulation. This is also observable by directly comparing the orientation of the galaxies in Figure 4.6 and Figure 4.7. After comparing the arrival-time surfaces and convergences, we suspect the image order is most likely wrong. In both cases, the arc to the north should have been diagnosed as arriving before the counterimage to the south, whereas in the models the opposite was done. The estimated semimajor and semiminor axes which appear in the complex ellipticity only as a ratio, also were generally too high compared to the SEAGLE simulations. This indicates that the lens ensemble models have more mass at higher radii from the centre relative to the total mass, as the semimajor and semiminor axes were estimated with the inertia ellipses of the convergences. This means, as we have already seen, that the models tend to be too shallow across the board.

#### 4.4.3 Roche potential comparison

After unblinding the actual convergence maps of the lenses in the top row, it became clear that a further comparison was desirable which quantified the goodness of the lens reconstruction with the effect of the steepness degeneracy taken out. We then formulated and calculated the lensing Roche potential. This is just the arrival time from equation (4.9) without the  $\theta \cdot \beta$  term and an arbitrary additive constant. Furthermore, the effect of the steepness degeneracy corresponds to an arbitrary multiplicative factor, as explained in Section 4.2.2. Thus, we are free to subtract the potential's value at the centre from the entire map and to normalize to the negative of its minimal value. This way the lowest minimum has the value  $-1$  and the map centre the value  $0$ , and takes out the effect of the steepness degeneracy. The results from the actual convergence maps and from the lens models are shown in Figures 4.10 and 4.11 respectively. These figures show contoured regions of equal level of the Roche potentials as in equation (4.5).

In a rough visual comparison, most lens models — except the already mentioned lenses in the bottom row — show the same main features and morphologically appear to agree with their SEAGLE counterpart. In particular, the position and shape of minima and the lens' orientation match quite well. For some quad systems such as the left one in the second-last row, there seems to be a tilt in the model which is suppressing one of the minima, which is not evident in the corresponding SEAGLE simulation. Similarly, some saddle regions of the models seem to have switched amplitudes causing lemniscates to wrap around the central maximum from a different side compared to the SEAGLE simulations.

A quantitative comparison of the Roche potentials was done by evaluating the scalar product (4.14). The black circles in Figures 4.10 and 4.11 indicate the radii within which integrals in the scalar product were evaluated. It was necessary to choose a radius smaller than the map radius as otherwise the scalar product would have been dominated by differences

on the edges of the image plane. Using a small integration radius instead, we observed that differences in the shape of the central region and regions near the saddle-contours of the potential dominate the scalar product.

Filtering out models from the ensemble which give low scalar product values will by construction yield an overall improved ensemble average, since the fraction of bad models shrinks.

It is now interesting to put in contrast the synthetic image and the Roche potential as criteria. This means comparing the distribution of  $\chi^2$  from the synthetic images and the distribution of scalar products of the Roche potentials  $\langle P^{\text{orig}}, P^{\text{mod}} \rangle$  within an ensemble. This comparison is illustrated by the hex-binned plots in Figure 4.12. Just as we expect a filtering of the ensemble in which only models with low  $\chi^2$  of the synthetic image are kept to improve the ensemble overall, filtering according to the Roche potential is expected to elevate the quality of ensembles as well. Hence we expect both methods to anticorrelate, meaning, models with a low  $\chi^2$  should have a scalar product of the Roche potential with a value close to 1, whereas higher  $\chi^2$  should have a low scalar product. At first glance, Figure 4.12 neither disproves this assumption, nor conclusively confirms it. None of the lenses clearly display tendencies towards anticorrelation between  $\chi^2$  and  $\langle P^{\text{orig}}, P^{\text{mod}} \rangle$ . However, it seems that mostly models with a diverse ensemble show an anticorrelative trend, whereas models with an already overall high-quality ensemble distribute rather uniformly in that parameter space. It is also interesting that some lenses, e.g. the lens in the middle row to the right (H30S0A0B90G0), show a wide spread in the scalar product of the Roche potentials, but a very low spread in  $\chi^2$ . This means that even though the shapes of the mass maps differ widely, the mass maps produce similar quality of synthetic images. This implies that filtering should improve broad ensemble models, however there is a point when optimizing an ensemble model does not change the model anymore, at least globally. This is probably due to the fact that those models seem to agree on the global structure of the convergence and continue fitting substructures.

An example of this is also shown Figure 4.2. The differences are minor, but reducing the ensemble to only 100 models with the lowest  $\chi^2$  visibly improves the synthetic image of the ensemble-averaged model, which was expected as the  $\chi^2$  is a direct measure of the synthetic images. However, trying to improve that ensemble again by filtering out the worst scalar products of the Roche potentials does not clearly improve upon the already filtered ensemble anymore. This can be explained by the fact that in the end synthetic images are a local, non-linear measure of the mass whereas the Roche potential is a direct measure of the global mass model.

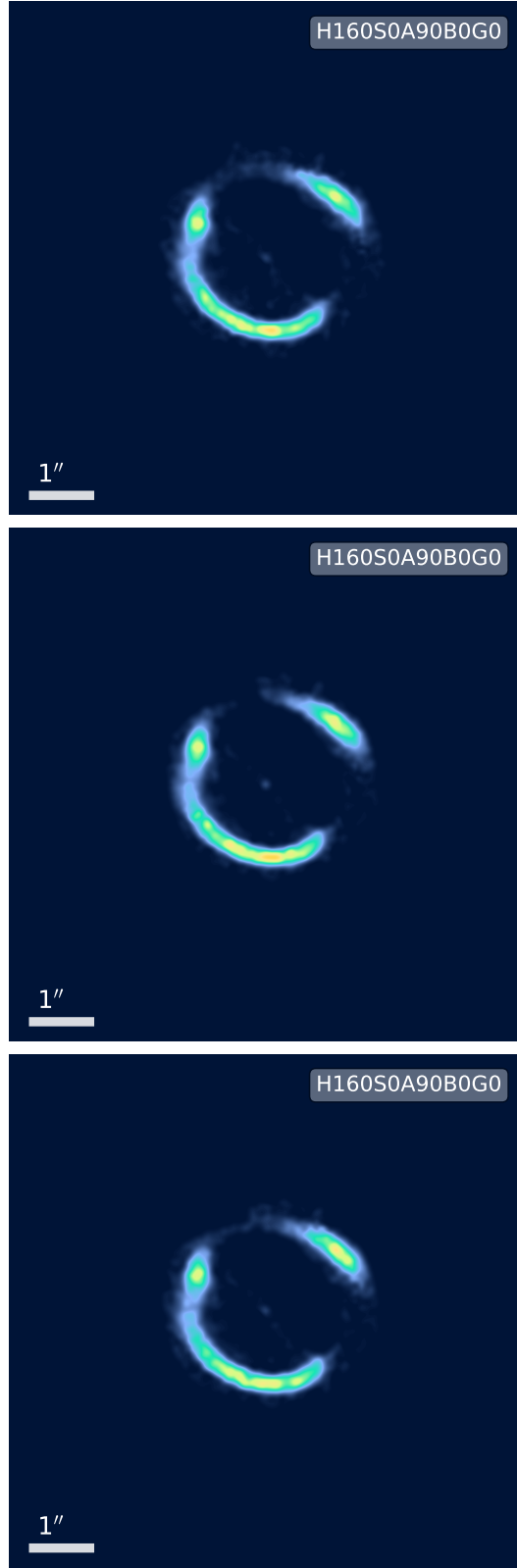


**Figure 4.2:** Alternative synthetic images of the lens H160S0A90B0G0 (cf. middle-left panel in Figure 4.4). Here, the image on top was generated from the unfiltered ensemble consisting of 1000 models. The middle shows the image generated with an ensemble containing 100 models with lowest  $\chi^2$ , and the bottom image shows the synthetic image from an ensemble containing 79 models which is the intersection of the set of lowest  $\chi^2$  and the scalar products of the Roche potentials closest to 1. The middle image shows a visible, albeit small, improvement compared to the top image, whereas the bottom image only shows slightly better relative brightness between the lens images compared to the middle, but no discernible improvement otherwise.

## 4.5 Conclusion

We need to prepare for the tens of thousands of strong gravitational lenses expected to be discovered with the next generation of wide-field telescopes: *Euclid* and *WFIRST (Wide-Field Infrared Survey Telescope)* in space and *LSST (Large Synoptic Survey Telescope)* on the ground. Lately, many efforts have been made to prepare for this data flood, from automatic identification of lens candidates with the use of machine learning, to automatic modelling of lenses with novel codes. While this paper does not address the problem of scalability for future big data sets, it demonstrates the necessity of such blind test, particularly for lens-modelling tools which were designed to scale up to thousands of lenses. It is still unclear how much we can trust the resulting lens models of such pipelines and what aspects of a lens model are robust against degeneracies. The only way to objectively test lens reconstruction techniques and avoid confirmation bias are blind tests with realistically simulated data.

In this work, we have used a sample of 15 simulated strong lenses from the state-of-the-art hydrodynamical simulation of EAGLE and modelled them blind with the GLASS code. We introduced a new lensing potential, the ‘Roche potential’ and showed that using this in free-form modelling we are successfully able to reconstruct the lensing systems without the mass-sheet or steepness degeneracy.

General properties like extended image information, Einstein radii, and shape of the convergence have been investigated and compared to the actual, subsequently unveiled convergence. Thereby, the following results stood out:

- It was straightforward to find models in the ensemble with good fitting synthetic images. Low-resolution models actually tended to perform better in this respect. It appears that high-resolution models start fitting substructures which predominantly impact the synthetic images. Also, low-resolution images produce smoother source images, which might also improve fits to the images. This can be seen when comparing Figure 4.1 which shows synthetic images constructed with low-resolution models and Figure 4.4 which displays the image reconstructions from high-resolution models.
- The Einstein radii were recovered quite well for most lenses, in some cases they were slightly overestimated.
- The position angles were also approximately in agreement, except for two lenses. In those two cases, the problems were traced back to having chosen the wrong image order in the lens reconstruction.
- The ellipticities of the mass maps were generally too round.
- The radially averaged convergence profiles were all found to be too shallow. However, this is an effect of the steepness degeneracy and could be resolved by multiplying the  $1 - \kappa$  surface by an arbitrary factor.

Even when all those properties are approximately recovered by a lens model, it was demonstrated that this does not necessarily mean the actual distribution has been found.

The reason why reconstructing lenses is so difficult lies in the many kinds of degeneracies that affect lens models. The most important of these is the steepness degeneracy (also called the mass-sheet degeneracy). The novel concept of a lensing Roche potential is introduced to remove the effect of the steepness degeneracy, that is, to compare models which have been differently affected by the steepness degeneracy. The scalar product of two Roche potentials gives a true measure of how alike models are to each other whilst ignoring the steepness degeneracy. A good match between model and truth simply means that up to an arbitrary rescaling of  $1 - \kappa$  the shape of  $\kappa$  agrees well with the truth. In the cases where the scalar product of the Roche potentials is far from 1, we have a bad match, meaning the actual shape of  $\kappa$  has not been recovered well enough.

We demonstrated that filtering out models where the synthetic images have the highest  $\chi^2$  seems to improve ensembles up to a point. However, once the global properties of the lens have been modelled, further optimization of the synthetic images does not improve fits to substructures and other local properties. This means, even if synthetic images from a model ensemble might show only minor variation, the underlying convergence might have major differences in comparison. This shows that the scalar product of Roche potentials is a better criterion to determine a model's quality when mass distributions are of primary interest.

In summary, this study not only confirms the well-known characteristic of lens modelling, that the Einstein radius of the mass distribution is generally well reproduced whereas its steepness is not, but also highlights additional points:

- To mitigate the problem of unbroken degeneracies, we recommend producing an ensemble of many solutions rather than a single model.
- While synthetic images represent a convenient visual diagnostic, they are useful only up to a point. Once a synthetic image is reasonably good (and well before the formal  $\chi^2$  criterion is achieved) the goodness of the synthetic image does not correlate with the goodness of the lens model. In other words, even if the model reproduces lensed images which resemble the data rather nicely, the mass map might still be far from the truth.
- Careful attention should be paid to the parity and time order of the images, because getting these incorrect, results in poor models.
- When testing lens-modelling tools against well-known lenses or simulations, the scalar product of the Roche potentials gives a measure of the shape similarity of the mass models which is robust against degeneracies. If this scalar product indicates a bad match, a recalibration of the lens-modelling tool might be needed.

## Funding statement

PD acknowledges support from the Swiss National Science Foundation. SM acknowledges the funding from the European Research Council (ERC) under the EU's Horizon 2020 research and innovation programme (COSMICLENS; grant agreement no. 787886).

## 4.6 Figures

This section contains all figures which are referenced in previous sections.

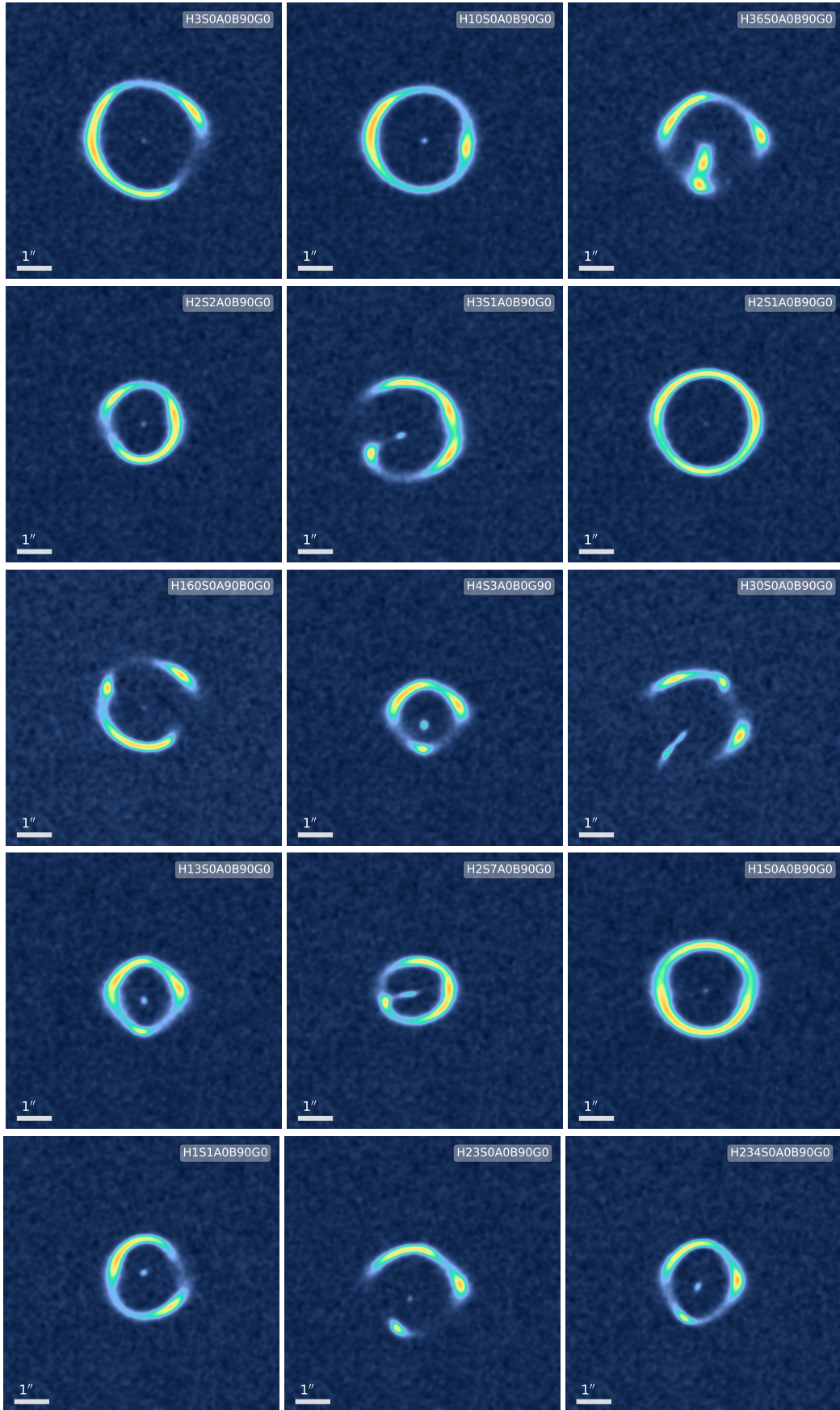


**Figure 4.3:** The SEAGLE-simulated lens data. The pictures show the lensed images without the lens in arbitrary units of brightness. They were the only information provided in the blind study. The scale bar on the lower left in each panel shows the physical scale in arcseconds.

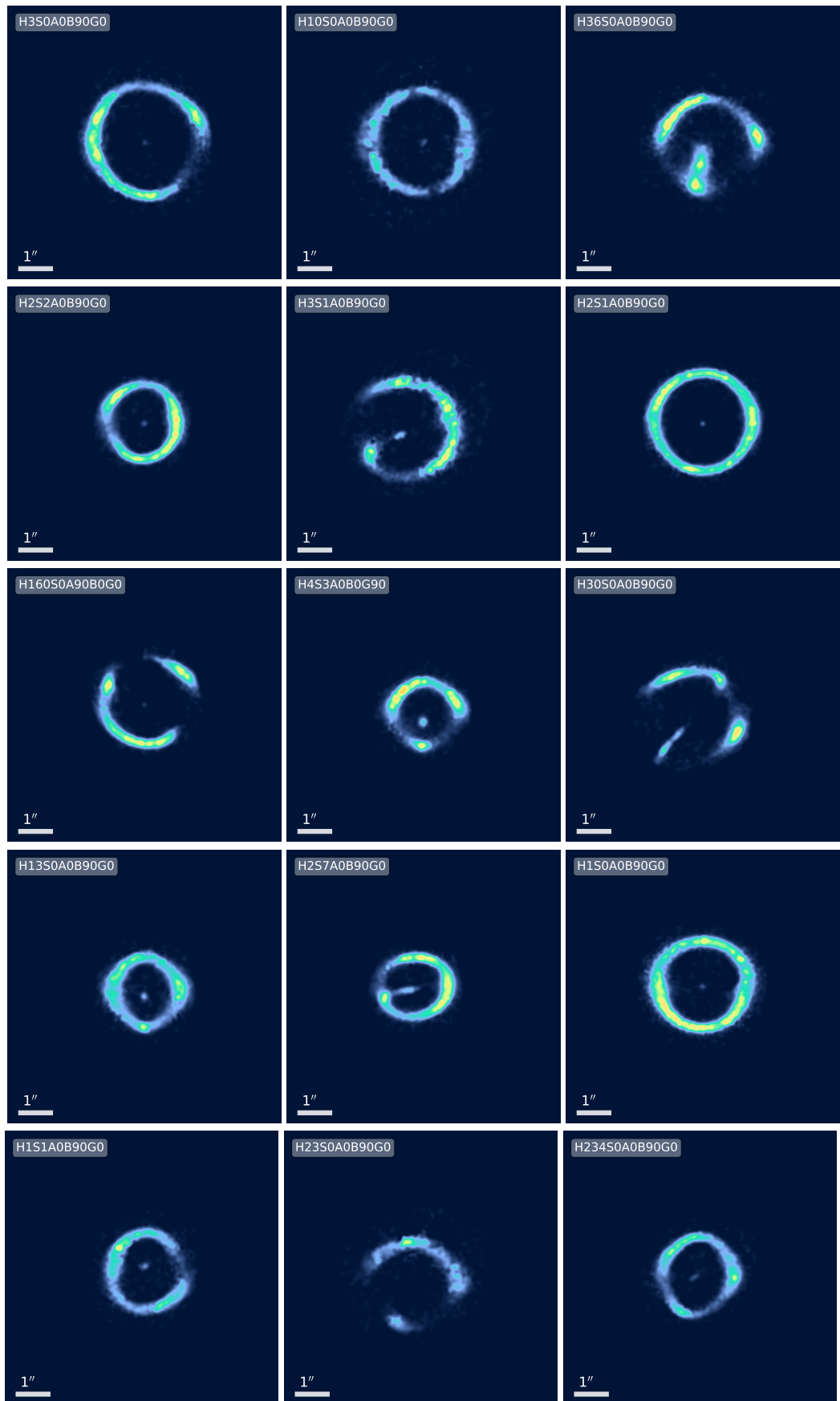


**Figure 4.4:** Synthetic images of the 15 reconstructed lenses using the best-fitting model from the ensemble solution. Scales are identical to the corresponding pictures in Figure 4.3.

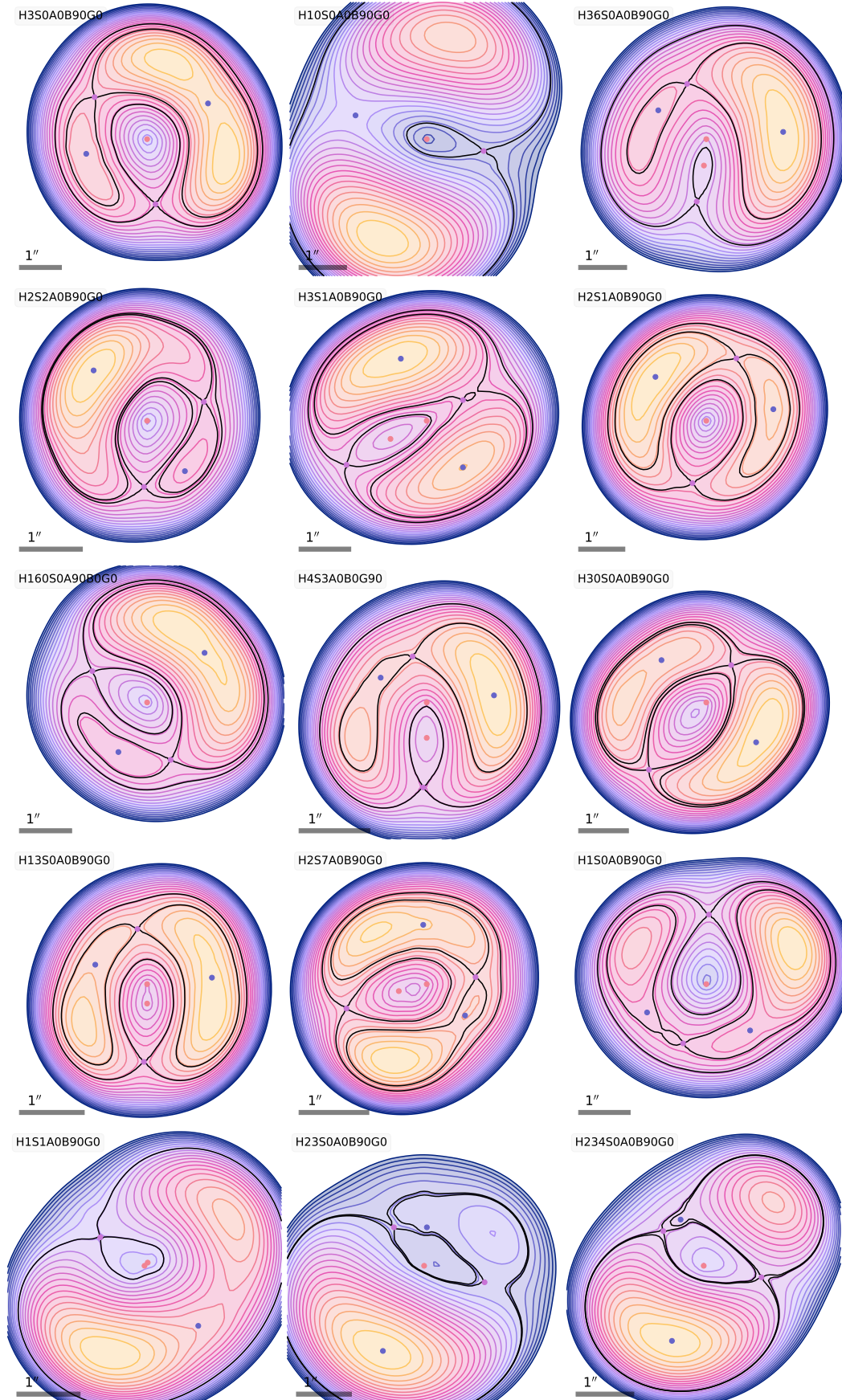


**Figure 4.5:** Arrival-time surfaces of the ensemble average of the 15 reconstructed lenses. Contours passing through saddle points are in black. The lens centre is indicated by a red dot, while the image-position constraints with minimum, saddle, and maximum parity are indicated by blue, purple, and red dots respectively. It is easy to identify unrealistic models by looking for irregularities in the arrival-time surface contours.

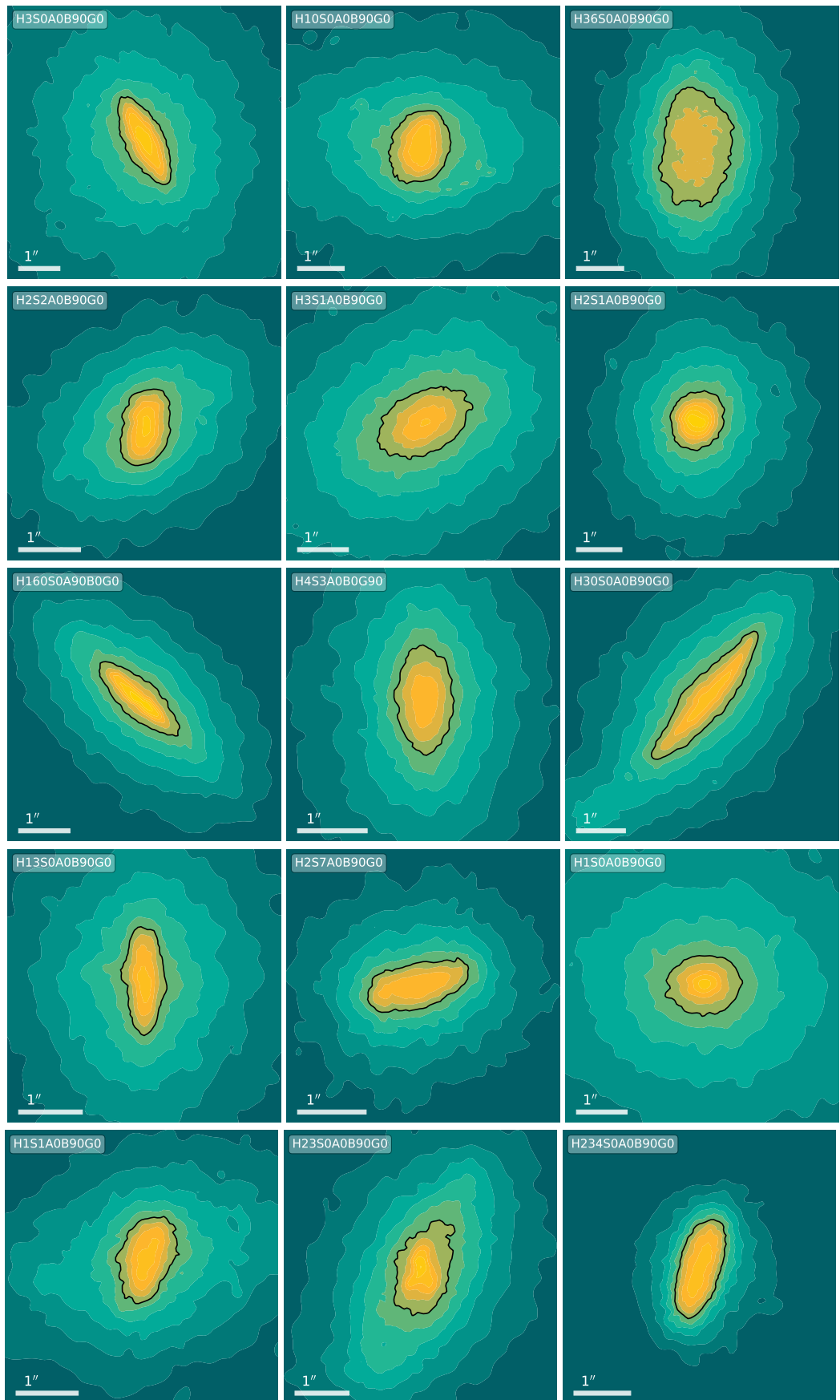


**Figure 4.6:** The actual convergence maps of SEAGLE-simulated lenses. Black contours indicate a  $\kappa = 1$ . They were unblinded after the lens reconstructions were completed.

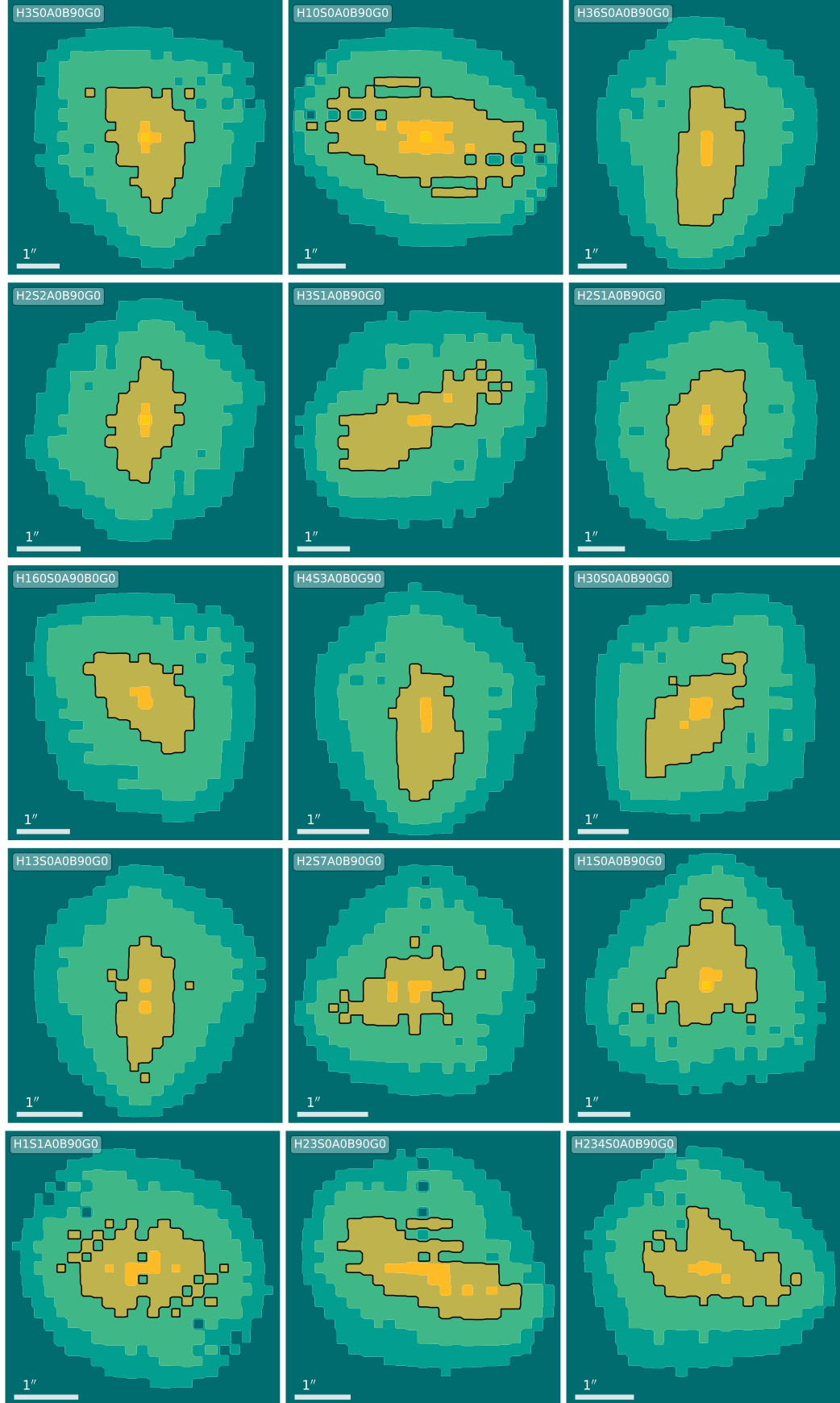


**Figure 4.7:** Model convergence maps (ensemble-averages) of all the lenses. Black contours indicate a  $\kappa = 1$ . Scales are identical to the corresponding pictures in Figure 4.6. Direct comparison of convergence maps usually fails, because they are affected by degeneracies. Nevertheless, the orientation of the lenses roughly match their SEAGLE counterparts.

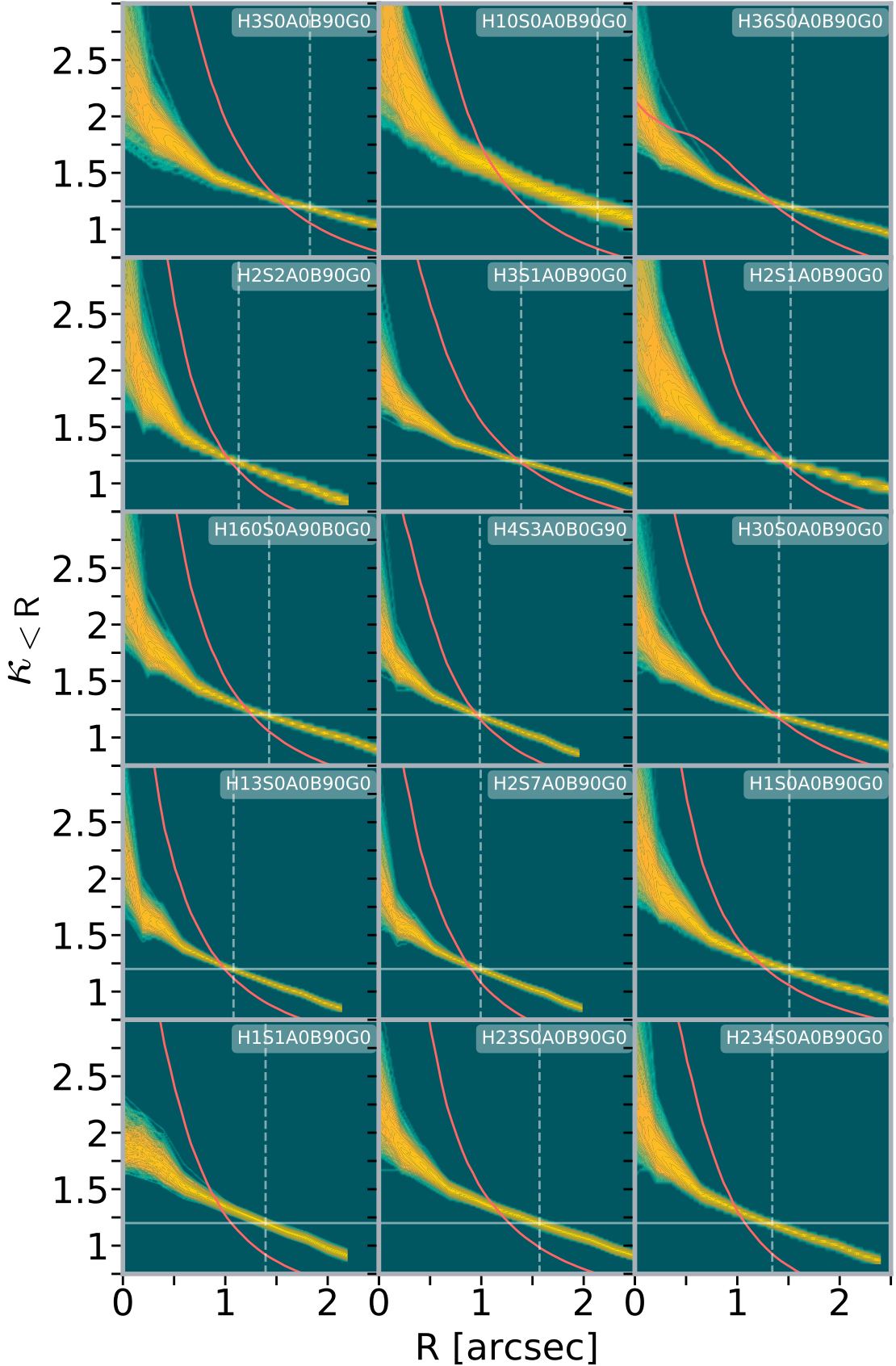


**Figure 4.8:** Circularly averaged enclosed surface density profiles of all reconstructed lenses. In other words, the plots show the enclosed mass as a mean  $\kappa_{<R}$  within a given projected radius from the lensing galaxies' center of mass. The ensemble is represented with a coloured region with a gradient from green to yellow indicating its number density. The vertical line shows the approximate Einstein radius of the ensemble average. The red line shows the same profile for the actual convergence map. The Einstein radii of quads are in good agreement with the SEAGLE lenses. It is harder to find the correct Einstein radius for doubles.

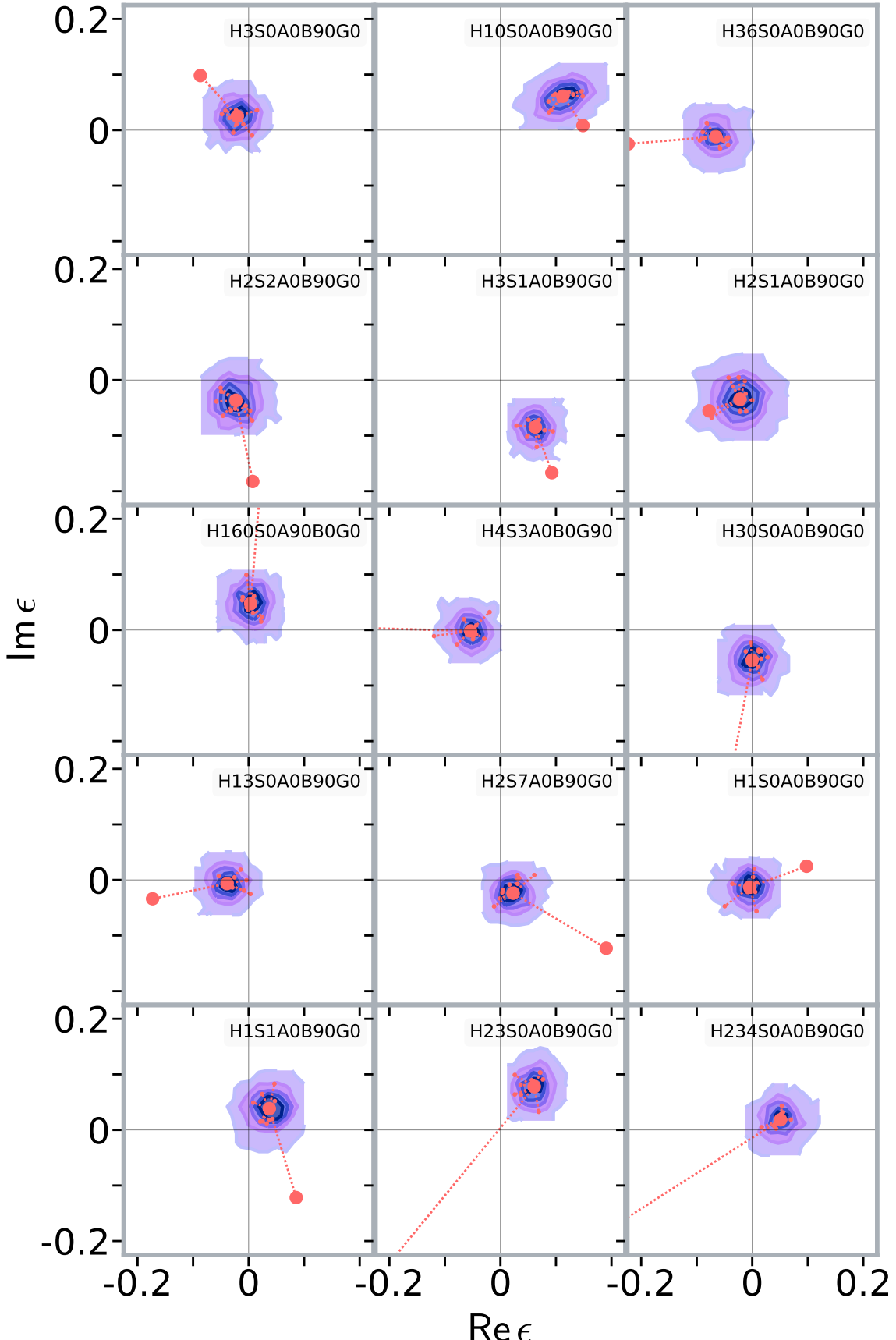


**Figure 4.9:** Complex ellipticity model distribution within each ensemble model, compared to the actual complex ellipticity of the SEAGLE-simulated lenses. The ellipticity of the SEAGLE lens is indicated with a large red dot which is connected to a graph with a center node indicated with another red dot representing the ellipticity of the model's ensemble average. The graphs leaf nodes are 20 randomly sampled points from the ensemble. In most cases, the models are too round, however their position angles roughly match.

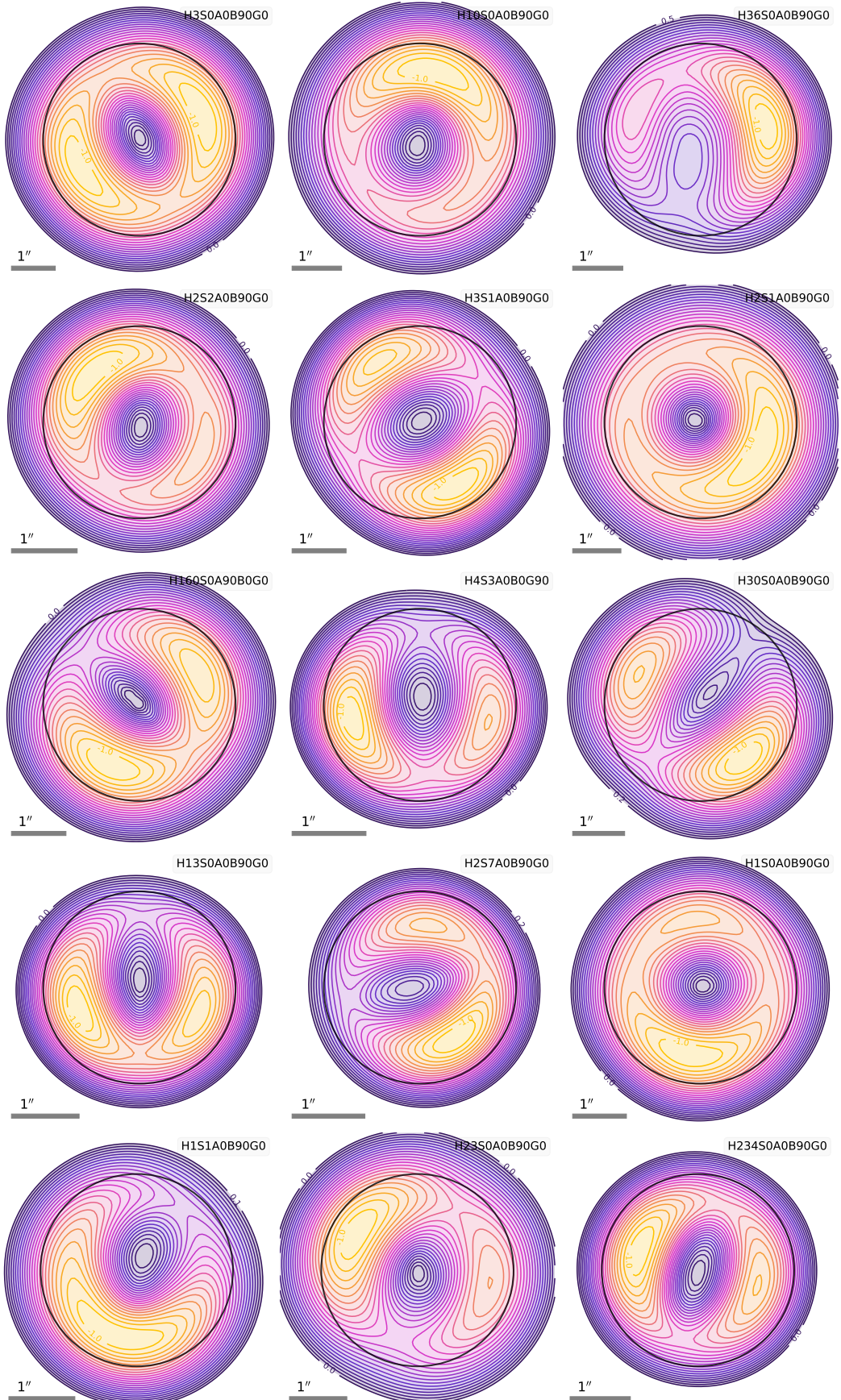


**Figure 4.10:** The actual Roche potentials of the SEAGLE-simulated lenses. The black circle indicates the area within which the scalar product (4.14) was evaluated. The potentials were shifted and scaled such that the center has a value of 0, and the global minimum a value of -1. This way, they offer a convenient way of comparing different models with the effect of the steepness degeneracy taken out.

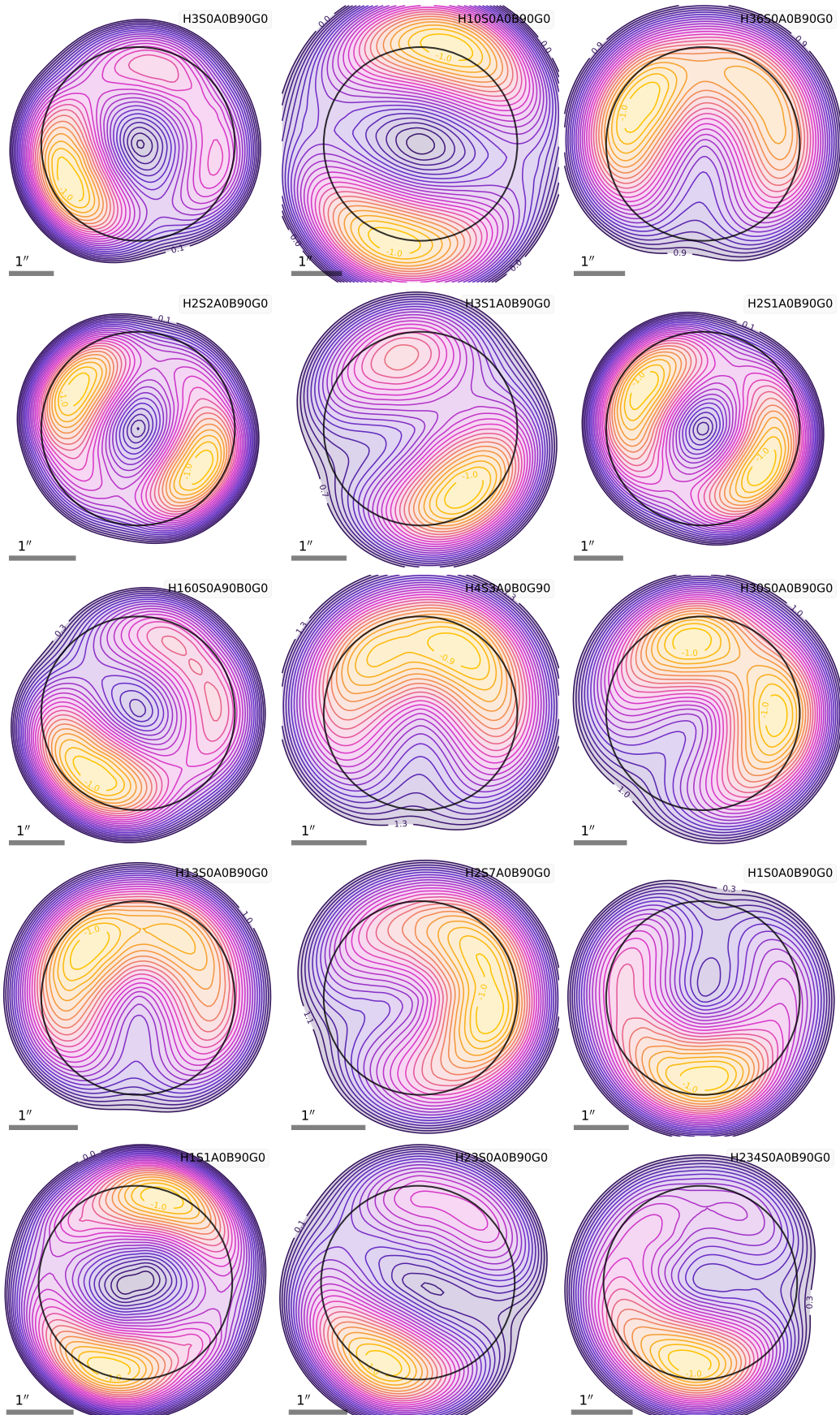


**Figure 4.11:** The Roche potentials of the 15 reconstructed lenses using the ensemble averaged model. All the scales are identical to the corresponding pictures in Figure 4.10.

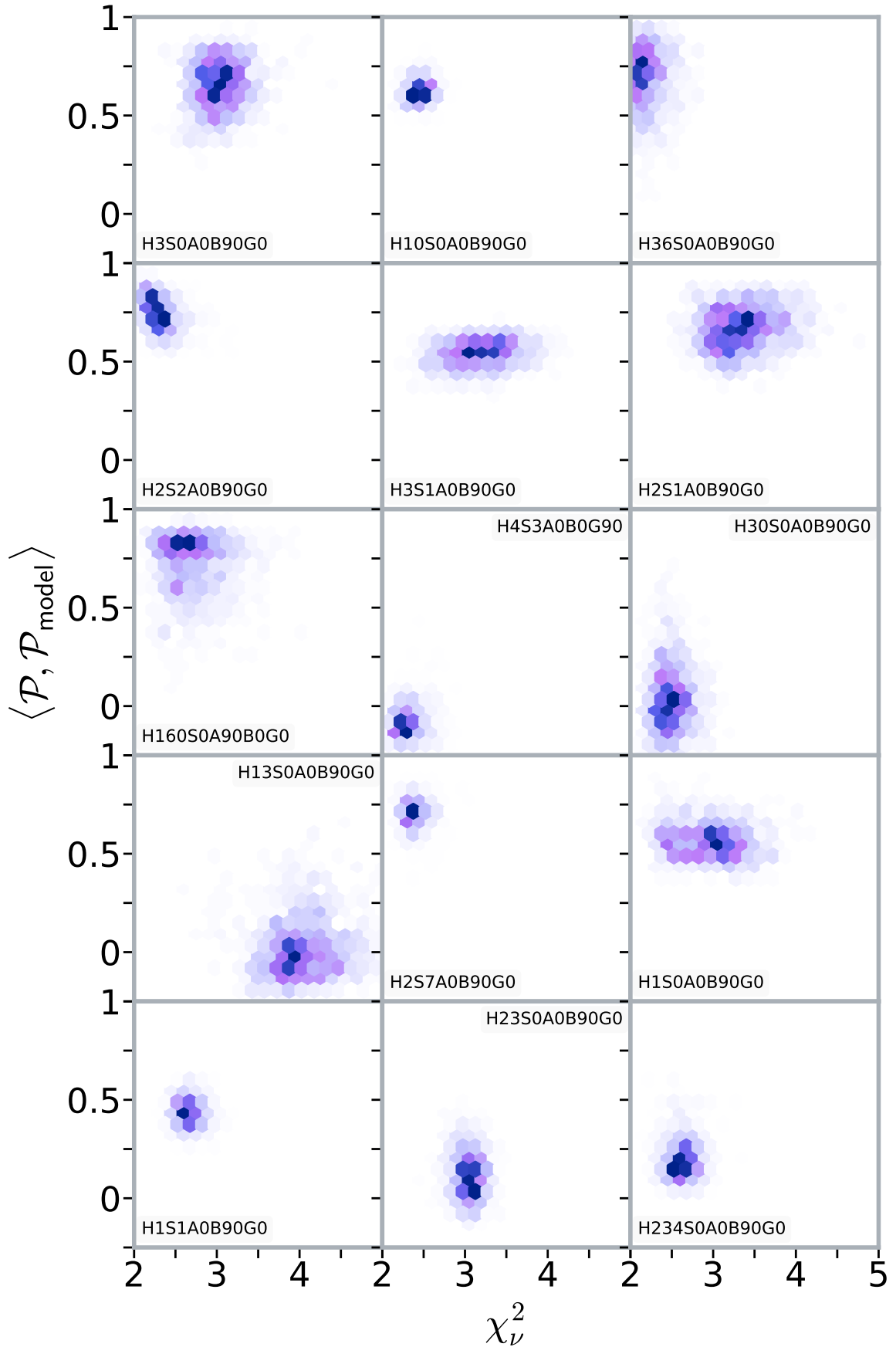


**Figure 4.12:** Hex-binned plots of distributions of reduced  $\chi_{\nu}^2$  from the lens image reconstructions against the distribution of the scalar product of Roche potentials for each ensemble model, see equations (4.11) and (4.14). Particularly good lens recovery is indicated by a scalar product close to 1 and a low  $\chi_{\nu}^2$ .



# MATCH

# 5

Original title:

## A NEW STRATEGY FOR MATCHING OBSERVED AND SIMULATED LENSING GALAXIES

Philipp Denzel<sup>1,2</sup>, Sampath Mukherjee<sup>3</sup>, Prasenjit Saha<sup>2,1</sup>

1 Institute for Computational Science, University of Zurich, 8057  
Zurich, Switzerland

2 Physics Institute, University of Zurich, 8057 Zurich, Switzerland

3 STAR Institute, Quartier Agora - Allée du six Août, 19c B-4000  
Liège, Belgium

5.1 Introduction . . . . .	101
5.2 The plausible-match method	102
Data adaptation . . . . .	103
Synthetic images . . . . .	104
5.3 SEAGLE . . . . .	106
A Constant Feedback (FB-const) . . . . .	107
Temperature variation in AGN heating (AGNdT8) . . . . .	107
5.4 The observed systems . . . . .	108
SDSSJ0029–0055 . . . . .	108
SDSSJ0737+3216 . . . . .	109
SDSSJ0753+3416 . . . . .	109
SDSSJ0956+5100 . . . . .	109
SDSSJ1051+4439 . . . . .	110
SDSSJ1430+6104 . . . . .	110
SDSSJ1627–0053 . . . . .	110
5.5 Results . . . . .	111
Images . . . . .	111
Source reconstructions . . . . .	112
Mass maps . . . . .	112
Lensing Roche potentials . . . . .	113
5.6 Discussion . . . . .	113
5.7 Figures . . . . .	115

Submitted to:

*Monthly Notices of the Royal Astronomical Society*

## Abstract

The study of strong-lensing systems conventionally involves constructing a mass distribution that can reproduce the observed multiply-imaging properties. Such mass reconstructions are generically non-unique. Here we present an alternative strategy: instead of modelling the mass distribution, we search cosmological galaxy-formation simulations for plausible matches. In this paper we test the idea on seven well-studied lenses from the SLACS survey. For each of these, we first pre-select a few hundred galaxies from the EAGLE simulations, using the expected Einstein radius as an initial criterion. Then, for each of these pre-selected galaxies, we fit for the source light distribution, while using MCMC for the placement and orientation of the lensing galaxy, so as to reproduce the multiple images and arcs. The results indicate that the strategy is feasible, and even yields relative posterior probabilities of two different galaxy-formation scenarios, though these are not statistically significant yet. Extension to other observables, such as kinematics and colours of the stellar population in the lensing galaxy, is straightforward in principle, though we have not attempted it yet. Scaling to arbitrarily large numbers of lenses also appears feasible. This will be especially relevant for upcoming wide-field surveys, through which the number of galaxy lenses will rise possibly a hundredfold, which will overwhelm conventional modelling methods.

## 5.1 Introduction

Four decades after the first discovery by Walsh et al. [7], galaxies exhibiting strong gravitational lensing seem almost commonplace. The SLACS sample [Sloan Lens ACS; 233–235] alone has over a hundred strong lensing galaxies. The next generation of wide-field surveys (LSST/Rubin from the ground, and Euclid and WFIRST/RST in space) promise many more. Extrapolation from small fields that have been surveyed at different resolutions indicate [see e.g., 236] that  $> 100'000$  strong-lensing galaxies await discovery. Many techniques for finding lenses in surveys, ranging from crowdsourcing [205] to neural networks [e.g., 237], have been developed in recent years, and one can confidently expect that  $10^5$  strong-lensing galaxies will be discovered.

Meanwhile, the past decade has seen significant progress on the structure and formation of galaxies. Within the  $\Lambda$ CDM paradigm, there is general agreement regarding the growth of density perturbations under gravity, from the level observed in the cosmic microwave background to the formation of dark-matter halos. The subsequent processes of star formation and the resultant feedback are less well understood and require sub-grid models to simulate, but still the galaxies formed in simulations like Illustris [160], FIRE [Feedback In Realistic Environments; 57], and EAGLE [Evolution and Assembly of GaLaxies and their Environments; 159] are much more credible than previous generations of simulated galaxies. The SEAGLE pipeline [Simulating EAGLE LEnses; 211] producing simulated lenses from EAGLE is of particular interest in this work. In addition to galaxy-formation simulations, there are also distribution-function models for galaxies, such as from AGAMA [action-based galaxy modelling architecture; 238], which provide self-consistent phase-space distributions for dark matter, stars and gas.

One would like to compare lensing observations with galaxy simulations. Let us first consider this task in a rather abstract way. Let  $F$  be some galaxy-formation scenario, and let  $D$  represent the observational data. In Bayesian terms, the posterior probability of  $F$  after comparison with  $D$  would be

$$P(F | D) = \frac{P(D | F) P(F)}{P(D)} \quad (5.1)$$

where  $P(F)$  represents the probability of  $F$  before the data, and  $P(D)$  is the probability of the data marginalized over all possible  $F$ . The factors  $P(F)$  and  $P(D)$  cancel if we compare two formation scenarios with equal prior probability, so it is really  $P(D | F)$  that is of interest. This quantity is given by the marginalisation

$$P(D | F) = \sum_g P(D | g) P(g | F) \quad (5.2)$$

where  $g$  represents galaxy properties. There will also be nuisance parameters (call these  $v$ ), such as the orientation of the ellipticity of a galaxy, which are also to be marginalised over, thus

$$P(D | g) = \sum_v P(D | g, v) P(v). \quad (5.3)$$

Conventional lens modelling consists of constructing  $g$  so as to optimise

[7]: Walsh et al. (1979)

[233]: Bolton et al. (2006)

[234]: Bolton et al. (2008)

[235]: Shu et al. (2017)

[236]: Collett (2015)

[205]: Marshall et al. (2016)

[160]: Vogelsberger et al. (2014)

[159]: Crain et al. (2015)

[211]: Mukherjee et al. (2018)

[238]: Vasiliev (2018)

[24]: Young et al. (1980)  
[239]: Yıldırım et al. (2020)

[240]: Wagner et al. (2019)  
[48]: Küng et al. (2018)

[141]: Saha et al. (2006)  
[241]: Barnabè et al. (2009)  
[50]: Coles et al. (2014)  
[53]: Ding et al. (2020)

[77]: Denzel et al. (2020)  
[58]: Denzel et al. (2020)

$P(D | g)$ . Here there are two basic approaches. One is to assume some parametric form for the lensing mass distribution and fit to the data. The idea goes back to the very first lens-modelling paper [24]. Recent parametric lens models [such as 239] are more elaborate, but still much simplified compared to a simulation from AGAMA or SEAGLE. Alternatively, one can let the lensing mass distribution be free-form, and sample the abstract space of mass distributions that fit the data. This approach is more common in cluster lensing [see e.g., 240] but also used in galaxy lensing [e.g., 48]. Free-form mass models are more complex, but they are not necessarily dynamically plausible. Neither style of lens modelling has much input from  $P(g | F)$ . Some comparisons of lens models against dynamical simulations of galaxies have been done [e.g. 50, 53, 141, 241], as have some model-independent comparisons of image statistics with substructure in  $\Lambda$ CDM [242], but all of these provide only qualitative information with respect to  $P(g | F)$ .

In this work we attempt for the first time a direct comparison of lensing data and galaxy-formation without conventional lens models. We use SEAGLE lenses as samples of  $P(g | F)$  from two different galaxy-formation scenarios. We then formulate  $P(D | g, \nu)$  so that a procedure for fitting source brightness distributions [developed earlier for conventional lens modelling 58, 77] can be repurposed. This allows us to find EAGLE galaxies that can account for the observed images in a small test sample of seven SLACS lenses (see Table 5.2). As this work is intended as proof of concept, we do not include data other than multiple images from extended sources.

The following Section 5.2 introduces what we may call the  $P(D | F)$  method. The subsequent Section 5.3 details the SEAGLE pipeline and summarizes how the catalogue of surface-density maps was compiled. The selected test-case lenses from the SLACS survey are presented in Section 5.4, and the results of these tests are reported in Section 5.5. Finally, a summary and discussion, in particular about possible expansions and applications of the lens-matching approach are given in Section 5.6.

## 5.2 The plausible-match method

To go beyond the simple abstractions above and discuss the actual method, let us rewrite Eqs. (5.2) and (5.3) as

$$P(D | F) \approx \sum_{s, \xi} P(I^{\text{obs}} | \alpha, s) P(\alpha | \xi, F) P(s, \xi). \quad (5.4)$$

Rather than galaxy properties  $g$  in general, we are concerned with a lensing deflection field  $\alpha$ . The  $\nu$  parameters consist of (a) location and rotation parameters (say  $\xi$ ) to produce  $\alpha$  from a simulated EAGLE galaxy, and (b) the unlensed brightness distribution  $s$  at the source redshift. The priors  $P(s, \xi)$  we take as flat. Hence it is on the factors  $P(D | \alpha, s)$  and  $P(\alpha | \xi, F)$  that we must concentrate.

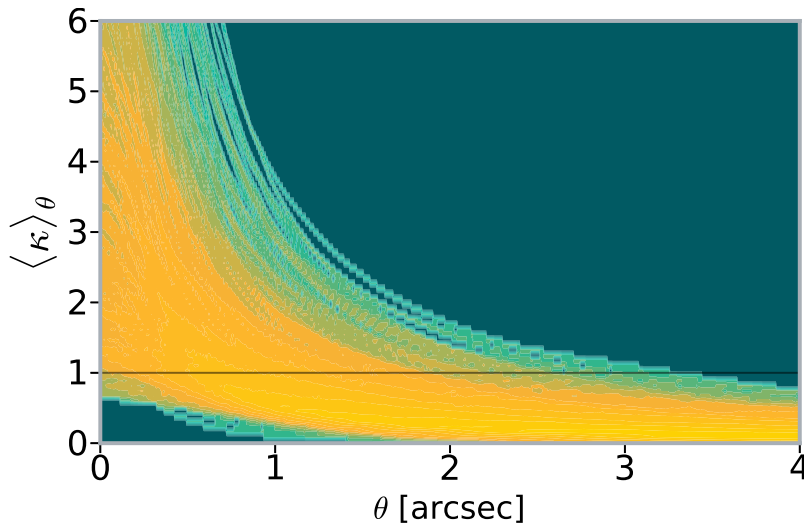


**Figure 5.1:** The distribution of radial profiles of the mean enclosed  $\langle \kappa \rangle$  within a given projected radius from the centre of the galaxies, for the entire catalogue, assuming  $z_L = 0.23, z_S = 0.8$ . The horizontal line at  $\kappa = 1$  indicates the notional Einstein radii.

### 5.2.1 Data adaptation

We now describe the ingredients for the factor

$$P(\boldsymbol{\alpha}, |\xi, F)$$

in equation (5.4).

The convergence map (that is, the lensing mass distribution in dimensionless form) is given by the usual projection of the 3D mass density as

$$\kappa(\boldsymbol{\theta}, \xi) = \frac{4\pi G}{cH_0} \frac{d_{LS}d_L}{d_S} \int \rho(\boldsymbol{\theta}, \xi, z) dz. \quad (5.5)$$

Here  $\boldsymbol{\theta}$  is the angle on the observer's sky,  $d_{LS}$  is the dimensionless angular-diameter distance from the lens to the source,  $d_L$  and  $d_S$  are analogous, and  $\xi$  represents the location and orientation of the 3D density  $\rho(\boldsymbol{\theta}, z)$ . A conventional  $\Lambda$ CDM cosmology is assumed.

In this work, we have limited the analysis to two galaxy-formation scenarios from the EAGLE simulations (details are in Section 5.3 below). From the two simulations, SEAGLE projected each of 554 simulated galaxies along three orthogonal axes to produce maps of  $\kappa(\boldsymbol{\theta})$  for the fiducial redshift values  $z_L = 0.23$  and  $z_S = 0.8$ . The  $\kappa$  maps have  $161 \times 161$  square pixels with a pixel size of  $0.05\text{arcsec}$ , yielding an angular size of about  $8\text{arcsec} \times 8\text{arcsec}$  for an entire map. The  $\kappa$  distributions differ in size and in shape. Figure 5.1 shows the distribution of mean enclosed  $\kappa$  as a function of radial distance from lens centre for the entire catalogue. The notional Einstein radius is the value of  $\theta_E$  for which  $\langle \kappa \rangle_{\theta_E} = 1$ . About 20 mass maps in the catalogue are always below  $\kappa = 1$  and hence are not strongly lensing for  $z_L = 0.23, z_S = 0.8$ . But most of the galaxies can produce multiple images, and the Einstein radii go up to  $3.15\text{arcsec}$ .

The convergence maps are then rescaled from  $z_L = 0.23, z_S = 0.8$  to the redshift values corresponding to each of the test-case lens system listed in Table 5.1. A subset of a few hundred  $\kappa$  maps with Einstein radius in the expected range for each system was then selected for further processing.

The next step was the computation of the lens potential  $\psi(\boldsymbol{\theta}) = 2\nabla^{-2}Q(\boldsymbol{\theta})$ . To reduce the computational time required, the  $\kappa$  maps were discretised to  $23 \times 23$  tiles. The potential is then expressed as

$$\psi(\boldsymbol{\theta}) = 2 \sum_n \kappa_n \nabla^{-2} Q(\boldsymbol{\theta} - \boldsymbol{\theta}_n) \quad (5.6)$$

where  $\kappa_n$  is the density of the  $n$ -th tile and  $Q(\boldsymbol{\theta} - \boldsymbol{\theta}_n)$  is the contribution of a square tile with constant  $\kappa = 1$  located at  $\boldsymbol{\theta}_n$ . The functional form of  $Q(\boldsymbol{\theta})$  is given in AbdelSalam et al. [142]. Note that only the mass distribution is reduced in resolution in this way, but  $\boldsymbol{\theta}$  and  $\psi(\boldsymbol{\theta})$  can still be evaluated at any desired resolution. The effect of the approximation (5.6) is expected to be very small.

[142]: AbdelSalam et al. (1998)

Once the lens potential is known we have the deflection angle as

$$\boldsymbol{\alpha}(\boldsymbol{\theta}) = \nabla \psi(\boldsymbol{\theta}). \quad (5.7)$$

### 5.2.2 Synthetic images

We now consider the factor  $P(I^{\text{obs}} \mid \boldsymbol{\alpha}, s)$  in equation (5.4).

As a result of the deflection (5.7) a light ray originating at a source at  $\boldsymbol{\beta}$  on the sky will be observed at  $\boldsymbol{\theta}$  which is related to  $\boldsymbol{\beta}$  by the usual lens equation

$$\boldsymbol{\beta} = \boldsymbol{\theta} - \boldsymbol{\alpha}(\boldsymbol{\theta}). \quad (5.8)$$

The lens equation amounts to a mapping  $L(\boldsymbol{\theta}, \boldsymbol{\beta})$  between the source and image planes, which can be discretised as a matrix. Any given  $\boldsymbol{\theta}$  corresponds to a unique  $\boldsymbol{\beta}$ , whereas a given  $\boldsymbol{\beta}$  may correspond to more than one  $\boldsymbol{\theta}$ . A source-brightness distribution  $s(\boldsymbol{\beta})$  produces an image-brightness distribution

$$I(\boldsymbol{\theta}) = \int L(\boldsymbol{\theta}, \boldsymbol{\beta}) s(\boldsymbol{\beta}) d^2\boldsymbol{\beta}. \quad (5.9)$$

The observed image brightness will involve a further convolution with the point-spread function (PSF)  $P(\boldsymbol{\theta} - \boldsymbol{\theta}')$  of the telescope and camera. The result

$$\bar{I}(\boldsymbol{\theta}) = \int P(\boldsymbol{\theta} - \boldsymbol{\theta}') I(\boldsymbol{\theta}') d^2\boldsymbol{\theta}' \quad (5.10)$$

we will call the synthetic image, and it is what will get compared with the data.

For the lens sample investigated here, appropriate PSFs have been employed which were modelled using `tinytim`\* [243].

[243]: Krist et al. (2011)

Assuming now that the detector noise is Gaussian with known  $\sigma_{\theta} \propto \sqrt{I^{\text{obs}}(\boldsymbol{\theta})}$  we take

$$P(I^{\text{obs}} \mid \boldsymbol{\alpha}, s) \propto \exp\left(-\frac{1}{2}\chi^2\right) \quad (5.11)$$

where

$$\chi^2 = \sum_{\boldsymbol{\theta}} \sigma_{\boldsymbol{\theta}}^{-2} [I^{\text{obs}}(\boldsymbol{\theta}) - \bar{I}(\boldsymbol{\theta}, \boldsymbol{\alpha}, s)]^2 \quad (5.12)$$

---

\*  <https://github.com/spacetelescope/tinytim>

From Eqs. (5.9) and (5.10) it is clear that the synthetic image  $\tilde{I}(\theta)$  is linear in the source-brightness distribution, even though it is completely non-linear in the mass distribution. Hence  $s(\beta)$  can be solved to optimise  $P(I^{\text{obs}} | \alpha, s)$  by linear least-squares. It is important, however, to mask the light from the lensing galaxy, since it is not part of  $I^{\text{obs}}(\theta)$ .

The fitting of synthetic images is the same as in conventional lensing modelling [our implementation is the same as in 58, 77], but plausible-matching requires a further issue to be solved, namely the alignment and orientation of the lens system. The nuisance parameters  $\xi = (p_{\text{rel}}, \phi_{\text{rel}})$ , where  $p_{\text{rel}}$  is the position,  $\phi_{\text{rel}}$  is the orientation of the mass map relative to the observation, needs to be marginalised out. The marginalisation is done using short Markov-Chain Monte-Carlo (MCMC) simulations. The result is an ensemble of plausible-matches, reminiscent of model ensembles in free-form lens modelling [50, 140] but having a different meaning, because they arise from galaxy-formation simulations.

The minimum of  $\chi^2$  in equation (5.12) need not correspond to a unique  $\alpha$ . In other words, very different galaxies can in principle produce identical synthetic images. This is the well-known problem of lensing degeneracies [for a review, see 76]. The plausible matching strategy automatically marginalises over simulated galaxies that are degenerate in the observables, so lensing degeneracies as such are not an obstacle to the method. If, however, the differences between galaxy-formation scenarios happen to be aligned along lensing degeneracies, lensing observables would be ineffective as discriminators between galaxy-formation models. Such a thing seems unlikely, but we cannot rule it out at present.

In total, 11634 MCMC simulations had to be executed until the solutions for all simulated galaxies and lens systems converged. This was relatively easily achieved within about 4–8 hours per lens through some optimisations and unfortunately some compromises. The inclusion of a PSF increases the non-sparseness of the synthetic-image mapping considerably, makes the generation of synthetics quite computationally intensive, and slows down the MCMC simulations by an average factor of  $\sim 50$ . Fortunately, initial tests showed that the omission of the PSF in equation (5.9) for this step caused acceptable differences. Since both the projected surface-density maps and cutouts from the observations have been centred well beforehand,  $p_{\text{rel}}$  never deviated from the centre by more than 0.05arcsec, which lead us to discard that parameter in the final stage. The convergence to optimal alignment rotation angles on the other hand was more relevant, especially for galaxies with high ellipticity, whereas for round galaxies the rotation angles were arbitrary and usually settled around  $0^\circ$ .

The subsequently described lens-matching method has been implemented in the public software `gleam`<sup>†</sup> (Gravitational Lens Extended Analysis Module) by PD. It is written in Python and thus comes with all of its flexibility and a large scientific library support. Computationally demanding tasks such as the calculation of potential gradients are alternatively also implemented in a mixture of C and Cython [231]. Similar to the lens modelling tool `GLASS`<sup>‡</sup> by Coles et al. [50], the module encompasses more general features, some of which are still in development, but

[77]: Denzel et al. (2020)

[58]: Denzel et al. (2020)

[140]: Saha et al. (2004)

[50]: Coles et al. (2014)

[76]: Wagner (2018)

[231]: Behnel et al. (2011)

[50]: Coles et al. (2014)

<sup>†</sup> GitHub repository: <https://github.com/phdenzel/gleam>

<sup>‡</sup> GitHub repository: <https://github.com/jpcoles/glass>

the lens-matching technique lies at its core. In particular, the synthetic imager described in Section 5.2.2 is implemented in the sub-module `gleam.reconsrc`.

The entire lens-matching method was intentionally kept relatively simple and lightweight in order to keep it scalable for a much bigger lens sample using larger catalogues and minimize the input required from the outside. The analysis presented here aimed for a proof-of-concept only. With a working basis, further refinements and improvements can easily be explored in isolation and afterwards properly implemented. In Section 5.6, we give some suggestions of what aspects could be improved first.

### 5.3 SEAGLE

[211]: Mukherjee et al. (2018)

[210]: Schaye et al. (2014)

[159]: Crain et al. (2015)

[213]: McAlpine et al. (2016)

[159]: Crain et al. (2015)

[223]: Mukherjee et al. (2019)

[211] introduced the SEAGLE pipeline to systematically study galaxy formation via simulated strong lenses from the EAGLE simulations [159, 210, 213]. SEAGLE used the GLAMER ray-tracing package [Gravitational Lensing with Adaptive Mesh Refinement; 219, 220] to create realistic lensed images and calculate all other lensing quantities used in their analysis. SEAGLE aims to investigate and possibly disentangle galaxy formation and evolution mechanisms by creating, modelling, and analysing simulated strong lens-galaxies to compare them with observations.

EAGLE is a suite of state-of-the-art hydrodynamical simulations that explored several feedback scenarios and model variations giving us a set of galaxy evolution scenarios to assess their impact on the present-day universe. Crain et al. [159] divided the simulations into two categories. The first comprises four simulations *calibrated* to yield the  $z = 0.1$  galaxy stellar mass function (GSMF) and central black hole (BH) masses as a function of galaxy stellar mass. The second category comprises simulations that each vary a single sub-grid physics parameter with respect to the Reference model but without considering whether they match the GSMF (i.e. they are not calibrated).

In Mukherjee et al. [223], using SEAGLE, the authors quantified that if the simulated lensed images are modelled similar to the observations, then the median total mass density slope of galaxies from an inefficient AGN feedback model (AGNdT8: Reference variation) and a constant feedback model (FBconst: Calibrated simulation) that becomes inefficient at denser environment gives slopes  $t=2.01$  and  $t=2.07$ , respectively, in good agreement with the observations of SLACS, SL2S (Strong Lensing Legacy Survey), and BELLS (Baryon Oscillation Spectroscopic Survey (BOSS) Emission-Line Lens Survey). Galaxies in the EAGLE Reference model (benchmark model), however, tend to have a steeper median total mass density slope ( $t=2.24$ ) than observed lens galaxies (i.e.  $t=2.08$  for SLACS,  $t=2.11$  for BELLS and  $t=2.18$  for SL2S).

The nomenclature of the SEAGLE-projected mass distributions in the catalogue depends on their halo, subhalo, and projection axis. A number following 'H' refers to the halo number, 'S' gives the subhalo, and letters 'A/B/G' refers to the projection the galaxy has undergone in Cartesian coordinates i.e.  $\alpha$ ,  $\beta$  and  $\gamma$  respectively. The feedback model denominations are prepended in this nomenclature.

For our analysis, we choose these two galaxy evolution scenarios (AGNdT8 and FBconst) as they are most realistic to the strong lensing observations. We briefly discuss the key features of these feedback models below.

In the calibrated simulations, the models differ in terms of their adopted efficiency of feedback associated with star formation, and how this efficiency depends upon the local environment. The general consensus shows that the properties of simulated galaxies are most sensitive to the efficiency of baryonic feedback [see e.g., 218, 244]. Below a certain resolution limit, the physical processes cannot be simulated via the dynamics of the particles. So they are incorporated via analytic prescriptions in all hydro-dynamic simulations including EAGLE. In EAGLE model variations, the efficiency of the stellar feedback and the BH accretion were calibrated to broadly match the observed local ( $z \approx 0$ ) GSMF. Also, several studies established that AGN feedback is a necessary ingredient for regulating the growth of massive galaxies [e.g. 218, 245, 246].

Below we briefly describe the EAGLE galaxy formation models which were used in this work.

[218]: Schaye et al. (2010)  
[244]: Vogelsberger et al. (2013)

[245]: Crain et al. (2009)  
[218]: Schaye et al. (2010)  
[246]: Haas et al. (2013)

### 5.3.1 A Constant Feedback (FBconst)

The simplest feedback model used in EAGLE is FBconst. In this calibrated model, independently from the local conditions, a fixed amount of energy per unit stellar mass is injected into the ISM. This fixed energy corresponds to the total energy discharged by type-II SNe ( $f_{\text{th}} = 1$ ). While the stellar feedback in this model was not calibrated, the model does reproduce the observables used for the calibration. Crain et al. [159] found that the thermal stellar feedback prescription employed in EAGLE becomes inefficient at high gas densities due to resolution effects [247]. Thus in this model, there is a lack of compensation for more energy at higher gas density. Thus the stellar feedback will be less effective in high-mass galaxies (where the gas tends to have higher densities) [159].

Schaye et al. [210] demonstrated that it is possible to calibrate the Reference model to reproduce the GMSF and the observed sizes (in different bands) of galaxies at  $z = 0.1$ . Crain et al. [159] conducted a series of simulations (listed in the lower section of Table 1 therein) for which the value of a single parameter was varied from that adopted in the Reference model. One of the parameters varied was AGN temperature.

[159]: Crain et al. (2015)  
[247]: Vecchia et al. (2012)  
[159]: Crain et al. (2015)  
[210]: Schaye et al. (2014)  
[159]: Crain et al. (2015)

### 5.3.2 Temperature variation in AGN heating (AGNdT8)

[210] have examined the role of the AGN heating temperature in EAGLE by adopting  $\Delta T_{\text{AGN}} = 10^{8.5}$  K and  $10^9$  K. They demonstrated that a higher heating temperature produces less frequent but more energetic AGN feedback episodes. They concluded it is necessary to reproduce the gas fractions and X-ray luminosities of galaxy groups. Brun et al. [248] also concluded that higher heating temperature yields more efficient AGN feedback. There are two Reference-model variation simulations with  $\Delta T_{\text{AGN}} = 10^8$  K (AGNdT8) and  $\Delta T_{\text{AGN}} = 10^9$  K (AGNdT9), besides the Reference model itself which adopted  $\Delta T_{\text{AGN}} = 10^{8.5}$  K. In massive

[248]: Brun et al. (2014)

[211]: Mukherjee et al. (2018)

galaxies, the heating events (less frequent but more energetic) are more effective at regulating star formation due to a higher heating temperature. AGNdT8 (AGNdT9) model has a higher (lower) peak star fraction compared to the Reference model. The reduced efficiency of AGN feedback, when a lower heating temperature is adopted, leads to the formation of more compact galaxies because gas can more easily accrete onto the centers of galaxies and form stars. Mukherjee et al. [211] showed that for galaxy-galaxy strong lenses, AGNdT8 produces closest analogs for SLACS. Thus, for this work, we use galaxies from the AGNdT8 simulation, in addition to the galaxies from the simpler FBconst model.

## 5.4 The observed systems

In order to test whether searching for plausible matches from EAGLE simulations is at all feasible, we selected a small sample of seven lens systems that have already been studied by other methods. The selection was based on three criteria. First, the system had to be clearly strongly lensed, with relatively easily identifiable images showing very clear evidence of multiple imaging. Second, the observations needed to have extended images and arcs with some imperfections (rather than point-like lensed quasars) so as to challenge the matching technique. Third, the sample had to be representative of a larger sample of lenses. The third criterion made it natural to choose from SLACS, and from the SLACS lenses of quality category “A” we selected seven, having a wide range of mean image radii, which is a rough proxy for Einstein radii. Figs. 5.2–5.8 in their top left panels show the lensed images in HST-image F814W bands. The most relevant information about the systems is listed in Table 5.1, including references to the discovery papers.

### 5.4.1 SDSSJ0029–0055

[234]: Bolton et al. (2008)

SDSSJ0029–0055 appears to be a relatively small, doubly lensing system observed on 12 September 2006. Initial reports by Bolton et al. [234] classify it as a single, early-type galaxy. The redshift of the foreground galaxy was spectroscopically measured to  $z_L = 0.2270$  and for the background source to  $z_S = 0.9313$ . It exhibits an almost fully closed ring which is relatively difficult to recognize due to the light pollution from the foreground galaxy. A de Vaucouleurs fit to the lensing galaxy gives a relatively high effective radius of 2.16 arcsec. It also has a well measured stellar velocity dispersion of  $\sigma_{\text{SDSS}} = 229 \pm 18 \text{ km/s}$ .

**Table 5.1:** Summary of the observed lensing systems. (1): Bolton et al. [234]; (2): Bolton et al. [233]; (3): Shu et al. [235]

Name	R.A. [hms]	Decl. [dms]	$z_l$	$z_s$	$\sigma_{\text{SDSS}}$ [km/s]	$R_{\text{eff}}$ [arcsec]	Reference
SDSSJ0029–0055	00:29:07.8	−00:55:50	0.23	0.93	$229 \pm 18$	2.16	(1)
SDSSJ0737+3216	07:37:28.5	+32:16:18	0.32	0.58	$310 \pm 15$	2.16	(2)
SDSSJ0753+3416	07:53:46.2	+34:16:33	0.14	0.96	$208 \pm 12$	1.89	(3)
SDSSJ0956+5100	09:56:29.8	+51:00:06	0.24	0.47	$299 \pm 16$	2.33	(2)
SDSSJ1051+4439	10:51:09.4	+44:39:08	0.16	0.54	$216 \pm 16$	1.66	(3)
SDSSJ1430+6104	14:30:34.8	+61:04:04	0.17	0.65	$180 \pm 15$	2.24	(3)
SDSSJ1627–0053	16:27:46.5	−00:53:57	0.21	0.52	$275 \pm 12$	2.08	(2)

The initial report presented a singular isothermal ellipsoid and light-traces-mass gravitational lens model which provided best fits using two source-plane components. However, the present work indicates that a single-component source (see second image in the left column in Figure 5.2) is also possible. The top image in Figure 5.2 in the left column shows the system from the HST/ACS-WFC1 observation (Advanced Camera System Wide Field Channel 1) using the F814W filter.

### 5.4.2 SDSSJ0737+3216

SDSSJ0737+3216 appeared in the first SLACS report by Bolton et al. [233]. A successive report [234] grades the quality of the single-multiplicity, early-type galaxy to be of type “A”. Its foreground and background redshifts were measured to  $z_L = 0.3223$  and  $z_S = 0.5812$  respectively. From SDSS spectroscopic data, a good estimate for the velocity dispersion of  $\sigma_{\text{SDSS}} = 338 \pm 17 \text{ km s}^{-1}$  was provided.

Parametric lens models from Bolton et al. [234] used two source-plane components to fit the astrometric data. The HST/ACS-WFC1 observation (on 21 September 2004) using the F814W filter is displayed in the top image in the left column of Figure 5.3. It shows two extended images of which the brighter image is most likely the product of two merged ones, and a point-like image connected via a dim arc, which would most likely classify it as a short-axis quad. Besides the initial modelling, Ferreras et al. [32] provided a free-form lens model for this lens system, along with a spatially resolved comparison to the stellar-mass surface distribution derived from population-synthesis models.

[233]: Bolton et al. (2006)

[234]: Bolton et al. (2008)

[234]: Bolton et al. (2008)

[32]: Ferreras et al. (2007)

### 5.4.3 SDSSJ0753+3416

The top image of the left column in Figure 5.4 shows SDSSJ0753+3416 (HST/ACS WFC1 F814W on 8 September 2010) as a clearly lensing system. It is a very interesting system with minimum eight (possibly even 12) lensed images of at least two sources. Shu et al. [235] reports ellipsoid lens models using even four source-plane components. Either way, this lens promises a much lower degree of degeneracy due to the high number of lensed images and sources.

[235]: Shu et al. (2017)

From the SDSS observations the lensing galaxy was classified as an early-type, single-multiplicity foreground galaxy with a well measured velocity dispersion  $\sigma_{\text{SDSS}} = 206 \pm 11 \text{ km s}^{-1}$ . The redshift estimates for the lens and source are  $z_L = 0.1371$  and  $z_S = 0.9628$ , respectively.

### 5.4.4 SDSSJ0956+5100

In the left column of Figure 5.5, the top image shows SDSSJ0956+5100 from the HST/ACS-WFC1 F814W observation from 1 November 2006. Bolton et al. [233] designates its lens an early-type, single foreground galaxy. The spectroscopic survey yielded a velocity dispersion of  $\sigma_{\text{SDSS}} = 299 \pm 16 \text{ km s}^{-1}$  and redshifts of  $z_L = 0.2405$  and  $z_S = 0.4700$  for the foreground and background source respectively.

[233]: Bolton et al. (2006)

The lens shows four lensed source images at various angular separations from the lensing galaxy in a short-axis quad configuration. Two of the images appear rather point-like and bright whereas the others are extended and fainter.

[32]: Ferreras et al. (2007)

It is another lens which was free-from modelled by Ferreras et al. [32]. The models predict it to be a rather high-mass galaxy with a total and stellar mass within the aperture image radius  $R_M$  of

$$M_{\text{tot}}(< R_M) = 66.4_{-16.7}^{+25.7} \cdot 10^{10} M_\odot \text{ and}$$

$$M_{\text{star}}(< R_M) = 41.8_{-4.0}^{+4.9} \cdot 10^{10} M_\odot,$$

where the aperture radius is  $2R_{\max} - R_{\min}$ , the difference of projected radii of twice the outermost and innermost lens images.

#### 5.4.5 SDSSJ1051+4439

[235]: Shu et al. (2017)

Shu et al. [235] reports SDSSJ1051+4439 as another early-type, single foreground-galaxy lens system. The SDSS data yields a velocity dispersion value of  $\sigma_{\text{SDSS}} = 216 \pm 16 \text{ kms}^{-1}$ ; the redshifts of the lens and background source are reported with  $z_L = 0.1634$  and  $z_S = 0.5380$  respectively. While the image shown in Figure 5.6 (left column, top panel) does not clearly indicate that the supposedly doubly lensing system is indeed lensing, its type is still classified as “A”.

#### 5.4.6 SDSSJ1430+6104

[235]: Shu et al. (2017)

Figure 5.7 (first image in the left column) depicts SDSSJ1430+6104 (HST/ACS-WFC1 F813W) as a very noisy lens system with faint lensed images, with considerable pollution by the host galaxy. Shu et al. [235] reports the early-type galaxy with a velocity dispersion value of  $\sigma_{\text{SDSS}} = 180 \pm 15 \text{ kms}^{-1}$ . The SDSS redshifts for the foreground and background objects are  $z_L = 0.1688$  and  $z_S = 0.6537$ .

The parametric, ellipsoid lens models use two source-plane components to fit the photometric data, with a total mass within the Einstein radius of  $1.02 \cdot 10^{11} M_\odot$ .

#### 5.4.7 SDSSJ1627–0053

[233]: Bolton et al. (2006)

On 12 March 2006, the HST/ACS-WFC1 observed SDSSJ1627–0053 as a double with an almost completely closed ring. Bolton et al. [233] reported it as an early-type foreground galaxy in a single-multiplicity system with redshifts  $z_L = 0.2076$  and  $z_S = 0.5241$ . The spectroscopically determined velocity dispersion is well measured with a value of  $\sigma_{\text{SDSS}} = 290 \pm 15 \text{ kms}^{-1}$ . A picture of the lens system can be found on the top panel of the left column in Figure 5.8.

**Table 5.2:** The most plausible match for each lens system. The SEAGLE nomenclature is explained in Section 5.3. The reduced  $\chi^2_{\nu}$  applies to the synthetic images,  $\phi_{\text{rel}}$  is the orientation about the line of sight with 68% interval from the MCMC. The last Einstein radii refer to the range among the 50 most plausible matches.

Lens	Best SEAGLE match	$\chi^2_{\nu}$	$\phi_{\text{rel}}[\text{°}]$	$\theta_E[\text{arcsec}]$
SDSSJ0029–0055	FBconst.HH44S1A0B90G0	2.6782	$1.0^{+0.1}_{-1.7}$	$0.92^{+0.07}_{-0.05}$
SDSSJ0737+3216	FBconst.HH21S1A90B0G0	3.4704	$267.1^{+3.7}_{-2.1}$	$1.12^{+0.28}_{-0.01}$
SDSSJ0753+3416	AGNdT8.HH1S9A0B0G90	2.7768	$358.7^{+0.1}_{-2.2}$	$1.31^{+0.03}_{-0.06}$
SDSSJ0956+5100	AGNdT8.HH17S1A90B0G0	3.4979	$152.8^{+2.9}_{-6.2}$	$1.64^{+0.12}_{-0.13}$
SDSSJ1051+4439	FBconst.HH48S3A0B90G0	2.6880	$225.1^{+1.7}_{-3.9}$	$1.52^{+0.47}_{-0.04}$
SDSSJ1430+6104	AGNdT8.HH3S1A90B0G0	2.4904	$3.3^{+1.0}_{-3.8}$	$1.16^{+0.35}_{-0.07}$
SDSSJ1627–0053	AGNdT8.HH205S0A90B0G0	2.3681	$359.3^{+0.1}_{-1.5}$	$1.39^{+0.18}_{-0.09}$

## 5.5 Results

The results on plausible matches for the seven lens systems considered are displayed in Figs. 5.2–5.8 and summarised in Table 5.2. Figs. 5.2–5.8 are devoted to one lens each, in the same order as in Tables 5.1 and 5.2. Each of these figures has eight panels, arranged as follows.

Observed image	Synthetic image
Source brightness	Residual Image
Lensing mass	Pixelized lensing mass
Lensing Roche potential	Mean enclosed convergence

As Table 5.2 indicates, the most-plausible match was sometimes from the galaxy-formation scenario FBconst and sometimes from AGNdT8. Considering the 50 most-plausible matches each lens, for J0753+3416 and J0956+5100 about 60% are from AGNdT8, whereas for the other lenses 65–70% are from FBconst. Thus, the results give a Bayesian evidence in the form

$$\frac{P(\text{AGNdT8} | D)}{P(\text{FBconst} | D)} \quad (5.13)$$

but the value is not significant yet.

We now discuss properties of the most-plausible matches as shown in Figs. 5.2–5.8.

### 5.5.1 Images

The top row of Figs. 5.2–5.8 shows the observed lensed images and the synthetic image from the most-plausible match. The lensing galaxy is masked out. The difference between these, scaled by the noise — in other words, the pixelwise  $\chi^2$  from equation (5.12) — is shown in the right panel of the second row.

For the MCMC over the orientation  $\phi_{\text{rel}}$  it is computationally simpler to rotate the image rather than the lens. As a result, there are some rotated-corner artifacts in the images, noticeable especially in Figure 5.6. These are, however, harmless, as only a circular region was considered for the  $\chi^2$  computation.

In all of the second-row right panels, it is evident that the contributions to  $\chi^2$  come mainly from an annular region where the multiply-imaged

features are. The black inner disc is of course just the masked-out lensing galaxy. The outer part in the  $\chi$  maps is dark (or at a lower level) because without multiple images the source brightness has the trivial solution

$$s(\boldsymbol{\theta} - \boldsymbol{\alpha}(\boldsymbol{\theta})) = I^{\text{obs}}(\boldsymbol{\theta}) \quad (5.14)$$

and then any contribution to  $\chi^2$  comes only because there are fewer pixels in the source plane than in the image plane. It would be better to consider only the multiply-imaged region when computing  $\chi^2$ , but it is not clear how to do so efficiently.

### 5.5.2 Source reconstructions

The left panel in the second row in each of Figs. 5.2–5.8 shows the reconstructed  $s(\boldsymbol{\beta})$  for the most-plausible match.

The source-fitting as implemented here does not guarantee that the reconstructed source will be blob-like and not a random scatter plot. However, plausible matching lenses are generally associated with plausible looking source maps. In cases where the data are more noisy the source plane also tends to be noisy; this is especially noticeable in J0737+3216, J1051+4439, and J1430+6104 (Figures 5.3, 5.6, and 5.7), where the bright specks from the data images (probably artifacts left by cosmic particles) also appear in the source plane. While most sources seem to be rather symmetric, J0753+3416 (Figure 5.4) and J0956+5100 (Figure 5.5) appear to be amorphous with multiple cores. This could be an indication of a merging system or multi-component source, however further investigation is needed to confirm this.

A curious artifact appears in the cases of J0956+5100 (Figure 5.5) and J1051+4439 (Figure 5.6). There the source appears to have bright edges in a curved diamond shape. The curved edges evidently correspond to the diamond caustic for four-image lenses, which correspond extreme magnification, and single pixels along these edges can map to large areas on the image plane. We conjecture that the source-fitting procedure is using this property of caustics to fit noise in the images.

### 5.5.3 Mass maps

The third row in each of Figs. 5.2–5.8 shows the  $\kappa$  maps from SEAGLE and the reduced-resolution  $\kappa_n$  maps that we actually used, for the most-plausible match. The dark contours indicate  $\kappa = 1$ .

Interestingly, while the catalogue did include many projected surface-densities with high ellipticity, the lens-matching approach seems to preferentially select rather round models. However, this of course depends on the selection of the lens system and considering to the light profiles of the lenses in the data, mass distributions with low ellipticity were to be expected. The mass models do, however, exhibit a moderate amount of substructure.

The bottom-right panel in each of Figs. 5.2–5.8 shows the mean enclosed density  $\langle \kappa \rangle_\theta$  within a given angular radius for the 10 most plausible matches in the sense of  $\chi^2$ . As in Figure 5.1  $\langle \kappa \rangle_\theta = 1$  is understood as the

Einstein radius. The value is well-constrained, even if we consider the 50 most-plausible matches (see Table 5.2).

### 5.5.4 Lensing Roche potentials

The bottom-left panels in Figs. 5.2–5.8 show another interesting quantity, a contour map of the *lensing Roche potential*

$$\mathcal{P}(\boldsymbol{\theta}) = \frac{1}{2}\boldsymbol{\theta}^2 - \psi(\boldsymbol{\theta}) \quad (5.15)$$

which we introduced in [77]. The lens equation (5.8) is equivalent to

$$\boldsymbol{\beta} = \nabla \mathcal{P}(\boldsymbol{\theta}) \quad (5.16)$$

and consequently the points where  $\nabla \mathcal{P} = 0$  are image locations from a source at  $\boldsymbol{\beta} = 0$ . These points are extrema (minima, maxima, and saddle-points) of  $\nabla \mathcal{P}$  and easy to discern on a contour map. The actual image positions will be somewhat different, depending on the details of  $s(\boldsymbol{\beta})$ , but nevertheless, the contours of the lensing Roche potential offer a simple confirmation that a plausible match is indeed a strongly lensing system, and that we have not simply stumbled upon the trivial solution (5.14).

## 5.6 Discussion

Mass reconstructions in gravitational lensing is in general non-unique. Even for strong-lensing clusters with tens of multiply-imaged systems over a range of redshifts, there is significant scatter among mass models even if they fit the data equally well [see e.g., 208]. For galaxy lenses the non-uniqueness of models is much more evident, and indeed has been known since the earliest days of lens modelling [249]. This facts suggests that the large catalogues of simulated galaxies in recent galaxy-formation simulations may contain plausible matches to individual observed lensing galaxies. In this work we search for and find plausible matches among EAGLE simulated galaxies to seven observed lensing galaxies from SLACS. The main computational part is to fit for (a) an orientation of a given simulated galaxy and (b) a source light distribution, such that the observed light distribution is reproduced. This is implemented in the new `gleam` code, but automated lens-modelling tools such as AutoLens [206] and Ensai [207] could probably also be adapted for the purpose, if required.

[208]: Meneghetti et al. (2017)

[249]: Young et al. (1981)

[206]: Nightingale et al. (2018)

The main conclusion of this work is that EAGLE — and presumably other comparable galaxy-formation simulations — contain plausible matches for observed lensing galaxies. Hence it appears feasible to use observed lensing galaxies as constraints on galaxy-formation scenarios, without conventional lens models. Obtaining statistically significant results, however, will need several issues to be addressed first, which we discuss briefly below.

1. In this work we have used single simulated galaxies, disregarding the environment and line-of-sight structures, and also approximated the projected mass as consisting of  $23 \times 23$  mass tiles. Furthermore, we have considered rotations only about three orthogonal candidate lines of sight, rather than arbitrary orientations in 3D. All these aspects of the implementation need to be improved, while keeping it efficient for the purpose of scaling up to larger lens samples.
2. The source reconstruction is another area that can be improved. The advantage of the procedure used in this work is that supervision at the level of individual lenses is not required, though this will not be true if the observation data is dominated by noise and extraneous light, because additional masks would be needed. The disadvantage of the current procedure is that the fitted source is just an arbitrary brightness map, and the principle of plausible matches is not being applied.
3. Since plausible-matching galaxies for any given lens always have very similar Einstein radii, even though they may differ in other ways, it is advantageous to pre-select the simulated galaxies to be within a suitable range of Einstein radii. In this work, we produced a conventional lens model first, but a more efficient method is desirable.
4. Provided the lensing galaxy is clearly visible in the data, stellar mass estimated from multi-band images using population synthesis [cf. [179](#)] could be incorporated into the likelihood  $P(D | g)$ . Stellar-maps from the simulations are, of course, known a priori. Ideally, the stellar light distribution would be subtracted from the entire observational data using models of the galaxy light.
5. Stellar kinematics would be an important ingredient in  $P(D | g)$ . Current simulations soften the gravitational dynamics on scales of order a kpc [see e.g., Table 2 in [210](#)], and it would be interesting to see if this strongly affects  $P(D | g)$ . It would also be interesting to see if an equilibrium galaxy-modelling framework like AGAMA, which resolves much smaller scales, yields higher  $P(D | g)$  than cosmological simulation.
6. Finally, although available for only a small fraction of lenses, time time-delays [for recent observations see [16](#)] would be interesting to incorporate in the plausible-match scheme. Lensing time delays are usually thought of as a way of measuring cosmological parameters, especially  $H_0$ . But the accuracy of the  $H_0$  inferences from lensing depends on how well  $P(g | F)$  of the universe is constrained. Hence time delays could be useful (if they turn out to be not the best way to measure  $H_0$ ) with cosmological parameter-values taken from other methods, as a way of constraining  $P(g | F)$ .

## Acknowledgments

We would like to thank Liliya L. R. Williams and Dominique Sluse for useful discussions and suggestions on how to improve this paper.

PD acknowledges support from the Swiss National Science Foundation. SM acknowledges the funding from the European Research Council (ERC) under the EUs Horizon 2020 research and innovation programme (COSMICLENS; grant agreement no. 787886).

This research is based on observations made with the NASA/ESA Hubble Space Telescope obtained from the Space Telescope Science Institute, which is operated by the Association of Universities for Research in Astronomy, Inc., under NASA contract NAS 5–26555. These observations are associated with programs #10886, #10174, #12210, #10494.

## Data availability

The data underlying this article are available at the STScI (<https://mast.stsci.edu/>; the unique identifiers are cited in the acknowledgements). The derived data generated in this research will be shared on request to the corresponding author, or can be replicated using the open-source software available at:  <https://github.com/phdenzel/gleam>.

## 5.7 Figures

This section contains all figures which are referenced in previous sections.

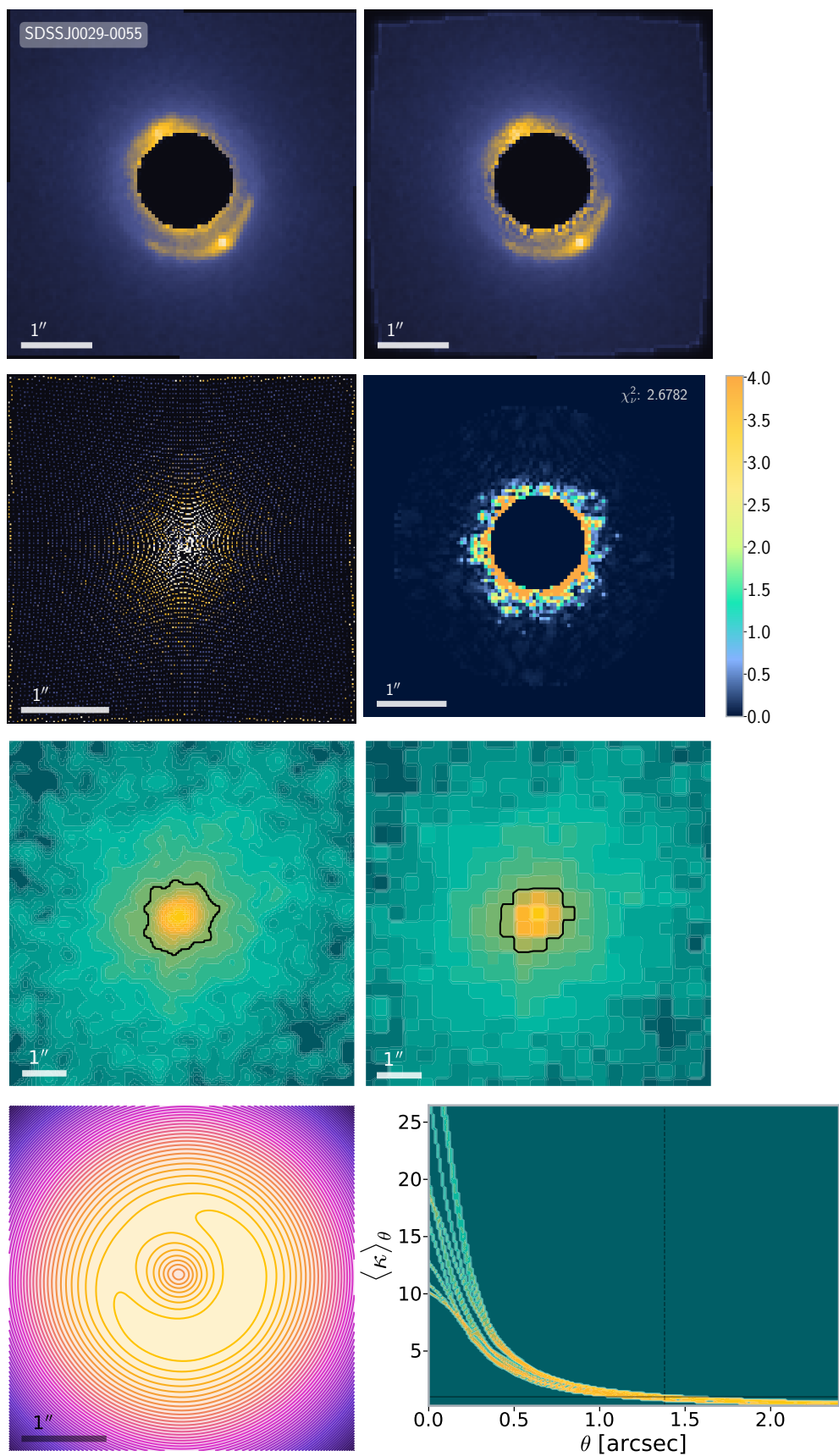


**Figure 5.2:** Results for SDSS J0029-0055. See Section 5.5 for details.

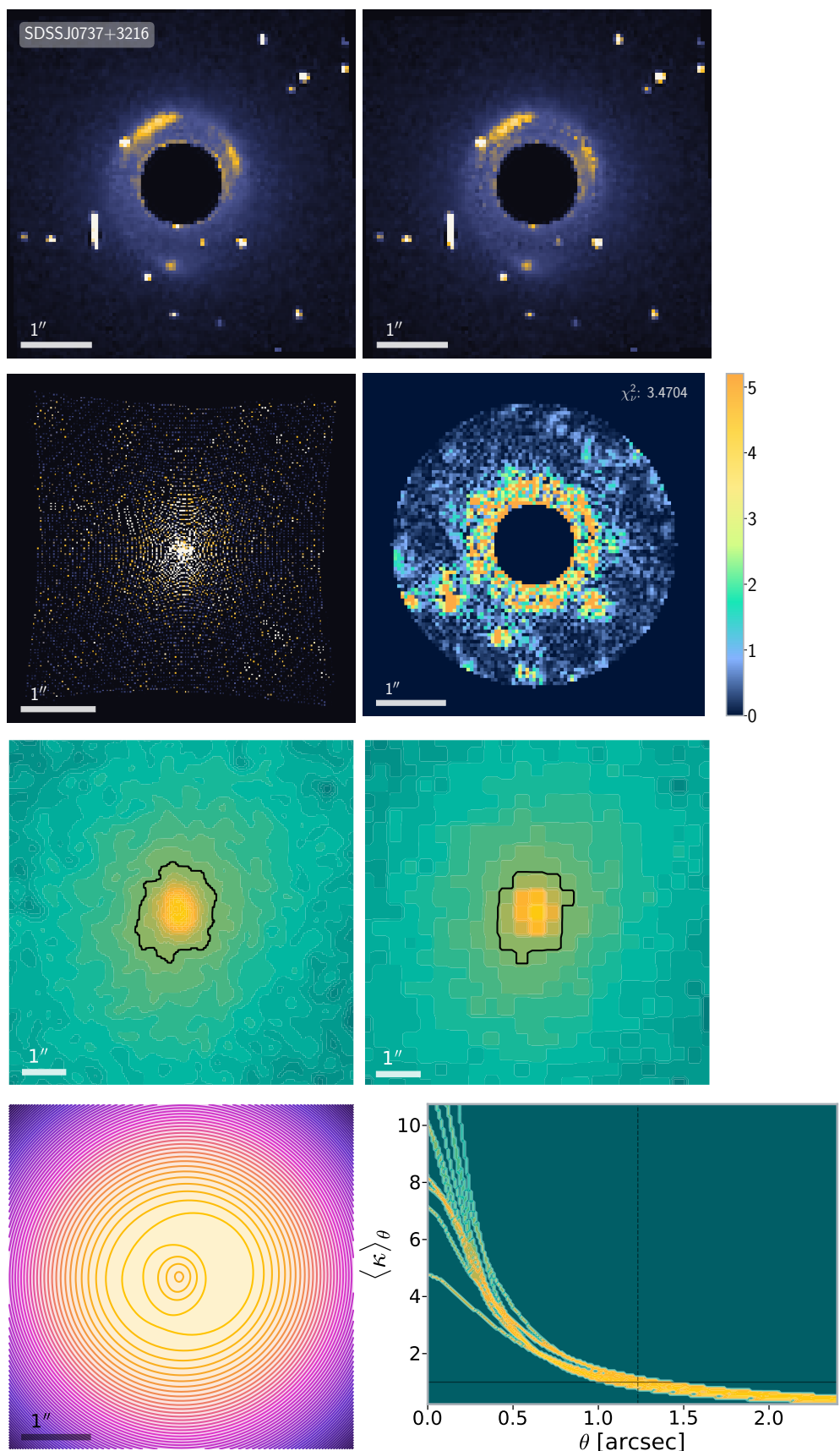
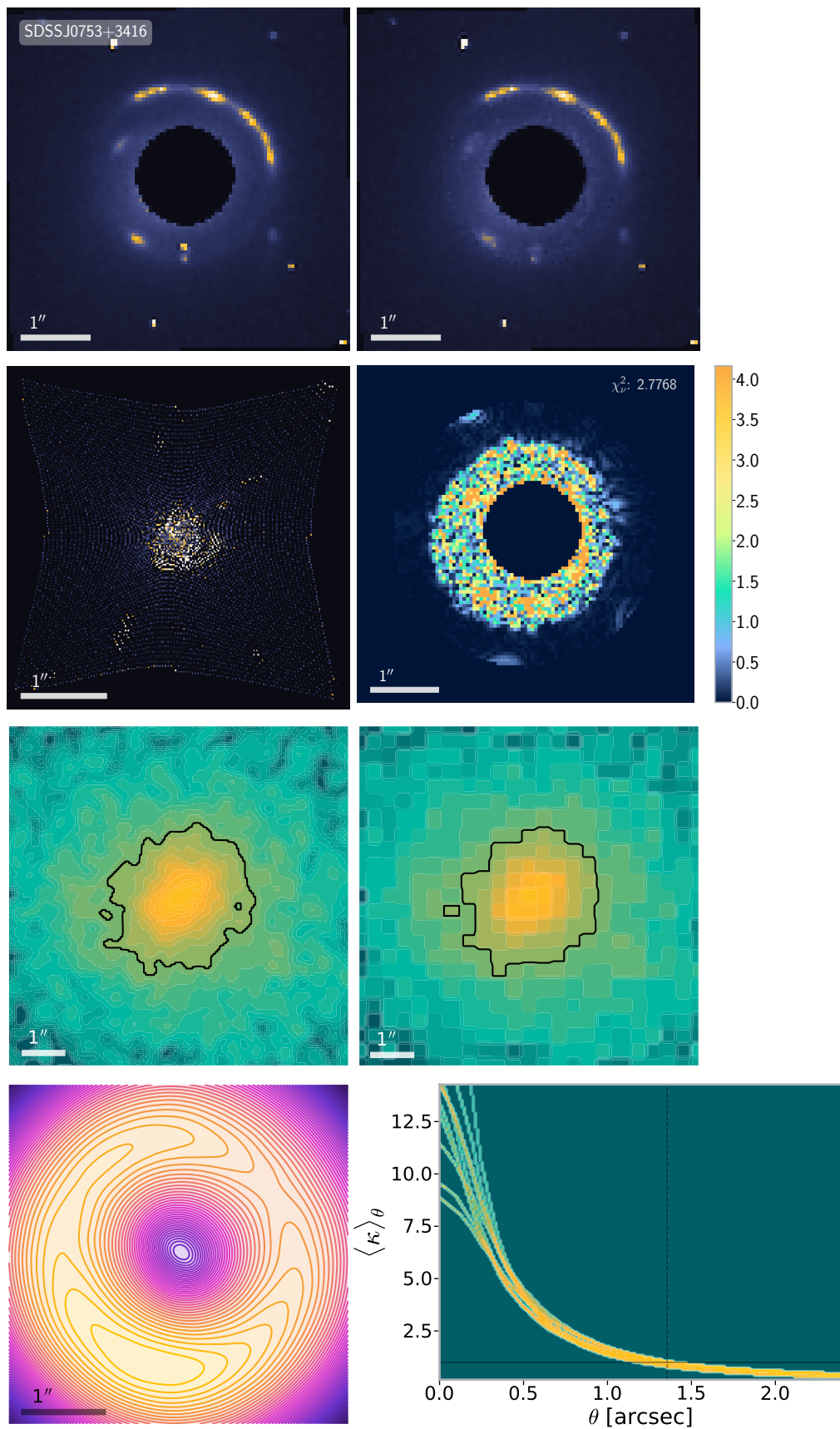
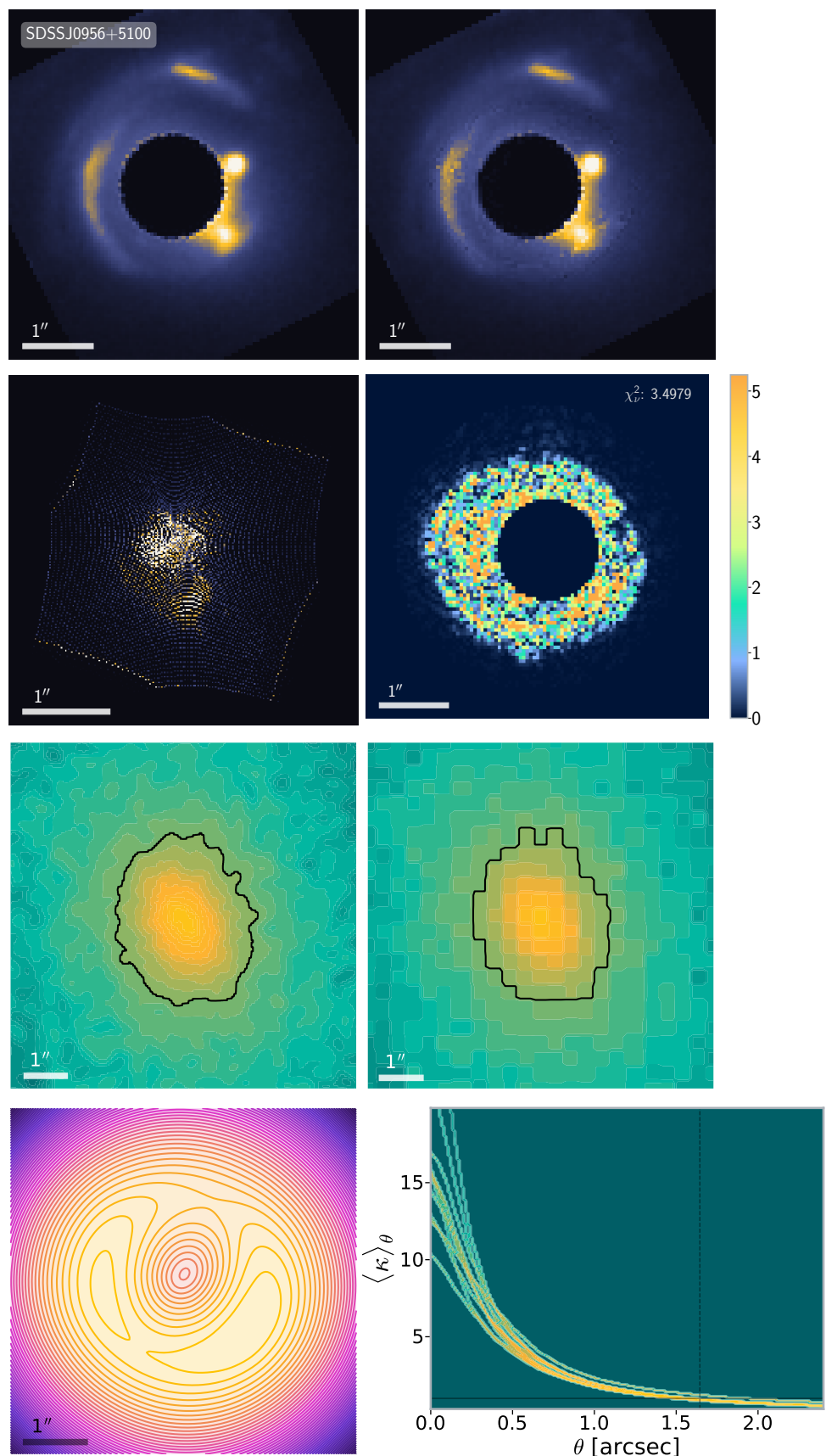


Figure 5.3: Results for SDSS J0737+3216. See Section 5.5 for details.



**Figure 5.4:** Results for SDSS J0753+3416. See Section 5.5 for details.



**Figure 5.5:** Results for SDSS J0956+5100. See Section 5.5 for details.

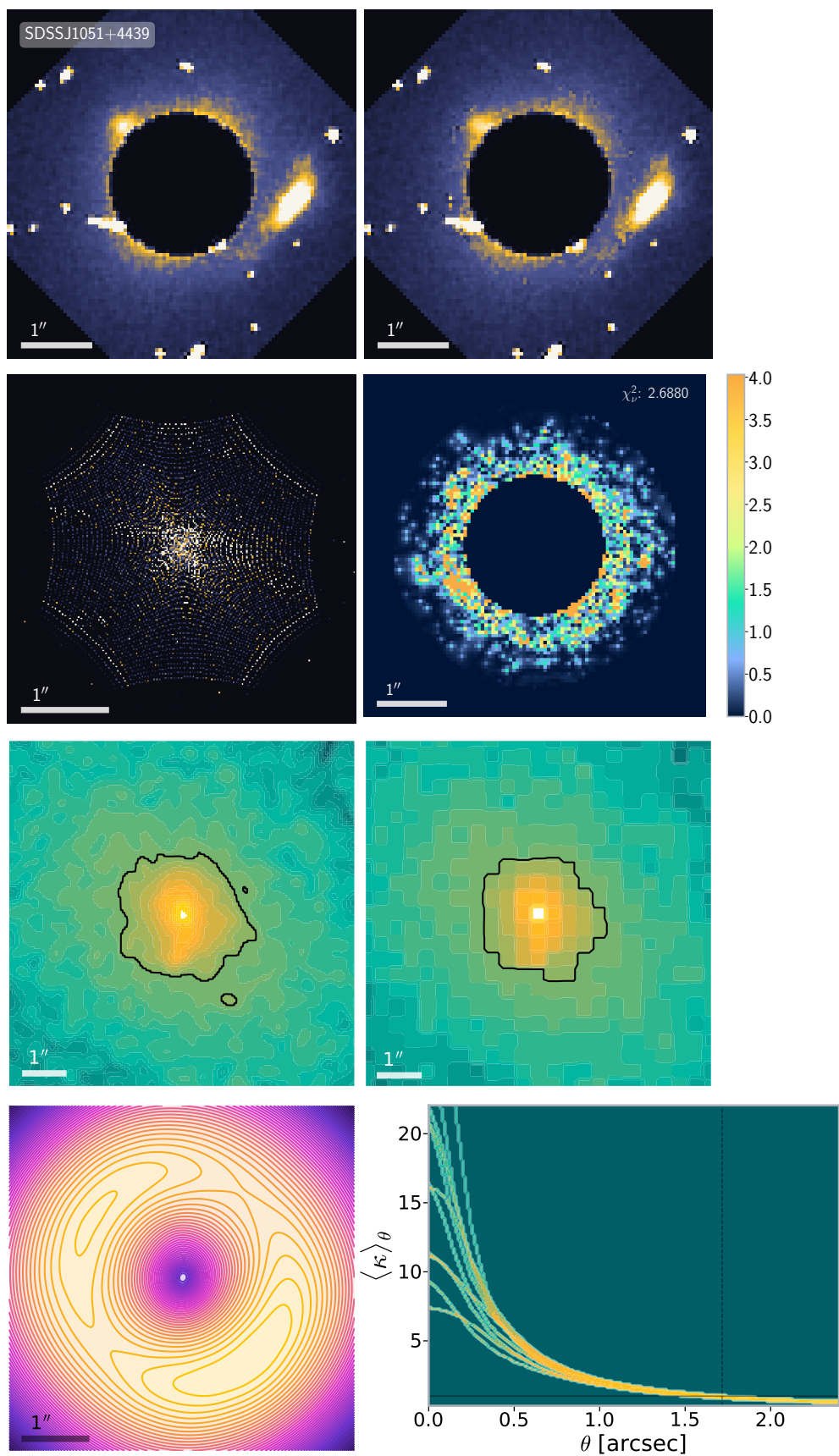


**Figure 5.6:** Results for SDSS J1051+4439. See Section 5.5 for details.

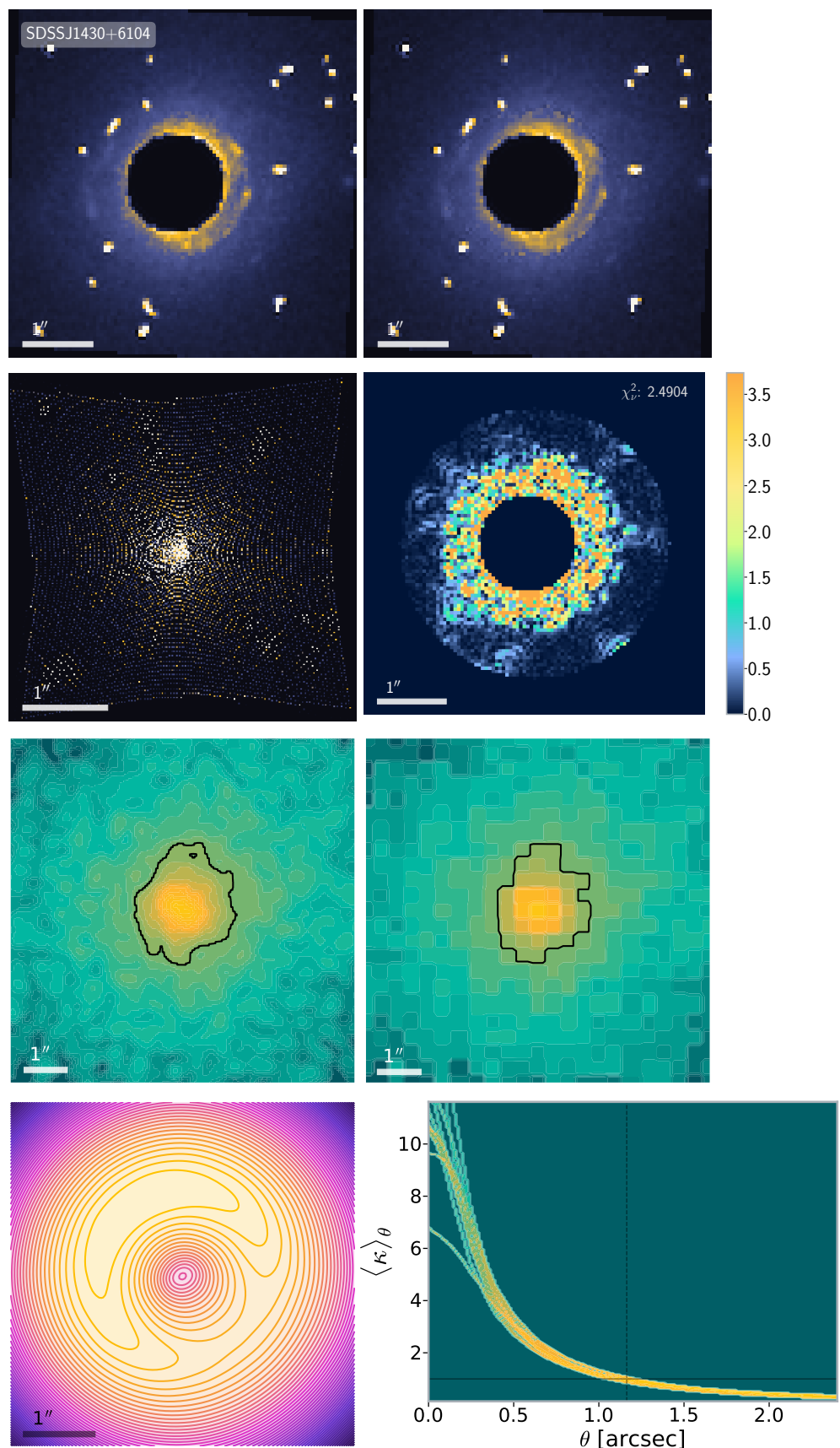


**Figure 5.7:** Results for SDSS J1430+6104. See Section 5.5 for details.

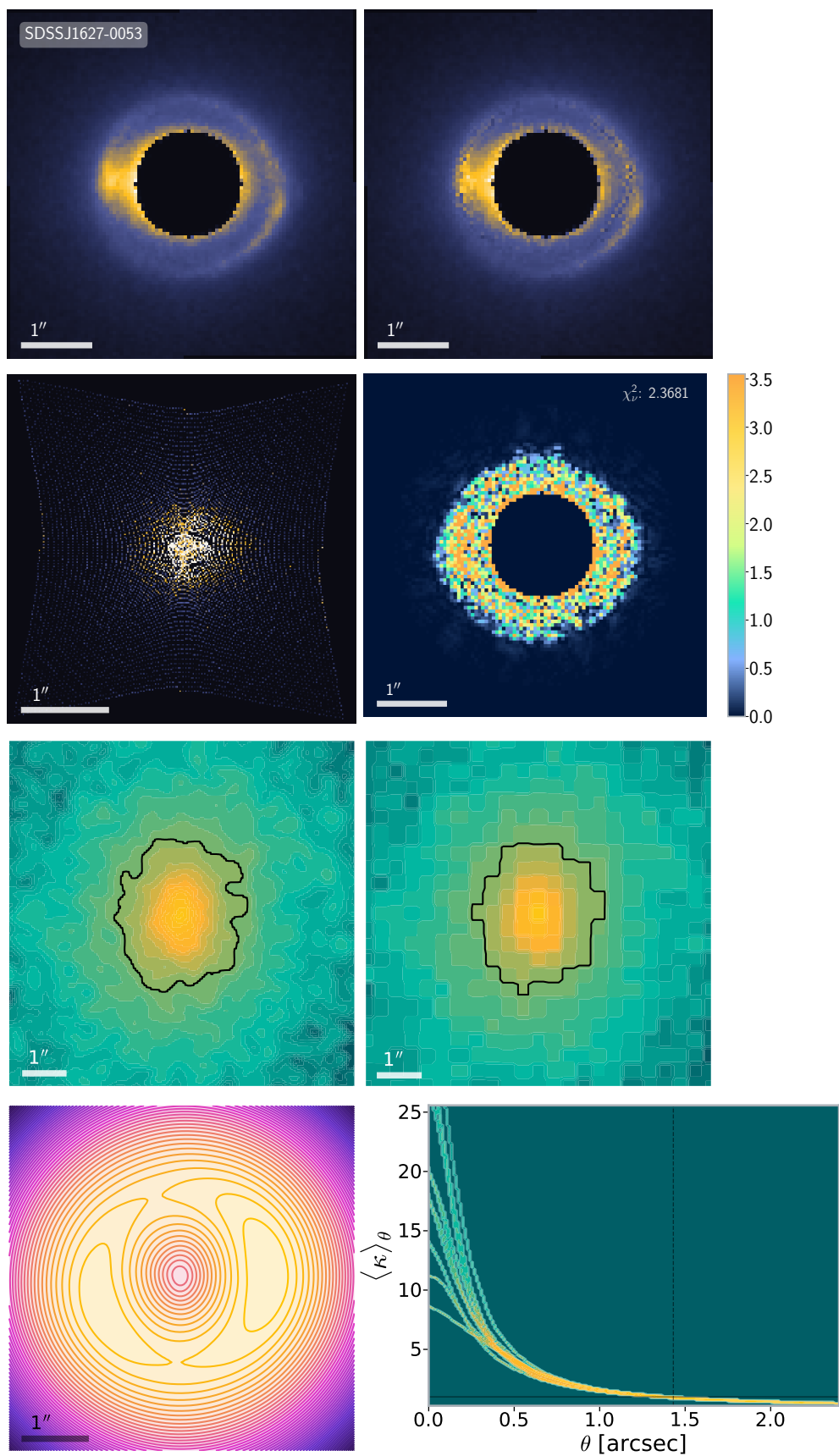


**Figure 5.8:** Results for SDSS J1627-0053. See Section 5.5 for details.

## **APPENDIX**



## Mathematical approximations

# A

Throughout this thesis some mathematical approximation were used, the following list contains in particular some useful unit conversions and estimates:

$$1 \text{ AU} \approx 500 \text{ lightsec} \quad (\text{A.1})$$

$$\tan(1 \text{ arcsec})^{-1} \approx 206265 \quad (\text{A.2})$$

$$1 \text{ lyr} \approx \pi \times 10^7 \text{ lightsec} \quad (\text{A.3})$$

$$GM_{\odot}/c^3 \approx 5 \times 10^{-6} \text{ s} \quad (\text{A.4})$$



# Bibliography

Here is the list of references in citation order.

- [1] Frank Watson Dyson, Arthur Stanley Eddington, and C. Davidson. 'IX. A determination of the deflection of light by the sun's gravitational field, from observations made at the total eclipse of May 29, 1919'. In: *Philosophical Transactions of the Royal Society of London. Series A, Containing Papers of a Mathematical or Physical Character* 220.571-581 (Jan. 1920), pp. 291–333. doi: [10.1098/rsta.1920.0009](https://doi.org/10.1098/rsta.1920.0009) (cited on page 1).
- [2] A. Einstein. 'Über den Einfluß der Schwerkraft auf die Ausbreitung des Lichtes'. In: *Annalen der Physik* 340.10 (1911), pp. 898–908. doi: [10.1002/andp.19113401005](https://doi.org/10.1002/andp.19113401005) (cited on page 1).
- [3] Philipp Denzel. *lensing.js: A javascript framework for mocking lenses*. [Online; accessed October 6, 2020]. 2018. URL: <https://github.com/phdenzel/lensing.js> (cited on page 1).
- [4] Prasenjit Saha and Paul A. Taylor. *The Astronomers' Magic Envelope*. Oxford University Press, July 2018 (cited on page 1).
- [5] Christopher J. Conselice et al. 'The Evolution of Galaxy Number Density at  $z < 8$  and its Implications'. In: *The Astrophysical Journal* 830.2 (Oct. 2016), p. 83. doi: [10.3847/0004-637x/830/2/83](https://doi.org/10.3847/0004-637x/830/2/83) (cited on page 2).
- [6] *Gravitational Lensing: Strong, Weak and Micro*. Jan. 2006 (cited on page 3).
- [7] D. Walsh, R. F. Carswell, and R. J. Weymann. '0957+561 A, B: twin quasistellar objects or gravitational lens?' In: *Nature* 279.5712 (May 1979), pp. 381–384. doi: [10.1038/279381a0](https://doi.org/10.1038/279381a0) (cited on pages 3, 71, 101).
- [8] Robert P. Kirshner. 'Hubble's diagram and cosmic expansion'. In: *Proceedings of the National Academy of Sciences* 101.1 (2004), pp. 8–13. doi: [10.1073/pnas.2536799100](https://doi.org/10.1073/pnas.2536799100) (cited on page 4).
- [9] E. Hubble. 'A relation between distance and radial velocity among extra-galactic nebulae'. In: *Proceedings of the National Academy of Sciences of the United States of America* 15 (1929), pp. 168–173. doi: [10.1073/pnas.15.3.168](https://doi.org/10.1073/pnas.15.3.168) (cited on pages 4, 43).
- [10] Adam G. Riess et al. 'Large Magellanic Cloud Cepheid Standards Provide a 1% Foundation for the Determination of the Hubble Constant and Stronger Evidence for Physics beyond  $\Lambda$ CDM'. In: *The Astrophysical Journal* 876.1 (May 2019), p. 85. doi: [10.3847/1538-4357/ab1422](https://doi.org/10.3847/1538-4357/ab1422) (cited on pages 6, 27, 28, 30, 52).
- [11] Planck Collaboration et al. *Planck 2018 results. VI. Cosmological parameters*. 2018 (cited on pages 6, 7, 17, 27, 28, 30, 52).
- [12] Sjur Refsdal. 'On the Possibility of Determining Hubble's Parameter and the Masses of Galaxies from the Gravitational Lens Effect'. In: *Monthly Notices of the Royal Astronomical Society* 128.4 (1964), p. 307. doi: [10.1093/mnras/128.4.307](https://doi.org/10.1093/mnras/128.4.307) (cited on pages 7, 28).
- [13] P. L. Kelly et al. 'Multiple images of a highly magnified supernova formed by an early-type cluster galaxy lens'. In: *Science* 347.6226 (Mar. 2015), pp. 1123–1126. doi: [10.1126/science.aaa3350](https://doi.org/10.1126/science.aaa3350) (cited on page 7).
- [14] A. Goobar et al. 'iPTF16geu: A multiply imaged, gravitationally lensed type Ia supernova'. In: *Science* 356.6335 (2017), pp. 291–295. doi: [10.1126/science.aal2729](https://doi.org/10.1126/science.aal2729) (cited on page 7).
- [15] S. Refsdal. 'On the Possibility of Testing Cosmological Theories from the Gravitational Lens Effect'. In: *Monthly Notices of the Royal Astronomical Society* 132.1 (Apr. 1966), pp. 101–111. doi: [10.1093/mnras/132.1.101](https://doi.org/10.1093/mnras/132.1.101) (cited on pages 7, 28).
- [16] M. Millon et al. *COSMOGRAIL XIX: Time delays in 18 strongly lensed quasars from 15 years of optical monitoring*. 2020 (cited on pages 7, 28, 32, 38, 114).

- [17] M. Millon et al. ‘TDCOSMO II: 6 new time delays in lensed quasars from high-cadence monitoring at the MPIA 2.2m telescope’. In: *arXiv e-prints*, arXiv:2006.10066 (June 2020), arXiv:2006.10066 (cited on pages 7, 28).
- [18] B. P. Abbott et al. ‘A gravitational-wave standard siren measurement of the Hubble constant’. In: *Nature* 551.7678 (Oct. 2017), pp. 85–88. doi: [10.1038/nature24471](https://doi.org/10.1038/nature24471) (cited on pages 8, 28).
- [19] I. Newton. *Opticks: Or, A Treatise of the Reflections, Refractions, Inflections and Colours of Light*. William Innys at the West-End of St. Paul’s, 1704 (cited on page 8).
- [20] Christiaan Huygens. *Treatise on Light, in which are explained the causes of that which occurs in reflexion, in refraction, and particularly in the strange refraction of Iceland crystal*. Chez Pierre vander Aa, marchand libraire, 1690 (cited on page 8).
- [21] Rajaram Nityananda and Joseph Samuel. ‘Fermat’s principle in general relativity’. In: *Physical Review D* 45.10 (May 1992), pp. 3862–3864. doi: [10.1103/physrevd.45.3862](https://doi.org/10.1103/physrevd.45.3862) (cited on page 8).
- [22] Irwin I. Shapiro. ‘Fourth Test of General Relativity’. In: *Physical Review Letters* 13.26 (Dec. 1964), pp. 789–791. doi: [10.1103/physrevlett.13.789](https://doi.org/10.1103/physrevlett.13.789) (cited on page 9).
- [23] R. Blandford and R. Narayan. ‘Fermat’s principle, caustics, and the classification of gravitational lens images’. In: *The Astrophysical Journal* 310 (Nov. 1986), pp. 568–582. doi: [10.1086/164709](https://doi.org/10.1086/164709) (cited on pages 9, 28, 73).
- [24] P. Young et al. ‘The double quasar Q0957+561 A, B - A gravitational lens image formed by a galaxy at z=0.39’. In: *The Astrophysical Journal* 241 (Oct. 1980), p. 507. doi: [10.1086/158365](https://doi.org/10.1086/158365) (cited on pages 12, 28, 71, 102).
- [25] P. Young et al. ‘The triple quasar Q1115+080A, B, C - A quintuple gravitational lens image’. In: *The Astrophysical Journal* 244 (Mar. 1981), pp. 723–735. doi: [10.1086/158750](https://doi.org/10.1086/158750) (cited on page 12).
- [26] Prasenjit Saha. ‘Lensing Degeneracies Revisited’. In: *Astronomical Journal* 120.4 (2000), p. 1654. doi: [10.1086/301581](https://doi.org/10.1086/301581) (cited on pages 12, 29, 61, 65, 71, 74).
- [27] Matthew R. Gomer and Liliya L. R. Williams. *Galaxy-lens determination of  $H_0$ : constraining density slope in the context of the mass sheet degeneracy*. 2019 (cited on pages 12, 44).
- [28] C S Kochanek. ‘Overconstrained gravitational lens models and the Hubble constant’. In: *Monthly Notices of the Royal Astronomical Society* 493.2 (Feb. 2020), pp. 1725–1735. doi: [10.1093/mnras/staa344](https://doi.org/10.1093/mnras/staa344) (cited on pages 12, 44).
- [29] David Harvey et al. ‘Exploiting flux ratio anomalies to probe warm dark matter in future large-scale surveys’. In: *Monthly Notices of the Royal Astronomical Society* 491.3 (Nov. 2019), pp. 4247–4253. doi: [10.1093/mnras/stz3305](https://doi.org/10.1093/mnras/stz3305) (cited on page 12).
- [30] S. J. Warren and S. Dye. ‘Semilinear Gravitational Lens Inversion’. In: *The Astrophysical Journal* 590.2 (June 2003), pp. 673–682. doi: [10.1086/375132](https://doi.org/10.1086/375132) (cited on pages 12, 78).
- [31] Matteo Barnabè and Leon V. E. Koopmans. ‘A Unifying Framework for Self-consistent Gravitational Lensing and Stellar Dynamics Analyses of Early-Type Galaxies’. In: *The Astrophysical Journal* 666.2 (Sept. 2007), pp. 726–746. doi: [10.1086/520495](https://doi.org/10.1086/520495) (cited on page 12).
- [32] Ignacio Ferreras, Prasenjit Saha, and Scott Burles. ‘Unveiling dark haloes in lensing galaxies’. In: *Monthly Notices of the Royal Astronomical Society* 383.3 (Dec. 2007), pp. 857–863. doi: [10.1111/j.1365-2966.2007.12606.x](https://doi.org/10.1111/j.1365-2966.2007.12606.x) (cited on pages 12, 109, 110).
- [33] A J Shajib et al. ‘STRIDES: a 3.9 per cent measurement of the Hubble constant from the strong lens system DES J0408-5354’. In: *Monthly Notices of the Royal Astronomical Society* 494.4 (Mar. 2020), pp. 6072–6102. doi: [10.1093/mnras/staa828](https://doi.org/10.1093/mnras/staa828) (cited on pages 12, 21, 29, 32, 39).
- [34] James Binney and Scott Tremaine. *Galactic Dynamics: Second Edition*. 2008 (cited on page 14).
- [35] F. Zwicky. ‘Die Rotverschiebung von extragalaktischen Nebeln’. In: *Helvetica Physica Acta* 6 (Jan. 1933), pp. 110–127 (cited on page 14).
- [36] H. C. van de Hulst. ‘Observations of the interstellar hydrogen line of wave length 21 CM made at Kootwijk, Netherlands.’ In: *The Astronomical Journal* 56 (Oct. 1951), p. 144. doi: [10.1086/106564](https://doi.org/10.1086/106564) (cited on page 14).

- [37] C. A. Muller and J. H. Oort. ‘Observation of a Line in the Galactic Radio Spectrum: The Interstellar Hydrogen Line at 1,420 Mc./sec., and an Estimate of Galactic Rotation’. In: *Nature* 168.4270 (Sept. 1951), pp. 357–358. doi: [10.1038/168357a0](https://doi.org/10.1038/168357a0) (cited on page 14).
- [38] H. C. van de Hulst, C. A. Muller, and J. H. Oort. ‘The spiral structure of the outer part of the Galactic System derived from the hydrogen emission at 21 cm wavelength’. In: *Bulletin of the Astronomical Institutes of the Netherlands* 12 (May 1954), p. 117 (cited on page 14).
- [39] P. L. Schechter. ‘Mass-to-light ratios for elliptical galaxies’. In: *The Astronomical Journal* 85 (July 1980), p. 801. doi: [10.1086/112742](https://doi.org/10.1086/112742) (cited on page 14).
- [40] R. L. Davies et al. ‘The kinematic properties of faint elliptical galaxies’. In: *The Astrophysical Journal* 266 (Mar. 1983), p. 41. doi: [10.1086/160757](https://doi.org/10.1086/160757) (cited on page 14).
- [41] Albert Bosma. ‘Hi in the Outskirts of Nearby Galaxies’. In: Springer International Publishing, 2017, pp. 209–254. doi: [10.1007/978-3-319-56570-5\\_7](https://doi.org/10.1007/978-3-319-56570-5_7) (cited on page 14).
- [42] Iminhaji Ablimit et al. ‘The Rotation Curve, Mass Distribution, and Dark Matter Content of the Milky Way from Classical Cepheids’. In: *The Astrophysical Journal* 895.1 (May 2020), p. L12. doi: [10.3847/2041-8213/ab8d45](https://doi.org/10.3847/2041-8213/ab8d45) (cited on page 14).
- [43] Marius Cautun et al. ‘The milky way total mass profile as inferred from Gaia DR2’. In: *Monthly Notices of the Royal Astronomical Society* 494.3 (Apr. 2020), pp. 4291–4313. doi: [10.1093/mnras/staa1017](https://doi.org/10.1093/mnras/staa1017) (cited on page 14).
- [44] Jo Bovy. ‘Galactic rotation in Gaia DR1’. In: *Monthly Notices of the Royal Astronomical Society: Letters* 468.1 (Feb. 2017), pp. L63–L67. doi: [10.1093/mnrasl/slx027](https://doi.org/10.1093/mnrasl/slx027) (cited on page 15).
- [45] Alis J Deason et al. ‘The edge of the Galaxy’. In: *Monthly Notices of the Royal Astronomical Society* 496.3 (June 2020), pp. 3929–3942. doi: [10.1093/mnras/staa1711](https://doi.org/10.1093/mnras/staa1711) (cited on page 15).
- [46] K. Migkas et al. ‘Probing cosmic isotropy with a new X-ray galaxy cluster sample through the LX-T scaling relation’. In: *Astronomy & Astrophysics* 636 (Apr. 2020), A15. doi: [10.1051/0004-6361/201936602](https://doi.org/10.1051/0004-6361/201936602) (cited on page 16).
- [47] Benjamin P. Moster, Thorsten Naab, and Simon D. M. White. ‘Galactic star formation and accretion histories from matching galaxies to dark matter haloes’. In: *Monthly Notices of the Royal Astronomical Society* 428.4 (Dec. 2012), pp. 3121–3138. doi: [10.1093/mnras/sts261](https://doi.org/10.1093/mnras/sts261) (cited on pages 17, 18).
- [48] Rafael Küng et al. ‘Models of gravitational lens candidates from Space Warps CFHTLS’. In: *Monthly Notices of the Royal Astronomical Society* 474.3 (2018), pp. 3700–3713. doi: [10.1093/mnras/stx3012](https://doi.org/10.1093/mnras/stx3012) (cited on pages 18, 21, 34, 36, 40, 58, 61, 71, 77, 102).
- [49] Rafael Küng. ‘SPAGHETTILENS: A software stack for modeling gravitational lenses by citizen scientists’. In: *Astronomy and Computing* 23, 115 (Apr. 2018), p. 115. doi: [10.1016/j.ascom.2018.02.007](https://doi.org/10.1016/j.ascom.2018.02.007) (cited on pages 18, 71).
- [50] Jonathan P. Coles, Justin I. Read, and Prasenjit Saha. ‘Gravitational lens recovery with glass: measuring the mass profile and shape of a lens’. In: *Monthly Notices of the Royal Astronomical Society* 445.3 (2014), p. 2181. doi: [10.1093/mnras/stu1781](https://doi.org/10.1093/mnras/stu1781) (cited on pages 19, 34, 61, 72, 76, 102, 105).
- [51] Philipp Denzel. *gleam: Gravitational Lens Extended Analysis Module*. [Online; accessed October 6, 2020]. 2020. URL: <https://github.com/phdenzel/gleam> (cited on pages 20, 24).
- [52] Kenneth C Wong et al. ‘H0LiCOW XIII. A 2.4% measurement of H0 from lensed quasars: 5.3 $\sigma$  tension between early and late-Universe probes’. In: *Monthly Notices of the Royal Astronomical Society* (June 2020). doi: [10.1093/mnras/stz3094](https://doi.org/10.1093/mnras/stz3094) (cited on pages 21, 29, 32).
- [53] X. Ding et al. ‘Time Delay Lens modelling Challenge: II. Results’. In: *arXiv e-prints*, arXiv:2006.08619 (June 2020), arXiv:2006.08619 (cited on pages 21, 29, 37, 44, 102).
- [54] Narciso Benítez. ‘Bayesian Photometric Redshift Estimation’. In: *The Astrophysical Journal* 536.2 (2000), p. 571 (cited on pages 21, 58).
- [55] G. Bruzual and S. Charlot. ‘Stellar population synthesis at the resolution of 2003’. In: *Monthly Notices of the Royal Astronomical Society* 344.4 (2003), pp. 1000–1028. doi: [10.1046/j.1365-8711.2003.06897.x](https://doi.org/10.1046/j.1365-8711.2003.06897.x) (cited on pages 22, 63).

- [56] Gilles Chabrier. ‘Galactic Stellar and Substellar Initial Mass Function’. In: *Publications of the Astronomical Society of the Pacific* 115.809 (2003), p. 763 (cited on pages 22, 63).
- [57] Philip F. Hopkins et al. ‘Galaxies on FIRE (Feedback In Realistic Environments): stellar feedback explains cosmologically inefficient star formation’. In: *Monthly Notices of the Royal Astronomical Society* 445.1 (Sept. 2014), pp. 581–603. doi: [10.1093/mnras/stu1738](https://doi.org/10.1093/mnras/stu1738) (cited on pages 22, 57, 101).
- [58] Philipp Denzel et al. ‘The Hubble constant from eight time-delay galaxy lenses’. In: *arXiv e-prints*, arXiv:2007.14398 (July 2020), arXiv:2007.14398 (cited on pages 25, 102, 105).
- [59] Douglas Scott. *The Standard Model of Cosmology: A Skeptic’s Guide*. 2018 (cited on page 27).
- [60] L. Knox and M. Millea. ‘Hubble constant hunter’s guide’. In: *Physical Review D* 101.4 (Feb. 2020). doi: [10.1103/physrevd.101.043533](https://doi.org/10.1103/physrevd.101.043533) (cited on page 28).
- [61] A. Sandage et al. ‘The Hubble Constant: A Summary of the Hubble Space Telescope Program for the Luminosity Calibration of Type Ia Supernovae by Means of Cepheids’. In: *The Astrophysical Journal* 653.2 (Dec. 2006), pp. 843–860. doi: [10.1086/508853](https://doi.org/10.1086/508853) (cited on page 28).
- [62] Wendy L. Freedman et al. ‘Carnegie Hubble Program: A Mid-Infrared Calibration of the Hubble Constant’. In: *The Astrophysical Journal* 758.1 (Sept. 2012), p. 24. doi: [10.1088/0004-637x/758/1/24](https://doi.org/10.1088/0004-637x/758/1/24) (cited on page 28).
- [63] Adam G. Riess et al. ‘A 2.4% Determination of the Local Value of the Hubble Constant’. In: *The Astrophysical Journal* 826.1 (July 2016), p. 56. doi: [10.3847/0004-637x/826/1/56](https://doi.org/10.3847/0004-637x/826/1/56) (cited on page 28).
- [64] Adam G. Riess et al. ‘Milky Way Cepheid Standards for Measuring Cosmic Distances and Application to Gaia DR2: Implications for the Hubble Constant’. In: *The Astrophysical Journal* 861.2 (Aug. 2018), p. 126. doi: [10.3847/1538-4357/aac82e](https://doi.org/10.3847/1538-4357/aac82e) (cited on page 28).
- [65] G. Pietrzyński et al. ‘A distance to the Large Magellanic Cloud that is precise to one per cent’. In: *Nature* 567.7747 (Mar. 2019), pp. 200–203. doi: [10.1038/s41586-019-0999-4](https://doi.org/10.1038/s41586-019-0999-4) (cited on page 28).
- [66] M. J. Reid, D. W. Pesce, and A. G. Riess. ‘An Improved Distance to NGC 4258 and Its Implications for the Hubble Constant’. In: *The Astrophysical Journal* 886.2 (Nov. 2019), p. L27. doi: [10.3847/2041-8213/ab552d](https://doi.org/10.3847/2041-8213/ab552d) (cited on page 28).
- [67] Wendy L. Freedman et al. ‘The Carnegie-Chicago Hubble Program. VIII. An Independent Determination of the Hubble Constant Based on the Tip of the Red Giant Branch’. In: *The Astrophysical Journal* 882.1 (Aug. 2019), p. 34. doi: [10.3847/1538-4357/ab2f73](https://doi.org/10.3847/1538-4357/ab2f73) (cited on pages 28, 30, 52).
- [68] G. Hinshaw et al. ‘Nine-year Wilkinson Microwave Anisotropy Probe (WMAP) Observations: Cosmological Parameter Results’. In: *The Astrophysical Journal, Supplement* 208.2, 19 (Oct. 2013), p. 19. doi: [10.1088/0067-0049/208/2/19](https://doi.org/10.1088/0067-0049/208/2/19) (cited on page 28).
- [69] T. M. C. Abbott et al. ‘Dark Energy Survey year 1 results: Cosmological constraints from galaxy clustering and weak lensing’. In: *Phys. Rev. D* 98 (4 Aug. 2018), p. 043526. doi: [10.1103/PhysRevD.98.043526](https://doi.org/10.1103/PhysRevD.98.043526) (cited on page 28).
- [70] T M C Abbott et al. ‘Dark Energy Survey Year 1 Results: A Precise H0 Estimate from DES Y1, BAO, and D/H Data’. In: *Monthly Notices of the Royal Astronomical Society* 480.3 (July 2018), pp. 3879–3888. doi: [10.1093/mnras/sty1939](https://doi.org/10.1093/mnras/sty1939) (cited on page 28).
- [71] Justin Alsing, Alan Heavens, and Andrew H. Jaffe. ‘Cosmological parameters, shear maps and power spectra from CFHTLenS using Bayesian hierarchical inference’. In: *Monthly Notices of the Royal Astronomical Society* 466.3 (Dec. 2016), pp. 3272–3292. doi: [10.1093/mnras/stw3161](https://doi.org/10.1093/mnras/stw3161) (cited on page 28).
- [72] H Hildebrandt et al. ‘KiDS-450: cosmological parameter constraints from tomographic weak gravitational lensing’. In: *Monthly Notices of the Royal Astronomical Society* 465.2 (Oct. 2016), pp. 1454–1498. doi: [10.1093/mnras/stw2805](https://doi.org/10.1093/mnras/stw2805) (cited on page 28).
- [73] Lauren Anderson et al. ‘The clustering of galaxies in the SDSS-III Baryon Oscillation Spectroscopic Survey: baryon acoustic oscillations in the Data Release 9 spectroscopic galaxy sample’. In: *Monthly Notices of the Royal Astronomical Society* 427.4 (Dec. 2012), pp. 3435–3467. doi: [10.1111/j.1365-2966.2012.22066.x](https://doi.org/10.1111/j.1365-2966.2012.22066.x) (cited on page 28).

- [74] Prasenjit Saha and Liliya L. R. Williams. ‘Gravitational Lensing Model Degeneracies: Is Steepness All-Important?’ In: *The Astrophysical Journal* 653.2 (2006), p. 936 (cited on pages 28, 61, 65, 71).
- [75] Peter Schneider and Dominique Sluse. ‘Source-position transformation: an approximate invariance in strong gravitational lensing’. In: *Astronomy and Astrophysics* 564, A103 (Apr. 2014), A103. doi: [10.1051/0004-6361/201322106](https://doi.org/10.1051/0004-6361/201322106) (cited on pages 28, 71).
- [76] Jenny Wagner. ‘Generalised model-independent characterisation of strong gravitational lenses’. In: *Astronomy & Astrophysics* 620 (Dec. 2018), A86. doi: [10.1051/0004-6361/201834218](https://doi.org/10.1051/0004-6361/201834218) (cited on pages 28, 105).
- [77] Philipp Denzel et al. ‘Lessons from a blind study of simulated lenses: image reconstructions do not always reproduce true convergence’. In: *Monthly Notices of the Royal Astronomical Society* 492.3 (Jan. 2020), pp. 3885–3903. doi: [10.1093/mnras/staa108](https://doi.org/10.1093/mnras/staa108) (cited on pages 28, 34, 36, 43, 62, 69, 102, 105, 113).
- [78] Agniva Ghosh, Liliya L R Williams, and Jori Liesenborgs. ‘Free-form gralre lens inversion of galaxy clusters with up to 1000 multiple images’. In: *Monthly Notices of the Royal Astronomical Society* 494.3 (Apr. 2020), pp. 3998–4014. doi: [10.1093/mnras/staa962](https://doi.org/10.1093/mnras/staa962) (cited on pages 29, 44).
- [79] Mauro Sereno and Danuta Paraficz. ‘Hubble constant and dark energy inferred from free-form determined time delay distances’. In: *Monthly Notices of the Royal Astronomical Society* 437.1 (2014), p. 600. doi: [10.1093/mnras/stt1938](https://doi.org/10.1093/mnras/stt1938) (cited on pages 29, 34, 71).
- [80] S. Birrer et al. *TDCOSMO IV: Hierarchical time-delay cosmography – joint inference of the Hubble constant and galaxy density profiles*. 2020 (cited on page 29).
- [81] Rouzbeh Allahverdi et al. ‘The First Three Seconds: a Review of Possible Expansion Histories of the Early Universe’. In: *arXiv e-prints*, arXiv:2006.16182 (June 2020), arXiv:2006.16182 (cited on page 29).
- [82] Robert Lupton et al. ‘Preparing Red-Green-Blue Images from CCD Data’. In: *Publications of the Astronomical Society of the Pacific* 116.816 (2004), p. 133 (cited on pages 31, 59).
- [83] S. T. Myers et al. ‘1608+656: A Quadruple-Lens System Found in the CLASS Gravitational Lens Survey’. In: *The Astrophysical Journal* 447.1 (July 1995). doi: [10.1086/309556](https://doi.org/10.1086/309556) (cited on page 30).
- [84] C. D. Fassnacht et al. ‘1608+656: A Gravitationally Lensed PostStarburst Radio Galaxy’. In: *The Astrophysical Journal* 460.2 (Apr. 1996). doi: [10.1086/309984](https://doi.org/10.1086/309984) (cited on page 30).
- [85] C. D. Fassnacht et al. ‘A Determination of  $H_0$  with the CLASS Gravitational Lens B1608+656. I. Time Delay Measurements with the VLA’. In: *The Astrophysical Journal* 527.2 (Dec. 1999), pp. 498–512. doi: [10.1086/308118](https://doi.org/10.1086/308118) (cited on pages 30, 38).
- [86] C. D. Fassnacht et al. *Measuring  $H_0$  with CLASS B1608+656: The Second Season of VLA Monitoring*. 1999 (cited on page 30).
- [87] C. D. Fassnacht et al. ‘A Determination of  $H_0$  with the CLASS Gravitational Lens B1608+656. III. A Significant Improvement in the Precision of the Time Delay Measurements’. In: *The Astrophysical Journal* 581.2 (Dec. 2002), pp. 823–835. doi: [10.1086/344368](https://doi.org/10.1086/344368) (cited on pages 30, 38).
- [88] E. Eulaers and P. Magain. ‘Time delays for eleven gravitationally lensed quasars revisited’. In: *Astronomy & Astrophysics* 536 (Dec. 2011), A44. doi: [10.1051/0004-6361/201016101](https://doi.org/10.1051/0004-6361/201016101) (cited on pages 30, 38).
- [89] R.F.L. Holanda. ‘The robustness of angular diameter distances to the lens in the B1608+656 and RXJ1131-1231 systems’. In: *Astroparticle Physics* 84 (Nov. 2016), pp. 78–81. doi: [10.1016/j.astropartphys.2016.09.001](https://doi.org/10.1016/j.astropartphys.2016.09.001) (cited on pages 30, 33).
- [90] L. V. E. Koopmans and C. D. Fassnacht. ‘A Determination of  $H_0$  with the CLASS Gravitational Lens B1608+656. II. Mass Models and the Hubble Constant from Lensing’. In: *The Astrophysical Journal* 527.2 (Dec. 1999), pp. 513–524. doi: [10.1086/308120](https://doi.org/10.1086/308120) (cited on pages 32, 38).
- [91] Liliya L. R. Williams and Prasenjit Saha. ‘Pixelated Lenses and  $H_0$  from Time-Delay Quasars’. In: *Astronomical Journal* 119.2 (Feb. 2000), pp. 439–450. doi: [10.1086/301234](https://doi.org/10.1086/301234) (cited on pages 32, 71).
- [92] L. V. E. Koopmans et al. ‘The Hubble Constant from the Gravitational Lens B1608+656I’. In: *The Astrophysical Journal* 599.1 (Dec. 2003), pp. 70–85. doi: [10.1086/379226](https://doi.org/10.1086/379226) (cited on pages 32, 38).

- [93] Chris Fassnacht et al. ‘Galaxy Groups Associated with Gravitational Lenses and  $H_0$  from B1608+656’. In: *Proceedings of the International Astronomical Union* 2004.IAUS225 (July 2004), pp. 311–317. doi: [10.1017/s1743921305002115](https://doi.org/10.1017/s1743921305002115) (cited on page 32).
- [94] S. H. Suyu et al. ‘Dissecting the Gravitational Lens B1608+656. II. Precision Measurements of the Hubble Constant, Spatial Curvature, and the Dark Energy Equation of State’. In: *The Astrophysical Journal* 711.1 (Feb. 2010), pp. 201–221. doi: [10.1088/0004-637x/711/1/201](https://doi.org/10.1088/0004-637x/711/1/201) (cited on page 32).
- [95] H. Lin et al. ‘Discovery of the Lensed Quasar System DES J0408-5354’. In: *The Astrophysical Journal* 838.2 (Mar. 2017), p. L15. doi: [10.3847/2041-8213/aa624e](https://doi.org/10.3847/2041-8213/aa624e) (cited on pages 32, 38).
- [96] F. Courbin et al. ‘COSMOGRAIL: the COSmological MONitoring of GRAVItational Lenses’. In: *Astronomy & Astrophysics* 609 (Jan. 2018), A71. doi: [10.1051/0004-6361/201731461](https://doi.org/10.1051/0004-6361/201731461) (cited on pages 32, 38).
- [97] A. Agnello et al. ‘Models of the strongly lensed quasar DES J0408-5354’. In: *Monthly Notices of the Royal Astronomical Society* 472.4 (Sept. 2017), pp. 4038–4050. doi: [10.1093/mnras/stx2242](https://doi.org/10.1093/mnras/stx2242) (cited on page 32).
- [98] T Treu et al. ‘The STRong lensing Insights into the Dark Energy Survey (STRIDES) 2016 follow-up campaign – I. Overview and classification of candidates selected by two techniques’. In: *Monthly Notices of the Royal Astronomical Society* 481.1 (Aug. 2018), pp. 1041–1054. doi: [10.1093/mnras/sty2329](https://doi.org/10.1093/mnras/sty2329) (cited on page 32).
- [99] L. Wisotzki et al. ‘HE 0435-1223: A wide separation quadruple QSO and gravitational lens’. In: *Astronomy & Astrophysics* 395.1 (Oct. 2002), pp. 17–23. doi: [10.1051/0004-6361:20021213](https://doi.org/10.1051/0004-6361:20021213) (cited on page 32).
- [100] N. D. Morgan et al. ‘The Lens Redshift and Galaxy Environment for HE 0435-1223’. In: *The Astronomical Journal* 129.6 (June 2005), pp. 2531–2541. doi: [10.1086/430145](https://doi.org/10.1086/430145) (cited on page 32).
- [101] C. S. Kochanek et al. ‘The Time Delays of Gravitational Lens HE 0435-1223: An Early-Type Galaxy with a Rising Rotation Curve’. In: *The Astrophysical Journal* 640.1 (Mar. 2006), pp. 47–61. doi: [10.1086/499766](https://doi.org/10.1086/499766) (cited on pages 32, 38).
- [102] D. Sluse et al. ‘H0LiCOW — II. Spectroscopic survey and galaxy-group identification of the strong gravitational lens system HE 0435-1223’. In: *Monthly Notices of the Royal Astronomical Society* 470.4 (June 2017), pp. 4838–4857. doi: [10.1093/mnras/stx1484](https://doi.org/10.1093/mnras/stx1484) (cited on page 32).
- [103] Kenneth C. Wong et al. ‘H0LiCOW — IV. Lens mass model of HE 0435-1223 and blind measurement of its time-delay distance for cosmology’. In: *Monthly Notices of the Royal Astronomical Society* 465.4 (Nov. 2016), pp. 4895–4913. doi: [10.1093/mnras/stw3077](https://doi.org/10.1093/mnras/stw3077) (cited on page 32).
- [104] V. Bonvin et al. ‘H0LiCOW – V. New COSMOGRAIL time delays of HE 0435-1223:  $H_0$  to 3.8 per cent precision from strong lensing in a flat  $\Lambda$ CDM model’. In: *Monthly Notices of the Royal Astronomical Society* 465.4 (2017), p. 4914. doi: [10.1093/mnras/stw3006](https://doi.org/10.1093/mnras/stw3006) (cited on pages 32, 38).
- [105] O Tihonova et al. ‘H0LiCOW VIII. A weak-lensing measurement of the external convergence in the field of the lensed quasar HE0435-1223’. In: *Monthly Notices of the Royal Astronomical Society* 477.4 (Apr. 2018), pp. 5657–5669. doi: [10.1093/mnras/sty1040](https://doi.org/10.1093/mnras/sty1040) (cited on page 32).
- [106] A. M. Nierenberg et al. ‘Probing dark matter substructure in the gravitational lens HE 0435-1223 with the WFC3 grism’. In: *Monthly Notices of the Royal Astronomical Society* 471.2 (June 2017), pp. 2224–2236. doi: [10.1093/mnras/stx1400](https://doi.org/10.1093/mnras/stx1400) (cited on page 32).
- [107] Ray J. Weymann et al. ‘The triple QSO PG1115 + 08: another probable gravitational lens’. In: *Nature* 285.5767 (June 1980), pp. 641–643. doi: [10.1038/285641a0](https://doi.org/10.1038/285641a0) (cited on pages 32, 38).
- [108] C. A. Christian, D. Crabtree, and P. Waddell. ‘Detection of the lensing galaxy in PG 1115 + 080’. In: *The Astrophysical Journal* 312 (Jan. 1987), p. 45. doi: [10.1086/164847](https://doi.org/10.1086/164847) (cited on page 32).
- [109] Tomislav Kundic et al. ‘Keck Spectroscopy of the Gravitational Lens System PG 1115+080: Redshifts of the Lensing Galaxies.’ In: *The Astronomical Journal* 114 (Aug. 1997), p. 507. doi: [10.1086/118489](https://doi.org/10.1086/118489) (cited on page 32).

- [110] John L. Tonry. ‘Redshifts of the Gravitational Lenses B1422+231 and PG 1115+080’. In: *The Astronomical Journal* 115.1 (Jan. 1998), pp. 1–5. doi: [10.1086/300170](https://doi.org/10.1086/300170) (cited on pages 32, 38).
- [111] Paul L. Schechter et al. ‘The Quadruple Gravitational Lens PG 1115+080: Time Delays and Models’. In: *The Astrophysical Journal* 475.2 (Feb. 1997), pp. L85–L88. doi: [10.1086/310478](https://doi.org/10.1086/310478) (cited on page 32).
- [112] Rennan Barkana. ‘Analysis of Time Delays in the Gravitational Lens PG 1115+080’. In: *The Astrophysical Journal* 489.1 (Nov. 1997), pp. 21–28. doi: [10.1086/304766](https://doi.org/10.1086/304766) (cited on pages 32, 38).
- [113] V. Bonvin et al. ‘COSMOGRAIL’. In: *Astronomy & Astrophysics* 616 (Aug. 2018), A183. doi: [10.1051/0004-6361/201833287](https://doi.org/10.1051/0004-6361/201833287) (cited on page 32).
- [114] N. Bade et al. ‘RX J0911.4+0551: A new multiple QSO selected from the ROSAT All-Sky Survey.’ In: *Astronomy and Astrophysics* 317 (Jan. 1997), pp. L13–L16 (cited on pages 33, 38).
- [115] I. Burud et al. ‘RX J0911.4+0551: a complex quadruply imaged gravitationally lensed QSO.’ In: *The Messenger* 92 (June 1998), pp. 29–32 (cited on pages 33, 38).
- [116] Jean-Paul Kneib, Judith G. Cohen, and Jens Hjorth. ‘RX J0911+05: A Massive Cluster Lens at z=0.769’. In: *The Astrophysical Journal* 544.1 (Nov. 2000), pp. L35–L39. doi: [10.1086/317285](https://doi.org/10.1086/317285) (cited on page 33).
- [117] Jens Hjorth et al. ‘The Time Delay of the Quadruple Quasar RX J0911.4+0551’. In: *The Astrophysical Journal* 572.1 (June 2002), pp. L11–L14. doi: [10.1086/341603](https://doi.org/10.1086/341603) (cited on pages 33, 38).
- [118] D. Sluse et al. ‘A quadruply imaged quasar with an optical Einstein ring candidate: 1RXS J113155.4–123155’. In: *Astronomy & Astrophysics* 406.2 (Aug. 2003), pp. L43–L46. doi: [10.1051/0004-6361:20030904](https://doi.org/10.1051/0004-6361:20030904) (cited on pages 33, 38).
- [119] D. Sluse et al. ‘Multi-wavelength study of the gravitational lens system RXS J1131-1231’. In: *Astronomy & Astrophysics* 468.3 (Mar. 2007), pp. 885–901. doi: [10.1051/0004-6361:20066821](https://doi.org/10.1051/0004-6361:20066821) (cited on pages 33, 38).
- [120] J.-F. Claeskens et al. ‘Multi wavelength study of the gravitational lens system RXS J1131-1231’. In: *Astronomy & Astrophysics* 451.3 (May 2006), pp. 865–879. doi: [10.1051/0004-6361:20054352](https://doi.org/10.1051/0004-6361:20054352) (cited on page 33).
- [121] S. H. Suyu et al. ‘Two Accurate Time-Delay Distances from Strong LensingL Implications for Cosmology’. In: *The Astrophysical Journal* 766.2 (Mar. 2013), p. 70. doi: [10.1088/0004-637x/766/2/70](https://doi.org/10.1088/0004-637x/766/2/70) (cited on page 33).
- [122] M. Tewes et al. ‘COSMOGRAIL: the COSmological MONitoring of GRAVItational Lenses’. In: *Astronomy & Astrophysics* 556 (July 2013), A22. doi: [10.1051/0004-6361/201220352](https://doi.org/10.1051/0004-6361/201220352) (cited on pages 33, 38).
- [123] Simon Birrer, Adam Amara, and Alexandre Refregier. ‘The mass-sheet degeneracy and time-delay cosmography: analysis of the strong lens RXJ1131-1231’. In: *Journal of Cosmology and Astroparticle Physics* 2016.08 (Aug. 2016), pp. 020–020. doi: [10.1088/1475-7516/2016/08/020](https://doi.org/10.1088/1475-7516/2016/08/020) (cited on pages 33, 38).
- [124] Simon Birrer, Adam Amara, and Alexandre Refregier. ‘Lensing substructure quantification in RXJ1131-1231: a 2 keV lower bound on dark matter thermal relic mass’. In: *Journal of Cosmology and Astroparticle Physics* 2017.05 (May 2017), pp. 037–037. doi: [10.1088/1475-7516/2017/05/037](https://doi.org/10.1088/1475-7516/2017/05/037) (cited on page 33).
- [125] S. H. Suyu et al. ‘H0LiCOW – I. H0 Lenses in COSMOGRAIL’s Wellspring: program overview’. In: *Monthly Notices of the Royal Astronomical Society* 468.3 (Feb. 2017), pp. 2590–2604. doi: [10.1093/mnras/stx483](https://doi.org/10.1093/mnras/stx483) (cited on pages 33, 71).
- [126] Naohisa Inada et al. ‘A gravitationally lensed quasar with quadrupole images separated by 14.62 arcseconds’. In: *Nature* 426.6968 (Dec. 2003), pp. 810–812. doi: [10.1038/nature02153](https://doi.org/10.1038/nature02153) (cited on pages 33, 38).
- [127] Masamune Oguri et al. ‘Observations and Theoretical Implications of the Large-Separation Lensed Quasar SDSS J1004+4112’. In: *The Astrophysical Journal* 605.1 (Apr. 2004), pp. 78–97. doi: [10.1086/382221](https://doi.org/10.1086/382221) (cited on pages 33, 38).
- [128] Liliya L. R. Williams and Prasenjit Saha. ‘Models of the Giant Quadrupole Quasar SDSS J1004+4112’. In: *The Astronomical Journal* 128.6 (Dec. 2004), pp. 2631–2641. doi: [10.1086/426007](https://doi.org/10.1086/426007) (cited on pages 33, 38).

- [129] Masamune Oguri. ‘The Mass Distribution of SDSS J1004+4112 Revisited’. In: *Publications of the Astronomical Society of Japan* 62.4 (Aug. 2010), pp. 1017–1024. doi: [10.1093/pasj/62.4.1017](https://doi.org/10.1093/pasj/62.4.1017) (cited on page 33).
- [130] Irshad Mohammed, Prasenjit Saha, and Jori Liesenborgs. ‘Lensing time delays as a substructure constraint: a case study with the cluster SDSS J1004+4112’. In: *Publications of the Astronomical Society of Japan* 67.2 (Mar. 2015). doi: [10.1093/pasj/psu155](https://doi.org/10.1093/pasj/psu155) (cited on pages 33, 40, 44).
- [131] J. Fohlmeister et al. ‘The Rewards of Patience: An 822 Day Time Delay in the Gravitational Lens SDSS J1004+4112’. In: *The Astrophysical Journal* 676.2 (Apr. 2008), pp. 761–766. doi: [10.1086/528789](https://doi.org/10.1086/528789) (cited on pages 33, 38).
- [132] J. Fohlmeister et al. ‘A Time Delay for the Cluster-lensed Quasar SDSS J1004+4112’. In: *The Astrophysical Journal* 662.1 (June 2007), pp. 62–71. doi: [10.1086/518018](https://doi.org/10.1086/518018) (cited on pages 33, 38).
- [133] Nicholas D. Morgan et al. ‘WFI J2026-4536 and WFI J2033-4723: Two New Quadruple Gravitational Lenses’. In: *The Astronomical Journal* 127.5 (May 2004), pp. 2617–2630. doi: [10.1086/383295](https://doi.org/10.1086/383295) (cited on pages 33, 38).
- [134] A. Eigenbrod et al. ‘COSMOGRAIL: the COSmological MOnitoring of GRAVItational Lenses III. Redshift of the lensing galaxy in eight gravitationally lensed quasars’. In: *Astronomy & Astrophysics* 451.3 (May 2006), pp. 759–766. doi: [10.1051/0004-6361:20054454](https://doi.org/10.1051/0004-6361:20054454) (cited on pages 33, 38).
- [135] D. Sluse et al. ‘Microlensing of the broad line region in 17 lensed quasars’. In: *Astronomy and Astrophysics* 544, A62 (Aug. 2012), A62. doi: [10.1051/0004-6361/201219125](https://doi.org/10.1051/0004-6361/201219125) (cited on pages 34, 71).
- [136] V. Bonvin et al. ‘COSMOGRAIL XVIII: time delays of the quadruply lensed quasar WFI2033-4723’. In: *Astronomy & Astrophysics* 629 (Sept. 2019), A97. doi: [10.1051/0004-6361/201935921](https://doi.org/10.1051/0004-6361/201935921) (cited on pages 34, 38).
- [137] Rafael Küng et al. ‘Gravitational lens modelling in a citizen science context’. In: *Monthly Notices of the Royal Astronomical Society* 447.3 (2015), p. 2170. doi: [10.1093/mnras/stu2554](https://doi.org/10.1093/mnras/stu2554) (cited on pages 34, 61, 71).
- [138] Claudio Bruderer et al. ‘Light versus dark in strong-lens galaxies: dark matter haloes that are rounder than their stars’. In: *Monthly Notices of the Royal Astronomical Society* 456.1 (Feb. 2016), pp. 870–884. doi: [10.1093/mnras/stv2582](https://doi.org/10.1093/mnras/stv2582) (cited on page 34).
- [139] M. Lubini et al. ‘Cosmological parameter determination in free-form strong gravitational lens modelling’. In: *Monthly Notices of the Royal Astronomical Society* 437.3 (Jan. 2014), pp. 2461–2470. doi: [10.1093/mnras/stt2057](https://doi.org/10.1093/mnras/stt2057) (cited on page 34).
- [140] Prasenjit Saha and Liliya L. R. Williams. ‘A Portable Modeler of Lensed Quasars’. In: *Astronomical Journal* 127.5 (2004), p. 2604. doi: [10.1086/383544](https://doi.org/10.1086/383544) (cited on pages 34, 61, 71, 76, 105).
- [141] Prasenjit Saha et al. ‘The Hubble Time Inferred from 10 Time Delay Lenses’. In: *The Astrophysical Journal* 650.1 (Aug. 2006), pp. L17–L20. doi: [10.1086/507583](https://doi.org/10.1086/507583) (cited on pages 34, 102).
- [142] H. M. AbdelSalam, P. Saha, and L. L. R. Williams. ‘Non-parametric reconstruction of cluster mass distribution from strong lensing: modelling Abell 370’. In: *Monthly Notices of the Royal Astronomical Society* 294 (Apr. 1998), pp. 734–746. doi: [10.1046/j.1365-8711.1998.01356.x](https://doi.org/10.1046/j.1365-8711.1998.01356.x) (cited on pages 34, 76, 104).
- [143] Mario Lubini and Jonathan Coles. ‘A sampling strategy for high-dimensional spaces applied to free-form gravitational lensing’. In: *Monthly Notices of the Royal Astronomical Society* 425.4 (Oct. 2012), pp. 3077–3084. doi: [10.1111/j.1365-2966.2012.21673.x](https://doi.org/10.1111/j.1365-2966.2012.21673.x) (cited on pages 35, 61, 71).
- [144] D. Sluse et al. ‘COSMOGRAIL: the COSmological MOnitoring of GRAVItational Lenses’. In: *Astronomy & Astrophysics* 538 (Feb. 2012), A99. doi: [10.1051/0004-6361/201015844](https://doi.org/10.1051/0004-6361/201015844) (cited on page 38).
- [145] Christopher W. Morgan et al. ‘X-Ray and Optical Microlensing in the Lensed Quasar PG 1115+080’. In: *The Astrophysical Journal* 689.2 (Dec. 2008), pp. 755–761. doi: [10.1086/592767](https://doi.org/10.1086/592767) (cited on page 38).
- [146] Xuheng Ding et al. ‘Time Delay Lens Modeling Challenge: I. Experimental Design’. In: *arXiv e-prints*, arXiv:1801.01506 (Jan. 2018), arXiv:1801.01506 (cited on page 36).

- [147] Prasenjit Saha and Liliya L. R. Williams. ‘Qualitative Theory for Lensed QSOs’. In: *The Astronomical Journal* 125.6 (June 2003), pp. 2769–2782. doi: [10.1086/375204](https://doi.org/10.1086/375204) (cited on page 39).
- [148] P. Saha et al. ‘COSMOGRAIL: the COSmological MOnitoring of GRAVItational Lenses’. In: *Astronomy & Astrophysics* 450.2 (Apr. 2006), pp. 461–469. doi: [10.1051/0004-6361:20052929](https://doi.org/10.1051/0004-6361:20052929) (cited on page 39).
- [149] Danuta Paraficz and Jens Hjorth. ‘The Hubble Constant Inferred from 18 Time-delay Lenses’. In: *The Astrophysical Journal* 712.2 (Apr. 2010), pp. 1378–1384. doi: [10.1088/0004-637X/712/2/1378](https://doi.org/10.1088/0004-637X/712/2/1378) (cited on pages 39, 71).
- [150] V. Chantry, D. Sluse, and P. Magain. ‘COSMOGRAIL: the COSmological MOnitoring of GRAVItational Lenses’. In: *Astronomy & Astrophysics* 522 (Nov. 2010), A95. doi: [10.1051/0004-6361/200912971](https://doi.org/10.1051/0004-6361/200912971) (cited on page 39).
- [151] Raymond A. Wynne and Paul L. Schechter. *Robust modeling of quadruply lensed quasars (and random quartets) using Witt’s hyperbola*. 2018 (cited on page 39).
- [152] Jaiyul Yoo et al. ‘The Lens Galaxy in PG 1115+080 is an Ellipse’. In: *The Astrophysical Journal* 626.1 (June 2005), pp. 51–57. doi: [10.1086/429959](https://doi.org/10.1086/429959) (cited on page 39).
- [153] Prasenjit Saha, Liliya L. R. Williams, and Ignacio Ferreras. ‘Meso-Structure in Three Strong-lensing Systems’. In: *The Astrophysical Journal* 663.1 (July 2007), pp. 29–37. doi: [10.1086/518083](https://doi.org/10.1086/518083) (cited on page 39).
- [154] Yuan Yan and Marc G. Genton. ‘The Tukey g-and-h distribution’. In: *Significance* 16.3 (2019), pp. 12–13. doi: [10.1111/j.1740-9713.2019.01273.x](https://doi.org/10.1111/j.1740-9713.2019.01273.x) (cited on page 42).
- [155] Allan Sandage. ‘Current Problems in the Extragalactic Distance Scale.’ In: *The Astrophysical Journal* 127 (May 1958), p. 513. doi: [10.1086/146483](https://doi.org/10.1086/146483) (cited on page 43).
- [156] A. Sandage and G. A. Tammann. ‘Steps toward the Hubble constant. VIII - The global value’. In: *The Astrophysical Journal* 256 (May 1982), p. 339. doi: [10.1086/159911](https://doi.org/10.1086/159911) (cited on page 43).
- [157] G. de Vaucouleurs and Jr. Corwin H. G. ‘The distance of the Hercules supercluster from supernovae and SBC spirals, and the Hubble constant’. In: *The Astrophysical Journal* 297 (Oct. 1985), p. 23. doi: [10.1086/163499](https://doi.org/10.1086/163499) (cited on page 43).
- [158] Allan Sandage and G. A. Tammann. ‘Steps Toward the Hubble Constant. Calibration of the Linear Sizes of Extra-Galactic H II Regions’. In: *The Astrophysical Journal* 190 (June 1974), p. 525. doi: [10.1086/152906](https://doi.org/10.1086/152906) (cited on page 43).
- [159] R. A. Crain et al. ‘The EAGLE simulations of galaxy formation: calibration of subgrid physics and model variations’. In: *Monthly Notices of the Royal Astronomical Society* 450 (June 2015), pp. 1937–1961. doi: [10.1093/mnras/stv725](https://doi.org/10.1093/mnras/stv725) (cited on pages 57, 75, 101, 106, 107).
- [160] Mark Vogelsberger et al. ‘Introducing the Illustris Project: simulating the coevolution of dark and visible matter in the Universe’. In: *Monthly Notices of the Royal Astronomical Society* 444.2 (Aug. 2014), pp. 1518–1547. doi: [10.1093/mnras/stu1536](https://doi.org/10.1093/mnras/stu1536) (cited on pages 57, 101).
- [161] S. D. M. White and M. J. Rees. ‘Core condensation in heavy halos: a two-stage theory for galaxy formation and clustering’. In: *Monthly Notices of the Royal Astronomical Society* 183.3 (July 1978), pp. 341–358. doi: [10.1093/mnras/183.3.341](https://doi.org/10.1093/mnras/183.3.341) (cited on page 57).
- [162] R. B. Tully. ‘Nearby groups of galaxies. II - an all-sky survey within 3000 kilometers per second’. In: *The Astrophysical Journal* 321 (Oct. 1987), pp. 280–304. doi: [10.1086/165629](https://doi.org/10.1086/165629) (cited on page 57).
- [163] G. A. Mamon. ‘Merger Rates in Simulated and Observed Groups of Galaxies’. In: *Large Scale Structures of the Universe*. Ed. by J. Audouze et al. Vol. 130. IAU Symposium. 1988, p. 545 (cited on page 57).
- [164] E. Tempel et al. ‘Merging groups and clusters of galaxies from the SDSS data - The catalogue of groups and potentially merging systems’. In: *A&A* 602 (2017), A100. doi: [10.1051/0004-6361/201730499](https://doi.org/10.1051/0004-6361/201730499) (cited on page 57).
- [165] T. J. Ponman et al. ‘A possible fossil galaxy group’. In: *Nature* 369 (June 1994), pp. 462–464. doi: [10.1038/369462a0](https://doi.org/10.1038/369462a0) (cited on page 57).

- [166] L. R. Jones et al. ‘The nature and space density of fossil groups of galaxies’. In: *Monthly Notices of the Royal Astronomical Society* 343.2 (2003), pp. 627–638. doi: [10.1046/j.1365-8711.2003.06702.x](https://doi.org/10.1046/j.1365-8711.2003.06702.x) (cited on page 57).
- [167] Joshua E. Barnes. ‘Evolution of compact groups and the formation of elliptical galaxies’. In: *Nature* 338 (Mar. 1989), pp. 123–126. doi: [10.1038/338123a0](https://doi.org/10.1038/338123a0) (cited on page 57).
- [168] E. Díaz-Giménez, H. Muriel, and C. Mendes de Oliveira. ‘Fossil groups in the Millennium Simulation - Evolution of the brightest galaxies’. In: *A&A* 490.3 (2008), pp. 965–973. doi: [10.1051/0004-6361:200809760](https://doi.org/10.1051/0004-6361:200809760) (cited on page 57).
- [169] Walter A. Santos, Claudia Mendes de Oliveira, and Laerte Sodré Jr. ‘Fossil Groups in the Sloan Digital Sky Survey’. In: *Astronomical Journal* 134.4 (2007), p. 1551 (cited on page 57).
- [170] F. La Barbera et al. ‘The Nature of Fossil Galaxy Groups: Are They Really Fossils?’ In: *Astronomical Journal* 137.4 (2009), p. 3942 (cited on page 57).
- [171] A. Dariush et al. ‘The mass assembly of fossil groups of galaxies in the Millennium simulation’. In: *Monthly Notices of the Royal Astronomical Society* 382.1 (Nov. 2007), pp. 433–442. doi: [10.1111/j.1365-2966.2007.12385.x](https://doi.org/10.1111/j.1365-2966.2007.12385.x) (cited on page 57).
- [172] John S. Mulchaey. ‘X-Ray Properties of Groups of Galaxies’. In: *Annual Review of Astronomy and Astrophysics* 38.1 (2000), pp. 289–335. doi: [10.1146/annurev.astro.38.1.289](https://doi.org/10.1146/annurev.astro.38.1.289) (cited on page 57).
- [173] Ali A. Dariush et al. ‘The mass assembly of galaxy groups and the evolution of the magnitude gap’. In: *Monthly Notices of the Royal Astronomical Society* 405.3 (June 2010), pp. 1873–1887. doi: [10.1111/j.1365-2966.2010.16569.x](https://doi.org/10.1111/j.1365-2966.2010.16569.x) (cited on page 57).
- [174] S. Zarattini et al. ‘Fossil group origins’. In: *Astronomy & Astrophysics* 565 (May 2014), A116. doi: [10.1051/0004-6361/201323351](https://doi.org/10.1051/0004-6361/201323351) (cited on page 57).
- [175] M. Schirmer et al. ‘J0454-0309: evidence of a strong lensing fossil group falling into a poor galaxy cluster\*’. In: *A&A* 514 (May 2010), A60. doi: [10.1051/0004-6361/200913810](https://doi.org/10.1051/0004-6361/200913810) (cited on page 57).
- [176] M. W. Auger et al. ‘The Sloan Lens ACS Survey X. Stellar, Dynamical, and Total Mass Correlations of Massive Early-type Galaxies’. In: *The Astrophysical Journal* 724.1 (2010), p. 511. doi: [10.1088/0004-637X/724/1/511](https://doi.org/10.1088/0004-637X/724/1/511) (cited on pages 57, 71).
- [177] Dominik Leier et al. ‘Resolving the Baryon-fraction Profile in Lensing Galaxies’. In: *The Astrophysical Journal* 740.2 (2011), p. 97. doi: [10.1088/0004-637X/740/2/97](https://doi.org/10.1088/0004-637X/740/2/97) (cited on pages 57, 71).
- [178] Katherine E. Whitaker et al. ‘Resolved Star Formation on Sub-galactic Scales in a Merger at z = 1.7’. In: *The Astrophysical Journal* 790.2 (2014), p. 143. doi: [10.1088/0004-637x/790/2/143](https://doi.org/10.1088/0004-637x/790/2/143) (cited on page 57).
- [179] Dominik Leier et al. ‘Strong gravitational lensing and the stellar IMF of early-type galaxies’. In: *Monthly Notices of the Royal Astronomical Society* 459.4 (2016), p. 3677. doi: [10.1093/mnras/stw885](https://doi.org/10.1093/mnras/stw885) (cited on pages 57, 71, 114).
- [180] T. E. Collett et al. ‘Core or cusps: The central dark matter profile of a redshift one strong lensing cluster with a bright central image’. In: *The Astrophysical Journal* 843.2 (July 2017), p. 148. doi: [10.3847/1538-4357/aa76e6](https://doi.org/10.3847/1538-4357/aa76e6) (cited on page 57).
- [181] James W Nightingale et al. ‘Galaxy structure with strong gravitational lensing: decomposing the internal mass distribution of massive elliptical galaxies’. In: *Monthly Notices of the Royal Astronomical Society* (Aug. 2019). doi: [10.1093/mnras/stz2220](https://doi.org/10.1093/mnras/stz2220) (cited on page 57).
- [182] Lucas E. Johnson et al. ‘Using Strong Gravitational Lensing to Identify Fossil Group Progenitors’. In: *The Astrophysical Journal* 856.2 (2018), p. 131 (cited on page 58).
- [183] Anupreeta More et al. ‘Space Warps – II. New gravitational lens candidates from the CFHTLS discovered through citizen science’. In: *Monthly Notices of the Royal Astronomical Society* 455.2 (2016), p. 1191. doi: [10.1093/mnras/stv1965](https://doi.org/10.1093/mnras/stv1965) (cited on pages 58, 71).
- [184] D. Foreman-Mackey et al. ‘emcee: The MCMC Hammer’. In: *PASP* 125 (2013), pp. 306–312. doi: [10.1086/670067](https://doi.org/10.1086/670067) (cited on page 63).

- [185] E. E. Salpeter. ‘The Luminosity Function and Stellar Evolution’. In: *The Astrophysical Journal* 121 (Jan. 1955), p. 161. doi: [10.1086/145971](https://doi.org/10.1086/145971) (cited on page 63).
- [186] J. A. Cardelli, G. C. Clayton, and J. S. Mathis. ‘The determination of ultraviolet extinction from the optical and near-infrared’. In: *The Astrophysical Journal, Part 2 – Letters* 329 (June 1988), pp. L33–L37. doi: [10.1086/185171](https://doi.org/10.1086/185171) (cited on page 64).
- [187] J. A. Cardelli, G. C. Clayton, and J. S. Mathis. ‘The relationship between infrared, optical, and ultraviolet extinction’. In: *The Astrophysical Journal, Part 1* 345 (Oct. 1989), pp. 245–256. doi: [10.1086/167900](https://doi.org/10.1086/167900) (cited on page 64).
- [188] Robert Feldmann et al. ‘The formation of massive, quiescent galaxies at cosmic noon’. In: *Monthly Notices of the Royal Astronomical Society: Letters* 458.1 (Feb. 2016), pp. L14–L18. doi: [10.1093/mnrasl/slw014](https://doi.org/10.1093/mnrasl/slw014) (cited on page 66).
- [189] Robert Feldmann et al. ‘Colours, star formation rates and environments of star-forming and quiescent galaxies at the cosmic noon’. In: *Monthly Notices of the Royal Astronomical Society* 470.1 (May 2017), pp. 1050–1072. doi: [10.1093/mnras/stx1120](https://doi.org/10.1093/mnras/stx1120) (cited on page 66).
- [190] Stuart P. D. Gill, Alexander Knebe, and Brad K. Gibson. ‘The evolution of substructure - I. A new identification method’. In: *Monthly Notices of the Royal Astronomical Society* 351.2 (2004), pp. 399–409. doi: [10.1111/j.1365-2966.2004.07786.x](https://doi.org/10.1111/j.1365-2966.2004.07786.x) (cited on page 66).
- [191] Steffen R. Knollmann and Alexander Knebe. ‘AHF: Amiga’s Halo Finder’. In: *The Astrophysical Journal, Supplement* 182.2 (2009), p. 608 (cited on page 66).
- [192] Dominik Leier. ‘A lensing view on the Fundamental Plane’. In: *Monthly Notices of the Royal Astronomical Society* 400.2 (Dec. 2009), pp. 875–886. doi: [10.1111/j.1365-2966.2009.15493.x](https://doi.org/10.1111/j.1365-2966.2009.15493.x) (cited on page 67).
- [193] Léon V. E. Koopmans and Tommaso Treu. ‘The Structure and Dynamics of Luminous and Dark Matter in the Early-Type Lens Galaxy of 0047-281 at  $z = 0.485$ ’. In: *The Astrophysical Journal* 583.2 (Feb. 2003), pp. 606–615. doi: [10.1086/345423](https://doi.org/10.1086/345423) (cited on page 71).
- [194] Tommaso Treu and Léon V. E. Koopmans. ‘Massive Dark Matter Halos and Evolution of Early-Type Galaxies to  $z = 1$ ’. In: *The Astrophysical Journal* 611.2 (2004), p. 739. doi: [10.1086/422245](https://doi.org/10.1086/422245) (cited on page 71).
- [195] J. I. Read, P. Saha, and A. V. Macciò. ‘Radial Density Profiles of Time-Delay Lensing Galaxies’. In: *The Astrophysical Journal* 667.2 (Oct. 2007), pp. 645–654. doi: [10.1086/520714](https://doi.org/10.1086/520714) (cited on page 71).
- [196] L. V. E. Koopmans et al. ‘The Structure and Dynamics of Massive Early-Type Galaxies: On Homology, Isothermality, and Isotropy Inside One Effective Radius’. In: *The Astrophysical Journal* 703.1 (Sept. 2009), pp. L51–L54. doi: [10.1088/0004-637x/703/1/l51](https://doi.org/10.1088/0004-637x/703/1/l51) (cited on page 71).
- [197] Matteo Barnabè et al. ‘Two-dimensional kinematics of SLACS lenses – III. Mass structure and dynamics of early-type lens galaxies beyond  $z = 0.1$ ’. In: *Monthly Notices of the Royal Astronomical Society* 415.3 (Aug. 2011), pp. 2215–2232. doi: [10.1111/j.1365-2966.2011.18842.x](https://doi.org/10.1111/j.1365-2966.2011.18842.x) (cited on page 71).
- [198] A. M. Nierenberg et al. ‘Probing dark matter substructure in the gravitational lens HE 0435-1223 with the WFC3 grism’. In: *Monthly Notices of the Royal Astronomical Society* 471.2 (June 2017), pp. 2224–2236. doi: [10.1093/mnras/stx1400](https://doi.org/10.1093/mnras/stx1400) (cited on page 71).
- [199] S. H. Suyu and A. Halkola. ‘The halos of satellite galaxies: the companion of the massive elliptical lens SL2S544-0121’. In: *A&A* 524 (2010), A94. doi: [10.1051/0004-6361/201015481](https://doi.org/10.1051/0004-6361/201015481) (cited on page 71).
- [200] Mihai Tomozeiu et al. ‘Microlensing as a possible probe of event-horizon structure in quasars’. In: *Monthly Notices of the Royal Astronomical Society* 475.2 (Apr. 2018), pp. 1925–1936. doi: [10.1093/mnras/stx3166](https://doi.org/10.1093/mnras/stx3166) (cited on page 71).
- [201] D. Hutsemékers et al. ‘Constraining the geometry and kinematics of the quasar broad emission line region using gravitational microlensing. II. Comparing models with observations in the lensed quasar HE0435-1223’. In: *Astronomy and Astrophysics* 629, A43 (Sept. 2019), A43. doi: [10.1051/0004-6361/201731087](https://doi.org/10.1051/0004-6361/201731087) (cited on page 71).

- [202] Masamune Oguri and Philip J. Marshall. ‘Gravitationally lensed quasars and supernovae in future wide-field optical imaging surveys’. In: *Monthly Notices of the Royal Astronomical Society* 405.4 (2010), p. 2579. doi: [10.1111/j.1365-2966.2010.16639.x](https://doi.org/10.1111/j.1365-2966.2010.16639.x) (cited on page 71).
- [203] F. Lanusse et al. ‘CMU DeepLens: Deep Learning For Automatic Image-based Galaxy-Galaxy Strong Lens Finding’. In: *Monthly Notices of the Royal Astronomical Society* 473.3 (July 2017), pp. 3895–3906. doi: [10.1093/mnras/stx1665](https://doi.org/10.1093/mnras/stx1665) (cited on page 71).
- [204] C. Jacobs et al. ‘Finding strong lenses in CFHTLS using convolutional neural networks’. In: *Monthly Notices of the Royal Astronomical Society* 471.1 (June 2017), pp. 167–181. doi: [10.1093/mnras/stx1492](https://doi.org/10.1093/mnras/stx1492) (cited on page 71).
- [205] Philip J. Marshall et al. ‘Space Warps – I. Crowdsourcing the discovery of gravitational lenses’. In: *Monthly Notices of the Royal Astronomical Society* 455.2 (2016), p. 1171. doi: [10.1093/mnras/stv2009](https://doi.org/10.1093/mnras/stv2009) (cited on pages 71, 101).
- [206] J W Nightingale, S Dye, and Richard J Massey. ‘AutoLens: automated modeling of a strong lens’s light, mass, and source’. In: *Monthly Notices of the Royal Astronomical Society* 478.4 (May 2018), pp. 4738–4784. doi: [10.1093/mnras/sty1264](https://doi.org/10.1093/mnras/sty1264) (cited on pages 71, 113).
- [207] Yashar D. Hezaveh, Laurence Perreault Levasseur, and Philip J. Marshall. ‘Fast automated analysis of strong gravitational lenses with convolutional neural networks’. In: *Nature* 548 (2017), pp. 555–557. doi: [10.1038/nature23463](https://doi.org/10.1038/nature23463) (cited on pages 71, 113).
- [208] M. Meneghetti et al. ‘The Frontier Fields lens modelling comparison project’. In: *Monthly Notices of the Royal Astronomical Society* 472.3 (Dec. 2017), pp. 3177–3216. doi: [10.1093/mnras/stx2064](https://doi.org/10.1093/mnras/stx2064) (cited on pages 71, 113).
- [209] P. Saha and L. L. R. Williams. ‘Non-parametric reconstruction of the galaxy lens in PG 1115+080’. In: *Monthly Notices of the Royal Astronomical Society* 292 (Nov. 1997), p. 148. doi: [10.1093/mnras/292.1.148](https://doi.org/10.1093/mnras/292.1.148) (cited on page 71).
- [210] Joop Schaye et al. ‘The EAGLE project: simulating the evolution and assembly of galaxies and their environments’. In: *Monthly Notices of the Royal Astronomical Society* 446.1 (Nov. 2014), pp. 521–554. doi: [10.1093/mnras/stu2058](https://doi.org/10.1093/mnras/stu2058) (cited on pages 72, 75, 106, 107, 114).
- [211] Sampath Mukherjee et al. ‘SEAGLE – I. A pipeline for simulating and modelling strong lenses from cosmological hydrodynamic simulations’. In: *Monthly Notices of the Royal Astronomical Society* 479.3 (July 2018), pp. 4108–4125. doi: [10.1093/mnras/sty1741](https://doi.org/10.1093/mnras/sty1741) (cited on pages 72, 75, 76, 79, 101, 106, 108).
- [212] Frederic Courbin, Prasenjit Saha, and Paul L. Schechter. ‘Quasar Lensing’. In: *Gravitational Lensing: An Astrophysical Tool*. Berlin, Heidelberg: Springer Berlin Heidelberg, 2002, pp. 1–54. doi: [10.1007/3-540-45857-3\\_1](https://doi.org/10.1007/3-540-45857-3_1) (cited on page 73).
- [213] S. McAlpine et al. ‘The EAGLE simulations of galaxy formation: Public release of halo and galaxy catalogues’. In: *Astronomy and Computing* 15 (Apr. 2016), pp. 72–89. doi: [10.1016/j.ascom.2016.02.004](https://doi.org/10.1016/j.ascom.2016.02.004) (cited on pages 75, 106).
- [214] J. W. Trayford et al. ‘Colours and luminosities of  $z = 0.1$  galaxies in the EAGLE simulation’. In: *Monthly Notices of the Royal Astronomical Society* 452 (Sept. 2015), pp. 2879–2896. doi: [10.1093/mnras/stv1461](https://doi.org/10.1093/mnras/stv1461) (cited on page 75).
- [215] M. Furlong et al. ‘Evolution of galaxy stellar masses and star formation rates in the EAGLE simulations’. In: *Monthly Notices of the Royal Astronomical Society* 450 (July 2015), pp. 4486–4504. doi: [10.1093/mnras/stv852](https://doi.org/10.1093/mnras/stv852) (cited on page 75).
- [216] M. Furlong et al. ‘Size evolution of normal and compact galaxies in the EAGLE simulation’. In: *Monthly Notices of the Royal Astronomical Society* 465 (Feb. 2017), pp. 722–738. doi: [10.1093/mnras/stw2740](https://doi.org/10.1093/mnras/stw2740) (cited on page 75).
- [217] M. Schaller et al. ‘Baryon effects on the internal structure of  $\Lambda$ CDM haloes in the EAGLE simulations’. In: *Monthly Notices of the Royal Astronomical Society* 451 (Aug. 2015), pp. 1247–1267. doi: [10.1093/mnras/stv1067](https://doi.org/10.1093/mnras/stv1067) (cited on page 75).

- [218] J. Schaye et al. ‘The physics driving the cosmic star formation history’. In: *Monthly Notices of the Royal Astronomical Society* 402 (Mar. 2010), pp. 1536–1560. doi: [10.1111/j.1365-2966.2009.16029.x](https://doi.org/10.1111/j.1365-2966.2009.16029.x) (cited on pages 75, 107).
- [219] R. B. Metcalf and M. Petkova. ‘GLAMER - I. A code for gravitational lensing simulations with adaptive mesh refinement’. In: *Monthly Notices of the Royal Astronomical Society* 445 (Dec. 2014), pp. 1942–1953. doi: [10.1093/mnras/stu1859](https://doi.org/10.1093/mnras/stu1859) (cited on pages 75, 76, 106).
- [220] M. Petkova, R. B. Metcalf, and C. Giocoli. ‘GLAMER - II. Multiple-plane gravitational lensing’. In: *Monthly Notices of the Royal Astronomical Society* 445 (Dec. 2014), pp. 1954–1966. doi: [10.1093/mnras/stu1860](https://doi.org/10.1093/mnras/stu1860) (cited on pages 75, 76, 106).
- [221] N. Tessore, F. Bellagamba, and R. B. Metcalf. ‘LENSED: a code for the forward reconstruction of lenses and sources from strong lensing observations’. In: *Monthly Notices of the Royal Astronomical Society* 463 (Dec. 2016), pp. 3115–3128. doi: [10.1093/mnras/stw2212](https://doi.org/10.1093/mnras/stw2212) (cited on page 75).
- [222] F. Bellagamba, N. Tessore, and R. B. Metcalf. ‘Zooming into the Cosmic Horseshoe: new insights on the lens profile and the source shape’. In: *Monthly Notices of the Royal Astronomical Society* 464 (Feb. 2017), pp. 4823–4834. doi: [10.1093/mnras/stw2726](https://doi.org/10.1093/mnras/stw2726) (cited on page 75).
- [223] Sampath Mukherjee et al. ‘SEAGLE-II: Constraints on feedback models in galaxy formation from massive early type strong lens galaxies’. In: *arXiv e-prints*, arXiv:1901.01095 (Jan. 2019) (cited on pages 76, 106).
- [224] L. V. E. Koopmans et al. ‘The Sloan Lens ACS Survey. III. The Structure and Formation of Early-Type Galaxies and Their Evolution since  $z \sim 1$ '. In: *The Astrophysical Journal* 649 (Oct. 2006), pp. 599–615. doi: [10.1086/505696](https://doi.org/10.1086/505696) (cited on page 76).
- [225] Elisabeth R. Newton et al. ‘The Sloan Lens ACS Survey. XI. Beyond Hubble Resolution: Size, Luminosity, and Stellar Mass of Compact Lensed Galaxies at Intermediate Redshift’. In: *The Astrophysical Journal* 734.2 (June 2011), p. 104. doi: [10.1088/0004-637X/734/2/104](https://doi.org/10.1088/0004-637X/734/2/104) (cited on page 76).
- [226] S. Dye and S. J. Warren. ‘Decomposition of the Visible and Dark Matter in the Einstein Ring 0047-2808 by Semilinear Inversion’. In: *The Astrophysical Journal* 623.1 (Apr. 2005), pp. 31–41. doi: [10.1086/428340](https://doi.org/10.1086/428340) (cited on page 78).
- [227] B. J. Brewer and G. F. Lewis. ‘The Einstein Ring 0047-2808 Revisited: A Bayesian Inversion’. In: *The Astrophysical Journal* 651.1 (Nov. 2006), pp. 8–13. doi: [10.1086/507475](https://doi.org/10.1086/507475) (cited on page 78).
- [228] S. H. Suyu et al. ‘A Bayesian analysis of regularized source inversions in gravitational lensing’. In: *Monthly Notices of the Royal Astronomical Society* 371.2 (Aug. 2006), pp. 983–998. doi: [10.1111/j.1365-2966.2006.10733.x](https://doi.org/10.1111/j.1365-2966.2006.10733.x) (cited on page 78).
- [229] S. Vegetti and L. V. E. Koopmans. ‘Bayesian strong gravitational-lens modelling on adaptive grids: objective detection of mass substructure in Galaxies’. In: *Monthly Notices of the Royal Astronomical Society* 392.3 (Jan. 2009), pp. 945–963. doi: [10.1111/j.1365-2966.2008.14005.x](https://doi.org/10.1111/j.1365-2966.2008.14005.x) (cited on page 78).
- [230] Amitpal S. Tagore and Charles R. Keeton. ‘Statistical and systematic uncertainties in pixel-based source reconstruction algorithms for gravitational lensing’. In: *Monthly Notices of the Royal Astronomical Society* 445.1 (Sept. 2014), pp. 694–710. doi: [10.1093/mnras/stu1671](https://doi.org/10.1093/mnras/stu1671) (cited on page 78).
- [231] Stefan Behnel et al. ‘Cython: The best of both worlds’. In: *Computing in Science & Engineering* 13.2 (2011), pp. 31–39 (cited on pages 78, 105).
- [232] Eric Jones, Travis Oliphant, Pearu Peterson, et al. *SciPy: Open source scientific tools for Python*. [Online; accessed October 6, 2020]. 2001. URL: <http://www.scipy.org/> (cited on page 78).
- [233] Adam S. Bolton et al. ‘The Sloan Lens ACS Survey. I. A Large Spectroscopically Selected Sample of Massive Early-Type Lens Galaxies’. In: *The Astrophysical Journal* 638.2 (Feb. 2006), pp. 703–724. doi: [10.1086/498884](https://doi.org/10.1086/498884) (cited on pages 101, 108–110).
- [234] Adam S. Bolton et al. ‘The Sloan Lens ACS Survey. V. The Full ACS Strong-Lens Sample’. In: *The Astrophysical Journal* 682.2 (Aug. 2008), pp. 964–984. doi: [10.1086/589327](https://doi.org/10.1086/589327) (cited on pages 101, 108, 109).

- [235] Yiping Shu et al. 'The Sloan Lens ACS Survey. XIII. Discovery of 40 New Galaxy-scale Strong Lenses'. In: *The Astrophysical Journal* 851.1 (Dec. 2017), p. 48. doi: [10.3847/1538-4357/aa9794](https://doi.org/10.3847/1538-4357/aa9794) (cited on pages 101, 108–110).
- [236] Thomas E. Collett. 'The Population of Galaxy–Galaxy Strong Lenses in Forthcoming Optical Imaging Surveys'. In: *The Astrophysical Journal* 811.1 (2015), p. 20 (cited on page 101).
- [237] Andrew Davies, Stephen Serjeant, and Jane M Bromley. 'Using convolutional neural networks to identify gravitational lenses in astronomical images'. In: *Monthly Notices of the Royal Astronomical Society* 487.4 (May 2019), pp. 5263–5271. doi: [10.1093/mnras/stz1288](https://doi.org/10.1093/mnras/stz1288) (cited on page 101).
- [238] Eugene Vasiliev. 'AGAMA: action-based galaxy modelling architecture'. In: *Monthly Notices of the Royal Astronomical Society* 482.2 (Oct. 2018), pp. 1525–1544. doi: [10.1093/mnras/sty2672](https://doi.org/10.1093/mnras/sty2672) (cited on page 101).
- [239] Akin Yıldırım, Sherry H Suyu, and Aleksi Halkola. 'Time-delay cosmographic forecasts with strong lensing and JWST stellar kinematics'. In: *Monthly Notices of the Royal Astronomical Society* 493.4 (Feb. 2020), pp. 4783–4807. doi: [10.1093/mnras/staa498](https://doi.org/10.1093/mnras/staa498) (cited on page 102).
- [240] Jenny Wagner, Jori Liesenborgs, and David Eichler. 'Multiply imaged time-varying sources behind galaxy clusters'. In: *Astronomy & Astrophysics* 621 (Jan. 2019), A91. doi: [10.1051/0004-6361/201833530](https://doi.org/10.1051/0004-6361/201833530) (cited on page 102).
- [241] Matteo Barnabè et al. 'Crash-testing the cauldron code for joint lensing and dynamics analysis of early-type galaxies'. In: *Monthly Notices of the Royal Astronomical Society* 393.4 (Mar. 2009), pp. 1114–1126. doi: [10.1111/j.1365-2966.2008.14208.x](https://doi.org/10.1111/j.1365-2966.2008.14208.x) (cited on page 102).
- [242] Matthew R Gomer and Liliya L R Williams. 'The impact of  $\Lambda$ CDM substructure and baryon-dark matter transition on the image positions of quad galaxy lenses'. In: *Monthly Notices of the Royal Astronomical Society* 475.2 (Dec. 2017), pp. 1987–2002. doi: [10.1093/mnras/stx3294](https://doi.org/10.1093/mnras/stx3294) (cited on page 102).
- [243] John E. Krist, Richard N. Hook, and Felix Stoehr. '20 years of Hubble Space Telescope optical modeling using Tiny Tim'. In: SPIE, Sept. 2011. doi: [10.1117/12.892762](https://doi.org/10.1117/12.892762) (cited on page 104).
- [244] Mark Vogelsberger et al. 'A model for cosmological simulations of galaxy formation physics'. In: *Monthly Notices of the Royal Astronomical Society* 436.4 (Oct. 2013), pp. 3031–3067. doi: [10.1093/mnras/stt1789](https://doi.org/10.1093/mnras/stt1789) (cited on page 107).
- [245] Robert A. Crain et al. 'Galaxies - intergalactic medium interaction calculation - I. Galaxy formation as a function of large-scale environment'. In: *Monthly Notices of the Royal Astronomical Society* 399.4 (Nov. 2009), pp. 1773–1794. doi: [10.1111/j.1365-2966.2009.15402.x](https://doi.org/10.1111/j.1365-2966.2009.15402.x) (cited on page 107).
- [246] Marcel R. Haas et al. 'Physical properties of simulated galaxy populations at  $z \geq 2$  – II. Effects of cosmology, reionization and ISM physics'. In: *Monthly Notices of the Royal Astronomical Society* 435.4 (Sept. 2013), pp. 2955–2967. doi: [10.1093/mnras/stt1488](https://doi.org/10.1093/mnras/stt1488) (cited on page 107).
- [247] Claudio Dalla Vecchia and Joop Schaye. 'Simulating galactic outflows with thermal supernova feedback'. In: *Monthly Notices of the Royal Astronomical Society* 426.1 (Sept. 2012), pp. 140–158. doi: [10.1111/j.1365-2966.2012.21704.x](https://doi.org/10.1111/j.1365-2966.2012.21704.x) (cited on page 107).
- [248] Amandine M. C. Le Brun et al. 'Towards a realistic population of simulated galaxy groups and clusters'. In: *Monthly Notices of the Royal Astronomical Society* 441.2 (May 2014), pp. 1270–1290. doi: [10.1093/mnras/stu608](https://doi.org/10.1093/mnras/stu608) (cited on page 107).
- [249] P. Young et al. 'Q0957+561 - Detailed models of the gravitational lens effect'. In: *The Astrophysical Journal* 244 (Mar. 1981), p. 736. doi: [10.1086/158751](https://doi.org/10.1086/158751) (cited on page 113).